DISSERTATION / DOCTORAL THESIS

Titel der Dissertation /Title of the Doctoral Thesis

„Petrographic, geochemical and isotopic investigations of early Archean impact spherule layers from the Barberton Greenstone Belt "

verfasst von / submitted by

Seda Özdemir

angestrebter akademischer Grad / in partial fulfilment of the requirements for the degree of

Doktorin der Naturwissenschaften (Dr. rer. nat)

Wien, 2017 / Vienna 2017
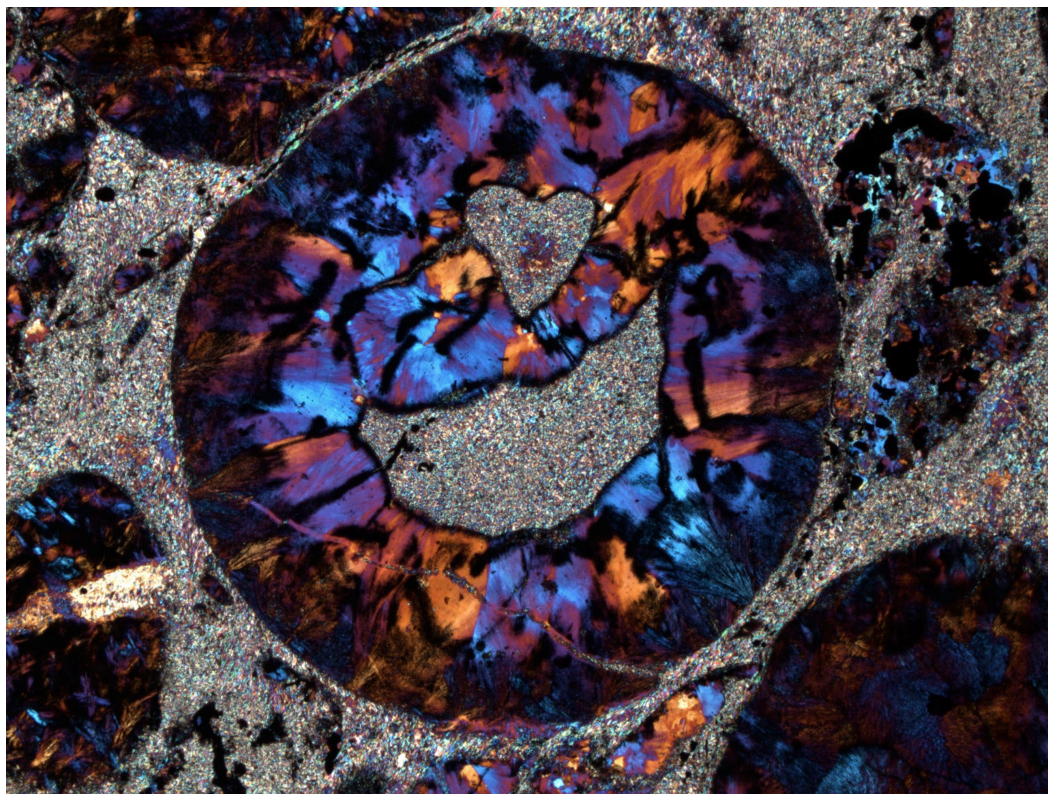
A smiley spherule from CT3 drill core at around 140 m depth.

The photo was taken by the thesis author.

THE HEART FOR SCIENCE!

This thesis is dedicated to my parents, Leyla and Faruk Özdemir and my uncle Arif Pecenek, I always miss you.

PREFACE

This thesis represents three years of work at the Department of Lithospheric Research, University of Vienna. The thesis discusses three main aspects related to the formation and development of impact spherule layers of the CT3 drill core from the Barberton Greenstone Belt (South Africa): 1) petrographic identification and classification of spherule layers as well as country rocks (chapter 3), 2) detection of traces of extraterrestrial components through determination of major/trace element compositions and geochemical comparison between spherule layers and country rocks (chapter 3), and finally, 3) using the Re-Os isotopic system as well as HSE abundances to obtain meteoritic signatures within spherule layers and to distinguish them from country rocks (chapter 4).

The results of the first two studies have been submitted to a peer-reviewed journal; Meteoritics & Planetary Science, currently in moderate revisions). The other manuscript is in progress to be submitted for publication in a peer-reviewed journal.

In addition to these chapters, the thesis contains an introduction of the impact cratering process and the impact spherules, and also a brief geological description of the Barberton Greenstone Belt (chapter 1). Finally, co-authored articles (chapter 5 and 6) related to this project are attached at the end of the thesis, which is concluded with the CV of the thesis' author.

ABSTRACT

In addition to the oldest known impact structure on Earth, the 2.02-billion-year-old Vredefort Structure in South Africa, the earliest evidence for impact processes on the Earth are Early Archean spherule beds, embedded in the 3.23 to 3.47-billion-year-old successions of the Barberton Greenstone Belt (BGB) South Africa, and the Pilbara Craton in Western Australia. These spherule layers, resulting from impacts by large extraterrestrial objects, represent the only known possible traces of the asteroid or and comet bombardment of the early Earth, and they have been interpreted as impact ejecta and may have formed as condensation products in the impact vapor plume and/or ballistically ejected liquid droplets.

Aiming at the identification of extraterrestrial components and the determination of diagenetic and metamorphic history of spherule layers, this study is focused on the CT3 drill core from the north-eastern BGB, South Africa, where 17 spherule layer intersections have been identified at various depths in the core. This work presents petrographic and geochemical data of spherule layers as well as their host rocks to provide new insight into the early terrestrial impact bombardment.

Chapter 3 of this thesis presents a full and detailed investigation of the seventeen spherule layers and intercalated country rocks regarding petrology and major and trace element geochemistry. This allows determining to identify alteration process, to study the depositional environment, to constrain any possible duplications of layers within the drill core, to classify the spherule layers and to correlate CT3 spherule layers with the other BGB spherule layers that have been investigated in previous studies. These mm-sized spherules have likely formed in a large meteorite impact event, with supporting evidence from the petrographic characteristics of the spherules being similar to previously investigated spherule layers from other parts of the BGB. The petrographic and geochemical findings indicate a moderate to strong hydrothermal overprint of all lithologies in the studied drill core section, at least in part, retained a meteoritic fingerprint. The impact hypothesis for the generation of the CT3 spherule layers is supported by correlations between the abundances of siderophile (Cr, Co, Ni, Ir) elements, whose peak concentrations and interelement ratios are within the range of those for chondrites.

Chapter 4 presents results of the Os isotopic and highly siderophile elements investigation of the CT3 layers, being complementary to Chapter 3 in order to investigate the possible presence of an extraterrestrial admixture within CT3 spherule layers. This study provides extremely enriched in highly siderophile element (Re, Os, Ir, Pt, Ru, and Pd) concentrations and rhenium-osmium isotope evidence for a chondritic projectile further support the impact

hypothesis. In addition, it cannot be excluded either that secondary effects, such as hydrothermal alteration and metamorphic overprint, may have affected the primary HSE element abundances of the spherule deposits.

The last two chapters 5 and 6 include two papers co-authored by the author of this thesis. These articles represent the investigations on four spherule layers from another drill core, the BARB5, from the central Barberton Greenstone Belt. In Chapter 5, Schulz et al. (under review), focuses on geochemical analyses and Re-Os isotope signatures of these four spherule horizons and undertakes the comparison with geochemical data obtained from earlier investigated layers. While geochemical fingerprints of other spherule layers are often obscured by extensive hydrothermal overprint, the BARB5 samples retain primary (impact-derived) signatures, allowing, for the first time, to disentangle geochemically the variations in impactor components within and between spherule layers. This work reveals the evidence for extraterrestrial admixtures, ranging between 40 and up to 100% and suggests moderate post-impact remobilization of transition metals and HSE.

Lastly, chapter 6 by Fritz et al. (2016), focuses on petrographic and sedimentary features, as well as major and trace element compositions of lithologies from the micrometer to kilometer-scale which contains spherule layers' occurrences in BARB5 drill core. This work presents the results of visual observation, infrared (IR) spectroscopic imaging, and micro-X-ray fluorescence (µXRF) of drill cores. The µXRF element maps show that spherule layers have similar petrographic and geochemical characteristics but differences in (1) sorting of two types of spherules and (2) occurrence of primary minerals (Ni-Cr spinel and zircon). In the end, the paper favors a single impact scenario followed by post-impact reworking and subsequent alteration.

ZUSAMMENFASSUNG

Neben der ältesten bekannten terrestrischen Impaktstruktur, der 2,02 Milliarden Jahre alten Vredefortstruktur in Südafrika, sind die ältesten Hinweise auf terrestrische Impaktprozesse die Früh-Archäischen Sphärulenlagen, eingebettet in 3,23 bis 3,47 Ga alten Abfolgen des Barberton Grünsteingürtels (BGG) in Südafrika sowie im westaustralischen Pilbara-Kraton. Diese aus Einschlägen großer extraterrestrischer Objekte resultierenden Sphärulenlagen repräsentieren die einzigen eventuellen Spuren eines Asteroiden- oder Kometenbombardements der frühen Erde. Sie werden als Impaktauswurfsmaterial interpretiert, die möglicherweise als Kondensationsprodukte der Impaktrauchwolke oder durch ballistischen Auswurf flüssiger Tröpfchen entstanden sind.

Diese Studie konzentriert sich auf die Analyse des CT3 Bohrkerns des nordöstlichen BGG, Südafrika, mit identifizierten 17 Sphärulenlagen, in dem diese auf extraterrestrische Komponenten und die diagenetische und metamorphe Geschichte untersucht wurden. Diese Arbeit präsentiert somit petrografische und geochemische Daten, sowohl der Sphärulenlagen als auch der umlagernden Muttergesteine, um neue Ansichten in das frühe terrestrische Impaktbombardement bereitzustellen.

Kapitel 3 dieser Doktorarbeit präsentiert eine umfassende detaillierte Untersuchung der 17 Sphärulenlagen, sowie der zwischengelagerten Nebengesteine, in Form von Petrologie und Haupt- und Spurenelementgeochemie. Dies erlaubt die Bestimmung von Alterationsprozessen, die Untersuchung des Ablagerungsraumes, das Belegen möglicher Duplikationen der Sphärulenlagen im Bohrkern, die Klassifizierung der Sphärulenlagen sowie die Korrelation der CT3 Sphärulenlagen mit anderen identifizierten Sphärulenlagen des BGG in vergangenen Studien. Diese millimetergroßen Sphärulen haben sich höchstwahrscheinlich in einem großen Meteoritenimpakt-Ereignis gebildet, wie petrografische Merkmale der Sphärulen belegen, die jenen vergangenen Untersuchungen an anderen Sphärulenlagen im BGG gleichen. Die petrografischen und geochemischen Erkenntnisse weisen auf eine moderate bis starke metamorphe Überprägung aller Lithologien im untersuchten Bohrkernabschnitt hin, aber diese haben sich zum Teil dennoch einen meteoritischen Fingerabdruck erhalten. Die Impakthypothese für die Entstehung der CT3-Sphärulen wird auch durch die Korrelation zwischen siderophilen Elementhäufigkeiten (Cr, Co, Ni, Ir) unterstützt, deren Höchstkonzentrationen und interelementaren Verhältniswerte im Bereich der Chondritwerte liegen.

Kapitel 4 präsentiert Ergebnisse der Osmiumisotopie und hochsiderophile Element (HSE)-Untersuchungen, die ebenfalls eine extraterrestrische

Beimengung belegen können. Die Impakthypothese wird durch hochangereicherte HSE-Konzentrationen (Re, Os, Ir, Pt, Ru, Pd) und durch Rhenium-Osmium Isotopenanalyse bestätigt, die ein chondritisches Projektil belegen. Es kann aber nicht völlig ausgeschlossen werden, dass Sekundäreffekte wie hydrothermale Alteration und metamorphe Überprägung die primäre HSE-Häufigkeiten der Sphärulenablagerungen beeinflusst haben.

Die letzten beiden Kapitel 5 und 6 beinhalten zwei Artikel, die die Autorin dieser Doktorarbeit mitverfasst hat. Diese Artikel stellen die Untersuchungen an vier Sphärulenlagen eines weiteren Bohrkerns (BARB5) des zentralen Barberton Grünsteingürtels vor.

In Kapitel 5 (Schulz et al., in Beurteilung) konzentriert sich auf geochemische Analysen und Re-Os-Isotopensignaturen dieser vier Sphärulenhorizonte und vergleicht die geochemischen Daten mit jenen vergangenen Studien. Während die geochemischen Fingerabdrücke anderer Sphärulenlagen meist durch extensive hydrothermale Überprägung verdeckt sind, bewahren die BARB5-Proben die primären impaktbezogenen Signaturen und erlauben somit erstmals die geochemischen Variationen der Impaktorkomponenten innerhalb und zwischen den Sphärulenlagen zu entflechten. Diese Arbeit zeigt Hinweise für extraterrestrische Beimischungen, zwischen 40% und bis zu 100% liegend, und deutet auf eine moderate Remobilisierung der Übergangsmetalle und HSE nach dem Einschlag hin.

Kapitel 6 (Fritz et al. 2016) schließlich konzentriert sich auf petrografische und sedimentäre Merkmale, sowie die Haupt- und Spurenelementzusammensetzung im Mikro- und Makrobereich von sphärulenführenden Lithologien des BARB5 Bohrkerns. Diese Arbeit präsentiert die Ergebnisse visueller Beobachtung, Infrarotspektroskopische Bildgebung und Mikroröntgenfluoreszenz an Bohrkernen. Mikroröntgenfluoreszenz-Elementkarten zeigen, dass die Sphärulenlagen ähnliche petrografische und geochemische Merkmale aufweisen, aber Unterschiede in (1) der Sortierung zweier Sphärulentypen und (2) dem Vorkommen von primären Mineralen (Nickel-Chrom-Spinell und Zirkon) zeigen. Der Artikel favoritisiert ein Einzelimpakt-Szenario, gefolgt von post-impaktogener Überarbeitung und Alteration.

Table of Contents

CHAPTER 1: INTRODUCTION TO IMPACT CRATERING

Meteorite impact structures are found on all planetary bodies in the Solar System with a solid surface, such as the Moon, Mars, and Mercury (Fig. 1.1). Indeed, meteorite impact structures are one of the most common geological landforms on all the rocky terrestrial planets, except Earth, and many of the rocky and icy moons of in the solar system.
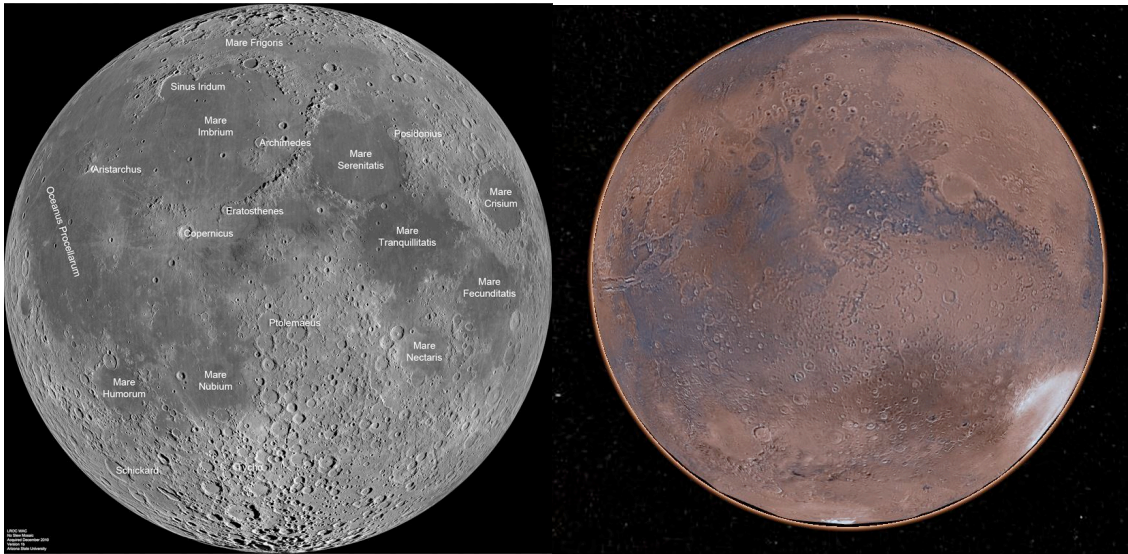
Figure 1.1. *Craters of the Moon (left) (http://www.lroc.asu.edu/images) and Mars (right) (http://marstrek.jpl.nasa.gov/).*

However, to understand impact cratering on Earth provides unique windows into the cratering record of other planets. Erosion, volcanic eruptions, and tectonic activities are continuously erasing impact crater from the surface of the planets and some satellites. In addition to these effects, on Earth, the situation is complicated by the fact that two-thirds of the Earth's surface is covered by oceans and it is harder to access the ocean floor for exploration. Therefore, currently, 190 (as of early 2017) confirmed impact sites have been recognized (Earth Impact Database; http://www.passc.net/EarthImpactDatabase/index.html) (Fig. 1.2) and each year new craters are being added to the list. Although some circular structures with a circular deformation pattern, circular gravity anomaly, fracturing, and brecciation may be of impact origin, their recognition as impact structures and separation from possible other terrestrial structures (formed by, e.g., volcanic eruption, dome formation, or tectonic deformation) needs to be supported by evidence of unambiguous shock deformation or traces of extraterrestrial matter (see below).

Even though craters were first observed on the Moon by Galileo Galilei in 1609, it was not until the 1960s and 1970s that the importance of impact cratering as a geological process was recognized. In 1893, the American Geologist Grove

Gilbert proposed an impact origin for these lunar craters, but it was not until the 1900s that the first impact crater was recognized on Earth: Barringer Crater (aka Meteor Crater) in Northern Arizona (Barringer 1905, Fig.1.3).

Figure 1.2. *Distribution of impact structures on Earth. The geographic location of the 190 currently identified impact structures is: North America has 60; South America 11; Europe 41; Asia and Russia 31; Africa 20 and Australia 27 impact structures (data and image from Earth Impact Database 2016; http://www.passc.net/EarthImpactDatabase/).*

Figure 1.3. *Barringer Crater, Arizona, USA. This is one of the first confirmed impact craters on Earth. Photo by author.*

In the 1960's, the development of the hypervelocity impact analytical model by Shoemaker (1963) and the discovery of the minerals coesite and stishovite, which are high-pressure polymorphs of quartz by Chao et al. (1960, 1962), opened the window to understand the extraterrestrial origin of the Barringer and Ries impact craters (Shoemaker and Chao 1961). After the determination of

impact produced K-Pg boundary (e.g., Alvarez et al. 1980, Smit and Hertogen 1980), impact cratering was recognized as a unique geological process.

1.1. Formation of meteorite impact structures

The formation of impact craters has been divided into three main stages (Gault et al. 1968 and Melosh 1989): (1) contact and compression, (2) excavation, and (3) modification (Fig. 1.4). As seen from the figure, at the beginning of the impact event the projectile penetrates the surface and generates a shock wave. A transient crater starts to form as the excavation begins. The transient crater reaches its maximum depth before reaching its maximum radius. When the excavation is complete, any remaining debris on the crater walls slumps inward to form a breccia lens. Melt will be distributed in the ejecta and any material that falls back on top of the breccia lens. If the crater-forming event is energetic enough, then melt will also be incorporated into the breccia lens (Kring 2007).

(1) Contact/Compression stage: The first stage of an impact event begins when the projectile, either an asteroid or comet, reaches the surface of the target. The projectile penetrates no more than 1–2 times its diameter (Kieffer and Simonds 1980) before transferring its kinetic energy to the target in the form of shock waves (Fig. 1.5) (Melosh 1989). These shock waves propagate
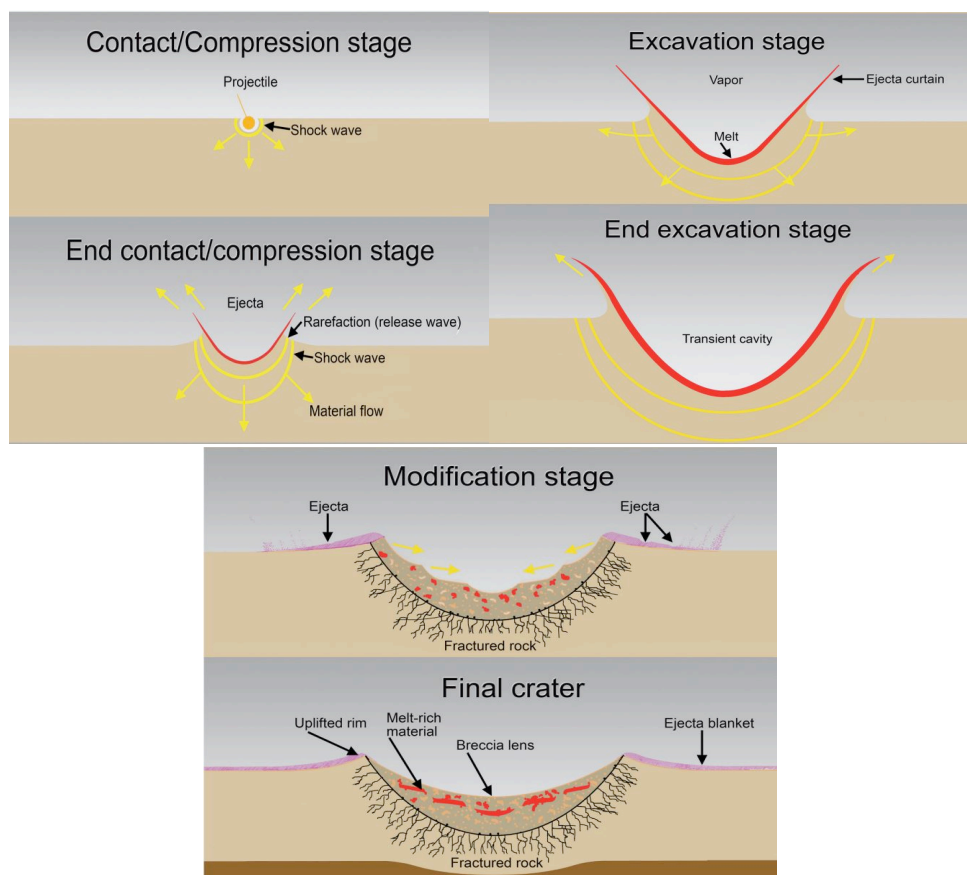
Figure 1.4. *Series of cross sections depicting the formation of a terrestrial simple impact crater (images from Kring 2007).*

3

into the target and are also reflected back into the impactor (French 1998). When the reflected shock wave reaches the free-upper surface of the projectile, it is again reflected back into itself (rarefaction waves). This process causes the projectile to unload at high shock pressure, resulting in the complete melting and/or vaporization of the projectile and a volume of target material close to the impact point (Gault et al. 1968, Melosh 1989). The duration of this stage takes milliseconds; this time also depends on the projectile size, composition, and impact velocity.
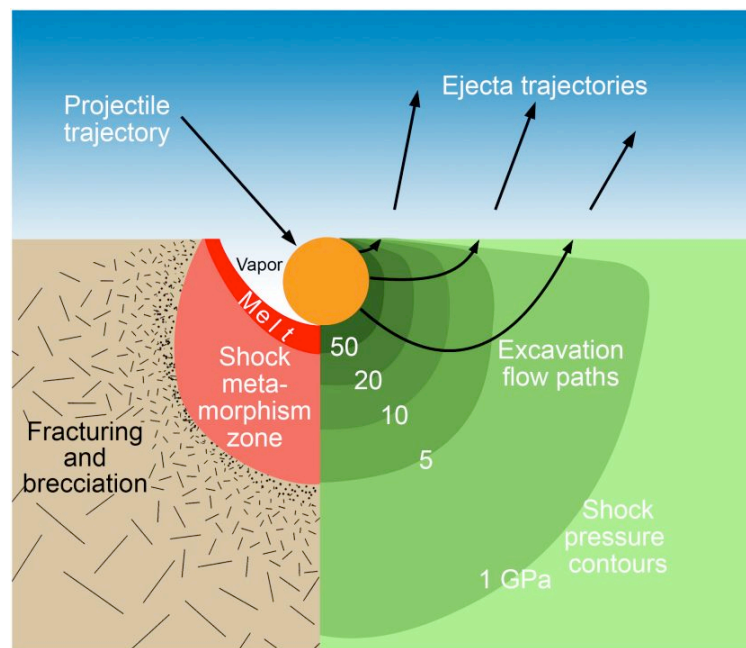
Figure 1.5. *Schematic diagram showing peak shock pressure isobars (in GPa) and the type of deformation produced by those shock conditions, developed in the target around the impact point. From the center outwards, the following zones exist: 1- melting (> 50GPa) and formation of melted part; 2- shocked deformation effects (5-50 GPs) such as planar fractures (PFs), planar deformation features (PDFs), higher pressure polymorphs and diaplectic glasses.; 3- fracturing and brecciation (1-5 GPa) (such as shatter cones). After the excavation stage two main processes occur: 1- the arrows crossing the isobars show the path of subsurface flow of the target material, which contains vaporized, melted, and shock-metamorphosed material and forms the transient crater; 2- the ejection leads to upward (spalling) ejection of large fragments and smaller ejecta (ejecta curtain) (image from Kring 2007).*

(2) Excavation stage: during this stage, the actual impact crater is opened up by the interaction between shock waves and the target surface. The hemispherical shock wave propagates out into the target sequence and causes the outward radial motion of the target material; while the upper part moves outward and upward, the lower part moves outward and downward.

The shock waves that initially traveled upward intersect the ground surface and generate rarefaction waves that propagate back downwards into the target sequence (Melosh 1989). The combination of the outward-directed shock waves and the downward-directed rarefaction waves produces an 'excavation flow' and generates a bowl-shaped depression, the so-called 'transient cavity' (French 1998). Eventually, the energy of those waves decreases and no longer move target rock and melt beyond the cavity rim. The material which is ejected beyond the cavity rim is called impact ejecta. The typical transient crater is 20-30 times larger than the diameter of the projectile (e.g., French 1998). This stage also takes a short time, although longer than the contact/compression stage. While the excavation flow velocity is on the order of 1 km/s, the 200 km-diameter transient crater can be developed in less than 2 minutes. For instance, the Barringer (Meteor) Crater, with a diameter of ~1.2 km, would have formed within about 6 seconds, while a 200 km-diameter crater would have been excavated in about 90 seconds (Melosh 1989). Small craters have a bowl-shaped
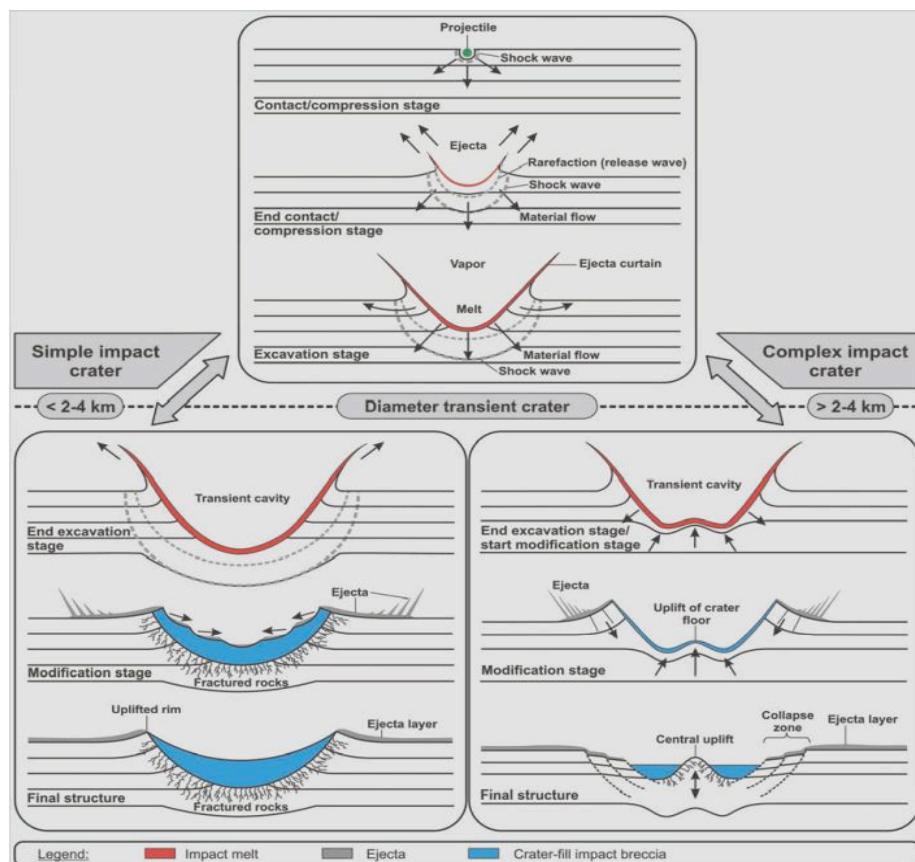
Figure 1.6. *Diagram showing the formation of impact structures in different stages and the development of simple send complex craters (source: Ferriere 2008).*

(3) appearance and are called simple craters; on Earth, they are smaller than 2-4 km in diameter). Complex craters (>2-4 km-diameter on Earth) generally have a structurally complicated rim and an uplifted central area (Melosh 1989 and French 1998) (Fig. 1.6).

(4) Modification Stage: this stage starts just after the transient cavity reaches its final size, and the shock waves decreased to low-pressure elastic stress. The main factors of modification no longer depend on shock waves, but gravity and rock mechanics. The steep walls of the transient crater collapse under gravitation forces and forming terraces. The modification stage takes typically a few minutes to be completed, but as French (1998) notes, this process has no clearly marked end.

1.2. Identification of impact structures on Earth

Several criteria may be used to recognize impact structures, including the presence of a crater form and/or unusual rocks; however, these indicators do not provide definitive evidence for the meteorite impact origin of a structure. To find the unique features of meteorite structures is very challenging, because their general circular form, a circular pattern of deformation, extensive fracturing and brecciation, circular gravity and magnetic anomalies, can also be produced by conventional processes, such as tectonic deformation, salt-dome formation, volcanic eruption, or internal igneous activity (e.g., French and Koeberl 2010). Therefore, the presence of these indicators must be confirmed; a list of important criteria is as follows (see also Table 1.1);

Table 1.1. *Hypervelocity impact deformation effects, diagnostic and non-diagnostic (French and Koeberl 2010).*

Diagnostic indicators for shock metamorphism and meteorite impact	Non-diagnostic features produced by meteorite impact and by other geological processes
-Preserved meteorite fragments	-Circular morphology
-Chemical and isotope projectile signatures	-Circular structural deformation
-Shatter cones	-Circular geophysical anomalies
-High-pressure (diaplectic) mineral glasses	-Fracturing and brecciation
-High-pressure mineral phases	-Kink banding in micas
-High-temperature glasses and melts	-Mosaicism in crystals
-Planar fractures (PFs) in quartz	-Pseudotachylite and pseudotachylitic breccias
-Planar deformation features (PDFs) in quartz	-Igneous rocks and glasses
	-Spherules and microspherules

➢ Shock-metamorphic effects, which are the result of impact-produced shock waves, exist as either megascopic (e.g., shatter cones) or microscopic (Fig. 1.7) phenomena, such as planar deformation features (PDFs), planar features (PFs), diaplectic glass, and high pressure mineral polymorphs, such as diamond, coesite, and stishovite (French and Koeberl 2010).

➢ Geochemical and isotopic traces of an extraterrestrial projectile (e.g., Koeberl et al. 2012).
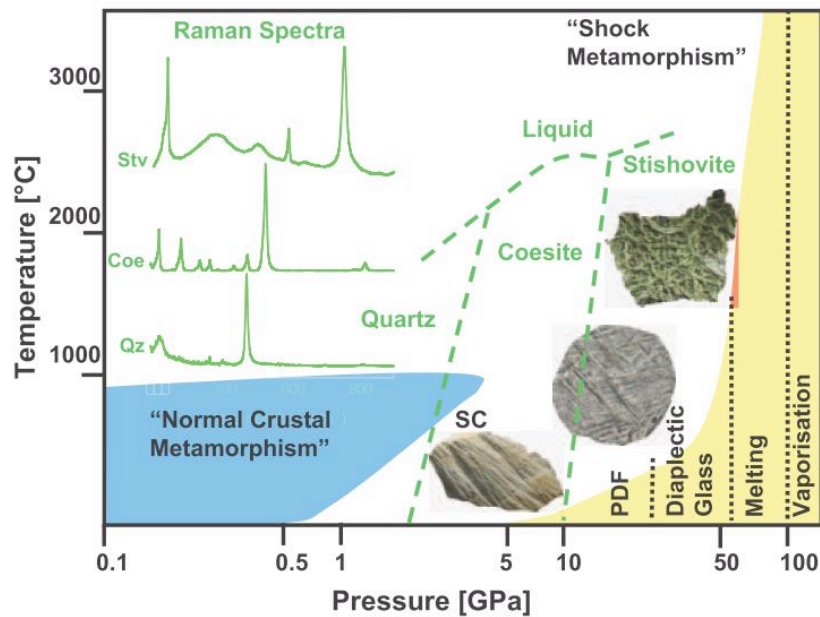
Figure 1.7. *Pressure (P) – temperature (T) diagram showing the different stages of both normal crustal and shock metamorphisms. Different shock metamorphic features are shown. Blue shaded area (P <5 GPa, T <1000°C) encloses the conventional facies for crustal metamorphism. Shock-metamorphic conditions (at right) extend from ~7 to >100 GPa and are clearly distinct from normal metamorphic conditions. The exponential curve (yellow part) ("Shock metamorphism") indicates the approximate post-shock temperatures produced by specific shock pressures in granitic crystalline rocks. Green dashed lines for high-pressure minerals (quartz-Qz, coesite-Coe, and stishovite-Stv) are shown for static equilibrium conditions and at upper left the typical Raman spectra of these minerals (SC=shatter cone; PDF= planar deformation feature) (diagram from Reimold and Jourdan 2012).*

Here I especially focus on impact produced spherules and geochemical and isotopic impact signatures on these spherules, to identify the impact traces.

1.2.1. Geochemical and isotopic signatures from the impactor

The identification of meteoritic component can be very problematical when we consider that the impactor is vaporized and slight amount of meteoritic melt and/or vapor is mixed with the melt/vapor of target rocks during the crater formation (French and Koeberl 2010, Koeberl 2014). Therefore, not only the contribution is generally very less, <1%, but also the possibility of a meteoritic component detection as well. For all that the meteoritic material is mostly dispersed, it can be determined by distinct chemical and isotopic signatures within the impact-derived rocks (e.g., Koeberl 1998, Tagle and Hecht 2006, Koeberl 2007, French and Koeberl 2010). There are elements that are very abundant in meteorites when we compare crustal rocks, such as siderophile elements (Ni, Co, Cr and Au), platinum group elements (PGEs; Ru, Rh, Pd, Os, Ir, and Pt) which can be used as impact indicators (e.g., Alvarez et al. 1980, Palme et al. 1981, Koeberl 1998, 2007). In addition to elemental abundances, the isotopic ratios of Os (Koeberl and Shirey 1993, Koeberl et al. 1996, 1997, Lee et al. 2006, Koeberl 2014) and Cr (Shukolyukov and Lugmair 1998, Shukolyukov et al. 1999; Koeberl 2007, 2014) can also be used not only as impact indicators but also to determine the type of impactor (e.g., Palme et al. 1981, 1982, Koeberl 2007, Koeberl et al. 2012, Koeberl 2014). These element ratios can also vary due to the different types of meteorites and their different compositions (e.g., Palme et al. 1982). While iron or chondritic meteoritic components can be more easily detected, an achondritic meteorite component is more difficult to determine, because of their similar lower siderophile element abundances compared to terrestrial rocks (French and Koeberl 2010). Another significant point is to analyze local target rocks while using these tracers, to obtain the precise background levels of these elements (cf. French and Koeberl 2010).

1.2.1.1. <u>Siderophile Elements and PGEs</u>

According to their geochemical tendency to partition into metal phases, these elements include the highly siderophile PGEs and also other siderophile elements (Cr, Co, and Ni) (McDonough and Sun 1995). It can be explained by the ratio of the concentration of an element in liquid or solid metal to that in silicate melt at given pressure, temperature and oxygen fugacity, and assuming equilibrium between metal and silicate (Palme 2008). Elements that have very high partition coefficients ($\sim 10^4$) are called highly siderophile elements (HSEs), and this group contains the PGEs, Re, and Au. With decreasing partition coefficient (10^2-10^3), the elements such as Ni and Co behave moderately siderophile (e.g., Kramers 1998). Although Cr is considered a siderophile element, it can also behave as a lithophile element (McDonough and Sun 1995, Lodders 2003).

The Ni, Co, and Cr abundances and their interelement ratios are applied to separate meteoritic component, especially the meteoritic component exceed 0.1%, it is also possible to differentiate chondrite and iron meteorite. Because chondrites have higher abundances of Cr (~0.26%) than iron meteorites, they have low Ni/Cr and Co/Cr ratios (e.g., Evans et al. 1993, Palme et al. 1978). Additionally, a strong correlation between these moderately and strongly siderophile elements in the impactites supports a common origin and likely excludes the presence of mafic or ultramafic contributions, as well as significant post-impact fractionation and remobilization (Palme 1980, Morgan and Wandless 1983).

In order to more precisely determine the presence of a meteoritic component, the abundances of the PGE and associated Au and Re abundances and their ratios can be measured (Koeberl 2014 and references therein). The PGE abundances in meteorites both in chondrites and most iron meteorites are several orders of magnitude higher than those in terrestrial crustal rocks (Fig. 1.8).
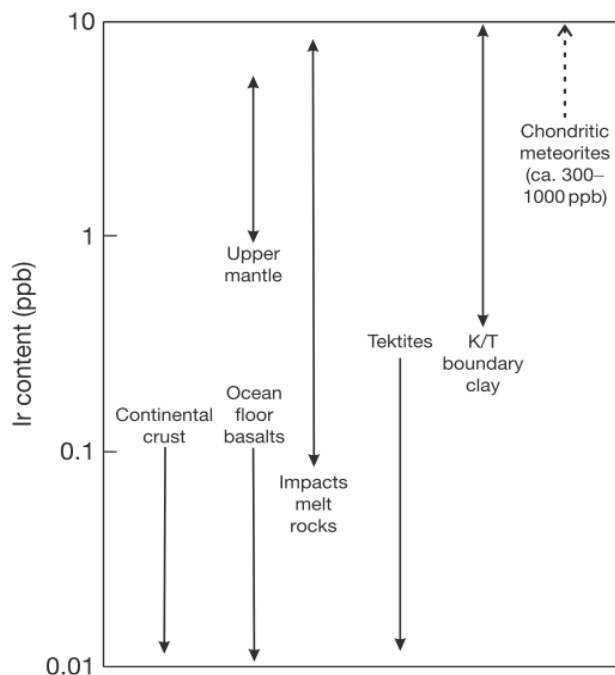
Figure 1.8. The r*ange of Ir contents in various terrestrial and extraterrestrial rocks. The Ir abundances differ between 0.02-0.1 ppb in crustal rocks, but in chondrites have a range between 400 to 800 ppb (Koeberl 2014 and references therein) (image from Koeberl 2014).*

Chondritic meteorites have average abundances of 700 ppb Ir, 1800 ppb Pt, 700 ppb Pd, and 900 ppb Ru (see Anders and Grevesse 1989), while mantle has those abundances of 2 ppb Ir, 5 ppb Pt, 2 ppb Pd, and 4 ppb Ru. Upper continental crust occurs those abundances two orders of magnitude lower than mantle rocks. For example, when 0.2 wt% of a chondritic impactor is mixed to the upper continental crust, the Ir abundance in an impactite (a mixture of

mostly target rock with minor meteoritic contribution) can be estimated at 700 x 0.002 = 1.4 ppb (Koeberl 2014).

The choice of this particular element derives from the ease of analyzing it using instrumental neutron activation analysis compared with the other PGEs.

1.2.1.2. The Os isotopic system

Similar to iridium, the abundance of Os in meteorites is several orders of magnitude (10^2-10^5) higher than in crustal rocks (Koeberl 2007). The isotope ^{187}Os is a daughter product that forms from ^{187}Re by β⁻ decay (half-life of 42.3±1.3 Ga). Therefore, the amount of ^{187}Os increases with time as a result of ^{187}Re. This decay can be described by normalizing to an Os isotope not affected by radioactive decay;

$$^{187}Os/^{188}Os = (^{187}Os/^{188}Os)_i + (^{187}Re/^{188}Os)(e^{\lambda t} - 1)$$

where ^{187}Os/^{188}Os and ^{187}Re/^{188}Os the measured ratios of these isotopes, (^{187}Os/^{188}Os)$_i$ is the initial isotopic ratio at the time when the system became closed for Re and Os, λ is the decay constant for ^{187}Re and t is the time elapsed since system closure for Re and Os. In contrast to crustal rocks, meteorites have low Re and high Os contents, resulting in less Re/Os ratios (~0.1), while it
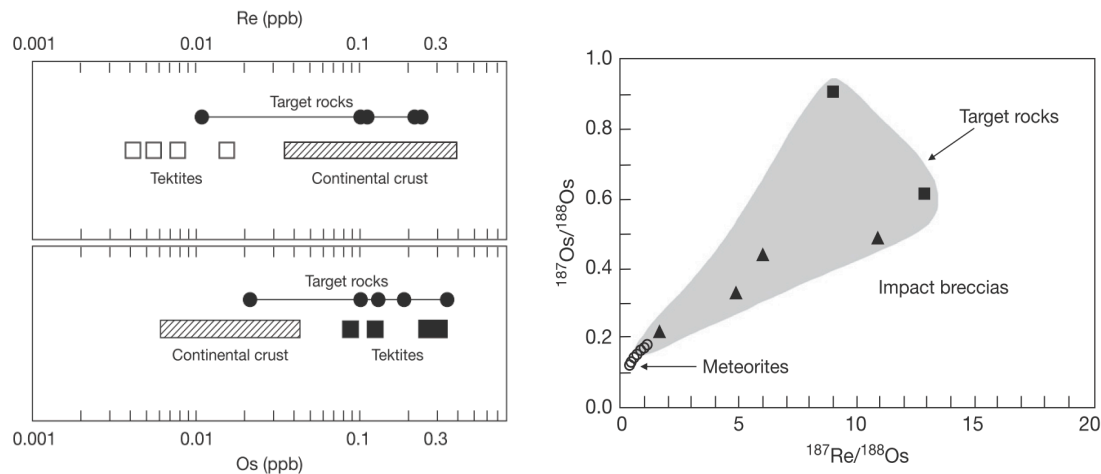
Figure 1.9. *a) The osmium and rhenium abundances in various terrestrial and extraterrestrial rocks (left diagram). b) An example of a Re-Os isotopic diagram; it shows the isotopic ratios of target rocks (squares), impact breccias (triangles), and meteorites (circles) from the Kalkkop impact crater in South Africa (Koeberl et al. 1994) and this diagram can also be used as a mixing diagram (images from Koeberl 2014).*

occurs not less than 10 on terrestrial crustal rocks (Fig. 1.9a). As a result of the high Re and low Os concentrations in old crustal rocks, their ^{187}Os/^{188}Os ratios increases in time (average upper crustal ^{187}Os/^{188}Os is 1-1.2). On the other hand, meteorites exhibit low ^{187}Os/^{188}Os ratios at about 0.11-0.18 (Fig. 1.9b),

and because of the high abundance of Os, this ratio does not differ much in time (Koeberl 2014 and references therein).

All laboratory and measurement processes are explained in detail in the methods section (see chapter 2.6).

1.2.1.3. The Cr Isotopic system

Another geochemical method to identify a meteoritic component is using the relative abundance of the ^{53}Cr isotope, a daughter isotope of ^{53}Mn (half-life is 3.7 Ma). The used ratio is ^{53}Cr/^{52}Cr, which does not show any variations in terrestrial rocks (Koeberl 2002, 2007). In contrast, most meteorite types exhibit various excesses of ^{53}Cr (Shukolyukov and Lugmair 2000). Therefore, this method is not only providing evidence for meteoritic component but is also very efficient to detect the type of impactor (Shukolyukov and Lugmair 1998).

This method was not used in this study but is often mentioned in the literature to identify the impactor type of a crater.

In addition, there are several other geochemical and isotopic methods that have been used to study impact cratering, such as the tungsten isotopic system, stable isotopes, helium-3, or beryllium-10.

1.2.2. Impact Spherules

Because the Earth is geologically active, most of the terrestrial impact structures have been obscured with time. A distal ejecta layer (the ejecta are deposited more than 2.5 crater diameter from crater source) can be preserved locally within sediments long after the source crater has been destroyed (Glass and Simonson 2012). The absence of these indicators from early Archean rocks means that the oldest confirmed impact structure on Earth is the 2 Ga Vredefort structure (e.g., Reimold and Koeberl 2014). The only evidence for earlier impacts exists in the form of Archean ejecta (spherule) layers. Several such layers, most dating from 3.4 to 3.2 Ga, are known, but no related impact crater structures have been observed. Thus, the spherule layers preserved in the geological record provide information about these early impact events. Even though the precise formation process of the spherules is still discussed, most of the impact spherules are probably generated during the early stages of crater formation, either in the form of ejected melt droplets or condensation products from the impact vapor plume. They have also been interpreted as ejecta that were (re)melted during re-entry into the Earth atmosphere (Melosh 1989).

Distal ejecta occur in various forms. For example, large (>1 cm) rapidly cooled melt droplets, which are composed entirely of glass, are called tektites (Koeberl et al. 2012); the areas where those tektites occur on Earth are called strewn fields. On the other hand, impact spherules are much smaller (~<1 mm) and can be divided into two types; (i) microtektites which consist of glass without

11

primary microlites/crystallites and (silica-rich) (ii) microkrystites, which contain primary microlites (mafic melt droplets) (Glass and Simonson 2013) (Fig. 1.10). Microtektites exhibit rotational shapes and often contain vesicles, some silica glass inclusions called lechatelierite (formed by melting of quartz grains), and if they are close to the impact source also relict quartz inclusions. All of these features are interpreted to indicate that most microtektites were formed as melt-ejecta droplets (Glass and Simonson 2012).
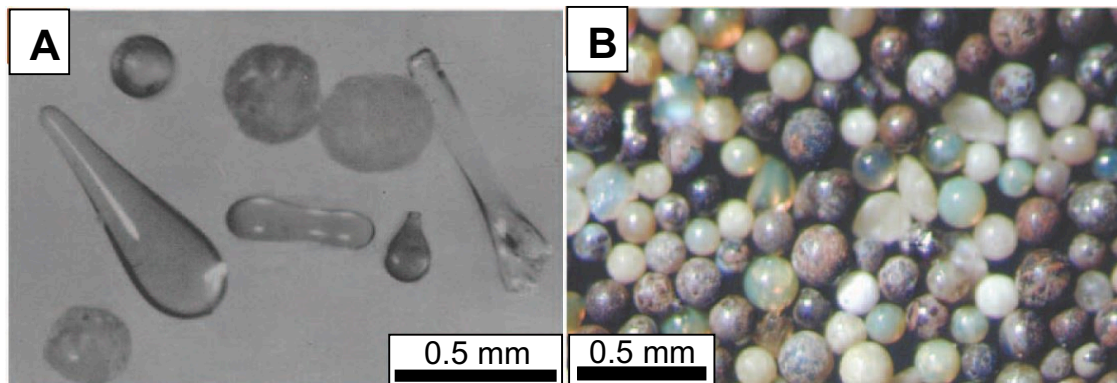
Figure 1.10. *Photomicrographs of A) microtektites with spherical, dumbbell, and teardrop shapes, B) microkrystites of mostly spherical shape. Images from Glass and Simonson (2012).*

Figure 1.11. *Macrophotographs of impact spherules. The hand specimen of a spherule layer from CT3 drill core, the BGB, South Africa (photo by author).*

As mentioned above, spherules are distally deposited impact melt droplets, which can be partially crystallized during rapid cooling (microkrystites) (Glass and Burns 1988). Because primary mineral phases and the impact glasses were converted to secondary by time, it is difficult to distinguish primary glass particles and partly/completely crystallized spherules. However, the best preserved Eocene spherule layers, called clinopyroxene (cpx)-bearing spherules, provide such an example from K/T boundary (Glass 2002, Glass and Simonson 2012). Beside mafic component of microkrystites (cpx, plagioclase), these vapor condensate droplets contain Ni-rich spinels. Notably, microkrystites can also be formed as melt droplets by impacts into mafic crust, which was, as expected, more common in the Precambrian (>2.4 Ga), but also microtektites,

12

which are condensation products from a vapor plume, were found in the Eocene spherule layer (Glass and Simonson 2013).

The impact-derived spherules can be identified by not only high Cr, Co, and Ni abundances (Glass et al. 2004), but also high iridium content and extraterrestrial chromium isotopic ratios (Shukolyukov and Lugmair 1998, Koeberl et al. 2007). These enrichments usually occur in association with dendritic Ni-rich spinel, which was first identified at the K/T boundary by Montanari et al. (1983), and later also within spherule layers in Barberton Greenstone Belt (Mohr-Westheide et al. 2015).

Table 1.2. *Precambrian age spherule layers. Except Acraman and Sudbury, the other source craters are unknown or not confirmed. Table is modified after Glass and Simonson (2012). Karelia spherules' data from Huber et al. 2014.*

Layer	Location	Age (Ma)	Layer	Location	Age (Ma)
Acraman	South Australia	~580	S5	Barberton, South Africa	~3230
Sudbury	Lake Superior, USA	~1850	S4	Barberton, South Africa	~3243
Grænsesø	West Greenland	~1990	S3	Barberton, South Africa	~3243
Karelia	Russia	~2020	S2	Barberton, South Africa	~3260
Dales Gorge	Western Australia	~2490	S6	Barberton, South Africa	~3330
Kuruman	South Africa	~2490	S7	Barberton, South Africa	~3410
Bee Gorge	Western Australia	~2540	S1	Barberton, South Africa	~3470
Reivilo	South Africa	~2560	Warrawoona	Western Australia	~3470
Paraburdoo	Western Australia	~2570			
Jeerinah	Western Australia	~2630			
Carawine	Western Australia	~2630			
Monteville	South Africa	~2650-2588			

Earth's oldest documented impact structures are the Vredefort impact structure, South Africa (2.02 Ga) and the Sudbury structure, Canada (1.85 Ga, Cannon et al. 2010). However, the oldest impact traces on Earth, impact spherules, were discovered in South Africa and Western Australia (Lowe et al. 2014, Reimold and Koeberl 2014, and references therein), and are concentrated in two narrow time periods, from 3.47 to 3.23 Ga (Lowe and Byerly 1986, 2010) and from 2.63 to 2.49 Ga (Hassler et al. 2011) (Table 1.2). Up to eight spherule layers (S1 to S8, Lowe et al. 2014 – not yet individually confirmed) have been preserved in the marine deposits of the Onverwacht and Fig Tree Groups of the BGB, but they have not been assigned to any impact crater structure and it is still not clear if these layers are duplications or are related to multiple impact events. The oldest of the South African layers, S1, might be correlated with the Warrawoona spherule layer from Pilbara, Western Australia (Byerly et al. 2002).

1.3. The Barberton Greenstone Belt (BGB)

The 3.55 to 3.10 Ga Barberton granite-greenstone terrain (BGGT) in South Africa and Swaziland is one of the oldest, best preserved early crustal sections on Earth (Lowe and Byerly 2007). Rocks of the BGGT can be subdivided into three constituents: 1. The BGB, which consists mostly of supracrustal successions; 2. The 3.55 to 3.21 Ga emplaced plutons, trondhjemite-tonalite-granodiorite (TTG) group intrusions, which are characterized by Na- rich and K-poor compositions; 3. The 3.14 to 3.10 Ga emplaced batholites, granite-monzonite-syenite (GMS) group. The rocks of the BGB and the TTG plutons are syngenetic, whereas the GMS plutons post-date the formation of the greenstone belt (Lowe and Byerly 2007). Regarding their general properties, two major rock units can be distinguished: (i) The low metamorphic grade supracrustal rocks of the BGB itself and (ii) the surrounding higher grade granite-gneiss units (Schoene et al. 2008) (Fig. 1.12).

The stratigraphic succession of BGB belt (assigned to the Barberton Supergroup, formerly Swaziland Supergroup) is subdivided into: (i) the ~8-10 km thick, >3570-3260 Ma volcanic-dominated *Onverwacht Group* (Viljoen and Viljoen 1969, Lowe and Byerly 2007, De Wit et al. 2011, Anhaeusser 2014); (ii) the up to 3 km thick, ca. 3260-3225 Ma *Fig Tree Group*, which includes mostly shale, banded iron-formation (BIF), and volcaniclastic sediments (Heinrichs and Reimer 1977, Condie 1997, Hofmann 2005, Lowe and Byerly 2007, Anhaeusser 2014); and (iii) the up to 3.7 km thick, coarse siliciclastic *Moodies Group* with ca. 3230 Ma depositional age (Eriksson 1977, Heubeck et al. 2013). These three groups are described in Chapter 3.

All BGB strata experienced several phases of major deformation, during which they were extensively folded, faulted, and altered (de Ronde and de Wit 1994, Lowe and Byerly 1999). A major fault system, the Saddleback-Inyoka fault (de Ronde and de Wit 1994), transects the belt almost in the middle and interpreted

as the collision zone between two arc and trench blocks formed during stage two of the BGB formation (around 3.2 Ga). Other faults, such as the Moodies fault, are of a similar age as the Inyoka system and supposedly formed during a major collision phase during the BGB's formation (Heubeck and Lowe 1994). Most boundaries between the BGB and its surrounding plutons are faults that are vertically to subvertically dipping (Heubeck and Lowe 1994). In the final stages of the BGB evolution, the extensive fault system most likely facilitated the hydrothermal overprint with ore-rich fluids. These alterations include serpentinization and carbonatization processes (Heubeck and Lowe 1994).
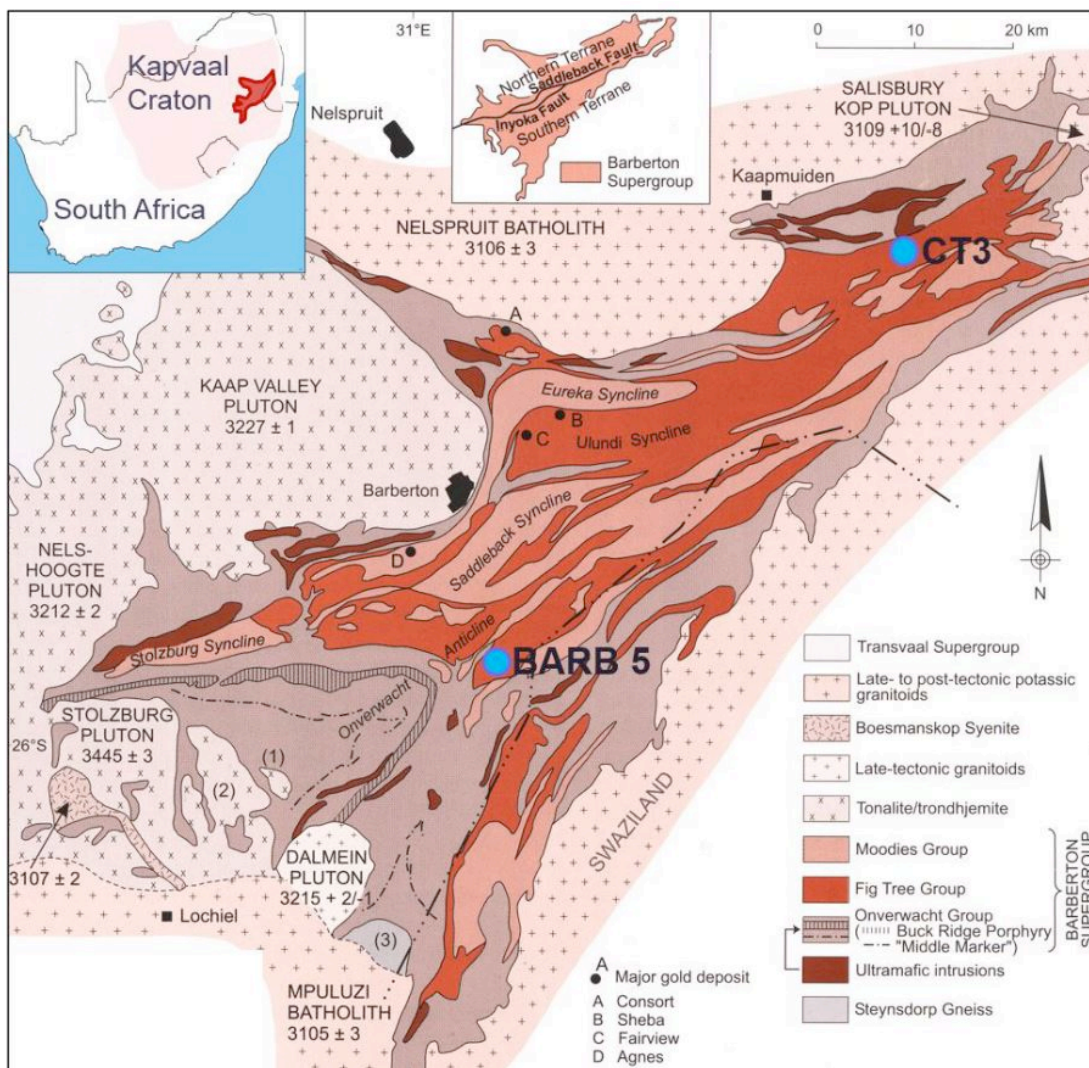
Figure 1.12. *The geological map of the BGGT, showing the different lithologies in the Barberton Supergroup and the surrounding granite-gneiss complexes. The locations of two investigated drill cores are shown by blue circles (image from Hoehnel 2016).*

Along the borders of the BGB numerous intrusive bodies can be found, such as the Kaap Valley Pluton (3.22 Ga) and the Mpuluzi batholith (3.10 Ga) (Fig.

1.12). These bodies document the magmatic activities which occurred in the Barberton area. Regarding their origin and composition, the granitoid bodies can be divided into two types TTG and GMS (see above). For the TTG plutons, a garnet-rich amphibolitic or eclogitic depleted upper mantle source in a depth of at least 40 km was suggested (Clemens et al. 2006). Over time the magma source changed. For the GMS batholiths a plagioclase-rich, garnet-poor source where at least parts of the already existing Greenstone crust got mixed in the magma is proposed (Yearron et al. 2003). The exact origin of the batholiths is still questioned; however, their emplacement occurred at the same time as a transition from a largely convergent (at ca. 3.23 Ga) to a trans-tensional tectonic regime in the BGB at around 3.08 Ga (de Ronde and de Wit 1994).

The rocks that host the impact spherule layers relevant to this project were sampled from the northeastern part of the BGB (CT3 drill core) and a companion project from the middle of BGB (BARB 5 drill core, see Chapter 5 and 6). Both cores were drilled from within the Fig Tree Group of the BGB.

References

Alvarez L. W., Alvarez W., Asaro F., and Michel H. V. 1980. Extraterrestrial cause for the Cretaceous-Tertiary extinction. Science 208:1095-1108.

Anhaeusser C. R. 2014. Archean greenstone belts and associated granitic rocks - A review. Journal of African Earth Sciences 100:684-732.

Anders E. and Grevesse N. 1989. Abundances of the elements: meteoritic and solar. Geochimica et Cosmochimica Acta 53:197-214.

Barringer D. M. 1905. Coon Mountain and Its Crater Source: Proceedings of the Academy of Natural Sciences of Philadelphia 57:861-886.

Byerly G. R., Lowe D. R., Wooden J., and Xie X. 2002. An Archean impact layer from the Pilbara and Kaapvaal cratons. Science 297:1325-1327.

Cannon W. F., Schulz K. J., Horton J. W. Jr., and Kring D. A. 2010. The Sudbury impact layer in the Paleoproterozoic iron ranges of northern Michigan, USA. Geological Society of America Bulletin 122:50-75

Chao E. C. T., Shoemaker E. M., and Madsen B. M. 1960. First natural occurrence of coesite. Science 132:220-222.

Chao E. C. T., Fahey J. J., Littler J., and Milton D. J. 1962. Stishovite, SiO_2, a very high-pressure new mineral from Meteor Crater, Arizona. Journal of Geophysical Research 67:419-421.

Clemens J. D., Yearron L. M., and Stevens G. 2006. Barberton (South Africa) TTG magmas: Geochemical and experimental constraints on source-rock petrology, pressure of formation and tectonic setting. Precambrian Research 151:53-78.

Condie K. C. 1997. Plate Tectonics and Crustal Evolution, 4th ed. Butterworth-Heinemann, Oxford, 282 p.

De Ronde C. E. J. and De Wit M. J. 1994. Tectonic history of the Barberton Greenstone Belt, South Africa: 490 million years of Archaean evolution. Tectonics 13(4): 983-1005.

De Wit M. J., Furnes H., Robins B. 2011. Geology and tectonostratigraphy of the Onverwacht Suite, Barberton greenstone belt, South Africa. Precambrian Research 186:1-27.

Eriksson K. A. 1977. Tidal deposits from the Archaean Moodies Group, Barberton Mountain Land, South Africa. Sedimentary Geology 18:257-281.

Evans N. J., Gregoire D. C. and Grieve R. A. F. 1993. Use of platinum- group elements for impactor identification-terrestrial impact craters and Cretaceous-Tertiary boundary. Geochimica et Cosmochimica Acta 57:3737-3748.

Ferrière L. 2008. Shock metamorphism and geochemistry of impactites from the Bosumtwi impact structure: A case study of shock-induced deformations and transformations in quartz and associated methodology. Ph.D. thesis, University of Vienna, Vienna, Austria, 279 p.

French B. M. 1998. Traces of Catastrophe. Handbook of Shock-Metamorphic Effects in Terrestrial Meteorite Impact Structures, Lunar and Planetary Institute, Houston, 120 p.

French B. M. and Koeberl C. 2010. The convincing identification of terrestrial meteorite impact structures: What works, what doesn't, and why. Earth Science Reviews 98:123-170.

Gault D. E., Quaide W.L., Oberbeck V.R. 1968. Impact cratering mechanics and structures, in: B.M. French and N.M. Short (Eds.), Shock Metamorphism of Natural Materials, Mono Book Corp., Baltimore, p. 87-99.

Glass B. P. 2002. Upper Eocene impact ejecta/spherule layers in marine sediments. Chemie der Erde 62:173-196.

Glass B. P. and Burns C. A. 1988. Microkrystites: A new term for impact-produced glassy spherules containing primary crystallites. Proceedings, Lunar and Planetary Science 18:455-458.

Glass B. P. and Simonson B. M. 2012. Distal impact ejecta layers: Spherules and more: Elements 8:43-48.

Glass B. P. and Simonson B. M. 2013. Distal impact ejecta layers. A record of large impacts in sedimentary deposits. Impact studies. Springer, Berlin Heidelberg, 716 p.

Glass B. P., Huber H. and Koeberl C. 2004. Geochemistry of Cenozoic microtektites and clinopyroxene-bearing spherules. Geochimica et Cosmochimica Acta 68:3971-4006.

Hassler S. W., Simonson B. M., Sumner D. Y. and Bodin L. 2011. Paraburdoo spherule layer (Hamersley Basin, Western Australia): Distal ejecta from a fourth large impact near the Archean-Proterozoic boundary. Geology 39:307-310.

Heinrichs T. K. and Reimer T. O. 1977. A sedimentary baryte deposit from the Archean Fig Tree Group of the Barberton Mountain Land (South Africa). Economical Geology 72:1426-1441.

Heubeck C. and Lowe D. R. 1994. Late syndepositional deformation and detachment tectonics in the Barberton Greenstone Belt, South Africa. Tectonics 13:1514-1536.

Heubeck C., Engelhard J., Byerly G. R., Zeh A., Sel B., Luber T. and Lowe D. R. 2013. Timing of deposition and deformation of the Moodies Group (Barberton Greenstone Belt, South Africa): Very-high-resolution of Archaean surface processes. Precambrian Research 231:236-262.

Hoehnel D. 2016. Petrographische und texturelle Analyse archäischer Sphärulenlagen und deren Nebengesteine aus den BARB 5 und CT3 Bohrkernen des Barberton Grünsteingürtels, Südafrika. Unpublished master thesis, University of Potsdam, 171 p.

Hofmann A. 2005. The geochemistry of sedimentary rocks from the Fig Tree Group, Barberton greenstone belt: implications for tectonic, hydrothermal and surface processes during mid-Archaean times. Precambrian Research 143:23-49.

Huber M. S., Crne A. E., McDonald I., Hecht L., Melezhik V. A., and Koeberl C. 2014. Impact spherules from Karelia, Russia: Possible ejecta from the 2.02 Ga Vredefort impact event. Geology 42:375–378.

Kieffer S. W. and Simonds C. H. 1980. The role of volatiles and lithology in the impact cratering process. Reviews of Geophysics and Space Physics 18:143-181.

Kring D. A. 2007. Guide to the Geology of Barringer Meteorite Crater, Arizona. Lunar and Planetary Institute, Houston, 150 p.

Koeberl C. 1994. Tektite origins by hypervelocity asteroidal or cometary impact: target rocks, source craters, and mechanisms. In: Dressler, B.O., Grieve, R.A.F., and Sharpton, V.L. (Eds.), Large Impact Structures and Planetary Evolution. Special Paper, Geological Society of America, Boulder, CO. 293:133-152.

Koeberl C. 1998. Identification of meteoritic components in impactites. In Meteorites: Flux with time and impact effects, edited by Grady M. M., Hutchinson R., McCall G. J. H., and Rothery D. A. Geological Society of London. Special Publication 140:133-153.

Koeberl C. 2002. Mineralogical and geochemical aspects of impact craters. Mineralogical Magazine 66:745-768.

Koeberl C. 2007. The geochemistry and cosmochemistry of impacts. In Treatise of Geochemistry, edited by Davis A. Online edition, Vol. 1, Elsevier, p. 1.28:1-52.

Koeberl C. 2014. The geochemistry and cosmochemistry of impacts. In Planets, Asteroids, Comets and The Solar System, Volume 2 of Treatise on Geochemistry (Second Edition). Edited by A. M. Davis. Elsevier, p.73-118.

Koeberl C. and Shirey S. B. 1993. Detection of a meteoritic component in Ivory Coast tektites with rhenium–osmium isotopes. Science 261:595-598.

Koeberl C. and Shirey S. B. 1997. Re-Os isotope systematics as a diagnostic tool for the study of impact craters and distal ejecta. Paleogeography, Paleoclimatology, Paleoecology 132:25-46.

Koeberl C., Reimold W. U. and Shirey S. B. 1996. A Re-Os isotope and geochemical study of the Vredefort Granophyre: clues to the origin of the Vredefort structure, South Africa. Geology 24:913-916.

Koeberl C., Bottomley R., Glass B., and Storzer D. 1997. Geochemistry and age of Ivory Coast tektites and microtektites. Geochimica et Cosmochimica Acta 61:1745-1772.

Koeberl C., Shukolyukov A., and Lugmair G. W. 2007. Chromium isotopic studies of terrestrial impact craters: Identification of meteoritic components at Bosumtwi, Clearwater East, Lappajärvi, and Rochechouart. Earth and Planetary Science Letters 256:534-546.

Koeberl C., Claeys P., Hecht L., and McDonald I. 2012. Geochemistry of impactites. Elements 8:37-42.

Kramers J. D. 1998. Reconciling siderophile element data in the Earth and Moon, W isotopes and the upper lunar age limit in a simple model of homogeneous accretion. Chemical Geology 145:461–478.

Lee S. R., Horton Jr. J. W., and Walker R. J. 2006. Confirmation of a meteorite component in impact-melt rocks of the Chesapeake Bay impact structure, Virginia, USA-evidence from osmium isotopic and PGE systematics. Meteoritics and Planetary Science 41:819-833.

Lodders K. 2003. Solar system abundances and condensation temperatures of the elements. Astrophysical Journal 591:1220-1247.

Lowe D. R. and Byerly G. R. 1986. Early Archean silicate spherules of probable impact origin, South Africa and Western Australia. Geology 14:83-86

Lowe D. R. and Byerly G. R. 1999. Stratigraphy of the west-central part of the Barberton Greenstone Belt, South Africa, in: Lowe, D.R., and Byerly, G.R. (Eds.), Geologic Evolution of the Barberton Greenstone Belt, South Africa. Geological Society of America Special Paper 329:1-36.

Lowe D. R. and Byerly G. R. 2007. An overview of the geology of the Barberton Greenstone Belt and vicinity: implications for early crustal development., in: Van Kranendonk, M. J., Smithies, R. H., and Bennett, V. H. (Eds.), Earth's Oldest Rocks. Elsevier (Developments in Precambrian Geology), Amsterdam, pp. 481-526.

20

Lowe D. R. and Byerly G. R. 2010. Did the LHB end not with a bang but a whimper? The geologic evidence. In: 41st Lunar and Planetary Science Conference (Abstract #2563).

Lowe D. R., Byerly G. R. and Kyte F. T. 2014. Recently discovered 3.42– 3.23 Ga impact layers, Barberton belt, South Africa: 3.8 Ga detrital zircons, Archean impact history, and tectonic implications: Geology 42:747-750.

McDonough W. F. and Sun S. S. 1995. The composition of the Earth. Chemical Geology 120:223-253.

Melosh H. J. 1989. Impact Cratering: A Geologic Process, Oxford University Press, New York 253 p.

Mohr-Westheide T., Reimold W. U., Fritz J., Koeberl C., Salge T., Hofmann A. and Schmitt R. T. 2015. Discovery of extraterrestrial component carrier phases in Archean spherule layers: Implications for estimation of Archean bolide sizes. Geology 43:299-302.

Montanari A., Hay R. L., Alvarez W., Asaro F., Michel H. V., Alvarez L. W. and Smit J. 1983. Spheroids at the Cretaceous-Tertiary boundary are altered impact droplets of basaltic composition. Geology 11:668-671.

Morgen J. W. and Wandless G. A. 1983. Strangsways Crater, Northern Territory, Australia: Siderophile element enrichment and lithophile element fractionation. Journal of Geophysical Research 88: A819-A829.

Palme H. 1980. The meteoritic contamination of terrestrial and lunar impact melts and the problems of indigenous siderophiles in the lunar highland. 11th Proceeding Lunar Planetary Science Conferences, 481-506.

Palme H. 2008. Platinum-group elements in cosmochemistry. Elements 4:233-238.

Palme H., Janssens M. J., Takahashi H., Anders E., and Hertogen J. 1978. Meteoritic material at five large impact craters. Geochimica and Cosmochimica Acta 42:313-323.

Palme H., Grieve R. A. F., and Wolf R. 1981. Identification of the projectile at the Brent crater, and further considerations of projectile types at terrestrial craters. Geochimica et Cosmochimica Acta 45:2417-2424.

Palme H., Spettel B., and Wlotzka F. 1982. Fractionation of refractory metals in Ca Al-rich inclusions from carbonaceous chondrite. Meteoritics 17:267.

Reimold W.U. and Jourdan F. 2012. IMPACT! - Bolides, craters and catastrophes. In: Jourdan, F., Reimold, W.U. (Eds.), IMPACT! Elements 8:19-24.

Reimold W. U. and Koeberl C. 2014. Impact structures in Africa: A review. Journal of African Earth Sciences 93:57-175.

Shoemaker E. M. 1963. Impact mechanics at Meteor Crater, Arizona. In The Moon, Meteorites, and Comets, edited by Middlehurst B. M. and Kuiper G. P. Chicago: University of Chicago. pp. 301-336.

Shoemaker E. M., and Chao E. C. T. 1961. New evidence for the impact origin of the Ries Basin, Bavaria, Germany. Journal of Geophysical Research 66:3371-3378.

Schoene B., Bowring S. A. and de Wit M. J. 2008. Mesoarchean assembly and stabilization of the eastern Kaapvaal craton: A structural-thermochronological perspective. Tectonics 27:TC5010.

Shukolyukov A. and Lugmair G. W. 1998. Isotopic evidence for the Cretaceous-Tertiary impactor and its type. Science 282:927-929.

Shukolyukov A. and Lugmair G. W. 2000. Extraterrestrial matter on Earth: Evidence from the Cr isotopes [abs.], in Catastrophic events and mass extinctions: Impacts and beyond: Houston, Texas, Lunar and Planetary Institute, LPI Contribution 1053:197-198.

Shukolyukov A., Lugmair G. W., Koeberl C., and Reimold W. U. 1999. Chromium in the Morokweng impact melt rocks: Isotope evidence for extraterrestrial component and type of the impactor [abs.]. Meteoritics and Planetary Science 34: A107-A108.

Shukolyukov A., Kyte F. T., Lugmair G. W., Lowe D. R. and Byerly G. W. 2000. The oldest impact deposits on Earth - First confirmation of an extraterrestrial component. Impacts and the Early Earth. In: Gilmour I., Koeberl C. (Eds.), Lecture Notes in Earth Science. Springer Verlag, Heidelberg 91:99-115.

Simonson B. and Glass B. 2004. Spherule Layers - Records of Ancient Impacts. Annual Review of Earth and Planetary Sciences 32:329-361.

Smit J. and Hertogen J. 1980. An extraterrestrial event at the Cretaceous-Tertiary boundary. Nature 285:198-200.

Tagle R. and Hecht L. 2006. Geochemical identification of projectiles in impact rocks. Meteoritics and Planetary Science 41:1721-1735.

Viljoen M. J. and Viljoen R. P. 1969. An introduction to the geology of the Barberton granite-greenstone terrain. Special Publication Geological Society of South Africa 2:9-28.

Yearron L. M. 2003. Archaean granite petrogenesis and implications for the evolution of the Barberton Mountain Land, South Africa. PhD Thesis, Kingston University, Kingston, UK, 315 p.

CHAPTER 2: ANALYTICAL METHODS

2.1. Optical Microscopy

Thin sections produced from each of the CT3 layers were examined by transmitted light microscopy as well as reflected light microscopy. These are the most widely applied techniques in geology; therefore, a detailed description will not be mentioned here.

2.2. Secondary electron microscopy (SEM) and electron probe micro-analyzer (EPMA)

Some selected samples were also analyzed with a scanning electron microscope (SEM), which scans a focused electron beam over a surface to create high magnification images. The electrons in the beam interact with the sample, producing various signals that can be used to obtain information about the surface topography and composition. A scanning electron microscope is comprised of an electron generating component called (1) the gun which is most often made of tungsten and emitted the electrons at energy from 5 to 30 keV. Through a column through which the electron beam travels, (2) the anode emits the electrons into (3) condenser lenses that focus the electron beam and transfer it to (4) objective lenses which finally focus the electrons onto the sample surface. A series of these electromagnetic lenses and (5) apertures, within the column, are used to reduce the diameter of the source of electrons and to place a small, focused beam of electrons (or spot) onto the specimen. The sample chamber at the base and a series of pumps are to keep the system under vacuum (Fig. 2.1a). The finally focused electron beam, which irradiates the sample. The electron beam can either be used to form an image through scanning over the sample surface, or a specific point may be analyzed. Through the interaction of the electron beam with the sample secondary electrons, backscattered electrons, characteristic X-rays, etc. are produced (Goldstein et al., 2003) (Fig. 2.1b). Secondary electrons (SE) and backscattered electrons (BSE) are the primary signals used for high-resolution imaging.

Secondary electrons are low energy (< 50 eV) electrons that are ejected from K-orbitals (ionized state) of atoms in inelastic scattering of incident atoms. They are generally used to obtain information from the surface of the samples (~1-10 nm), such as topography, similar to Auger electrons.

In contrast, back-scattered electrons are in a high energy state and produced by elastic scattering of primary electron beam with the sample, and gives the opportunity to access the images within higher depth than SE (ca. 0.5 of penetration depth). Elements which have high atomic number reflect electrons better than those with lower atomic number, and the generated images appear

brighter. Therefore, BSE images are also useful to estimate the composition of samples.
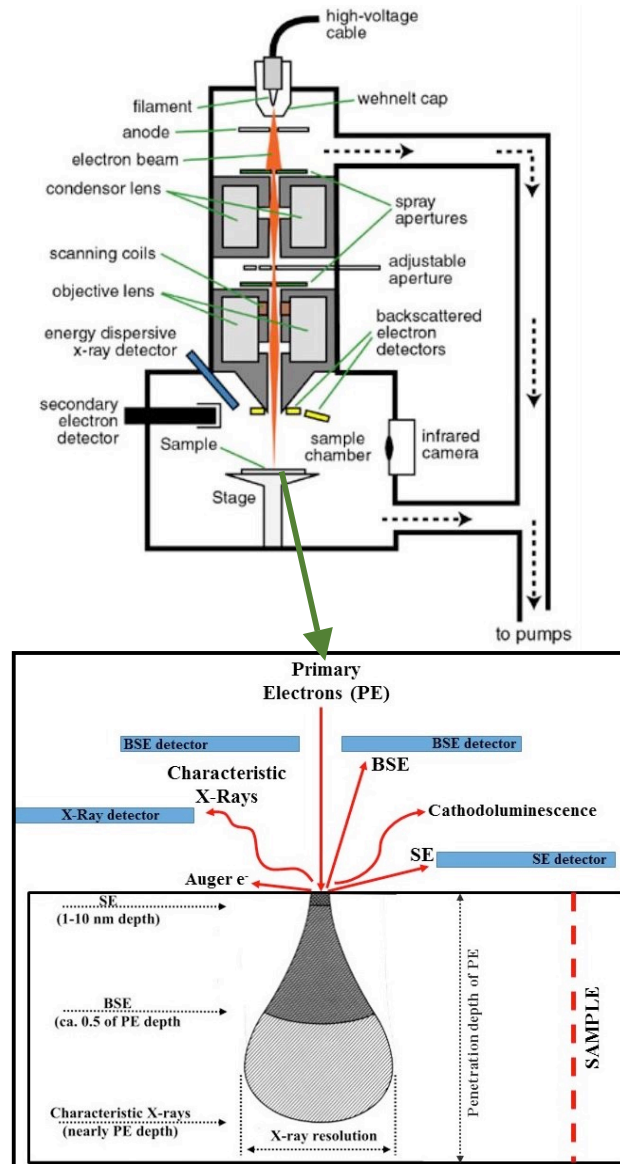
Figure 2.1. *a) Schematic scanning electron microscope overview (image from http://nau.edu/cefns/labs/electron-microprobe/glg-510-class-notes/instrumentation/) and b) pear-shaped model of the electron volume and volume/depth from which different signals originate (modified after the image from http://materialsworld.utep.edu).*

Characteristic X-rays are generated only in the pear-shaped volume (interaction volume) in which the electron ionization energy exceeds the ionization energy of the inner shell and can be used to obtain information about the chemical composition of the sample. The dimensions of the sample interaction volume depend mostly on the energy of the electron beam and on the atomic number of

24

the sample. These X-rays can be used to measure either with an energy dispersive spectrometer (EDS), mostly for qualitative analyses, or with a wavelength dispersive spectrometer (WDS) for quantitative analyses.

An electron-probe micro-analyzer (EPMA) is the most common instrument for non-destructive in-situ X-ray micro-analysis investigations, with very high spatial resolution and sensitivity. However, the principle is very similar to that of the SEM; however, the EPMA has more than one WDS detectors around the electron column. Therefore, this allows the precise and simultaneous measurement of different elements. The chemical composition of a sample is determined by comparing the intensity of X-rays from reference standards with the intensity from the investigated sample.

More information about SEM and EPMA can be found in Potts (1987), Lee (1993), Reimer (1998), Goldstein et al. (2003), Severin (2004), and Bartosova (2010).

In this study, the samples were coated with a thin layer of carbon to prevent the accumulation of electric charge on the surface of the samples and thus avoid image artifacts. The SEM-EDS (energy dispersive spectrometry) system was used for semi-quantitative chemical analysis and recording high-resolution secondary-electron and backscattered-electron images. Electron images and EDS spectra were collected using an excitation voltage of 15 kV and spot sizes 60 and 65, at a working distance between 11 and 16 mm (optimum count rate for different SEM analyses). The quantitative chemical analyses performed by EPMA, which was calibrated by using Astimex and Smithsonian international mineral standards. The analyses were carried out by using a JEOL JSM-6610LV scanning electron microscope (SEM) and a JEOL JXA-8500F field-emission electron-probe microanalyzer (EPMA), both at MfN. Additional analyses were undertaken using a JEOL JSM 6610 LV SEM and a JEOL JXA 8520F field-emission EPMA at NHM Vienna. Mineral analyses were obtained at 15 kV accelerating voltage and 10 nA by wavelength-dispersive spectrometry (WDS-EPMA). Standardization was done using the main Astimex and Smithsonian international standard suites of the MfN and NHM analytical facilities, i.e., pure elements for Al, Fe, Co, and Ni, and mineral reference standards for Na (plagioclase), Mg (diopside), Si (quartz), P (apatite), S (celestine), K (sanidine), Ca (diopside), and Ti (rutile). Counting times were set to 10 s on peak and 5 s on upper and lower background, respectively, and matrix effects were corrected using the ZAF routine provided by the JEOL operating system. Detection limits are 82 ppm for Si, 50 ppm for Al, 134 ppm for Cr, 206 for Ti, 35 ppm for K, 49 ppm for Ca, 100 ppm for Fe, 77 ppm for Mn, 121 ppm for Ni, 40 ppm for Na, 45 ppm for Mg, 133 ppm for As, 271 ppm for Zn, 51 ppm for S, 215 ppm for Pb, 132 ppm for Co, 194 ppm for Cu and 175 ppm for Sb. The accuracy of the WDS analyses is better than 3 rel% for major

elements >5 wt% and in the range of 10–15 rel% for minor elements <0.5 wt%. Precision is much better than 5 rel% for major elements >5 wt% and in the range of several tens of percent for minor elements <0.5 wt%.

2.3. X-Ray Fluorescence (XRF) Spectrometry

An X-ray fluorescence (XRF) spectrometer is an x-ray instrument used for routine, relatively non-destructive chemical analyses of rocks, minerals, sediments, and fluids. It works on wavelength-dispersive spectroscopic principles that are similar to that of an electron microprobe. However, an XRF instrument cannot generally make analyses at the small spot sizes typical of EPMA work (2-5 micrometers), so it is typically used for bulk analyses of larger fractions of geological materials. The relative ease and low cost of sample preparation, and the stability and ease of use of x-ray spectrometers make this one of the most widely used methods for analysis of major and trace elements in rocks, minerals, and sediment.
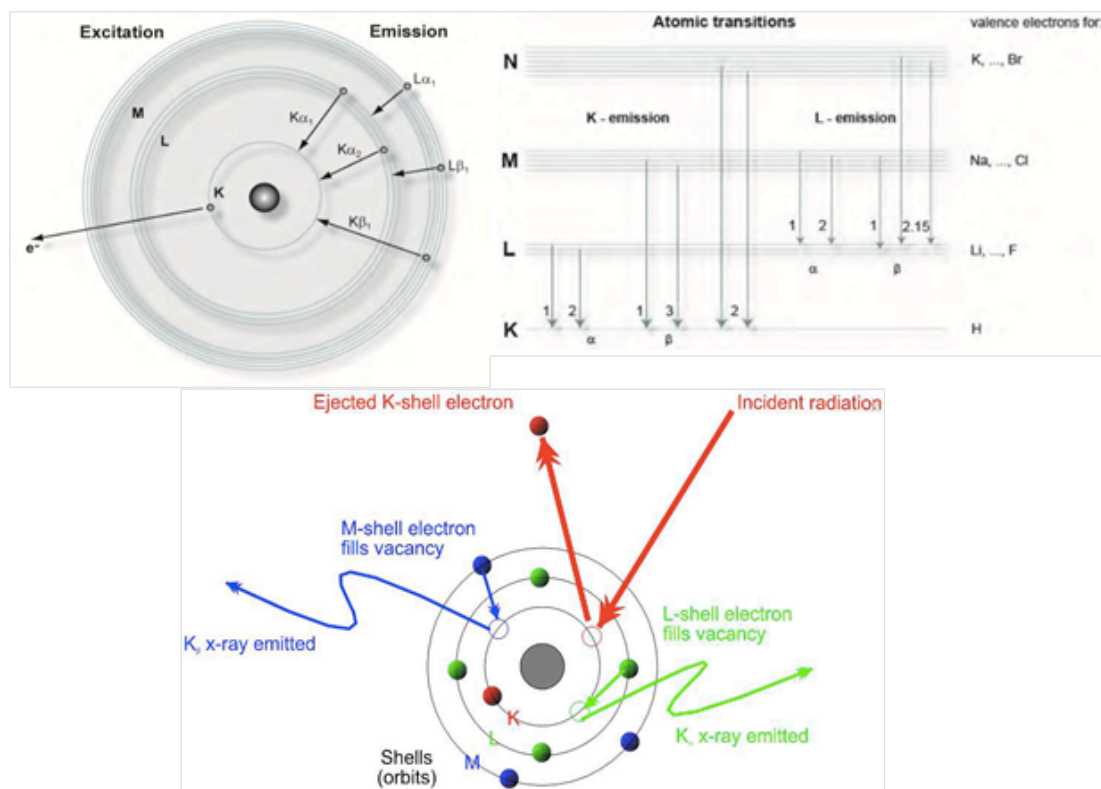
Figure 2.2. *a) Bohr's atomic model (shell model) (modified after Bohr 1913), b) X-ray line labeling, c) the main principle of X-ray fluorescence; emission of X-rays (images from https://www.bruker.com/products/x-ray-diffraction-and-elemental-analysis/handheld-xrf/how-xrf-works.html).*

The analysis of the contents of major and trace elements in geological materials by x-ray fluorescence is made possible by the behavior of atoms as they interact with radiation. When materials are excited with high-energy, short

wavelength radiation (e.g., X-rays), they can become ionized. If the energy of the radiation is sufficient to dislodge a tightly-held inner electron, the atom becomes unstable, and an outer electron replaces the missing inner electron. When this happens, energy is released due to the decreased binding energy of the inner electron orbital compared with an outer one (Fig. 2.2). The emitted radiation is of lower energy than the primary incident X-rays and is termed fluorescent radiation. Because the energy of the emitted photon is characteristic of a transition between specific electron orbitals in a particular element, the resulting fluorescent X-rays can be used to detect the abundances of elements that are present in the sample.

A simple explanation of such an instrument would be: an X-ray source and a detector are the two major components of the instrument; primary x-rays are generated by the source and directed at the sample's surface, sometimes passing through a filter to modify the beam. The XRF generates X-rays from an X-ray tube (the primary radiation source), which then travel to a sample holder, a primary collimator (to orient photons), an analyzing crystal, a secondary collimator, and a detector (Fig. 2.3).
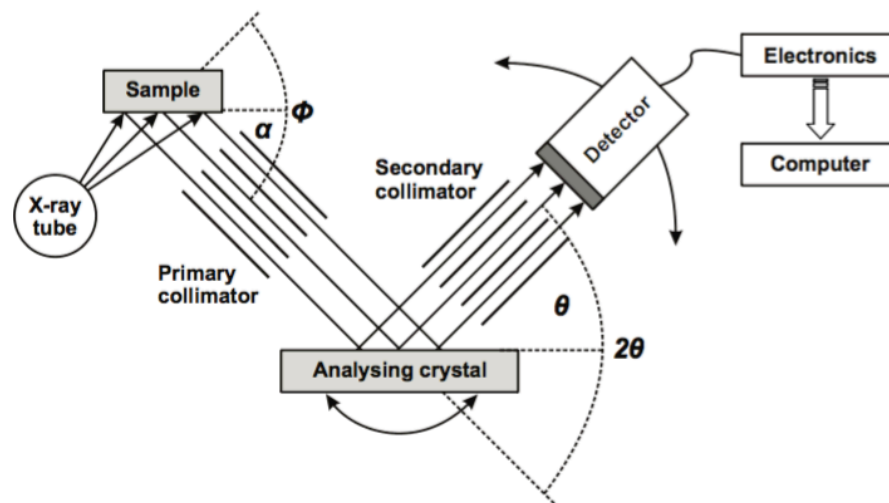
Figure 2.3. *Schematic outline of an XRF spectrometer (modified after Gill 1997).*

When the beam reaches the atoms in the sample, they are being excited and generate secondary x-rays, which are processed by the detector to produce a spectrum showing the x-rays intensity peaks vs. their energy. The peak energy identifies the elements, and their intensity gives an estimation of element amount in the sample. Lastly, the analyzer uses this information to calculate the elemental composition of the sample (Fig 2.4).
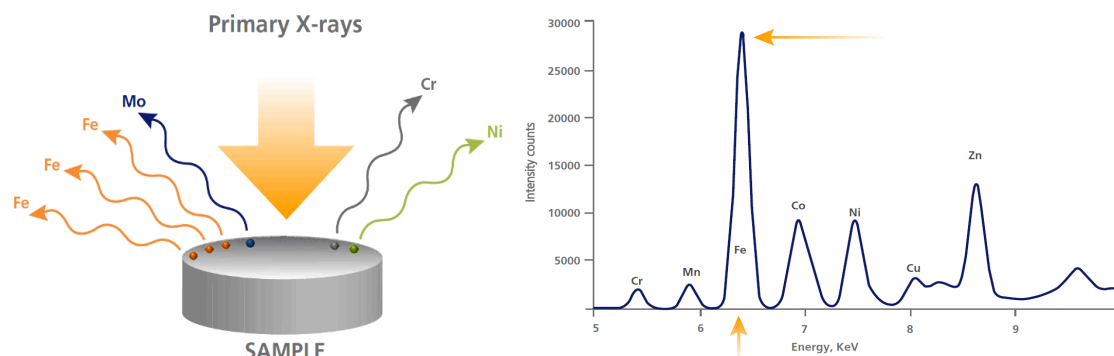
Figure 2.4. *a) The illustration is showing emitted x-rays that are characteristic of each element, b) An example of an X-ray spectrum (images from http://www.the-experts.com/x-ray-fluorescence-xrf-explained).*

In this study, XRF measurements were performed at the Museum für Naturkunde, Berlin, to determine the abundances of major oxides, such as SiO_2, TiO_2, Al_2O_3, Fe_2O_3, MnO, MgO, CaO, Na_2O, K_2O, and P_2O_5. Details about the sample preparation procedure and the instrumentation are described in Raschke et al. (2013).

2.4. Instrumental Neutron Activation Analysis (INAA)

Instrumental neutron activation analysis (INAA) is used to determine the concentrations of trace and major elements in a variety of matrices. A sample is subjected to a neutron flux, and radioactive nuclides are produced. In this process, some stable isotopes are converted into radioactive isotopes. As these radioactive nuclides decay, having half-lives varying from seconds to years, they emit gamma rays whose energies are characteristic for each nuclide. This gamma radiation is measured with semi-conductor gamma-ray spectrometers. Specific radionuclides emit gamma radiation of characteristic wavelengths or energies. So if there is a peak in the gamma-spectrum at a certain energy, it can be determined to which isotope it corresponds. The peak area gives information about the amount of this isotope present in the sample. Comparison of the intensity of these gamma rays with those emitted by a standard permits a quantitative measure of the concentrations of the various nuclides.

Elements that do not yield gamma-ray emitting radionuclides cannot be analyzed with INAA. The detection limits improve with the amount of radioactivity the element yields and the intensity of the gamma-rays that are emitted. There is no simple rule relating the elements to their detection limits.

The whole analytical procedure can be divided into four steps: preparation, irradiation, measurements and data processing.

2.4.1. Sample Preparation

Firstly, the homogenized sample powder was prepared by using jaw crusher, agate mill and space agate mill from sample chunks. From these sample powders, approximately 150 mg were weighed and packed in high purity polyethylene capsules and sealed. For each batch, a maximum of 14 capsules filled together with standards. Three standards (90 mg per standard) were used: The AC-E granite (Centre de Recherche Petrographique et Geochimique, Nancy, France; Govindaraju, 1994); the Allende carbonaceous chondrite (ALL; Smithsonian Institute, Washington D.C., USA; Jarosewich et al., 1987); and Devonian Ohio Shale (SDO1; United States Geological Survey; Govindaraju, 1989). Finally, the whole package is packed in an irradiation container to be irradiated at the Atomic Institute of the Austrian Universities, Vienna, Austria.
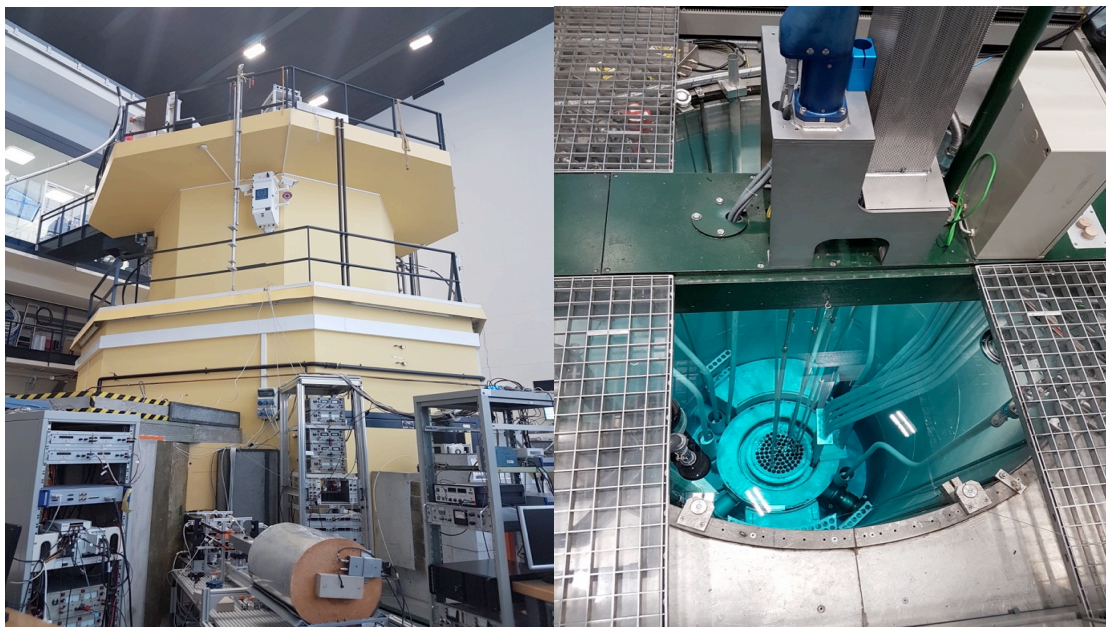
Figure 2.5. *Triga Mark-II reactor in Atomic Institute of the Austrian Universities, Vienna. Right photo shows reactor core (Photos by author).*

2.4.2. Irradiation

Although there are different sources used for the irradiation with neutrons, such as nuclear reactors, accelerators, or radio isotopic emitters, nuclear reactors with their high fluxes of neutrons from uranium fission are most commonly used in routine INAA. In our study we irradiated our samples in Atomic Institute, Vienna, by using the research reactor, TRIGA (Training, Research, Isotope Production, General Atomic) Mark-II (Fig. 2.5). This reactor has a maximum continuous power output of 250 kW (thermal) (for details about the reactor, see www.ati.tuwien.ac.at).

As mentioned above, the n-gamma (γ) reaction is the fundamental reaction for NAA. When we give an example to illustrate this reaction by using Fe isotopes:

$$^{58}Fe + {}^{1}n \rightarrow {}^{59}Fe + \beta^{-} + \gamma\text{-rays}$$

Stable isotope   Radioactive isotope
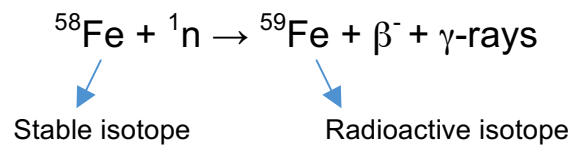
The gamma rays emitted during the decay of the ^{59}Fe nucleus and these gamma ray energies are characteristic for this nuclide.

The probability of a neutron interacting with a nucleus is a function of the neutron energy. This probability is referred to as the capture cross-section, and each nuclide has its relationship between neutron energy and capture cross-section. For many nuclides, the capture cross-section is greatest for low energy neutrons (referred to as thermal neutrons). Some nuclides have greater capture cross-sections for higher energy neutrons (epithermal neutrons). For routine neutron activation analysis, we are looking at nuclides that are activated by thermal neutrons (Fig. 2.6).
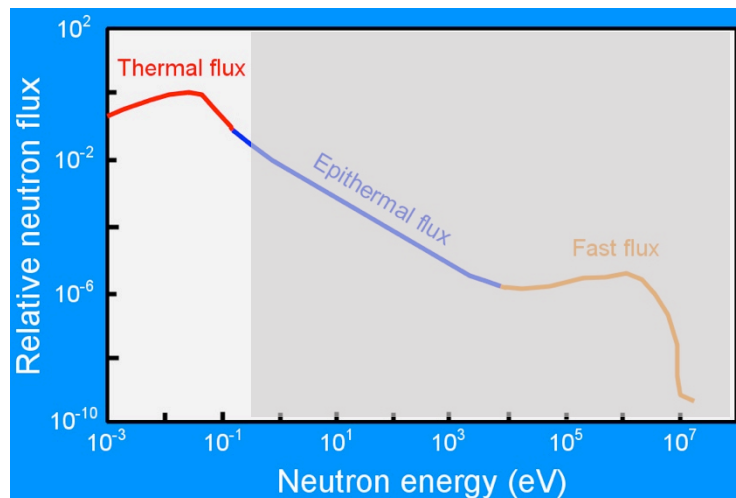
Figure 2.6. *The diagram of neutron energy vs. neutron flux. The area point towards low energy neutrons, which are preferably used in INAA (image from http://serc.carleton.edu/research_education/geochemsheets/techniques/INAA.html)*

The activity of a particular radionuclide, at any time t during irradiation, can be calculated from the following equation:

$$A_t = N\ \sigma_{act}\ \varphi\ (1 - e^{-\lambda t})$$

Where A_t is the activity in a number of decays per unit time, N is a number of target atoms, σ_{act} is the activation (neutron capture) cross section in cm^{-2}, φ is

the neutron flux in cm^{-2}s^{-1}, λ is the decay constant of the produced radionuclide and t is the irradiation time.

2.4.3. Measurements

After the samples are arrived back from irradiation, they are unpacked, decontaminated, and measured on semi-conductor (Ge) detectors depending on the amount of radio-activity formed. Due to which elements we are interested in, a waiting time is applied in order to let the nuclides with shorter half-life times decay, which gives a lower background and less interference. There are three counting cycles due to the different half-life of the various nuclides. At first (L1), 3 to 5 days after irradiation, all samples are measured for about one hour to determine the elements with short-lived radionuclides. The second cycle (L2) starts after about 15 days, to determine the medium-lived radionuclides and takes 3 hours per sample. And finally L3 is processed one month after irradiation to determine long-lived radionuclides for about 12 to 24 hours. After this third measurement, all 3 spectra of each sample are interpreted together.
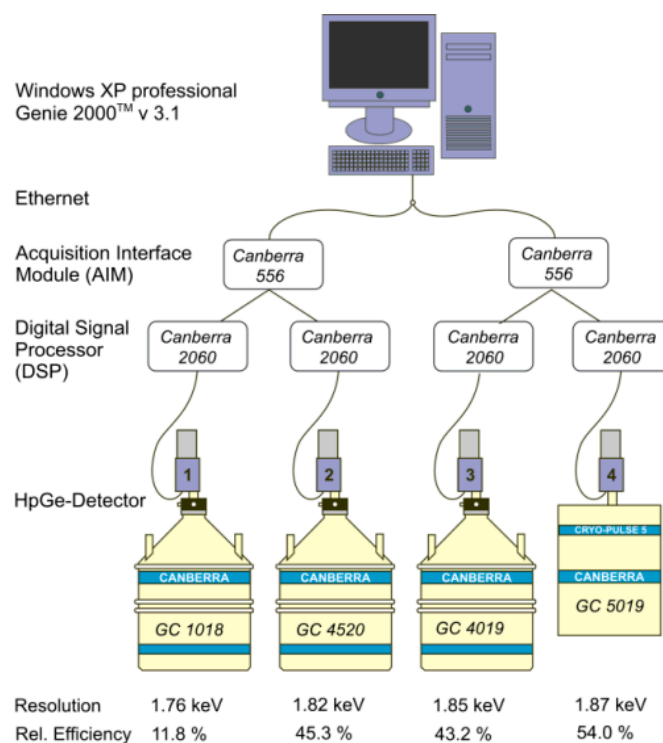
Figure 2.7. *The schema of the INAA system at the Department of Lithospheric Research, University of Vienna (source:* http://homepage.univie.ac.at/dieter.mader/gamma.html*).*

Gamma-rays help to elevate the electrons into the conduction band and leave electron holes in the valence band. The electron hole pairs are moved in a high-

voltage electric field to the opposite-charged electrode. Electric signal, proportional to the energy of the rays, is obtained. The semiconductor detectors (Li-drifted Ge detectors, which were used earlier, and high purity Ge detectors, which have been used since the past 20 years or so) have both high efficiency and high-energy resolution. These detectors have to be cooled with liquid nitrogen to minimize thermal excitation. The electric signal is amplified in a preamplifier and main amplifier. Then the signal is processed by a digital signal processor and stored in a multichannel analyzer. Every channel stores a signal of certain energy and the signals are combined in the spectrum. The resolution of a detector is a capability to separate adjacent ray lines.

2.4.4. Data Processing

After the measurements, the Genie 2000 analysis sequence for peak searching and calculation of the elemental concentrations is done by customized PNAA software (PC-based Neutron Activation Analysis software). The output of a PNAA calculation is an Excel-file with the elemental concentrations from each measuring cycle of each sample, reported in parts per million. These data are then manually checked, averaged, and processed for publication.

For more detailed information on the technique as performed at the University of Vienna, see Mader and Koeberl (2009), and for more information on the INAA method, see Ehmann and Vance (1991), Koeberl (1993), Koeberl (1995), and Gill (1997).

Table 2.1. *Elements determined by INAA (from Ferriere, 2008).*

Element	Indicator isotope	Energy lines [keV]	Half-life $T_{1/2}$	Measurement cycle
Na	^{24}Na	1368.6	14.96 h	L1
K	^{42}K	1524.7	12.36 h	L1
Sc	^{46}Sc	889.3; 1120.5	83.79 d	L2, L3
Cr	^{51}Cr	320.1	27.70 d	L2, L3
Fe	^{59}Fe	192.3; 1099.2; 1291.6	44.50 d	L2, L3
Co	^{60}Co	1173.2; 1332.5	5.27 y	L3
Ni	^{58}Co	810.8	70.82 d	L2, L3
Zn	^{65}Zn	1115.5	244.26 d	L3
As	^{76}As	559.1	26.32 h	L1
Br	^{82}Br	554.3; 776.5	35.30 h	L1
Sr	^{85}Sr	514.0	64.84 d	L2, L3
Rb	^{86}Rb	1076.6	18.63 d	L2, L3
Zr	^{95}Zr	724.2; 756.7	64.02 d	L2, L3
Sb	^{124}Sb	1691.0	60.0 d	L3
	^{122}Sb	564.1	2.70 d	L1
Cs	^{134}Cs	795.8	2.06 y	L3
Ba	^{131}Ba	496.3	11.50 d	L2, L3
La	^{140}La	328.8; 487.0; 1596.2	1.68 d	L1, L2
Ce	^{141}Ce	145.4	32.50 d	L2, L3
Nd	^{147}Nd	91.1; 531.0	10.98 d	L2
Sm	^{153}Sm	103.2	46.27 h	L1, L2
Eu	^{152}Eu	121.8; 1408.0	13.54 y	L2, L3
Gd	^{153}Gd	97.4; 103.2	241.6 d	L3
Tb	^{160}Tb	298.6; 897.4; 966.2; 1178.0	72.3 d	L2, L3
Tm	^{170}Tm	84.3	128.6 d	L2, L3
Yb	^{175}Yb	282.5; 396.3	4.18 d	L1, L2
	^{169}Yb	177.2; 198.0	32.03 d	L1, L2
Lu	^{177}Lu	208.4	6.73 d	L1, L2
Hf	^{181}Hf	482.2	42.39 d	L2, L3
Ta	^{182}Ta	67.7; 222.1; 1221.4; 1231	114.43 d	L2, L3
W	^{187}W	685.8	23.72 h	L1
Ir	^{192}Ir	299.0; 308.5; 316.5; 468.1	73.83 d	L3
Au	^{198}Au	411.8	2.70 d	L1
Th	^{233}Pa	300.3; 312.2	26.97 d	L2, L3
U	^{239}Np	228.2; 277.6	2.36 d	L1

Energy lines and half lives are from Firestone and Shirley (1996); "h" for hour, "d" for day, and "y" for year.

2.5. Mass spectrometry (MS)

Mass spectrometry (MS) is an effective analytical method, which measures the mass-to-charge ratio of ions to identify and quantify molecules in simple and complex mixtures. Mass spectrometry is a sensitive technique used to measure isotope ratios of specific elements and to detect, identify, and quantitate molecules based on their mass to charge (m/z) ratio. All mass spectrometers consist of (i) an ion source, (ii) a mass analyzer (i.e., a magnet), and (iii) an ion detector (see Fig. 2.8). The nature of these components varies based on the type of the mass spectrometer, the type of data required, and the physical properties of the sample. For geological analyses many different types of mass spectrometers have been used, such as thermal ionization mass spectrometry (TIMS), inductively coupled plasma mass spectrometry (ICP-MS), secondary ion mass spectrometry (SIMS), accelerator mass spectrometry (AMS). For this study, two types of mass spectrometer were used; TIMS in negative mode and using an electron multiplier to obtain ^{187}Os/^{188}Os ratios and the Os concentration of the spiked samples, and single collector ICP-MS to measure the concentrations of Re, Ir, Pt, Ru, and Pd (see chapter 2.6.2).

Figure 2.8. *Schematic of the basic components of a mass spectrometer.*

The first step during mass spectrometry is the ionization of the sample and the acceleration of ions (which, e.g., in TIMS, can have negative or positive charge) by applying a high voltage. The accelerated ions are then deflected by using electromagnetic deflection within the mass analyzer (one of six types; quadrupole time of flight, magnetic sector, electrostatic sector, quadrupole ion trap or ion cyclotron resonance) which is used for the separation of ions in mass spectrometry. Finally, ions are properly aligned and reach the either an electron multiplier detector (single collector mode) or of Faraday cups (multi-collector mode). After detection of the ions and amplification of the signal, isotope ratios are reported on an external computer (Fig. 2.9).

More information on mass spectrometry can be found in, e.g., Potts (1987), Gill (1997), de Groot (2004); these references were used for the elaboration of this review.
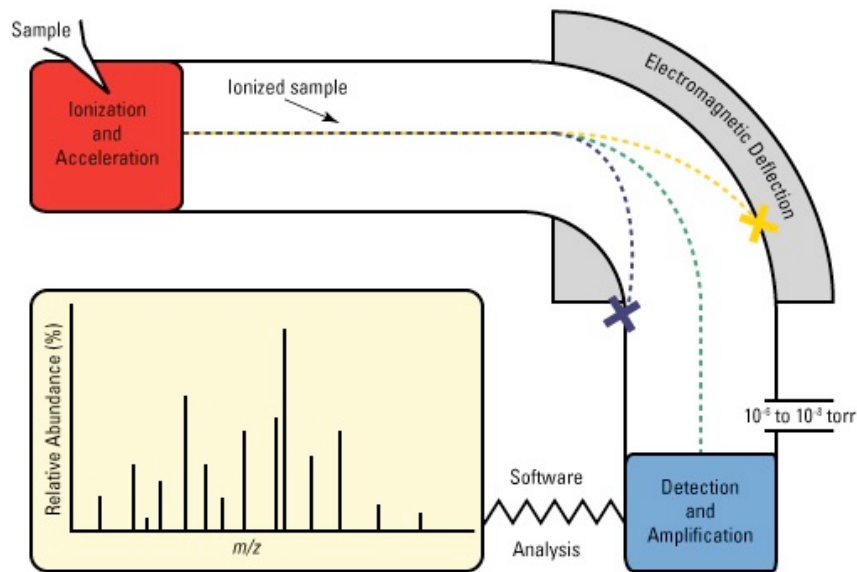
Figure 2.9. *Diagram of a mass spectrometer (source:* https://www.thermofisher.com)*.*

The mathematical principles of mass spectrometry are described as follows:

1st the ion acceleration phase is;

$$eV = 1/2\ mv^2 \Rightarrow v = (2eV\ /\ m)^{1/2}$$

eV is the electrical energy (e is the ion's charge and V is the potential difference), $1/2mv^2$ is the kinetic energy (m is ion mass and v is its speed)

2nd when magnetic deflection is given by equating the magnetic force Bev (B is the magnetic field) to centripetal acceleration (v^2/R) (R is the radius of curved deflected path) multiplied by mass m;

$$Bev = m\ (v^2\ /\ R) \rightarrow v = BeR\ /\ m$$

3rd when we equal both v values: $m/e = B^2R^2\ /\ 2V$

4th after balance the different units, the atomic mass is:
$$m = (B^2R^2\ /\ 20721\ V) \times 10^{12}$$

(B is in teslas, m in atomic mass units, R in meters, and V in volts).

2.5.1. Important corrections in mass spectrometry

In mass spectrometry, two corrections have to be applied in order to generate precise isotope ratio measurements: mass fractionation correction and mass interference.

2.5.1.1. Mass fractionation correction

One phenomenon that occurs during thermal ionization mass spectrometric analysis is the preference of lighter isotopes to preferentially evaporate from the sample reservoir (which was loaded onto an electrically heated filament). This means that the ion beam will be richer in light isotopes compared to the sample that remained on the filament. During the analysis, the sample will become increasingly depleted in light isotopes and the ratio of light isotopes to heavy isotopes continuously changes during the measurement. This effect, called mass fractionation, can produce variations in specific isotope ratios up to several percent during a single measurement. A correction of this effect can be achieved by applying mass fractionation correction. The principle is to measure the ratio of two isotopes that are not radiogenic, this ratio should not vary in nature. For Os, as an example, we measure the ratio of ^{192}Os/^{188}Os. By convention, we consider that the value of this ratio is equal to 3.083 (Brandon et al. 2006, Luguet et al. 2008). Any (measured) deviation from this value can then be assumed to result from mass fractionation in the mass spectrometer. If we know the magnitude of the deviation of the measured ^{192}Os/^{188}Os ratio from the true (literature) value, we are able to calculate the amount of fractionation for any other Os isotope ratios.

When we write *the linear mass fractionation law*:

$$\propto (a,b) = \left[\frac{R_{ab}^{N}}{R_{ab}^{M}} \text{-}1 \right] / \Delta m_{ab}$$

where α is fractionation factor between two isotopes (a and b), Δm is the mass difference between a and b isotopes (e.g., 4 for 186 and 190), R^N is the true isotope ratio (e.g., 3.083 for 192/188), R^M is the measured ratio. The correction to the ratio of two other isotopes (e.g., ^{186}Os/^{188}Os) is then calculated as;

$$R_{xy}^{C} = R_{xy}^{M} (1 + \propto (x,y)\Delta mxy)$$

where R^C is the corrected ratio and R^M is the measured ratio of x to y and,

$$\propto (x,y) = \frac{\propto (a,b)}{1 - \propto (a,b)\Delta M_{by}}$$

For example, after Luguet et al. (2008), when we know true ratio of ^{192}Os/^{188}Os which is 3.083 (Brandon et al. 2006) to correct the ^{186}Os/^{188}Os ratio;

$$\left(\frac{^{186}Os}{^{188}Os}\right)^{c} = \left(\frac{^{186}Os}{^{188}Os}\right)^{M} \left[1 + \left\{\frac{3.083}{(^{192}Os/^{188}Os)^{M}} - 1\right\}/2\right]$$

A more accurate description of mass fractionation is the _power law_. The fractionation factor is:

$$\propto = \left[\frac{R_{ab}^{N}}{R_{ab}^{M}}\right]^{\frac{1}{\Delta m_{ab}}} - 1$$

The corrected ratio is computed as:

$$R_{x,y}^{C} = R_{x,y}^{M}[1 - \propto]^{\Delta m_{x,y}}$$

$$R_{x,y}^{C} = R_{x,y}^{M}\left[1 + \propto \Delta m_{x,y} + \frac{1}{2}\Delta m_{x,y}(\Delta m_{x,y} - 1)\propto^{2} + \cdots\right]$$

Finally, it is claimed that the power law correction is not accurate and that the actual fractionation is described by an _exponential law_, from which the fractionation factor computed as:

$$\propto = \frac{ln[R_{ab}^{N}/R_{ab}^{M}]}{m_{y}ln(m_{a}/m_{b})}$$

and the correction is:

$$R_{x,y}^{C} = R_{x,y}^{M}\left(\frac{m_{x}}{m_{y}}\right)^{\propto m_{y}} = R_{x,y}^{M}\left[1 + \propto \Delta m_{x,y} - \propto \frac{m_{x,y}^{2}}{2m_{y}} + \propto^{2}\frac{m_{x,y}^{2}}{2} + \cdots\right]$$

The exponential law provides the most accurate correction for mass fractionation. However, all of the above laws are empirical rather than theoretical. The processes of evaporation and ionization are complex, and there is yet no definitive theoretical treatment of mass fractionation during this process.
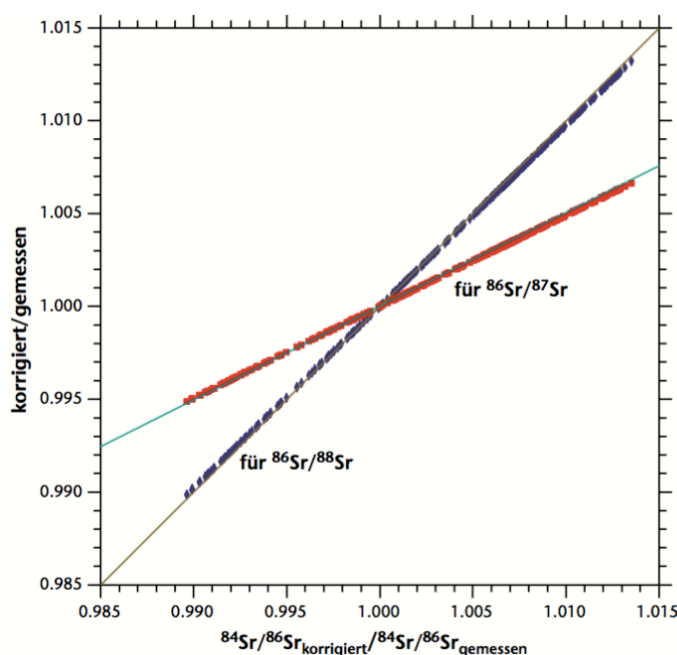
Figure 2.10. *Mass fractionation correction diagram for different Sr isotopes. The ratios* $(^{86}Sr/^{88}Sr_N) / (^{86}Sr/^{88}Sr_M)$ *and* $(^{86}Sr/^{87}Sr_N) / (^{86}Sr/^{87}Sr_M)$ *against* $(^{84}Sr/^{86}Sr_N) / (^{84}Sr/^{86}Sr_M)$ *are plotted (diagram from Stosch 1999).*

2.5.1.2. Isobaric (mass) interference correction

Isobars are atoms (nuclides) with different numbers of protons but equal mass numbers. In mass spectrometry this causes problems because mass signals of interest (detected in either Faraday cups or an electron multiplier) do not necessarily are generated by the isotope of interest alone. An isobaric isotope could also contribute to the signal. This contribution needs to be subtracted from the signal in order to calculate the contribution from the isotope of interest. Such corrections can occur, for example, for mass number 87 with contributions from ^{87}Rb and ^{87}Sr or for mass 187, where both ^{187}Re and ^{187}Os contribute to the resulting signal. To avoid such interferences, chemical separation of the (interfering) elements has to be applied. However, this never results in a full separation and interfering "contaminants" still occur during mass spectrometry. In principle, isobaric contributions can be subtracted by simultaneously measuring another isotope of the interfering element that has no isobaric interferences. For example, the signal on mass 187 is, see above, generated by ^{187}Re and ^{187}Os. To calculate the contribution of ^{187}Re to this signal one has to simultaneously measure the signal on mass 185, which solely is generated by the interference-free isotope ^{185}Re. By knowing the constant ^{185}Re/^{187}Re ratio of the sample (literature value) one can simply calculate the contribution of ^{187}Re

on mass 187. In case of negative TIMS and Os measurements (as applied in this study) a further complication arises due to the fact that all Os isotopes are measured as oxide species (OsO_3^-). The different stable oxygen isotopes then dictate the molecular mass that is measured in the end (for example, mass 240 for $^{192}Os^{16}O_3^-$). The different combination of ^{16}O, ^{17}O, and ^{18}O in such a molecular species (Os trioxide ion) then cause numerous additional isobaric interferences which have to be subtracted from each signal. This can be done mathematically by knowing the relative abundances of the oxygen isotopes in the gas phase (assumed to be the Nier composition; Nier 1937). Table 2.2 gives an example of such interferences.

Table 2.2. *Osmium trioxide species for calculation of Os and O isotope ratios*

Mass number	$Os^{16}O_3^-$	$Os^{16}O_2^{17}O^-$	$Os^{16}O_2^{18}O^-$
232	$^{184}Os^{16}O_3^-$		
233		$^{184}Os^{16}O_2^{17}O^-$	
234	$^{186}Os^{16}O_3^-$		$^{184}Os^{16}O_2^{18}O^-$
235	$^{187}Os^{16}O_3^-$	$^{186}Os^{16}O_2^{17}O^-$	
236	$^{188}Os^{16}O_3^-$	$^{187}Os^{16}O_2^{17}O^-$	$^{186}Os^{16}O_2^{18}O^-$
237	$^{189}Os^{16}O_3^-$	$^{188}Os^{16}O_2^{17}O^-$	$^{187}Os^{16}O_2^{18}O^-$
238	$^{190}Os^{16}O_3^-$	$^{189}Os^{16}O_2^{17}O^-$	$^{188}Os^{16}O_2^{18}O^-$
239		$^{190}Os^{16}O_2^{17}O^-$	$^{189}Os^{16}O_2^{18}O^-$
240	$^{192}Os^{16}O_3^-$		$^{190}Os^{16}O_2^{18}O^-$
241		$^{192}Os^{16}O_2^{17}O^-$	
242			$^{192}Os^{16}O_2^{18}O^-$

For detailed information and mathematical correction calculations and, see Liu et al. 1998, Meija and Caruso 2004, and Luguet et al. 2008.

2.5.2. Isotope Dilution

The basic principle of the isotope dilution technique is that a known amount of a spike (or tracer) of known isotopic composition and elemental concentration is added to a sample of unknown isotopic composition and unknown elemental concentration. From the measured isotopic composition of the spiked sample, the isotopic composition and elemental concentration of the unknown sample can be calculated. From the viewpoint of arithmetic, this is a simple mixing problem:

$$\frac{X^A_{mix}}{X^B_{mix}} = \frac{X^A_{sample} + X^A_{spike}}{X^B_{sample} + X^B_{spike}} = \frac{X^B_{sample}\left(\dfrac{X^A_{sample}}{X^B_{sample}}\right) + X^B_{spike}\left(\dfrac{X^A_{spike}}{X^B_{spike}}\right)}{X^B_{sample} + X^B_{spike}}$$

If we know the X^B content of the spike, the content of element X in the rock can be derived by simply measuring the isotopic ratio of the mixture. This method can be used for all chemical elements with several stable isotopes for which spikes have been prepared that are artificially enriched in one or more isotopes.
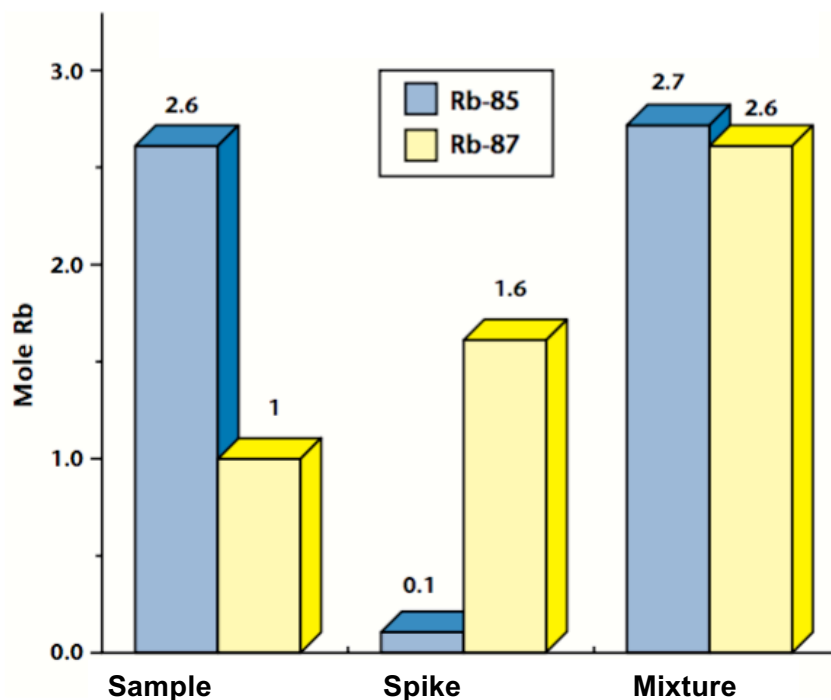
Figure 2.11. *Illustration of the principle of isotope dilution analysis for two Rb isotopes, of mass 85 and 87 (from Stosch 1999).*

When we apply this calculation for Os isotope measurements;

$$\left(\frac{^{187}Os}{^{188}Os}\right)_{mix} = \left(\frac{(^{187}Os)_{rock} + (^{187}Os)_{spike}}{(^{188}Os)_{rock} + (^{188}Os)_{spike}}\right)$$

$$= \frac{\left(\frac{^{187}Os}{^{188}Os}\right)_{spike} + \left(\frac{^{187}Os}{^{188}Os}\right)_{rock}\left[\frac{^{188}Os_{rock}}{^{188}Os_{spike}}\right]}{\left[1 + \frac{^{188}Os_{rock}}{^{188}Os_{spike}}\right]}$$

All parts are divided by ^{188}Os;

$$^{188}Os_{rock} = {}^{188}Os_{spike}\left(\frac{^{187}Os}{^{188}Os}\right)_{spike}\left[\frac{\left(\frac{^{187}Os}{^{188}Os}\right)_{spike} - \left(\frac{^{187}Os}{^{188}Os}\right)_{mix}}{\left(\frac{^{187}Os}{^{188}Os}\right)_{mix} - \left(\frac{^{187}Os}{^{188}Os}\right)_{rock}}\right]$$

As explained above, by knowing the ^{188}Os content of spike and measuring the Os isotope ratio of the mixture, we can obtain the Os content of the rock.

2.5.3. Chemistry and measurements applied in this study

The HSE chemistry

One of the most fundamental tools used in impact science (to identify and quantify meteoritic admixtures to impactites) are siderophile element concentrations. These elements are highly enriched in extraterrestrial materials relative to the upper continental crust (31 ppt for Os, 22 ppt for Ir, 210 ppt for Ru, 510 ppt for Pt, 520 ppt for Pd, Peucker-Ehrenbrink and Jahn 2001). Due to this marked contrast in the PGE budgets, abundances of these elements can be used as a proxy for the presence of extraterrestrial admixtures in impactites in comparison to country rocks (rocks unaffected from the impact event but representing the target lithology).

A prominent example for the successful application of this tool was the discovery of a globally distributed Ir anomaly at the Cretaceous-Tertiary boundary by Alvarez et al. (1980), now known to have been produced by the Chicxulub impact event (66.04 Ma Swisher et al. 1992, Sharpton et al. 1992, Krogh et al. 1993). Very high PGE concentrations were recognized globally in the corresponding stratigraphic layer (e.g., Luck and Turekian 1983). The Ir anomaly (up to 6 ppb, Koeberl et al. 1994), in that case, unambiguously confirmed the presence of a meteoritic component. So far, this tool was applied to numerous other impactites from impact structures around the world with the goal to identify (and probably characterize) meteoritic admixtures.

However, considering the high PGE abundances in the spherule layers (up to slightly superchondritic values, requiring meteoritic components of 100% or more, which is not observed for any other impactites worldwide) led to the suggestion that such enrichments may be due to secondary processes (Koeberl et al. 1993 and Koeberl and Reimold 1995). These authors pointed out numerous problems with the original impact hypothesis that was formulated by Lowe and Byerly (1986) and Lowe et al. (1989). Moreover, e.g., Reimold et al. (2000) explained the elevated concentrations of PGEs and other highly siderophile elements with secondary sulfide mineralization, although they did not exclude the possibility that an impactor component might be responsible for such high concentrations. Finally, such extreme enrichments could also result from element fractionation during spherule formation as well as fractionation during deposition and/or diagenetic and metasomatic processes (Lowe et al. 2003). The final argument in favor of an impact origin of at least some of the Archean spherule layers (S2, S3 and S4 layers) from the Barberton area came in the form of Cr isotope evidence, suggesting a carbonaceous chondritic impactor (Kyte et al. 2003; Shukolukov et al. 2000).

Despite their widespread use in impact science, elemental abundances alone are often ambiguous and difficult to interpret. This is the case, for example, when the target material contains mafic lithologies, mafic lithologies exhibit higher PGE concentrations and the abundance differences to chondrites are, thus, lower. In such cases the ^{87}Sr and ^{143}Nd isotope signatures can serve as a discriminator between mafic contaminations or meteoritic admixtures as the cause for enhanced PGE abundances. In addition, the ^{187}Re-^{187}Os system can be applied to impactites. This is because of the (above mentioned) difference between the ^{187}Os/^{188}Os ratios of meteorites in contrast to felsic terrestrial lithologies (like the upper continental crust). However, mafic lithologies exhibit more mantle-like (and, thus, nearer to chondritic) ^{187}Os signatures. A careful petrographic inspection of the samples analyzed in conjunction with coupled ^{87}Sr-^{143}Nd isotope analysis is always a prerequisite in the discussion of both, PGE abundance and ^{187}Os/^{188}Os isotope data of impactites.

The ^{187}Re-^{187}Os systematics

Osmium is a member of the platinum group elements (PGE: Ru, Rh, Pd, Pt, Os, and Ir). Although Re is commonly associated with the PGEs (according to its similar geochemical behavior) it cannot be considered as a member of this group. Rhenium, however, can be assigned as a highly siderophile elements (HSE), a term, which can also collectively be used for all PGEs. Osmium exhibits seven naturally occurring isotopes, whose individual abundances are ~0.02% for ^{184}Os, 1.59% for ^{186}Os, 1.51% for ^{187}Os, 13.29% for ^{188}Os, 16.22% for ^{189}Os, 26.38% for ^{190}Os and 40.98% for ^{192}Os (Shirey and Walker 1998). For

mass spectrometry analysis, the radiogenic isotope ^{187}Os (the daughter product of ^{187}Re) is normalized by the abundance of the isotope ^{188}Os, which is unaffected by natural long-lived radioactive decay.

Rhenium consist of two naturally occurring isotopes, ^{185}Re and ^{187}Re. The concentration of ^{185}Re remains constant over time in a geologic sample. ^{187}Re is unstable and decays to ^{187}Os with a half-life of 41.8 Ga (Smoliar et al. 1996). This is the basis of the ^{187}Re-^{187}Os decay system. The ^{187}Re-^{187}Os system has several applications, such as dating of geological samples and understanding sulfide ore genesis and related tectonic events, constraining mantle evolution and crustal growth, characterizing diamond formation or the identification of the oceanic osmium isotope budget.

Such applications benefit from the geochemical behavior of Re and Os. The ^{187}Re-^{187}Os isotope system differ from other, conventionally used, long-lived radioactive systems in that both elements (Re and Os) are siderophile, whereas the ^{87}Rb-^{87}Sr, ^{147}Sm-^{143}Nd or ^{176}Lu-^{176}Hf radionuclide systems solely comprise lithophile elements. In addition, Os behaves more compatible compared to Re, resulting in successively more radiogenic (more enriched in ^{187}Os) signatures in granites (or the average upper continental crust) compared to mantle rocks or meteorites (e.g., chondrites). The range of present day values of ^{187}Os/^{188}Os (during mass spectrometric analyses ^{187}Os is always normalized to stable ^{188}Os) are 0.1263±0.0008 for carbonaceous chondrites, 0.1283±0.0008 for enstatite and 0.1289±0.0022 for ordinary chondrites (Shirey and Walker 1998). In comparison, the upper continental crust values vary between ~1.4 and ~1.9 (Peucker-Ehrenbrink and Jahn 2001).

Besides geological and geochronological applications, the Re-Os isotopic signature has been used to quantify meteoritic components in impactites. This application is explained in more detail below, as it is the basic tool applied to the CT3 drill core samples in this study.

2.5.3.1. The HSE chemistry and the Os-Re systematics applications in this study

Historically, a number of techniques for Os separation have been used. The main difficulty, that has to be accounted for, is the volatility of Os in its oxidized form at relatively low temperatures and pressures (~130°C at 105 Pa). Samples can, thus, not simply be dissolved in oxidizing solutions in conventional Teflon beakers (Reisberg et al. 2002). Methods applied during the last decades are briefly summarized in table Table 2.3., including the high pressure asher technique, which is used in this study.

In this study, between ~0.1 and ~0.6 g of homogenized sample powder were spiked with a mixed tracer solution (enriched in ^{99}Ru, ^{105}Pd, ^{185}Re, ^{190}Os, ^{191}Ir

and ^{194}Pt). The sample - spike mixtures were digested in 7 ml inverse aqua regia (HNO$_3$-HCl: 5+2 ml) and leached at 250°C and 100-130 bars in an Anton-Paar high pressure asher for 12 hours. Osmium and the PGEs (and Re as a highly siderophile element) were then separated according to extraction (Cohen and Waters 1996), microdistillation (Birck et al. 1997) and anion exchange chemistries (Rehkämper and Halliday 1997 and Coggon et al. 2013), which are described below in detail.

Table 2.3. *The various digestion techniques and summary of their dis-/advantages (Table from Reisberg et al. 2002).*

Digestion Technique	Advantages	Disadvantages
Dissolution in reducing media (HBr, HCl-ethanol) Walker (1988), Birck *et al.* (1997)	Prevents loss of OsO$_4$ Very low blanks achievable	Incomplete sample digestion, often serious
Alkaline fusion Morgan and Walker (1989)	Complete digestion	May have high and irreproducible Re and Os blanks, depending on reagent batch Problems with spike-sample equilibration reported
NiS fire assay Hoffman *et al.* (1978), Ravizza and Pyle (1997)	Complete or nearly complete digestion	Usually produces unreliable Re results May have high Os blanks, depending on reagent batch Possible loss of volatile-hosted Os
Carius tubes Shirey and Walker (1995), Shen *et al.* (1996)	Nearly complete digestion Very low blanks achievable	Minor digestion problems with refractory phases Somewhat dangerous
High pressure asher Meisel *et al.* (2001)	Complete, rapid digestion Very low blanks achievable	Expensive apparatus required Sample size limited to less than 3 grams
Leaching techniques Pegram *et al.* (1992), Peucker-Ehrenbrink *et al.* (1995)	Allows selective analysis of leachable phases Very low blanks achievable	Leached phases not always well constrained Possible fractionation of Re and Os during leaching

A detailed summary of the laboratory procedures for Os and PGE chemistries including cleaning procedures is given below

1. Cleaning beakers and vials: The first step before performing the chemical separation is to clean beakers and glass vials to avoid any Os and Re contamination. Glass vials used for digestion in the high pressure asher were cleaned in an ultrasonic cleaner. They were filled with Mili-Q (MQ) water mixed with 2 ml of 2.5 M HCl and placed vertically into ultrasonic cleaner, which is also filled with MQ. After 60 minutes at 60°C the glass vials were taken from the cleaner, washed with MQ, and dried. Following this procedure all glass vials were further cleaned for 4 hours at ~200 °C and 100-130 bars in the high pressure asher using 5 ml inverse aqua regia.

   Savillex beakers (15 ml) and rocket beakers (5 ml), were cleaned in a procedure including (i) hydrobromic acid- HBr (for two days on a hotplate at ~100°C), nitric acid- HNO$_3$ (for several days on a hotplate at ~100°C) and a final MQ wash (for several days on a hotplate at ~100°C).

2. Digestion: About 0.1 to 0.5 g of homogenized sample powder was weighed and carefully transported into the glass vials. After calculating the amount of spike needed (to avoid over- or underspiking and to achieve a $^{192}Os/^{190}Os$ ratio of the sample-spike mixture of approximately 2), the spike solutions were weighed and added to the respective sample powders. There are two types of spikes in hand (one optimized for peridotitic samples, with 43 ppb Os, and one spike optimized for basalt samples, with 4 ppb Os). The peridotite spike was used in this study for all samples, due to high (up to near chondritic) Os concentrations of the samples. All blank measurements where obtained using the basalt spike. After spiking, all sample-spike mixtures where diluted in 5 ml aqua-regia (2 ml of HCl+3 ml HNO_3). All vials where sealed with teflon band and glass caps and placed into the reaction chamber of the high pressure asher. All samples were then processed at 110-130 bar and 250-260°C for 12 hours. During this procedure all platinum-group elements and most of the Re were leached into the aqua regia.

3. The separation of platinum-group elements and rhenium

Solvent extraction: After extraction of the samples from the high pressure asher, all solutions (excluding the undissolved sample) were transferred into precleaned 50 ml centrifuge tubes. 2 ml of tetracarbonchloride (CCl_4) was directly added to the solutions in order to prevent any loss of volatile Re or Os. Sequential additions of further 2 ml entities of CCl_4 solution to the sample solutions and mixing of the solutions on a sample-mixer, were followed by successive removal of the CCl_4 solutions (which, according to its higher density is clearly separated from the aqua regia) into 15 ml Savillex beakers using 2 ml pipette tips. These beakers were prefilled with 4 ml HBr. During this procedure a total of 7 ml CCl_4 was added sequentially to all centrifuge tubes (which contain the samples PGE, Re solutions) and finally transferred into the 15 ml Savillex beakers. The HBr/CCl_4 mixtures (containing the Os) were then mixed on the sample mixer for 12 hours. The remaining aqua regia solutions of all samples (including Re and all PGEs excluding Os) were then reunited with the undissolved sample material from the glass vials and dried down at 120°C on a hotplate in order to prepare the samples for anion exchange chemistry (a procedure described below). The principles behind this procedure, called solvent extraction, is that Os (initially dissolved with Re and all other PGEs in the aqua regia) tends to partition into the CCl_4. Osmium is, thus, separated from Re and all other PGEs during this procedure. Finally, the CCl_4, containing the Os, is then added to pure HBr in order to transfer Os into a stable bromo complex.

Back-extraction: In the back extraction procedure the CCl_4 is separated from the CCl_4-HBr mixtures (two, according to their different densities clearly

separated solutions) using a 1 ml micro pipette tip. Osmium partitioned during the mixing procedure at the end of the solvent extraction step (see above) from the CCl$_4$ into the HBr. The separated CCl$_4$ solutions were discarded and the (Os containing) HBr solutions dried down at not more than 60°C to avoid any loss of volatilized osmium.

Micro-distillation: The dried down Os cuts from each sample were redissolved in 10 µl of H$_2$SO$_4$ and carefully transferred into the cap of a rocket beaker. 10 µl of Cr$_2$O$_3$ solution was added into the H$_2$SO$_4$ bubble, which is placed in the middle of rocket beaker lid. The chromium solution acts as an oxidizing agent. The necks of the rocket beakers were covered with a Teflon band to avoid any leak of Os and 10 µl of HBr was added to the bottom part of theses rocket beakers. The bottom beaker filled with HBr was carefully turned upside down and screwed onto the upside down lid containing the sample with H$_2$SO$_4$ and Cr$_2$O$_3$. The surface tension between HBr and the rocket beaker walls keeps the liquid in place. An aluminum foil was carefully wrapped around the beaker and the samples were transported to the hot plate at 90°C for 90 minutes. After unscrewing the beakers, the Os fraction (the 10 µl HBr drop) was put on the hot plate and dried down until 1µl remained, then sealed with parafilm to store for measuring.

4. *Anion-exchange chemistry:* During the leaching process in the HPA most but not all of the Re from the sample partitioned into the aqua regia. The PGE sample cuts from the solvent extraction step (see above) were, therefore, redissolved using a procedure with steps including HF, HCl, and HNO$_3$. The PGE column chemistry was performed using 1 ml BIORAD AGIx8 (200-400 mesh) anion exchange resin and using the recipe as shown in table 2.4. The PGEs were separated in two steps, the first including Re, Pt and Ir, the second including Ru and Pd. After eluting of the elements all solutions were dried down and redissolved for the final clean-up chemistry involving Ln spec resin (see table 2.4). All elutions were dried down and prepared for measurements.

Table 2.4. *The procedure of PGE anion column and LN spec column chemistry from Chu et al. 2014.*

ANION COLUMN		LN-Spec COLUMN	
	Resin Amount 1 ml		
Resin Cleaning	10 ml H_2O	Resin Cleaning	4 ml H_2O
	10 ml 6M HNO_3		4 ml 6M HCl
	10 ml conc HNO_3		4 ml 6M HCl
	2 ml H_2O		4 ml 2M HF
	10 ml conc HCl		4 ml 6M HCl
	2 ml H_2O		4 ml 2M HF
Equilibration	2ml 1M HCl		4 ml H_2O
	2ml 0.5M HCl	Equilibration	4 ml 1M HCl
Load sample	**10 ml 0.5M HCl**	**Load Pd and collect Pd**	**1 ml 1M HCl**
	5 ml 1M HCl	**Collect Pd**	**4 ml 1M HCl**
	2 ml 0.8M HNO_3	**Load Ir-Pt-Re-Ru and collect**	**1 ml 1M HCl**
	2 ml 0.8M HNO_3	**Collect Ir-Pt-Re-Ru**	**5 ml 1M HCl**
Collect Re-Ir-Pt-Ru	**15 ml conc HNO_3**	Cleaning	4 ml 2M HF
	2 ml H_2O		4 ml 2M HF
Collect Pd	**15 ml conc HCl**		4 ml 6M HCl
Collect Pd	**10 ml conc HCl**		4 ml 2M HF
Collect Pd	**10 ml conc HCl**		4 ml 6M HCl
			4 ml 2M HF
Dried down both cuts and redissolved in 1ml 1M HCl			4 ml 6M HCl

2.5.3.2. Measurements

The first Os isotopic composition measurements were performed by Nier 1937, using electron bombardment of Os tetroxide gas. Following 1960s, first Os isotopic analyses on meteorites and molybdenites again by using Os tetroxide in gas source spectrometry (Herr et al 1961 and Hirt et al 1963). On this method, tens of micrograms of Os were required to obtain few percentage of precisions. Therefore, during the time, the methods were improved by using different spectrometers to have high precision (1 to 3 %) with very small amount of Os (up to several hundred femtograms) by using secondary ionization mass spectrometer (SIMS, Luck 1983), resonance ionization mass spectrometer (RIMS, Walker and Fassett 1986) and negative thermal ionization mass spectrometer (NTIMS, Creaser et al. 1991, Völkening et al. 1991, Levasseur et al. 1998), respectively. Finally, the application of Faraday multi collector into NTIMS allowed to obtain extremely high precision (less than 0.005 %) out of moderate quantities (tens of nanograms) of Os (Brandon et al. 1999).

In this study, the $^{187}Os/^{188}Os$ ratios and the Os concentrations were determined at the Department of Lithospheric Research at the University of Vienna, Austria, by using a ThermoFinnigan Triton Thermal Ionization Mass Spectrometer operating in negative ion mode, because Os is, due to its comparably high ionization potential, difficult to ionize in conventional positive ion mass spectrometry (P-TIMS). A solution of Os, as bromide ($OsBr_3$), loaded on Pt ribbon filaments (0.02 mm thick, 1 cm wide). Furthermore, the saturated $Na(OH)/Ba(OH)_2$ solution (electron emitter/activator, see Völkening et al. 1991, Creaser et al. 1991, Birck et al. 1997, Luguet et al. 2008) was applied to cover the Os. The runs were performed with an oxygen bleed in order to raise ionization yields. Osmium was measured as OsO_3 ions in a peak hopping mode using the SEM detector. Oxygen corrections were performed using $^{17}O/^{16}O$ of 0.0003708 and $^{18}O/^{16}O$ of 0.00203450 (Nier 1950). Corrections for mass interferences of ^{187}Re on ^{187}Os and mass fractionation (using $^{192}Os/^{188}Os$ = 3.083; Brandon et al. 2005; Luguet et al. 2008) were calculated (see above). The Os total procedural blank was ~10 pg (n = 3) contributing less than 0.05% to most of the measured Os concentration of all samples. In the other cases a blank correction was applied.

At the beginning of each N-TIMS measurement we performed repeated measurements (n = 3) of 10 pg loads of a DROsS (Durham Romil Osmium Standard) solution using an electron multiplier at signal intensities that were typically achieved during our sample runs (~10000 to ~1000000 counts on mass 192). The DROsS measurements yield 0.160924 for $^{187}Os/^{188}Os$, 1.219691 for $^{189}Os/^{188}Os$, and 1.983726 for $^{190}Os/^{188}Os$ ratios. These values agree within the 2σ uncertainty of the average values reported by Luguet et al.

(2008) obtained for much larger Os loads of DROsS. The long-term external reproducibilities are ±0.4% for $^{187}Os/^{188}Os$, ±0.2% for $^{189}Os/^{188}Os$ and ±0.3% for $^{190}Os/^{188}Os$.

The remaining Re and PGE concentrations were determined using a Thermo Element ICP-MS in single collector mode at the Steinmann Institute at the University of Bonn, Germany, using methods described in Luguet et al. (2015).

Briefly, instrumental mass fractionation was quantified by analyzing a 1 ppb HSE standard solution multiple times, at the beginning, middle, and end of the analytical session. To monitor isobaric and oxide interferences caused by Cd, Y, Zr, and Mo on Pd and by Hf on Ir and Pt, a 1ppb Y-Zr- Mo solution and a 1 ppb Hf solution were run at the beginning and end of the analytical session. Rhenium, Ir, and Pt were measured with a cyclonic borosilicate glass spray chamber, while Ru and Pd were analyzed using an ESI Apex HF desolvation system. Total blanks for this study (n = 4) were 3–4 pg for Re, 0.5–3 pg for Ir, 20–70 pg for Ru, 20–60 pg for Pt, and 20–50 pg for Pd. Due to the low HSE contents of the analyzed samples, blank corrections, except for Pt and Pd, were significant but <10% in all cases (Schulz et al. 2016).

References

Alvarez L. W., Alvarez W., Asaro F., and Michel H. V. 1980. Extraterrestrial cause for the Cretaceous-Tertiary extinction. Science 208:1095-1108.

Allegre C. J. 2008. Isotope geology. Cambridge University Press, New York, 510 p.

Bartosova K. 2010. Geochemical, mineralogical, and petrographic investigations of the Eyreville drill cores from the Chesapeake Bay impact structure. Ph.D. thesis, University of Vienna, Vienna, Austria, 433 p.

Birck J. L., Barman M. R. and Capmas F. 1997. Re-Os isotopic measurements at the femtomole level in natural samples. Geostandards Newsletter 20:19-27.

Bohr N. 1913. On the Constitution of Atoms and Molecules, Part I. Philosophical Magazine. 26 (151): 1-24.

Brandon A. D., Norman M. D., Walker R. J. and Morgan J. W. 1999. ^{186}Os-^{187}Os systematics of Hawaiian picrites. Earth and Planetary Science Letters 174:25-42.

Brandon A. D., Humayun M., Puchtel I. S., Leya I. and Zolensky M. 2005. Geochemistry: Osmium isotope evidence for an s-process carrier in primitive chondrites. Science 309:1233-1236.

Brandon A. D., Walker R. J., and Puchtel I. S. 2006. Platinum–osmium isotope evolution of the Earth's mantle: constraints from chondrites and Os-rich alloys. Geochimica et Cosmochimica Acta 70: 2093-2103.

Chu Z., Yan Y., Chen Z., Guo J., Yang Y., Li C. and Zhang Y. 2014. A Comprehensive Method for Precise Determination of Re, Os, Ir, Ru, Pt, Pd Concentrations and Os Isotopic Compositions in Geological Samples. Geostandards and Geoanalytical Research 39 (2):151-169.

Cohen A. S. and Waters F. G. 1996. Separation of osmium from geological materials by solvent extraction for analysis by thermal ionisation mass spectrometry. Analytica Chimica Acta 332: 269-275.

Coggon J. A., Luguet A., Nowell G. M., and Appel P. W. U. 2013. Hadean mantle melting recorded by southwest Greenland chromitite ^{186}Os signatures. Nature Geoscience 6:871-874.

Coggon J., Luguet A., Fonseca R., Lorand J. P., Heuser A., and Appel P. 2015. Understanding Re-Os systematics and model ages in metamorphosed Archean ultramafic rocks: A single mineral to whole-rock investigation. Geochimica et

Cosmochimica Acta 167:205-240.

Creaser R. A., Papanastassiou D. A., and Wasserburg G. J. 1991. Negative thermal ion mass-spectrometry of osmium, rhenium, and iridium. Geochimica et Cosmochimica Acta 74:356-379.

de Groot P. A. 2004. Handbook of stable isotope analytical techniques, Vol. 2. Belgium: Elsevier, 1323 p.

Ehmann W. D. and Vance D.E. 1991. Radiochemistry and nuclear methods of analysis. New York: John Wiley and Sons, 531 p.

Ferrière L. 2008. Shock metamorphism and geochemistry of impactites from the Bosumtwi impact structure: A case study of shock-induced deformations and transformations in quartz and associated methodology. Ph.D. thesis, University of Vienna, Vienna, Austria, 279 p.

Gill R. 1997. Modern analytical geochemistry: an introduction to quantitative chemical analysis techniques for earth, environmental and materials scientists. Harlow, England: Addison Wesley Longman Limited, 329 p.

Goldstein J., Newbury D., Joy D., Lyman C., Echlin P., Lifshin E., Sawyer L., and Michael J. 2003. Scanning electron microscopy and X-ray microanalysis. New York: Springer, 690 p.

Govindaraju K. 1989. 1989 compilation of working values and sample description for 272 geostandards: Geostandards Newsletter 13:1-113.

Govindaraju K. 1994. 1994 compilation of working values and sample description for 383 geostandards. Geostandards Newsletter 18:1-158.

Herr W., Wolfe R., Eberhardt P. and Kopp E. 1961. Development and recent applications of the Re/Os dating method. In: Radioactive dating and methods of low level counting. IAEA (Vienna), p. 499-508.

Hirt B., Tilton G., Herr W. and Hoffmeister W. 1963. The half-life of ^{187}Re. In: Geiss J. and Goldberg E. D. (eds), Earth science and meteoritics. North-Holland Publishing Company (Amsterdam), p. 273-280.

Hoffman E. L., Naldrett A. J., van Loon J. C., Hancock R. G. and Manson A. 1978. The determination of all the platinum-group elements and gold in rocks and ore by neutron activation analysis after preconcentration by a nickel sulphide fire-assay technique on large samples. Analytica Chimica Acta 102:157-166.

Jarosewich E., Clarke R. S. J., and Barrows J. N. 1987. The Allende meteorite

reference sample. Smithsonian Contributions to Earth Sciences 27:1-49.

Koeberl C. 1993. Instrumental neutron activation analysis of geochemical and cosmochemical samples: a fast and reliable method for small sample analysis. Journal of Radioanalytical and Nuclear Chemistry 168: 47-60.

Koeberl C. 1995. Neutron activation analysis. In Methods and instrumentations: results and recent developments, Advanced mineralogy, Vol. 2, edited by Marfunin A. S. Berlin, Heidelberg, New York: Springer 322-329.

Koeberl C. and Reimold W. U. 1995. Early Archean spherule beds in the Barberton Mountain land, South Africa: no evidence for impact origin. Precambrian Research 74:1-33.

Koeberl C., Reimold W. U. and Boer R. H. 1993. Geochemistry and mineralogy of Early Archean spherule beds, Barberton Mountain Land, South Africa: evidence for origin by impact doubtful. Earth Planetary Science Letters 119:441-452.

Koeberl C., Sharpton V. L., Schuraytz B. C., Shirey S. B., Blum J. D. and Marin L. E. 1994. Evidence for a meteoritic component in impact melt rocks from the Chicxulub structure. Geochimica et Cosmochimica Acta 58 (6):1679-1684.

Krogh T. E., Kamo S. L., Sharpton V. L., Marin L. E. and Hildebrand A. R. 1993. U-Pb ages of single shocked zircons linking distal K/T ejecta to the Chicxulub crater. Nature 366:731-734.

Kyte F. T., Shukolyukov A., Lugmair G. W., Lowe D. R. and Byerly G. R. 2003. Early Archean spherule beds: chromium isotopes confirm origin through multiple impacts of projectiles of carbonaceous chondrite type. Geology 31:283–286.

Lee R. E. 1993. Scanning electron microscopy and X-ray microanalysis. Englewood Cliffs, New Jersey: PTR Prentice–Hall, Inc., 458 p.

Levasseur S., Birck J. L. and Allègre C. J. 1998. Direct measurement of femtomoles of osmium and the $^{187}Os/^{186}Os$ ratio in seawater. Science 282:272-274.

Liu Y., Huang M., Masuda A. and Inoue M. 1998. High-precision determination of osmium and rhenium isotope ratios by in-situ oxygen isotope correction using negative thermal ionisation mass spectrometry. International Journal of Mass Spectrometry and Ion Processes 173:163-175.

Lowe D. R. and Byerly G. R. 1986. Early Archean silicate spherules of probable impact origin, South Africa and Western Australia. Geology 14:83-86

Lowe D. R. and Byerly G. R. 1999. Stratigraphy of the west-central part of the Barberton Greenstone Belt, South Africa, in: Lowe, D.R. and Byerly, G.R. (Eds.), Geologic Evolution of the Barberton Greenstone Belt, South Africa. Geological Society of America Special Paper 329:1-36.

Lowe D. R., Byerly G. R., Asaro F., and Kyte F. T. 1989. Geological and geochemical record of 3400- million- year-old terrestrial meteorite impacts. Science 245:959–962.

Lowe D. R., Byerly G. R., Kyte F. T., Shukolyukov A., Asaro F. and Krull A. 2003. Spherule beds 3.47-3.24 billion years old in the Barberton Greenstone Belt, South Africa: a record of large meteorite impacts and their influence on early crustal and biological evolution. Astrobiology **3:**7-47.

Luck J.M. and Turekian K.K. 1983. Osmium-187/Osmium-186 in manganese nodules and the Cretaceous-Tertiary boundary. Science 222:613-615.

Luguet A., Nowell G. M. and Pearson D. G. 2008. ^{184}Os/^{188}Os and ^{186}Os/^{188}Os measurements by Negative Thermal Ionisation Mass Spectrometry (N-TIMS): Effects of interfering element and mass fractionation corrections on data accuracy and precision. Chemical Geology 248:342-362.

Luguet A., Behrens M., Pearson D. G., König S., Herwartz D. 2015. Significance of the whole rock Re–Os ages in cryptically and modally metasomatized cratonic peridotites: Constraints from HSE–Se–Te systematics. Geochimica et Cosmochimica Acta 164:441-463.

Mader D. and Koeberl C. 2009. Using instrumental neutron activation analysis for geochemical analyses of terrestrial impact structures: Current analytical procedures at the University of Vienna Geochemistry activation analysis laboratory. Applied Radiation and Isotopes 67: 2100-2103.

Meija J., and Caruso J. A. 2004. Deconvolution of isobaric interferences in mass spectra. Journal of American Society for Mass Spectrometry 15:654-658.

Meisel T., Moser J., Fellner N., Wegscheider W. and Schoenberg R. 2001. Simplified method for the determination of Ru, Pd, Re, Os, Ir and Pt in chromitites and other materials by isotope dilution ICP-MS and acid digestion. The Analyst 126:322-328.

Morgan J. W. and Walker J. M. 1989. Isotopic determinations of rhenium and osmium in meteorites by using fusion, distillation and ion-exchange separations. Analytica Chimica Acta 222:291-300.

Nier A.O. 1937. The isotopic composition of osmium. Physical Review 52:885.

Nier A.O. 1950. A Redetermination of the Relative Abundances of the Isotopes of Carbon, Nitrogen, Oxygen, Argon, and Potassium. Physical Reviews C 77:789-793.

Pegram W. J., Krishnaswami S., Ravizza G. E. and Turekian K. K. 1992. The record of sea water $^{187}Os/^{186}Os$ variation through the Cenozoic. Earth and Planetary Science Letters 113:569-576.

Peucker-Ehrenbrink B. and Jahn B. 2001. Rhenium-osmium isotope systematics and platinum group element concentrations: Loess and the upper continental crust. Geochemistry, Geophysics, Geosystems 2, 10.1029/2001GC000172.

Peucker-Ehrenbrink B., Ravizza G. and Hofmann A. W. 1995. The marine $^{187}Os/^{186}Os$ record of the past 80 million years. Earth and Planetary Science Letters 130:155-167.

Potts P. J. 1987. A handbook of silicate rock analysis. Glasgow: Blackie, 622 p.

Potts P. J., Bowles J. F. W., Reed S. J. B., and Cave M. R. 1995. Microprobe techniques in the earth sciences. London: Chapman & Hall, 419 p.

Raschke U., Schmitt R. T., and Reimold W. U. 2013. Petrography and geochemistry of impactites and volcanic bedrock in the ICDP drill core D1c from Lake El'gygytgyn, NE Russia. Meteoritics & Planetary Science 48:1251-1286.

Ravizza G. and Pyle D. 1997. PGE and Os isotope analyses of single sample aliquots with NiS fire assay preconcentration. Chemical Geology 141:251-268.

Rehkämper M. and Halliday A. N. 1997. Development and application of new ion-exchange techniques for the separation of the platinum group and other siderophile elements from geological samples. Talanta 44:663–672.

Reimer L. 1998. Scanning electron microscopy, Physic of image formation and microanalysis. Second edition. Heidelberg: Springer, 527 p.

Reimold W. U., Koeberl C., Johnson S. and McDonald I. 2000. Early Archean Spherule Beds in the Barberton Mountain Land, South Africa: Impact or Terrestrial Origin? In: Impacts and the Early Earth (Eds. I Gilmour and C. Koeberl), Lecture Notes in Earth Sciences 91, Springer Verlag, Heidelberg, p. 117-180.

Reisberg L. and Meisel T. 2002. The Re-Os isotopic system: A review of analytical techniques. Geostandards Newsletter 26:249-267.

Severin K. P. 2004. Energy dispersive spectrometry of common rock forming minerals. Dordrecht, Netherlands: Kluwer Academic Publishers, 225 p.

54

Schulz T., Luguet A., Wegner W., van Acken D. and Koeberl C. 2016. Target Rocks, impact glasses, and melt rocks from the Lonar crater, India: Highly siderophile element systematics and Sr-Nd-Os isotopic signatures. Meteoritics and Planetary Science 51:1323-1339.

Sharpton V. L., Dalrymple G. B., Luis E. M., Ryder G., Schuraytz B. C. and Urrutia-Fucugauchi J. 1992. New links between the Chicxulub impact structure and the Cretaceous/Tertiary boundary. Nature 359:819-821.

Shen J. J., Papanastassiou D. A. and Wasserburg G. J. 1996. Precise Re-Os determinations and systematics of iron meteorites. Geochimica et Cosmochimica Acta 60:2887-2900.

Shirey S. B. and Walker R. J. 1995. Carius tube digestion for low-blank rhenium-osmium analysis. Analytical Chemistry 67:2136-2141.

Shirey S. B. and Walker R. J. 1998. The Re-Os isotope system in cosmochemistry and high-temperature geochemistry. Annual Review of Earth and Planetary Science 26:423-500.

Shukolyukov A., Kyte F. T., Lugmair G. W., Lowe D. R. and Byerly G. W. 2000. The oldest impact deposits on Earth - First confirmation of an extraterrestrial component. Impacts and the Early Earth. In: Gilmour I., Koeberl C. (Eds.), Lecture Notes in Earth Science. Springer Verlag, Heidelberg 91:99-115.

Smoliar M. I., Walker R. J., and Morgan J. W. 1996. Re-Os Ages of Group IIA, IIIA, IVA, and IVB Iron Meteorites. Science 271 (5252):1099-1102.

Stosch H. G. 1999. Einführung in die Isotopengeochemie. Institute für Mineralogie und Geochemie, Universitäte Karlsruhe, 250 p.

Swisher C. C. 3rd, Grajales-Nishimura J. M., Montanari A., Margolis S. V., Claeys P., Alvarez W., Renne P., Cedillo-Pardoa E., Maurrasse F. J., Curtis G.H., Smit J., McWilliams M. O. 1992. Coeval 40Ar/39Ar Ages of 65.0 Million Years Ago from Chicxulub Crater Melt Rock and Cretaceous-Tertiary Boundary Tektites. Science 257(5072):954-8.

Van Acken D., Hoffmann J. E., Schorscher J. H. D., Schulz T., Heuser A., and Luguet A. 2016. Mantle sources of High-Al komatiites from the Mesoarchaean Quebra Osso Group, Minas Gerais, Brazil: Trace elements, HSE systematics and Os isotopic signatures. Chemical Geology 422:108-121.

Völkening J., Walczyk T., and Heumann K. G. 1991. Osmium isotope ratio

determinations by negative thermal ionization mass-spectrometry. International Journal of Mass Spectrometry and Ion Processes 105:147–159.

Wainwright A. N., Luguet A., Fonseca R. O. C., and Pearson D. G. 2015. Investigating metasomatic effects on the [187]Os isotopic signature: A case study on micrometric base metal sulfides in metasomatised peridotite from the Letlhakane kimberlite (Botswana). Lithos 232:35-48.

Walker R. J. 1988. Low-blank chemical separation of rhenium and osmium from gram quantities of silicate rock for measurement by resonance ionization mass spectrometry. Analytical Chemistry 60:1231-1234.

Walker R. J. and Fassett J. D. 1986. Isotopic measurement of subnanogram quantities of rhenium and osmium by resonance ionization mass spectrometry. Analytical Chemistry 58: 2923-2927.

Watt I. M. 1997. The principles and practice of electron microscopy, 2nd ed. Cambridge: Cambridge University Press, 484 p.

CHAPTER 3: EARLY ARCHEAN SPHERULE LAYERS FROM THE BARBERTON GREENSTONE BELT, SOUTH AFRICA: MINERALOGY AND GEOCHEMISTRY OF THE SPHERULE BEDS IN THE CT3 DRILL CORE

Seda Ozdemir[1*], Toni Schulz[1], Christian Koeberl[1,2], Wolf Uwe Reimold[3,4,5], Tanja Mohr-Westheide[3,6], Desiree Hoehnel[3,6], Ralf Thomas Schmitt[3], and Axel Hofmann[7]

[1] Department of Lithospheric Research, University of Vienna, Althanstrasse 14, 1090 Vienna, Austria

[2] Natural History Museum, Burgring 7, 1010 Vienna, Austria

[3] Museum für Naturkunde - Leibniz Institute for Evolution and Biodiversity Science, Invalidenstrasse 43, 10115 Berlin, Germany

[4] Humboldt Universität zu Berlin, Unter den Linden 6, 10099 Berlin, Germany

[5] Geochronology Laboratory, University of Brasilia, Brazil

[6] Frei Universität Berlin (FU Berlin), Institut für Geologische Wissenschaften, Malteserstrasse 74-100, D12249 Berlin, Germany

[7] Department of Geology, University of Johannesburg, Auckland Park 2006, South Africa

* Corresponding author (E-mail:seda.oezdemir@univie.ac.at)

Abstract

Very little is known of the Hadean and the Archean impact record on Earth. The CT3 drill core from the Fig Tree Group of the northern Barberton Greenstone Belt contains 17 spherule layers, and, therefore, provides an outstanding new opportunity to gain insights into meteorite bombardment of the early Earth. We undertook a detailed mineralogical and geochemical inspection of these new spherule layer occurrences, and intermittent spherule-free layers (country rocks), to look for the possible occurrence of meteoritic components and to compare with other spherule occurrences in the Barberton Greenstone Belt.

CT3 spherules, as primary features, mostly exhibit textural patterns similar to those of the other Barberton spherule layers, but locally mineralogical and chemical composition differences are observed, likely as a result of various degrees of alteration. Individual layers exhibit either K or Al enrichment. The observed mineralogy of spherule layers is of secondary origin and comprises K-feldspar, phyllosilicates, carbonates, sulfides, and oxides, with the exception of chromite that is of primary origin.

Spherule compositions and textural features allow to classify spherules into four main types; i) polycrystalline, K-feldspar filled (K-rich), ii) polycrystalline, silicate (K-feldspar and quartz) filled, iii) phyllosilicate filled (Al-rich), and iv) K-feldspar-phyllosilicate filled zoned spherules (K-Al-rich). These spherule types occur

both in deformed and undeformed forms. The fibrous and radial growth (botryoidal) textures of some spherules also point towards formation as formerly molten droplets. Our petrographic investigations suggest alteration by K-metasomatism, sericitization and silicification and carbonatization.

Siderophile element contents show significant enrichment in Ni (up to 2 wt%) and Ir (up to ~3 ppm) compared to previously studied spherule layers. These values indicate the presence of a meteoritic component. On the other hand, lithophile and chalcophile element abundances indicate that hydrothermal overprint that dominates the rocks of the whole Barberton region also affected the CT3 samples; this may also have influenced the redistribution of the meteoritic component.

Lastly, we group CT3 spherule layers due to all similar petrographic and geochemical features (SL1 and SL2 in interval A, SL3 to SL14 in interval B and SL15-SL17 in interval C). This classification of layers indicates the presence of at least three distinct impact events before tectonic overprint that may have affected the original deposits.

Keywords: Barberton, spherules, geochemistry, impact, Archean

3.1. Introduction

The impact history of Earth during the Early Archean is not well known (e.g., Koeberl 2006a, b). Whilst the Moon shows a continuous cratering record for over 4 billion years (e.g., Wetherill 1975; Ryder 1990; Neukum et al. 2001; Stöffler and Ryder 2001; Stöffler et al., 2007), the terrestrial impact crater population is strongly biased towards the last 250 million years (e.g., Jourdan et al. 2012). Only a few impact structures with Precambrian ages are known and none have so far been observed in Archean terranes. The Sudbury structure in Canada (~1.85 Ga; Krogh et al., 1984, 2011) and the Vredefort impact structure in South Africa (~2.02 Ga; Kamo et al. 1996) are the oldest impact structures known on Earth. For the early Earth, impacts are recorded in the form of impact spherule deposits - mainly in the Barberton Greenstone Belt (BGB), Kaapvaal Craton, South Africa, and the Pilbara Craton in Western Australia. The ages for these impact deposits range from 3.2 to 3.4 Ga, and a few have ages of ~2.5 Ga (e.g., Lowe and Byerly 1986; Shukolyukov et al. 2000; Simonson et al. 2000, 2009; Byerly et al. 2002; Lowe et al. 2003; Hofmann et al. 2006; Glass and Simonson 2013; Lowe et al. 2014).

Diverse interpretations for the Barberton spherule beds, such as silicified marine carbonate ooids, accretionary lapilli, or ocelli/variolites derived from weathered volcanics, were initially offered (Ramsey et al. 1963; Lowe and Knauth 1977, 1978; Heinrichs 1984; de Wit et al. 1986), but their textural appearance (quench textures), their similarity to chondrules, and anomalous Ir

abundances of up to many hundreds of ppb were later interpreted in terms of condensation products from impact plumes, molten impact ejecta, and/or impact ejecta that were melted during atmospheric re-entry (e.g., Lowe et al. 1989; Johnson and Melosh 2014). However, the extremely high (up to multiple chondritic) concentrations of Ir and other platinum group elements (PGEs) within some spherule samples would require meteoritic components in excess of 100%, a value which is two to three orders of magnitude higher than reported for any other impactite occurrences worldwide. Koeberl et al. (1993) and Koeberl and Reimold (1995), thus, suggested that these enrichments could rather be due to secondary processing and questioned the impact origin hypothesis. Moreover, Reimold et al. (2000) explained the elevated concentrations of the PGEs (and other elements such as Au), also observed by these authors in some country rock samples adjacent to spherule beds, by secondary sulfide mineralization, although they did not exclude the possibility that a possible impactor component could be the source of these elements. Finally, it was emphasized that such extreme enrichments in the abundances of the PGEs and other highly siderophile elements (HSEs) could also result from element fractionation during spherule formation, as well as hydraulic fractionation during deposition and/or diagenetic and metasomatic processes (Lowe et al. 2003). Although the detailed mechanisms of PGE enrichments in some spherule horizons still remain unresolved, the final argument in favor of an impact origin was provided by Cr isotope evidence, unambiguously indicating carbonaceous chondritic impactors for several of the known Archean spherule layers from the Barberton area (Kyte et al. 2003; Shukolyukov et al. 2000).

This study focuses on new spherule layer findings in the recently drilled CT3 core, containing no less than 17 spherule layer intersections within a 150 m thick depth interval. This work presents (i) an investigation of the spherule layers according to the possible tectonic modification, (ii) a full petrographic and geochemical characterization of the individual layers, separately analyzing spherules and groundmass, as well as the interbedded country rocks, (iii) the identification of a meteoritic component, and (iv) a comparison of our findings with other spherule occurrences of the Barberton Greenstone Belt.

3.2. The Barberton Greenstone Belt

3.2.1. Geological overview

The 3.2-3.5 Ga old Swaziland Supergroup of the Barberton Greenstone Belt comprises the Onverwacht Group (predominantly ultrabasic to basic volcanic rocks with an average thickness of about 15 km), the Fig Tree Group (mainly greywackes, shales, cherts, and felsic volcaniclastic rocks; average thickness of about 2 km), as well as the about 3.5 km thick Moodies Group of feldspathic

and quartzose sandstones, conglomerate, some siltstone, and minor shale (e.g., Lowe and Byerly 1999, 2007 and 2014; Goodwin 1996; Hofmann 2005). The Inyoka fault zone, which occurs in the central part of the greenstone belt, can be considered as a tectono-stratigraphic boundary between the northern and southern parts of the belt.

The *Onverwacht Group* consists of seven formations (from base to top: Sandspruit, Theespruit, Komati, Hooggenoeg, Noisy, Kromberg, and Mendon), which are partly separated by faults, shear zones, and angular unconformities (e.g., Lowe and Byerly 1999; Hofmann 2005; Anhaeusser 2014, and references therein). The formations are composed of (a) komatiites and komatiitic basalt, assumed to be derived from metasomatized mantle above subducted altered oceanic crust, (b) tholeiitic basalt and felsic volcanic rocks, interpreted to be derived from melting of subducted amphibolites and eclogite, as well as (c) minor sedimentary rocks that formed in a deep to shallow marine environment (e.g., Anhaeusser 2014). Although the ages of the formations are mostly unknown, de Wit (2011) inferred that they cover the 3.2-3.5 Ga interval according to the stratigraphic relationships of the units.

The predominantly sedimentary *Fig Tree Group* above the volcanic Onverwacht Group formed between 3260 and 3226 Ma (Brandl et al. 2006). North of the Inyoka Fault, five formations have been distinguished, the Ulundi (shales and cherts overlying altered Onverwacht komatiites), Sheba (turbiditic sandstone and minor shales), Belvue Road (shales and minor turbiditic sandstones), Bien Venue (schists derived from mainly dacitic volcaniclastic protoliths), and Schoongezicht (turbidites intercalated with shale) formations. South of the Inyoka fault, the Fig Tree Group is subdivided into the Mapepe Formation (chert clast conglomerate, parallel- and ripple-laminated shale, volcaniclastic rocks) and the Auber Villiers Formation (volcaniclastic conglomerate, breccia and sandstone). The formations of the Fig Tree Group were deposited in a variety of sedimentary environments, ranging from deep to shallow water, and fan delta to alluvial (e.g., Hofmann et al. 2005; Lowe and Byerly 2007; Anhaeusser 2014).

The *Moodies Group* was deposited ~3230 Ma ago (Heubeck et al. 2013) and is made up of three formations, each of which is a fining-upward sequence of conglomerate or pebbly sandstone at the base, thick sandstone units in the middle, and siltstone, shale and banded iron formations at the top, all deposited in a shallow marine to fluvial setting (Hofmann et al. 2005; Brandl et al. 2006).

3.2.2. Spherule layer occurrences

Since the early 1980s (Heinrichs 1984; Lowe and Byerly, 1986; Lowe et al. 1989, 2003, 2014; Koeberl et al. 1993; Byerly and Lowe, 1994; Koeberl and Reimold, 1995; Byerly et al. 1996; Reimold et al., 2000; Byerly et al. 2002; Simonson and Glass, 2004; Hofmann et al. 2006) outcrops and drill core

intersections with spherule containing horizons have been described from throughout the Barberton Greenstone Belt (BGB). They occur in either the Onverwacht or Fig Tree groups and have been traditionally assigned to four spherule beds, termed S1 to S4 (compare Fig. 1b). More recently it has been suggested that the number of known spherule beds in the BGB could be as high as eight (layers S5 to S8 as proposed by Lowe and Byerly, 2010 and by Lowe et al. 2014; see also Fig. 1b), but further investigations have to confirm the origin of these additional spherule beds and whether they actually represent additional events or belong to any of the four original layers.

Spherule bed S1 (3470 ± 3 Ma; Byerly et al. 2002) was found in the Hooggenoeg Formation of the Onverwacht Group in the southern part of the BGB, situated in a thin chert horizon resting on altered komatiitic volcanic rocks (Lowe et al. 1989; Lowe and Byerly 1999; Byerly et al. 2002, Lowe et al. 2003, Hofmann et al. 2006). In the southcentral part of the BGB the *S2 spherule bed* (~3260 Ma, Byerly et al. 1996) is situated at the contact between the Onverwacht and the Fig Tree groups (e.g., Lowe and Byerly, 1986; 1999; Lowe et al. 1989; Koeberl et al. 1993; Koeberl and Reimold 1995; Byerly et al. 1996; Reimold et al. 2000; Lowe et al. 2003; Hofmann et al. 2006). In the southern and northern parts of the BGB, the spherule bed at the lower contact of the Fig Tree Group, which is also the contact between the Onverwacht and the Fig Tree groups, has been called the *S3 spherule bed* (Lowe and Byerly 1986; 1999; Lowe et al. 1989; Koeberl et al. 1993; Koeberl and Reimold 1995; Reimold et al. 2000; Lowe et al. 2003; Hofmann et al. 2006), which has been assigned an age of 3243 ± 3 Ma (Kröner et al. 1991; Lowe et al. 2003). In the southern BGB the *S4 spherule bed* is represented by only one outcrop. It has an age of about 3.24 Ga and occurs stratigraphically just 6.5 m above S3 (Lowe et al. 2003) in the middle Mapepe Formation of the Fig Tree Group (Lowe et al. 1989; Shukolyukov et al. 2000; Kyte et al. 2003; Lowe et al. 2003; Hofmann et al. 2006). *The spherule bed S5* (3225 ±3 Ma, Lowe et al. 2014) occurs in the northern part of the BGB at the base of the Belvue Road Formation of the Fig Tree Group, where it was observed at just two localities. *Spherule bed S6* was observed at only one locality in the Mendon Formation (unit M3c) of the Onverwacht Group and has been assigned with an age of ~3256 Ma (Lowe et al. 2014). The 3416 Ma (Kröner et al. 1991, Lowe et al. 2014) *spherule bed S7* occurs near the base of the Buck Reef Chert. Lastly, *spherule bed S8* occurs in the Mendon Formation (unit M2c) of the Onverwacht Group, where it was observed at only two locations. Its age has been indicated as ~3298 Ma (Lowe et al. 2014).

Recently, an International Scientific Drilling Program (ICDP) project in the Barite Valley Syncline in the central BGB recovered the BARB5 drill core with a length of 760 m (Arndt et al. 2012, 2013). Five relatively thin spherule layers, each

about 4 cm thick, were identified in the core interval between 511.29 and 511.51 m depth, separated by shales and cherts of the Fig Tree Group (Hoehnel et al. 2016; Mohr-Westheide et al. 2015; Fritz et al. 2016). Stratigraphically, some or all of these layers may belong to the same interval as the previously studied S3 and S4 layers (Hoehnel et al. 2016). Another core, CT3 (25°30' 50.76"S, 31°33'10.08"E), was drilled by an exploration company (Sabi Gold) in 2008 in the northeastern part of the BGB. The drilled interval consists entirely of Fig Tree Group strata that may be correlative with the Sheba and/or Belvue Road formations. This core, which is the topic of the present study, contains 17 spherule layer intersections within three intervals in the 7 to 150 m depth section (see Fig. 2).

3.3.   Samples and Methods

3.3.1. Samples

This study exclusively focuses on spherule layers (each consisting of spherules and groundmass, in which the spherules are embedded) and intercalated sedimentary rocks within a section of the CT3 drill core between 7 and 150 m depth. The CT3 spherule layer intersections occur within three depth intervals: from 7.78 to 10.15 m (containing two spherule layer intersections), from 65.07 to 72.57 m (containing twelve spherule layer intersections), and from 145.02 m to 150.00 m (containing three spherule layer intersections), which are named here the A, B, and C intervals (Fig. 2). Samples analyzed in this study represent either spherule layers or intervening shale and chert layers. Quarter core was sampled at the Council for Geoscience Core Library, then the cores were split and thin sections were prepared at the Museum für Naturkunde Berlin (MfN). All sub-samples for geochemical analysis were cut from the core using a diamond wire saw at the Natural History Museum Vienna (NHM).

The spherules are variously distributed in the respective layers. The contacts to country rock are not always sharp (e.g., the contacts shown in Fig. 3, especially at layer SL-9). It was, therefore, not possible in every case to clearly separate spherule layer and adjacent country rock during sample preparation. As a consequence, some country rocks from the vicinity of a spherule layer contain minor amounts of spherules, and some spherule layer samples contain minor country rock portions (see Table 1). The respective sample fragments were then used for the production of thin sections and bulk powders for further analysis (see below). For our work we prepared 35 thin sections and 69 bulk rock samples, covering the A, B, and C intervals (named A-SL1 and A-SL2 for the A-interval, B-SH1 to B-SH20 for the B interval, and C-SH21 and C-SH26 for the C interval). While spherule layer subsamples are labeled SL, country rocks are labeled SH for shale layers and CH for chert layers. Additionally, country rock samples containing sulfide veins are labelled with an "s" after the

abbreviation of the host lithology (e.g., SHs for shale containing sulfide, or CHs for cherts containing sulfide).

3.3.2. Analytical Methods

Mineral Analysis: Due to intra-layer inhomogeneity (caused by irregular spherule distribution or alteration effects), more than one thin section were occasionally obtained from one spherule layer intersection. In total, 31 thin sections were made from the 17 spherule layers. Four thin sections were obtained from the typical country rocks in the three intervals. Eight spherule containing thin sections were coated with a thin layer of carbon and analyzed using a JEOL JSM-6610LV scanning electron microscope (SEM) and a JEOL JXA-8500F field-emission electron probe microanalyzer (EPMA), both at MfN. Additional analyses were undertaken using a JEOL JSM 6610 LV SEM and a JEOL JXA 8520F field-emission EPMA at NHM Vienna. Mineral analyses were obtained at 15 kV accelerating voltage and 10 nA by wavelength-dispersive spectrometry (WDS-EPMA). Standardization was done using the main Astimex and Smithsonian international standard suites of the MfN and NHM analytical facilities, i.e., pure elements for Al, Fe, Co, and Ni, and mineral reference standards for Na (plagioclase), Mg (diopside), Si (quartz), P (apatite), S (celestine), K (sanidine), Ca (diopside), and Ti (rutile). Counting times were set to 10 s on peak and 5 s on upper and lower background, respectively, and matrix effects were corrected using the ZAF routine provided by the JEOL operating system. Detection limits are 82 ppm for Si, 50 ppm for Al, 134 ppm for Cr, 206 for Ti, 35 ppm for K, 49 ppm for Ca, 100 ppm for Fe, 77 ppm for Mn, 121 ppm for Ni, 40 ppm for Na, 45 ppm for Mg, 133 ppm for As, 271 ppm for Zn, 51 ppm for S, 215 ppm for Pb, 132 ppm for Co, 194 ppm for Cu and 175 ppm for Sb. Accuracy of the WDS analyses is better than 3 rel% for major elements >5 wt% and in the range of 10–15 rel% for minor elements <0.5 wt%. Precision is much better than 5 rel% for major elements >5 wt% and in the range of several tens of percent for minor elements <0.5 wt%.

Whole Rock Chemical Analysis: A total of 69 sub-samples from the A, B, and C intervals, including 34 samples from the 17 spherule layers and 35 samples from country rocks, were crushed into small chips using a jaw crusher and pulverized using an agate mill. These whole-rock powders typically weighed between 1 and 10 g. Concentrations of major elements were determined with a Bruker S8 Tiger X-ray fluorescence (XRF) spectrometer at MfN using glass tablets containing 0.6 g of dried (4 hr at 105 °C) sample powder and 3.6 g of di-lithiumtetraborate flux. Accuracy as well as precision values are 0.5 wt% for SiO_2; 0.1 wt% for Al_2O_3; 0.05 wt% for Fe_2O_3, MgO, CaO, Na_2O, and K_2O; 0.01 wt% for TiO_2, MnO, and P_2O_5. The detection limits are: 1.0 wt% for SiO_2; 0.5 wt% for Al_2O_3; 0.05 wt% for Fe_2O_3; and 0.01 wt% for TiO_2, MnO, MgO, CaO, Na_2O, K_2O, and P_2O_5. Reference materials used were reported in detail in

Raschke et al. (2013), who also provided information on data quality. About 0.5 g of dried sample powder were used for determining the loss on ignition (LOI). The sample material was heated in porcelain crucibles in a furnace for 4 hr at 1000 °C. LOI was calculated using the weight difference before and after heating. Due to limited sample amounts only 39 out of the 69 samples were measured for major elements using XRF.

The concentrations of some major (Na, K, and Fe) and the majority of minor and trace elements (including rare earth elements, REEs) were determined by Instrumental Neutron Activation Analysis (INAA) for all 69 samples. For analysis ~150 mg of each sample were sealed in polyethylene capsules and irradiated in the 250 kW Triga Mark-II reactor at the Atominstitut, Vienna. After a cooling period of up to five days, samples, including international rock standards (the carbonaceous chondrite Allende, Smithsonian Institution, Washington DC, USA, Jarosewich et al. 1987; the Ailsa Craig Granite AC-E, Centre de Recherche Petrographique et Geochimique, Nancy, France, Govindaraju 1989; and the Devonian Ohio Shale SDO-1, United States Geological Survey, Govindaraju 1989) were measured in three counting cycles (according to the half-lives of the nuclides) in the Gamma Spectrometry Laboratory of the Department of Lithospheric Research, University of Vienna. More details on the instrumentation, method, and accuracies are given by Koeberl (1993) and Mader and Koeberl (2009). Element concentrations that were determined by both, XRF and INAA (Na, K, and Fe) were in good agreement in all cases (see Table 4)**.**

3.4. Results

3.4.1. Macroscopic and Microscopic Observations

Layer duplication and inter-layer correlation: One of the basic questions that needs to be addressed in order to discuss the implications of the new spherule layer intersections in the CT3 drill core is the exact number of distinct spherule beds that was actually intersected. Tectonic duplication could decrease the number of spherule layers within the analyzed core section. Along this section, spherule layers intercalated with shales and cherts are folded (Hoehnel et al, 2016). Folding is most pronounced in the B-interval, which also exhibits the highest number of spherule layers (intervals A and C contain 3 and interval B 12 spherule layer intersections). Such duplication of spherule layers on a centimeter to decimeter scale has also been reported for the S2 spherule layer from the Barberton area (e.g., Reimold et al. 2000). Along the core section, there is a ca. 55 m interval without spherule layer occurrences between the A and B intervals, and 72 m between the B and C intervals. These core intervals show no evidence of folding.

Country Rocks: As already shown for the S2 to S4 layers (see Reimold and Koeberl, 2014, for a review), the main country rock lithologies along the CT3 core are shale and chert and they generally show parallel lamination. Shales are dominant in all three intervals with ~70 %, while the chert sections only sum to 30 % (see also, Drabon 2011). Sulfide veins are occasionally observed in the shale and chert horizons in the B interval (from 55.25 to 72.33 m) but are absent in the A and C intervals.

Shale (SH) forms beds ~0.5 to ~20 cm thick that are composed of laminated, fine-grained, clastic sediment. The colors of the shale layers vary from black to light/greenish gray, to brown, possibly due to presence or absence of carbonate.

Chert (CH) forms thin beds and includes massive to laminated, dark grey and milky white varieties. Chert layers within the three intervals frequently contain brownish-black, undulating, 2 mm to 1 cm wide bands that are characteristic for carbonaceous material associated with sulfide minerals (Drabon, 2011). The sulfides are mostly pyrite and pyrrhotite, as confirmed by electron microprobe analysis (see below for details).

Spherules frequently occur in the shale and chert horizons in the immediate contact zones with spherule layers, in all intervals (e.g., Fig. 3 - SL9).

Spherule layers: Spherules from all three core intervals are either embedded in a groundmass of sericite which consist of a fine-grained sericitic material including some illite or smectite (Figs. 6a, b, d, and e) or carbonaceous shale (Fig. 6c).

In interval A, spherule layer thicknesses vary from about 4 to 20 cm. In interval B (exhibiting the highest number of spherule layers) thicknesses vary from 1 to 21 cm. In interval C, thicknesses are about 13 cm (compare Fig. 2). Such thicknesses are comparable to the findings for the S2 to S4 layers, where layer thicknesses vary between 2 and 30 cm (Lowe et al. 2003, and references therein).

Spherules range in size from ~0.5 to ~2.5 mm (Table 1), which is in the range of spherule sizes reported from other Archean spherule layers from the BGB (e.g., Reimold et al. 2000, Krull-Davatzes et al. 2015, and references therein). There is no evidence for size sorting so far, in individual layers, except the two spherule layer samples; PU10-20 from Princeton section of Agnes Mine described earlier by Reimold et al. (2000) for the S2 layer and from this work C-SL15 (Hoehnel et al., 2016). Notably, the CT3 drill core locally contains a few variations of the spherule to groundmass ratio within individual layers (e.g., samples B-SL8 and B-SL9, see Fig. 3). Irrespective of whether they are deformed or not, spherules exhibit (i) gray to light gray color, (ii) polycrystalline

fill, and (iii) are zoned or unzoned. While some spherules have two-phase zonation of sericite-K-feldspar (Fig. 4a), quartz-K-feldspar (Fig. 4b), or quartz-sericite (Fig. 4c), others have multiple sericite-K-feldspar zonations (Fig. 4d) or quartz-sericite-K-feldspar (Fig. 4e) zones.

Most spherules have intersertal (Fig. 4f) or barred (Fig. 4g) textures, and often fibrous outer rims. Some spherules exhibit a botryoidal texture (Fig. 4h), similar to what was previously observed by Krull-Davatzes et al. (2006) for S3 samples. Spherules occurring in the CT3 core are either deformed or undeformed. One factor determining the shape of the spherules is the groundmass in which they are embedded – i.e., either sericite or shaly; phyllosilicate ± carbonate. Undeformed spherules in the CT3 core are predominantly present in a shale groundmass, whereas deformed spherules are almost exclusively observed in a sericite groundmass.

Undeformed spherules generally show spherical, ovoid, and tear-drop shapes (Fig. 5), which were also previously described for the S1 to S4 layers from the Barberton region (see, e.g., Glass and Simonson 2012). They are polycrystalline and predominantly composed of K-feldspar, except for vesicle or crack fills that are composed of groundmass component (sericite) or quartz, and more rarely, carbonate or barite. While undeformed spherules are absent in the A interval, they are dominant in the B and C intervals.

Spherules are characterized by three main compositional features. Either spherules have (i) an entirely polycrystalline filling (mostly K-feldspar) embedded in sericitic groundmass, (ii) a polycrystalline K-feldspar filling but with thin cracks and veins that are filled by groundmass material (sericite), or (iii) a polycrystalline silicate filling (K-feldspar and quartz) within shaly groundmass. For example, samples B-SL16 and C-SL17 contain K-feldspar filled spherules in a sericitic groundmass (case i; see Fig. 6a), whereas spherules of samples B-SL3 and B-SL5 exhibit K-feldspar fills with thin cracks and veins in the spherules that, in turn, are embedded in a sericitic groundmass (case ii; see Fig. 6b). Finally, samples B-SL9 and B-SL10 (in part, also sample B-SL5) are examples for case iii, showing spherules with a silicate fill embedded in a shaly groundmass (see Fig. 6c). Besides K-feldspar being the main mineral of spherule fillings, quartz occasionally occurs within the spherules as either vesicle fillings (Figs. 4b and 6a) or micro-granular (mosaic) aggregates filling entire spherules (Fig. 6c).

Deformed spherules have only partly preserved primary spherical shape. According to the classification scheme of Krull-Davatzes et al. (2006), deformed spherules can be subdivided into three main groups; (i) flattened spherules (observed only in A-SL2), (ii) crushed or collapsed spherules, and (iii) sheared spherules. Flattened spherules are mostly elongated perpendicular to the main

compaction stress and have axial ratios from ~0.3 to ~0.5 (Fig. 6d). Such axial ratios are comparable to those of deformed spherules from other localities within the Barberton area (e.g., Krull-Davatzes et al. 2012; Lowe et al. 2003). They are typically composed of phyllosilicates, most likely indicating that the flattening process occurred after alteration of the spherules, which was already concluded by Krull-Davatzes et al. (2006) for the S3 layer. Crushed or collapsed spherules (Fig. 6e) display broken rims and occur in the various spherule types, in accordance with conclusions on the S3 layer by Krull-Davatzes et al. (2006). However, we can report here that the degree of spherule deformation is clearly related to spherule composition. Spherules predominantly composed of K-feldspar and/or granular quartz, and completely crystallized (K-feldspar) types were generally not subject to deformation. Sheared spherules (Fig. 6f) are composed of sericite, elongated, and dominant in the A interval (e.g., sample A-SL1) and in the B interval (samples B-SL3, B-SL4, B-SL5, B-SL11 and B-SL14). It is sometimes difficult to distinguish such spherule bodies from the fine-grained sericite groundmasses in which they are embedded.

3.4.2. Mineral Chemistry

The current main mineralogy of the spherules is of secondary origin and, thus, related to alteration, diagenesis, and metamorphic processes. Primary silicate minerals and glass were replaced by fine-grained phyllosilicates (sericite, chlorite, Illite, smectite), K-feldspar, quartz, oxide minerals (rutile, ilmenite), and minor carbonate (e.g., Simonson 2003). K-feldspar and phyllosilicates are the most common minerals within the spherules. Quartz can be found as microcrystals, fine-grained mosaics (Fig. 7a and b), and as relatively coarser-grained domains in a few spherules, or as vesicle fillings in the interior of spherules (Figs. 7c-e). Only one layer (A-SL2) contains quartz veins that cut through spherules (Fig. 7a). Minor carbonate mostly accompanies quartz in vesicle fillings (Fig. 7b) and rarely fills vesicles by itself (Fig. 7f). The only remaining primary mineralization is Ni-Cr rich spinel occurring in some CT3 spherule layers (Fig. 8a), displaying euhedral spinel habits - as also shown and discussed by, for example, Mohr-Westheide et al. (2015) for the BARB5 spherule layers.

Sulfide mineralization occurs almost exclusively in the form of rims around spherules or in/around vesicle fillings. The main sulfide minerals are subhedral pyrrhotite and pentlandite (Figs. 8b, c, d, e and f). The frequent occurrence of pentlandite could be considered a consequence of hydrothermal overprint on Ni-rich mineral phases. Especially deformed spherules contain these sulfide minerals in their fill and along their rims. Other ore mineral phases comprise pyrite, chalcopyrite and galena, as well as sphalerite. Frequently, carbonate minerals (siderite, magnesio-siderite) accompany the sulfides. Ilmenite and rutile are typically found along the rims of spherules (Figs. 8c, e and 10e).

These oxides may also accompany sulfides in fillings of vesicles. Furthermore, very fine-grained Ti-oxide (mainly ilmenite) fills the cracks or forms narrow veins in undeformed spherules (Figs. 10j-o).

Representative thin sections were selected for electron microprobe analysis of all spherule types occurring in the CT3 core. Microprobe (EPMA) analyses were carried out with the aim to analyze the composition of the spherule fillings and to identify sulfide minerals and vein and crack fillings in spherules and groundmass. Analyses were performed on spherules from three different layers (B-SL5, B-SL8 and B-SL9); the results are illustrated in Figs. 8, 9 and 10. Average compositions calculated for multiple EPMA spot analyses of specific minerals (occurring either at the rim or within spherules) are summarized in Tables 2 and 3. The selected spherule layers for analysis exhibit a representative cross-section through all observed spherule types. Whereas the rims of these spherules from all three layers predominantly consist of ilmenite, rutile or sulfide minerals, spherule fills are mostly composed of sericite and K-feldspar. Biotite and the phyllosilicates smectite and illite are dominant components of the groundmass. If the spherules contain cracks, veins, and/or vesicles, the same groundmass material occurs within the spherules, too (Fig. 6b).

Figure 9 shows microprobe analyses of silicate minerals of both spherule fillings and groundmass. K-feldspar and microcrystalline quartz, as well as sericite, are major silicate minerals of spherule fills. The sericite and other phyllosilicate minerals in spherules have similar Al and K abundances as the groundmass minerals. Considering the relative abundances of phases, the groundmass material exhibits slightly higher Al but lower K abundances than the spherule fills (Fig. 9). According to mineral compositions, spherules can be subdivided into three different types (Fig. 10): (i) Al-rich spherules, (ii) K-rich spherules, and (iii) K-Al-rich spherules. Aluminum-rich spherules are exclusively deformed and their primary mineral content was, almost entirely, replaced by phyllosilicate (Figs. 10a-d). Potassium-rich spherules are predominantly undeformed and their fillings are entirely composed of polycrystalline K-feldspar (Figs. 10f-i). Spherules rich in K and Al all belong to the deformed spherule type, and also include zoned spherules (Figs. 10k-m).

Table 3 also contains the results of multiple EPMA analyses of sulfide minerals in samples B-SL5, B-SL8 and B-SL9. In order of abundance, the most common sulfide minerals are pyrrhotite, pentlandite, sphalerite and galena. These sulfide minerals were mostly observed around the vesicles and the rims of spherules, or as replacement of core fillings. In general, the observed sulfide mineralogy is very similar to that described in Koeberl and Reimold (1995) and Reimold et al. (2000) for the S2 layer. On the other hand, the sulfide mineral assemblages differ from those observed in previous studies (Koeberl and Reimold 1995;

Reimold et al. 2000) in that sulfides of the S2 layer included gersdorffite, which at the time was presumed to be the likely carrier phase for the high Ir contents.

3.4.3. Geochemistry

The results of whole-rock chemical analyses of all 69 samples are given in Table 4. Here, we review the abundances of specific key elements and compare them to analyses of other spherule layers from the Barberton area.

Major and minor elements: The most pronounced difference in the major element composition between spherule layers and essentially spherule-free layers (country rocks) from all three intervals is their *potassium* content. The K_2O ranges from ~6 to ~12 wt% in the spherule layer samples and is usually below or around 1 wt% in the country rocks. However, locally K_2O contents can reach up to 8.5 wt% even in the country rock samples, likely due to contamination from adjacent (under- or overlying) spherule layers. The general overlap (6 to 8.5 wt% - between spherule layers and country rocks) is not surprising in the light of the sericitic groundmasses and often K-feldspar dominated replacement of spherules. In Fig. 11 K_2O and Al_2O_3 are positively correlated and show elevated abundances in spherule layers, thus exhibiting a clear distinction between spherule layers and country rocks. Some samples that fall between these two groups in this plot can be related to mutual contamination by spherules or by country rock material.

The geochemical data reveal also a positive correlation between the abundances of titanium and aluminum for all samples analyzed in this study. Moreover, spherule layers and country rocks exhibit different concentrations of these immobile elements (Fig. 11). While spherule layers generally have elevated Al_2O_3 concentrations between ~16 and ~30 wt% and low TiO_2 abundances between ~1.2 and 2.3 wt%, country rocks range from ~1 to ~13 wt% Al_2O_3 and from ~0.1 to ~0.3 wt% TiO_2. Sulfide containing country rocks (e.g., SH19s), however, have TiO_2 concentrations up to ~1 wt% (see Discussion).

Figure 12 shows the abundance patterns for the elements Co, Cr, Ni, and Ir for all analyzed samples. Especially within the B-interval, spherule layers SL5, SL8, SL12 and their over- or underlying layers show nearly the same patterns with extreme enrichments in Ir (up to 2.8 ppm), Ni (up to 2.02 wt%), Co (up to 652 ppm), and Cr (up to 0.9 wt%).

The concentration of the *lithophile element* Cr (Fig. 12) ranges from 11 and 9161 ppm in the CT3 drill core samples. The spherule layers show Cr contents from 132 to 8402 ppm and the pure country rocks from 11 to 108 ppm. However, Cr contents in country rock samples can be significantly higher when spherules occur in the under- or overlying country rock samples. In that case,

Cr concentrations can be as high as 9161 ppm, clearly indicating that spherules – or the micro-phases associated with them (Mohr-Westheide et al. 2015) - are the carriers of chromium.

The chalcophile element Zn presents a wide variation in content between 19 and 3177 ppm within CT3, with the lower and upper extreme values both related to country rock samples. Country rock samples that contain some spherules only have up to 45 ppm Zn. On the other hand, spherule layer samples range from a minimum of 32 ppm to a maximum of 1183 ppm.

Koeberl and Reimold (1995) pointed out that spherule-bearing rocks from the S2 layer exhibit concentrations of *arsenic* and *antimony* that correlate with the sulfide content of the respective samples (and also with the siderophile element abundances; see discussion below). However, this is not the case for samples from the CT3 core. There is also no correlation between As and Sb abundances for the samples analyzed in this study. For example, sulfide-containing sample B-SH2s exhibits As and Sb concentrations of ~2.6 and ~0.3 ppm, respectively. These values are far below the typical concentrations for spherule layer samples and some of the country rocks that reach up to 354 ppm As and 13.8 ppm Sb (sample B-SL5b) and 161 ppm As and ~3.2 ppm Sb (shale sample B-SH17), respectively. The correlation between especially the As and sulfide contents in the Barberton spherule layer samples analyzed in other studies might be related to the presence of the arsenic-rich sulfide gersdorffite as well as secondary alteration, which seems to be absent from the sulfide parageneses observed in the CT3 samples. Most notably, our samples have As and Sb concentrations that are orders of magnitude lower compared to those found in samples from the S2 layer by Koeberl and Reimold (1995) and Reimold et al. (2000), who reported abundances as high as 1 wt% for As and ~1400 ppm for Sb.

<u>*Rare Earth Elements and Hf:*</u> All CT3 layers are characterized by generally flat REE patterns (average La_n/Yb_n= 2.97) with slight enrichment of LREE and unfractionated to very little enriched HREE. They exhibit an extremely wide range of ΣREE from 17 to 5723 ppm. All layers of the CT3 core vary in Hf abundance. The chondrite-normalized REE patterns of chert layers (Fig. 13a) are generally flat (average La_n/Yb_n= 2.40) and contain positive Eu anomalies. The Hf abundances of chert layers follow the flat REE patterns, however there are two exceptions with negative Hf anomalies (A-CH1 and B-CH7) and one layer with slightly increased Hf value (C-CH9). Shale layers (Fig. 13b) show a similarly flat trend, as well as positive Eu anomalies, but show a wider range of ΣREE abundances from 34 ppm to 5723 ppm (average REE=388 ppm). On the other hand, Hf abundances are more varied than the range of abundances for the chert layers. While three samples of shale layers (B-SH9, C-SH22 and C-

SH25) exhibit increased Hf values, six of them (B-SH16, B-SH20, C-SH21, C-SH23, C-SH24, C-SH26) have decreased abundances. Chondrite-normalized REE patterns of spherule layers are not significantly different from those of the country rocks; they show also a relatively flat pattern with low La_N/Yb_N ratios (average 2.87) (Fig. 13c). The variation of REE patterns of spherule layer samples is very limited (Fig. 13c) and shows slight depletion of HREE (Gd_n/Yb_n=1.27-2.85). Two layers (B-SL5 and B-SL10), which contain sulfide zones, have extremely high ΣREE values (around 608 and 840 ppm). These two layers show obvious positive Eu anomalies, in contrast to the general spherule layer pattern. Notably all spherule layers yielded extreme Hf enrichment, again with these two exceptions. In general, sulfide containing layers have the highest REE abundances in the CT3 drill core, and especially samples B-SL5, B-SH13 and B-SH19s exceed the typical REE abundances by an order of magnitude and are accompanied by higher La_N/Yb_N ratios (4.75 to 5.03) (see Discussion).

Siderophile elements: Nickel values (Fig. 12) vary significantly among the samples from the CT3 drill core section, with respect to both spherule layer and country rock samples. Concentrations of Ni in the spherule layers range from 143 (A-SL1c) to 16024 (B-SL5b) ppm, averaging at ~600 ppm, whereas country rock (shale and chert) values range from 24 ppm (B-SH16) to 21692 ppm (C-SH26), averaging at ~650 ppm. There is no correlation between the sulfide contents and Ni abundances of specific samples. Notably, the highest values are superkomatiitic (komatiites average at ~2000 ppm; e.g., Puchtel et al. 2013) and superchondritic (CI average at ~11.000 ppm; e.g., Anders and Grevesse, 1989). The values are comparable to Ni concentrations in other spherule layers from the BGB (e.g., Koeberl et al. 1995; Reimold et al. 2000). However, a few samples (B-SL5b, B-SL12b, C-SL17, B-SH13, B-SH15, B-SH19s, B-CH8, and C-SH26) exhibit extreme enrichments in Ni. Interestingly, these samples are both spherule layer (e.g., samples B-SL5b ~1.6 wt% Ni) and country rock (e.g., chert sample B-CH8 with ~0.5 wt% Ni or shale sample C-SH26 with ~2.2 wt% Ni) derived, or are sulfide-bearing samples (e.g., shale sample B-SH19s, containing about 2 wt% Ni). These concentrations are the highest reported for any spherule layer from the BGB analyzed so far (cf., e.g., Reimold et al. 2000), also significantly exceeding the concentrations measured for samples from the S2 layer, which were collected from drill cores from the Princeton and Mt. Morgan gold mines (Koeberl and Reimold 1995) and for which the literature suggests that secondary hydrothermal overprint in the course of gold-sulfide mineralization was responsible for non-impact related enrichment (e.g., Koeberl and Reimold 1995).

Cobalt concentrations (between 2-721 ppm) roughly correlate with Ni abundances (Figs. 12 and 15b) and are slightly superkomatiitic (~100 ppm; e.g.,

Puchtel et al. 2013) and superchondritic (~505 ppm; Anders and Grevesse, 1989). Concentrations between 28 and 528 ppm have been measured for the spherule layers and 2 and 721 ppm for the country rocks from all intervals. The highest concentrations for Co were obtained for the high-Ni samples mentioned above (~530 ppm for sample B-SL5b, ~720 ppm for shale sample C-SH26 and ~650 for sample B-SH19s). In contrast to the Ni concentrations, the elevated Co contents reported here are comparable to the values obtained for samples from the S2 layer (e.g., Koeberl and Reimold 1995; Reimold et al. 2000). Moreover, the huge variations reported here for Ni and Co cannot only be observed for different spherule layer samples (and intercalated country rocks), but also within a single layer. For example, layer B-SL5 was probed with two samples (B-SL5a and B-SL5b) spaced 2 mm apart. These samples exhibit extremely different Ni and Co concentrations (0.1 to almost 1.6 wt% Ni and 42 to 530 ppm Co), although no petrographic differences between these samples were observed at the microscopic scale. Interestingly, in the case of spherule layer SL1, which varies along the interval with respect to deformation (A-SL1c spherules were sheared), only slight concentration changes can be reported for the three subsamples (A-SL1a to A-SL1c in Table 4).

Highly siderophile elements (HSEs) analyzed in this study include Ir and Au (Fig. 12). Spherule layer samples and some of the spherule-bearing country rock samples exhibit Ir and Au concentrations between 2.5 and 2832 ppb Ir and between 0.5 and 52 ppb Au. This contrasts with the significantly lower concentrations for the majority of country rocks between 0.7 and 22 ppb Ir and 0.4 to 9.8 ppb Au. Especially in the B-interval, spherule layer samples B-SL5, B-SL8, and B-SL12 and country rocks in close vicinity to these samples exhibit extreme enrichment of up to 2832 ppb Ir (correlating with up to ~2 wt% Ni, up to 652 ppm Co, and up to 9161 ppm Cr). Such high values were previously only reported by Reimold et al. (2000) from the S2 layer.

3.5. Discussion

A number of criteria have been proposed in the last decades (e.g., Glass and Simonson, 2012) to ascertain an impact origin of spherules and to exclude an origin from volcanic activity. These include (i) the absence of comparable spherules in the surrounding strata, (ii) the presence of dumbbell- or teardrop-shaped spherules, (iii) the presence of vesicles and inward-radiating quench crystallites, and (iv) the presence of Ni-enriched chromium spinel (e.g., Glass and Simonson, 2012).

Accretionary lapilli (Lowe and Knauth 1977, 1978; Ramsey et al. 1963; Heinrichs et al. 1984) in the Barberton region commonly have graded bedding, whereas only a few spherule layers with this characteristic have been described so far (Koeberl and Reimold 1995, sample BA-1 from S2 layer; and Hoehnel

2016, SL15 in CT3). Accretionary lapilli can also be identified by the presence of vitric tuff particles, in- and outside of spherules, together with concentric micro-zonation, and in contrast to impact deposits, their distribution is very limited over much smaller areas (e.g., Hofmann et al. 2006). On the other hand, the Barberton spherules occur over wide areas (Simonson 2003).

Shapes and textural features (intersertal or barred textures, fibrous outer rims, botryoidal texture) of spherules from the Barberton area have been considered primary (e.g., Krull-Davatzes et al. 2006, 2012, and references therein). Most of these primary features can also be applied to CT3 drill core spherule layers analyzed in this study (see below). They are consistent with an origin as either impact melt droplets and/or condensation products from an impact plume. The CT3 spherules display similar features as those reported for any other Archean spherule occurrence in the BGB. According to all given textural evidence presented in this study, it is reasonable to assume that the original textures of spherules are similar to those of meteoritic chondrules (e.g., Sears 2004) or some terrestrial devitrified impact glasses.

In contrast, spherule mineral components are mostly secondary and the result of pervasive alteration. In general, the mineralogy of the Fig Tree and Onverwacht groups suggests that the rocks were affected by a low metamorphism of lower greenschist facies grade and experienced intense alteration due to silica metasomatism (Lowe et al. 1999; Hofmann et al 2005). It is, thus, near-impossible to estimate the original compositions of the spherule beds.

Deformation of spherules

The CT3 spherules were affected by deformation. While spherules composed of sericite were susceptible to deformation, spherules with somewhat coarser-grained interiors tended to keep their original shapes. Additionally, the groundmass components (shaly or sericitic), into which the spherules are embedded, exhibit obvious different ductilities due to their different mineralogical compositions. While spherules embedded in sericitic groundmass are mostly deformed and composed of sericite or other phyllosilicate, spherules within shaly groundmass are mostly undeformed and dominantly composed of K- feldspar.

Flattened spherules are most frequent in the A interval. Flattened spherules are not observed at greater depth, although the deeper layers were more affected by compaction due to overburden. Consequently, this kind of spherule deformation must be considered to be related to tectonic deformation, affecting the successions heterogeneously.

Depositional environment of spherule beds

Spherule deposition in the BGB, according to Lowe et al. (2003, 2014), took place in a mostly quiet, deep water environment, but it appears that at least locally, spherule deposits were exposed to currents and wave action, possibly in the wake of impact-generated tsunami (e.g., BARB5, Mohr-Westheide et al. 2015). In CT3 case, shale and chert hosting spherule layers and some shale bands within-spherule layers suggest that these beds were deposited in a low-energy, marine environment well below wave base. Either the presence of cross lamination of the layers or the absence of graded bedding in most of the CT3 spherule layer intersections can be considered as the result of the gentle effect of currents and waves on the layers during sedimentation. The absence of detrital material within the layers can be interpreted as indicating that the effectiveness of these currents and waves was not intense and, thus, likely relates to a deep water environment. However, there is sample evidence in the field for inclusion of large chert rafts and/or, winnowing of spherules.

Textural evidence for impact derived spherules

The intersertal and barred textures of CT3 spherules can best be interpreted as resembling those of olivine-rich chondrules (e.g., Krull-Davatzes et al. 2006; Brearley and Jones 1998). The radial devitrification textures, inward-radiating growth textures, and the botryoidal texture suggest that CT3 spherules were originally composed of glass (see also Simonson and Glass 2004 and Krull-Davatzes et al. 2006, for similar observations on other BGB spherule layers).

From current mineralogy of spherules to possible primary occurrences and alterations

In CT3 spherules preserved crystal growths have been entirely replaced by authigenic K-feldspar, which might indicate that the original compositions of spherules were similar to those of basalts (Simonson and Harnik 2000; Simonson 2003; Simonson and Glass 2004). Lowe et al. (2003) observed that the main current mineral phases of spherules are quartz, occurring as microquartz and as cavity-filling relatively coarser quartz, and microcrystalline phyllosilicates, mainly sericite and chlorite. They referred to post-depositional diagenesis and metasomatism of the Onverwacht and Fig Tree groups, resulting in extensive alteration including Na, Ca, Fe, and Mg loss, silicification, and/ or carbonatisation, and K enrichment. This led to complete alteration/replacement of primary silicate minerals but with preservation of primary zircon, chromium spinel, rutile, and tourmaline.

The S3 spherules were divided into different groups, including quartz, quartz-phyllosilicate and phyllosilicate-phyllosilicate spherules by Krull-Davatzes et al. (2006). Also Lowe et al. (2003) described spherule compositions of S1, S2 and S3 layers as ranging from nearly pure silica to nearly pure sericite or chlorite. In the CT3 case, there are some spherules with microcrystalline quartz fill, but K-

Al-rich spherules are by far dominant. These are differentiated into K-rich, Al-rich, and K-Al-rich spherules. The current spherule compositions are related to different alteration types and degrees. The very high potassium abundances of some spherules relate to K-metasomatism, and the existence of quartz and carbonates within the spherules point towards silicification and carbonatization (expressed as vesicle fillings or spherules cut by quartz veins) during lithification of the CT3 spherule layers. These alterations show overlapping relationships. K-alteration seems to be earliest, followed by sericitization. Besides sericitization, also silicification and carbonatization were observed. The occurrence of quartz veins crosscutting spherules suggests that silicification followed spherule deposition. However, our observations did not allow to clearly determine the sequence of alteration processes following the K-alteration. Detailed investigations would be required to constrain the order of alteration events, but this is beyond the scope of this work.

Chemical distinction between country rocks and spherule layers and possible meteoritic component

The elevated K_2O abundances (~9 wt% on average) of spherule layer samples compared to those of the country rock samples (average 1.30 wt%) can be interpreted as a result of alteration processes (K-metasomatism). Contrary to the chemical data for more mobile elements, aluminum as an immobile element could provide a hint at the primary mineralogy (Fritz et al. 2016). Spherule layers exhibit distinctly higher Al_2O_3 abundances than shale and chert layers. At first sight, this may be expected, as all spherules contain K-feldspar and phyllosilicates, but Al_2O_3 is selectively enriched in some spherules of a layer, while other spherules are mostly enriched in potassium. This can be interpreted as indicative of a situation whereby the primary mineralogy of some spherules also contained Al-rich components (see also Krull-Davatzes et al. 2006). Fritz et al. (2016) also favored primary Al_2O_3 content such as a basaltic primary composition, which was exposed to diagenetic Al_2O_3 enrichment that now distinguishes spherule layers from country rocks regarded as Al_2O_3-poor marine sediments.

Titanium, another immobile element, is hosted in rutile and ilmenite mostly at the rims of deformed and zoned spherules. This is reflected in elevated TiO_2 abundances in the spherule layer samples compared to the country rocks. Hofmann et al. (2005) indicated that depletion of Al_2O_3, TiO_2 and K_2O within Fig Tree sediments and the positive correlation between their abundances may suggest that these elements reside in phyllosilicates. For CT3, this may be applicable for country rocks (except some shale layers which have somewhat elevated phyllosilicate content), but very high enrichments of these elements within spherule layers cannot be explained only with occurrence of phyllosilicate. The association of Ti-bearing minerals (such as ilmenite and

75

rutile) with sulfide minerals located at the rim of most spherules might also point to hydrothermal effects as a cause of these enrichments.

Hofmann et al. (2006) pointed out that the S2, S3, and S4 layers are characterized by enriched LREE and unfractionated HREE patterns identical to those of the underlying/overlying country rock layers, similar to what has since been observed by Krull-Davatzes et al. (2012) for the S3 layer, as well as some sedimentary rocks of the Fig Tree Group, which are characterized by flat HREE patterns (Hofmann et al. 2005). It is obvious (Fig. 13d) that the CT3 spherule layers have similar patterns as the under/overlying shale and chert layers, but slightly depleted HREE (Fig. 13d). Generally, we can interpret the low abundances of REE elements due to regional alteration. Elevated ∑REE abundances in three specific layers (B-SL5, B-SH13, B-SH19s), which notably contain sulfides and shale groundmass, are accompanied by enrichment in clay fractions, likely as a result of hydrothermal alteration. Additionally, the existence of a positive Eu anomaly in all layers in CT3 can be explained by either an effect of hydrothermal overprint or komatiitic (ultra-mafic) primary source rocks. This could also represent an Archean seawater component that was characterized by a positive Eu anomaly (Hofmann et al. 2005).

Multi-element geochemical analysis of both spherule layer and country rock samples reveals complex relationships between selected key elements. In accord with earlier findings on the S2 layer (e.g., Reimold et al. 2000), several siderophile-chalcophile interelement correlations point toward pervasive secondary hydrothermal overprint on the whole stratigraphy of the CT3 core. For example, the Ir vs. Zn (Fig. 14a) and the Ir vs. As (Fig. 14b) plots show great scatter of all spherule layer and country rock data, but there is a weak correlation in the Ir vs Sb plot (Fig. 14c). Arsenic and Sb abundances generally favor secondary overprint on Barberton spherule layers. Lack of correlation of As and Ir abundances and limited correlation of As and Sb contents suggest that Ir abundances, which are only slightly disturbed, are near the primary values for the spherule layer samples. Reimold et al. (2000) reported a significant correlation between the Ni and As abundances for S2 spherule layer samples, which was at the time interpreted in favor of a common host phase for As and Ni, as well as PGEs, in secondary sulfide mineralization such as gersdorffite. The absence of gersdorffite and of intensive sulfide mineralization, and the lack of such a correlation for the samples analyzed in this study (Fig. 14d), point at extreme primary Ir enrichments in some samples and secondary hydrothermal overprint. Collectively, all evidence presented here supports more or less strong hydrothermal overprint of the whole sample suite.

The Ni versus Cr correlation (Fig. 15a) is weak for both spherule layer and country rock samples. While the trend is restricted by the komatiitic values for country rocks, samples from spherule layers exceed even the chondritic values.

76

Importantly, country rock samples that also reach chondritic values exhibit spherule contamination. The Ni/Cr ratio of spherule layer samples varies from ~0.12 to ~3.56, which partly overlaps with chondritic values (~2.5-4, e.g., Anders and Grevesse 1989). Relatively lower Ni/Cr ratios for spherule layer samples have been interpreted as a result of Ni depletion during silicification by Hoffmann et al. (2006). When we consider that all spherule layers were affected by different degrees of silicification (i.e., presence of secondary quartz as demonstrated in the above petrographic section), it would be expected that the Ni/Cr values vary within this lower range from 2 to 4. Furthermore, Ni and Co (Fig. 15b), two elements whose concentrations would be essentially of meteoritic origin (Reimold et al. 2000), show a good correlation of their abundances in many spherule layer and country rocks. The Ni/Co ratio of spherule layer samples varies between ~3.6 and ~30, which includes and exceeds the chondritic value of ~22 (Anders and Grevesse 1989). To the contrary, Ni/Co ratios of country rocks range to komatiitic (~2) values, again except the samples that contain spherule contamination.

Siderophile elements exhibit extreme (even significantly beyond chondritic values for some samples – Fig. 15c) enrichments in both spherule layer and country rock samples. Nickel and Ir abundances (Fig. 15c) are, at best, weakly correlated. The highest enrichments are observed in the layers of the B and C intervals at concentrations that would require meteoritic components (C1 chondrite) of 100 % or more. Such high values are comparable to what was found in earlier investigations of the S1 to S4 layers (Lowe et al. 1989, 2003, 2014; Koeberl et al. 1993; Byerly and Lowe, 1994; Koeberl and Reimold, 1995; Byerly et al. 1996; Reimold et al. 2000; Byerly et al. 2002) and, for some parts, slightly exceed these values.

It was stated in earlier studies (e.g., Koeberl and Reimold 1994) that such high meteoritic admixtures are improbable in the light of the typical values observed for impactites from more recent events, and Reimold et al. (2000) observed association between PGEs and sulfide mineralization (see above). In the following, Hofmann et al. (2006) already mentioned that the elevated PGE abundances can be related to secondary processes such as hydrothermal and metasomatic alteration, reworking and depositional effects, and metamorphism. Notably, Mohr-Westheide et al. (2015) observed that these extreme variations of siderophile element values are related to the very localized presence of Ni-rich chromium spinel clusters with PGE-rich metal alloy (interpreted as impact produced primary phases) and PGE-rich sulfarsenide phases (interpreted as the result of secondary alteration). In the CT3 case, so far no dedicated investigation for the presence of PGE metalloids has been carried out, but the analyzed samples do not contain significant sulfide components – with the notable exception of some samples from the B-interval (denoted "-s").

Correlation of Ni and Ir abundances would require both elements to be similarly affected by secondary redistribution processes, which is surprising in the light of their different fluid mobilities. Therefore, the reason of these enormous variations of siderophile element values is seemingly related not to secondary enrichments but to the likely presence of PGE-rich metal alloys, which remains to be confirmed.

Reimold et al. (2000) stated that some of the country rocks highly enriched in Ni and Ir are separated from the next spherule layer by at least 1.5 m. Secondary redistribution, whatever its cause, might thus be the only viable explanation for these observations. The highest siderophile element enrichments (e.g., Ni and Ir) in country rocks from the CT3 core section always occur in samples that are in close proximity to the over- or underlying spherule layers, requiring element diffusion only on a cm scale. Therefore, these enrichments can be related to reworking of spherule bed material and incorporation into subsequent sedimentation.

There is a possibly even more convincing argument in favor of significant extraterrestrial admixtures (higher than any of the typically observed admixtures in impactites from more recent events) as a cause for the observed element enrichments and minor secondary redistribution on a cm-scale. Figure 16 shows a plot of the Cr vs. Ir abundances, summarizing all data for Archean spherule beds obtained so far from the Barberton area (Koeberl and Reimold 1995; Reimold et al. 2000; Lowe et al. 2003). Based on a more limited data-set on specific spherule occurrences, it was stated earlier (Koeberl and Reimold 1995; Reimold et al. 2000; Lowe et al. 2003) that there is a strong correlation between abundances of these two elements for all spherule bed samples. As can be seen, our data, with one exception (spherule layer sample B-SL5b, at the right upper corner of the plot), fit well into the earlier trend, whose upper range coincides remarkably well with chondritic abundances (Ir abundances of chondrites exhibit a wide range from ~470 ppb in CI type to ~740 ppb in CO and CV type). The star symbol in Fig. 16 represents CI chondrites; other chondrite groups would, in part, plot at even higher concentrations. The reason for using CI chondritic abundances lies in the Cr isotope evidence for the S2 to S4 layers, which indicates a CI chondritic projectile (Shukolyukov et al. 2000; Kyte et al. 2003). If hydrothermal or any other secondary processes would cause a significant redistribution (and enrichment) of specific elements (such as Cr or siderophile elements), why then would it result in such a coincidence with a chondritic (or very slightly super-CI-chondritic) upper range? Completely detached from the Cr isotope evidence, it might be more reasonable to assume enormous meteoritic admixtures predating some hydrothermal overprint. Additionally, in some cases elevated concentrations of PGEs in country rocks within close proximity to the next spherule layers, as well as the occasionally

near-chondritic PGE-interelement ratios, might arise from (i) admixture of spherule matter from earlier deposited impact debris to the sediments or (ii) might have been derived from komatiites, which represent the dominant volcanic lithology in the BGB and are likely precursors of the Fig Tree sediments.

Similarities between spherule layers and possible layer duplication: multiple impact events?

The 17 spherule layer intersections in CT3 have been divided into three main intervals (A to C). Every interval contains several spherule layers within close proximity of each other. Based on this first-order observation, we attempt to evaluate the possibility of layer duplication based on stratigraphic, petrographic and geochemical characteristics described above (Table 5, Fig. 17).

Densely packed spherule layers A-SL1 and A-SL2, which are the uppermost spherule occurrences below surface, are petrographically very similar to each other, and their siderophile element abundances are very similar, too. Notably, spherule layer one contains sheared spherules which point toward a possible deformation event. The As abundances infer that the A interval (7-10 m) was seriously altered.

Approximately 40 m below the A interval, the B interval begins with laminated shale and chert intercalations. Spherules occur at 65 m below surface with B-SL3. Surprisingly, the B interval exhibits 12 spherule layers within an only 10 m wide depth interval. Table 5 represents petrographic similarities, and points out – within the B interval - at least 4 repetitions (SL3, SL5, SL9 and SL14). Folding can be viewed as a possible reason for spherule layer duplication according to several observed fold hinges at 65 to 72 m depths. On the other hand, most of these layers exhibit similar geochemical abundances or petrographically similar spherules as observed also in other intervals. The correlation between As and siderophile element abundances in Fig. 17 can be interpreted to indicate that hydrothermal secondary processes also affected the B interval but not as much as the A interval (see above).

Interval C (beginning at 144 m) has only 3 spherule layers, C-SL15, C-SL16 and C-SL17. However, their petrographic features are similar to spherules in layers B-SL5 and B-SL9 as well as B-SL14. Duplication at the decameter scale is unlikely, however possible. Therefore, they might not represent possible duplications between intervals. Moreover, uncorrelated As and siderophile element abundances in the C interval might reflect that these three layers were the least affected spherule occurrences along the CT3 drill section (Fig. 17). This indicates that the effect of alteration decreases with depth.

Based on the observations, discussed above, the 17 CT3 spherule layer intersections might represent three impact events that are represented by (i) interval A with spherule layers SL1 and SL2, (ii) interval B which contains spherule layers from SL3 to SL14, and (iii) interval C with spherule layers SL15, SL16 and SL17.

At the moment the exact stratigraphic position of the CT3 drill core is not well constrained. Therefore, it remains entirely unclear if some (or all) of the CT3 spherule layers are correlated with the S2 to S4 layers of the BGB (Lowe and Byerly 2014), which occur in the same stratigraphic interval (Fig Tree Group). Additionally, it is not even clear whether the S3 and S4 layers represent one or two spherule deposits.

3.6.   Conclusions

Detailed mineralogical, petrographic, and geochemical studies of Early Archean spherule layers from the CT3 drill core in the Barberton Greenstone Belt (3.2-3.5 Ga) reveal:

1- Not less than 17 spherule layers intercalated with Fig Tree Group shales and cherts occur in an interval between 7 and 150 m depth. It appears likely that some of these layers are the result of duplication due to folding (which is in evidence along the core).

2- The spherules are embedded in two types of groundmass, a phyllosilicate-dominated (mostly sericite) and a shale-dominated type. Spherules exhibit different shapes and textural features that are considered primary features and point toward an origin as impact melt droplets and/or condensation products from an impact plume.

3- Sedimentary analysis along the core in conjunction with textural observations on spherules indicates that they were deposited in a low-energy deep water environment, and were only slightly affected by current and wave action.

4- The main spherule minerology is of secondary origin, whereby primary silicate minerals and glass were replaced by phyllosilicate (sericite, chlorite, illite, smectite), K-feldspar, quartz, carbonate (siderite, Mg-siderite), sulfide (pyrrhotite, pentlandite, pyrite, chalcopyrite, galena, and sphalerite) and Ti-bearing minerals (rutile, ilmenite). Only observed primary phase are chromium spinels. This secondary mineralization is naturally related to chemical alterations, and obviously points toward hydrothermal alteration.

5- Compositionally different spherules types (K-rich, K-Al-rich, and Al-rich), as well as the existence of quartz and minor carbonate, suggest different alteration processes or different compositions of primary materials. K-metasomatism, sericitization, silicification and carbonatization all played a role.

6- Highly enriched siderophile element abundances and siderophile-chalcophile-lithophile interelement ratios within analyzed samples can be related to:
- ✓ Extraterrestrial and/or komatiitic components of spherule layer materials.
- ✓ The variations of siderophile element abundances could possibly be explained by PGE rich metal alloys associated with Ni-rich chromium spinels, as recently demonstrated for the BARB 5 spherule layer intersections. CT3 samples need to be investigated for this.
- ✓ Hydrothermal overprint of the whole CT3 core, which was also suggested by previous workers for the other spherule layers of the BGB, contributed somewhat to the siderophile enrichment of these spherule layers.
- ✓ We interpret the observed elemental signatures to indicate a considerable meteoritic admixture that was then affected by a hydrothermal overprint.

7- As a consequence of all petrographic and geochemical similarities of spherule layers it is possible to consider a scenario of 3 possible impact events that might cover all 17 spherule intersections in CT3.

References

Anhaeusser C.R. 2014. Archean greenstone belts and associated granitic rocks – A review. Journal of African Earth Sciences 100: 684-732.

Anders E., and Grevesse N. 1989. Abundances of the elements: meteoritic and solar. Geochimica et Cosmochimica Acta 53:197-214.

Artemieva N. A. and Simonson B. M. 2012. Elucidating the formation of Archean-Proterozoic boundary spherule layers (abstract #1372). 43rd Lunar Planetary Science Conference.

Brandl G., Cloete M. and Anhaeusser C.R. 2006. Archaean Greenstone belts. In: Johnson, M.R., Anhaeusser, C.R., Thomas, R.J. (Eds.), The Geology of South Africa. Geological Society of South Africa/Council for Geoscience, Johannesburg/Pretoria, pp. 9–56.

Brearley A. J. and Jones R. H. 1998. Chondritic meteorites. Reviews in Mineralogy and Geochemistry 36:3.1-3.398.

Byerly G. R., and Lowe D. R. 1994. Spinel from Archean impact spherules: Geochimica et Cosmochimica Acta 58: 3469–3486.

Byerly G. R., Kröner A., Lowe D. R., Todt W., and Walsh M.M. 1996. Prolonged magmatism and time constraints for sediment deposition in the early Archean Barberton greenstone belt: Evidence from the Upper Onverwacht and Fig Tree groups: Precambrian Research 78:125–138.

Byerly G. R., Lowe D.R., Wooden J.L. and Xie X. 2002. An Archean impact layer from the Pilbara and Kaapvaal cratons. Science 297:1325-1327.

De Wit M. J. 1986. A possible origin for chondrules-like particles in the 3.6-3.3 Ga Barberton Greenstone Belt, South Africa (abs.). Lunar Planetary Science 17:182-183.

De Wit M. J., Furnes H. and Robins B. 2011. Geology and tectonostratigraphy of the Onverwacht Suite, Barberton Greenstone Belt, South Africa. Precambrian Research 186:1-27.

Drabon N. 2011. Technical report Core CT3. University of Johannesburg, South Africa.

Fritz J., Tagle R., Ashworth L., Schmitt R. T., Hofmann A., Luaiss B., Harris P. D., Hoehnel D., Özdemir S., Mohr-Westheide T. and Koeberl C. 2016. Nondestructive spectroscopic and petrochemical investigations of Paleoarchean spherule layers from the ICDP drill core BARB5, Barberton Mountain Land, South Africa. Meteoritics & Planetary Science. Doi: 10.1111/maps.12736.

Glass, B. P. and Simonson B. M., 2012. Distal impact ejecta layers: Spherules and more. Elements 8:43–48.

Glass B.P. and Simonson B.M. 2013. Distal impact ejecta layers. Impact studies. Springer; Berlin-Heidelberg, 716 pp.

Goodwin A. M. 1996. Principles of Precambrian Geology. Academic Press, London pp. 91-94.

Govindaraju K. 1989. Compilation of working values and sample description for 272 geostandards. Geostandards Newsletter 13:113.

Heinrichs T. 1984. The Umsoli chert: turbidite testament for a major phreatoplinian event at the Onverwacht/Fig Tree transition (Swaziland Supergroup, Archean, South Africa). Precambrian Research 24:237-283.

Hofmann A. 2005. The geochemistry of sedimentary rocks from the Fig Tree Group, Barberton greenstone belt: Implications for tectonic, hydrothermal and surface processes during mid-Archaean times. Precambrian Research 143:23-49.

Hofmann A., Reimold W. U. and Koeberl C. 2006. Archean spherule layers in the Barberton Greenstone Belt, South Africa: A discussion of problems related to the impact interpretation. In Reimold W.U. and Gibson R.L. (eds), Processes on the Early Earth. Geological Society of America Special Paper 405:33-56.

Hoehnel D. 2016. Petrographische und texturelle Analyse archäischer Sphärulenlagen und deren Nebengesteine aus den BARB 5 und CT3 Bohrkernen des Barberton Grünsteingürtels, Südafrika. Unpublished master thesis, University of Potsdam.

Huebeck C., Engelhardt J., Byerly G. R., Zeh A., Sell B., Luber T., and Lowe D. R. 2013. Timing of deposition and deformation of the Moodies Group (Barberton Greenstone Belt, South Africa): Very high resolution of Archean surface processes. Precambrian Research 231: 236-262.

Jarosewich E., Clark Jr. R.S. and Barrows J.N. 1987. The Allende Meteorite Reference Sample. Smithsonian Contributions to the Earth Sciences 27:1-49.

Johnson B. C. and Melosh H. J. 2014 Formation of melt droplets, melt fragments, and accretionary impact lapilli during a hypervelocity impact. Icarus 228:347-363.

Jourdan F., Reimold W. U., and Deutsch A. 2012. Dating Terrestrial Impact Structures. Elements 8:49-53.

Kamo S. L., Reimold W. U., Krogh T. E., and Colliston W. P. 1996. A 2.023 Ga age for the Vredefort impact event and a first report of shock metamorphosed

zircons in pseudotyachylitic breccias and Granophyre. Earth Planetary Science Letter 144: 369-388.

Koeberl C. 1993. Instrumental neutron activation analysis of geochemical and cosmochemical samples: A fast and reliable method for small sample analysis. Journal of Radioanalytical and Nuclear Chemistry 168:47-60.

Koeberl C. 2006a. Impact processes on the early Earth. Elements 2:211-216.

Koeberl C. 2006b. The Record of impact processes on the early Earth – A review of the first 2.5 billion years. In: Processes of the Early Earth (eds. Reimold W.U., and Gibson R.). Boulder, Geological Society of America Special Paper 405:1-22.

Koeberl C. and Reimold W. U. 1994. Archean spherule beds: Impact or terrestrial origin? Reply to the comment by A. Glikson. Earth and Planetary Science Letters 126: 497-499.

Koeberl C. and Reimold W. U. 1995. Early Archean spherule beds in the Barberton Mountain Land, South Africa: No evidence for impact origin. Precambrian Research 74:1–33.

Koeberl C., Reimold W. U. and Boer R. H. 1993, Geochemistry and mineralogy of early Archean spherule beds, Barberton Mountain Land, South Africa: Evidence for origin by impact doubtful. Earth and Planetary Science Letters 119:441–452.

Koeberl C., Reimold W. U. and Schulz T. 2015. Remnants of Early Archean impact deposits on Earth: Search for a meteoritic component in the BARB5 and CT3 drill cores (Barberton Greenstone Belt, South Africa). Proceedings of the 13th Hypervelocity Impact Symposium, Procedia Engineering 103:310-317.

Krull-Davatzes A. E., Lowe D. R., and Byerly G. R. 2006. Compositional grading in an ~3.24 Ga impact-produced spherule bed, Barberton greenstone belt, South Africa: A key to impact plume evolution. South African Journal of Geology 109:233–244.

Krull-Davatzes A. E., Lowe D. R. and Byerly G. R. 2012. Mineralogy and diagenesis of 3.24 Ga meteorite impact spherules. Precambrian Research 196–197:128–148.

Krull-Davatzes A. E., Byerly G. R., and Lowe D. R. 2014. Paleoarchean ocean crust and mantle excavated by meteor impact: Insight into early crustal processes and tectonics. Geology 42: 635-638.

Krull-Davatzes A. E., Swartz N., and Enos M. 2015. Petrologic and impact size controls on Precambrian spherule diameters. Geological Society of America Special Paper 518:115-125.

Krogh T. E., Davis D. W., and Corfu F. 1984. Precise U-Pb zircon and baddeleyite ages for the Sudbury area. Geology and Ore Deposits of the Sudbury Structure (eds. E. G. Pye, A. J. Naldrett and P. E. Giblin), Ontario Geological Survey Special Vol. 1: 431-446.

Krogh T. E., McNutt R., and Davis G. L. 2011. Two high precision U-Pb zircon ages for the Sudbury Nickel irruptive. Canadian Journal of Earth Sciences 19 (4): 723-728.

Kyte F. T., Shukolyukov A., Lugmair G. W., Lowe D. R. and Byerly G. R. 2003. Early Archean spherule beds: Chromium isotopes confirm origin through multiple impacts of projectiles of carbonaceous chondrite type. Geology 31:283-286.

Lowe D. R. and Byerly G. R. 1986. Early Archean silicate spherules of probable impact origin, South Africa and Western Australia. Geology 14:83-86.

Lowe D. R., and Byerly G. R., 1999. Stratigraphy of the west-central part of the Barberton Greenstone Belt, South Africa, in Lowe, D.R., and Byerly, G.R., eds., Geologic Evolution of the Barberton Greenstone Belt, South Africa: Geological Society of America Special Paper 329: 1–36.

Lowe D. R., and Byerly G. R. 2007. An overview of the geology of the Barberton Greenstone Belt and vicinity: implications for early crustal development. In van Kranendonk M., Smithies H., and Bennett V. (Editors). Earth's Oldest Rocks: Elsevier, Amsterdam. Developments in Precambrian Geology 15: 481–526.

Lowe D. R., and Byerly G. R. 2010. Did LHB end not with a bang but a whimper? The geologic evidence. 41st Lunar and Planetary Science Conference. Abstract #2563.

Lowe D. R. and Knauth L. P. 1977. Sedimentology of the Onverwacht Group (3.4 billion years), Transvaal, South Africa, and its bearing on the characteristics and evolution of the early earth. Journal of Geology 85:699-723.

Lowe D. R. and Knauth L. P. 1978. The oldest marine carbonate ooids reinterpreted as volcanic accretionary lapilli, Onverwacht Group, South Africa. Journal of Sedimentology and Petrology 48:709-722.

Lowe D. R., Byerly G. R., Asaro F. and Kyte F. T. 1989. Geological and geochemical record of 3400-million-year-old terrestrial meteorite impacts. Science 245:959–962.

Lowe D. R., Byerly G. R., Kyte F. T., Shukolyukov A., Asaro F. and Krull A. 2003. Spherule beds 3.47-3.24 billion years old in the Barberton Greenstone Belt, South Africa: a record of large meteorite impacts and their influence on early crustal and biological evolution. Astrobiology 3:7-47.

Lowe D. R., Byerly G. R. and Kyte F. T. 2014. Recently discovered 3.42–3.23 Ga impact layers, Barberton Belt, South Africa: 3.8 Ga detrital zircons, Archean impact history, and tectonic implications. Geology 42:747-750.

Mader D. and Koeberl C. 2009. Using Instrumental Neutron Activation Analysis for geochemical analyses of terrestrial impact structures: Current analytical procedures at the University of Vienna Geochemistry Activation Analysis Laboratory. Applied Radiation and Isotopes 67:2100-2103.

Mohr-Westheide T., Reimold W. U., Fritz J., Koeberl C., Salge T., Hofmann A. and Schmitt R.T. 2015: Discovery of extraterrestrial component carrier phases in Archean spherule layers: Implications for estimation of Archean bolide sizes. Geology 43:299-302.

Mohr-Westheide T., Reimold W. U., Greshake A., Hoehnel D., Fritz J., Schmitt R. T., Salge T., Hofmann A., Oezdemir S., Schulz T. and Koeberl C. 2015. PGE chemistry and systematics of some Archean spherule layers in the Barberton Mountain Land (abstract). Meteoritics and Planetary Science 78. Abstract # 5060.

Neukum G., Ivanov B. and Hartmann W.K. 2001. Cratering records in the inner Solar System in relation to the lunar reference system. Space Science Reviews 96:55-86.

Palme H. and Jones A. 2003. Solar system abundances of the elements. In: Meteorites, comets, and planets, edited by Davis A.M., Holland H.D. and Turekian K.K. New York: Elsevier, 41-61.

Raschke U., Reimold, W. U., and Schmitt R. T. 2013. Petrography and geochemistry of the impactites and volcanic bedrock of the ICDP drill core D1c from Lake El´gygytgyn, NE Russia. Meteoritics & Planetary Science 48:1251-1286.

Reimold W.U. and Koeberl C. 2014. Impact Structures in Africa: A review. Journal of African Earth Sciences 93: 57-175.

Reimold W. U., Koeberl C., Johnson S. and McDonald I. 2000. Early Archean spherule beds in the Barberton Mountain Land, South Africa: Impact or terrestrial origin? In: Gilmour, I. and Koeberl, C. (eds.), Impacts and the early Earth: Berlin, Springer-Verlag, 117-180.

Ryder G. 1990. Lunar samples, lunar accretion, and the early bombardment history of the Moon. EOS Transactions American Geophysical Union. 71: 313–323.

Robin-Popieul C. C. M., Arndt N. T., Chauvel C., Byerly G. R., Sobolev A. V., and Wilson A. 2012. A new model for Barberton komatiites: Deep critical melting with high melt retention. Journal of Petrography 53:2191-2229.

Sears D. 2004. The origin of chondrules and chondrites. Cambridge University Press, New York, 199 pp.

Shukolyukov A., Kyte F. T., Lugmair G. W., Lowe D. R. and Byerly G.R. 2000. The oldest impact deposits on Earth - First confirmation of an extra-terrestrial component. In: Gilmour I. and Koeberl C. eds., Impacts and the early Earth. Springer-Verlag, Berlin, pp. 99-116.

Simonson B. M. 2003. Petrographic criteria for recognizing certain types of impact spherules in well-preserved Precambrian successions. Astrobiology 3:49-65.

Simonson B. M. and Glass B. B. 2004. Spherule layer records of ancient impacts. Annual Review of Earth and Planetary Sciences 32:329-361.

Simonson B. M. and Harnik P. 2000. Have distal impact ejecta changed through geologic time? Geology 28:975-978.

Simonson B. M., Hassler S. W. and Beukes N. J. 1999. Late Archean impact spherule layer in South Africa that may correlate with a Western Australian layer, in Dressler B. O., and Sharpton V. L. (eds.). Impact cratering and planetary evolution II: Geological Society of America Special Paper 339:249–262.

Simonson B. M., Koeberl C., McDonald I. and Reimold W. U. 2000. Geochemical evidence for an impact origin for a Late Archean spherule layer, Transvaal Supergroup, South Africa. Geology 28:1103-1106.

Simonson B.M., McDonald I., Shukolyukov A., Koeberl C., Reimold W.U. and Lugmair G.W. 2009. Geochemistry of 2.63-2.49 Ga impact spherule layers and implications for stratigraphic correlations and impact processes. Precambrian Research 175:51–76.

Stöffler D. and Ryder G. 2001. Stratigraphy and isotope ages of lunar geologic units: Chronological standard for the inner Solar System, Space Science Reviews 96:9-54.

Stöffler D. and Grieve R.A.F. 2007. Impactites. In: Fettes D., and Desmons J. (Eds.), Metamorphic Rocks: A Classification and Glossary of Terms,

Recommendations of the International Union of Geological Sciences. Cambridge University Press, Cambridge, UK, 82–92, 111–125, and 126–242.

Wetherill G. W. 1975. Late heavy bombardment of the Moon and terrestrial planets. The 6th Lunar Science Conference, Proceedings. Pergamon Press, Inc., New York. 2: 1539-1561.

3.7. Figures and Tables of Chapter 3
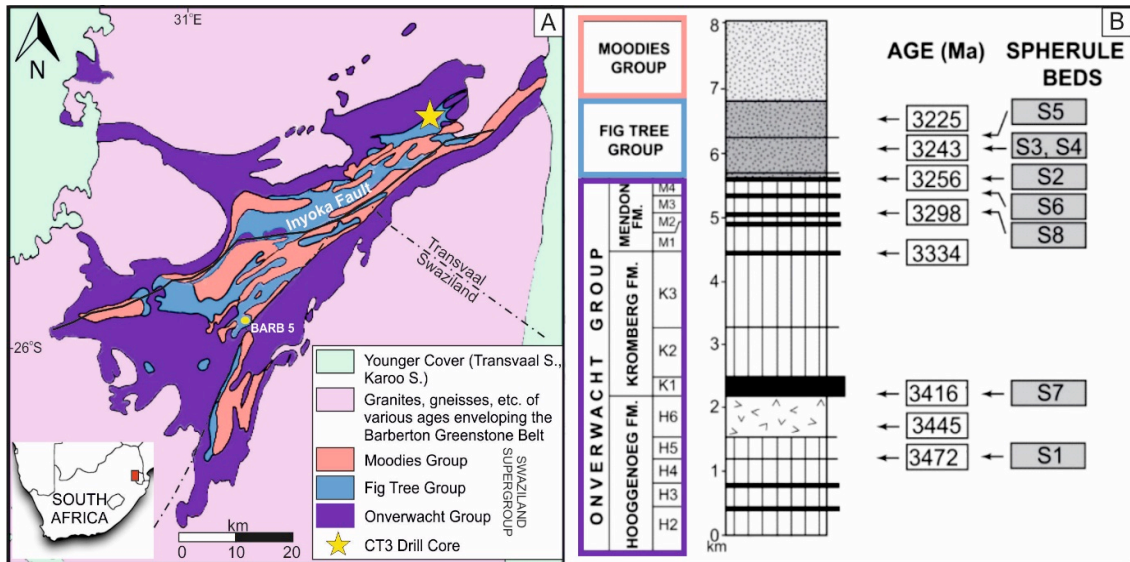
Figure 1. *a) Schematic geological map of the Barberton Greenstone Belt (modified after Koeberl and Reimold 1995); the CT3 drilling location is marked by a star (b) Simplified stratigraphy for the Barberton Greenstone Belt (modified after Lowe and Byerly 2014) with approximate stratigraphic positions of the S1-S8 spherule layers indicated.*
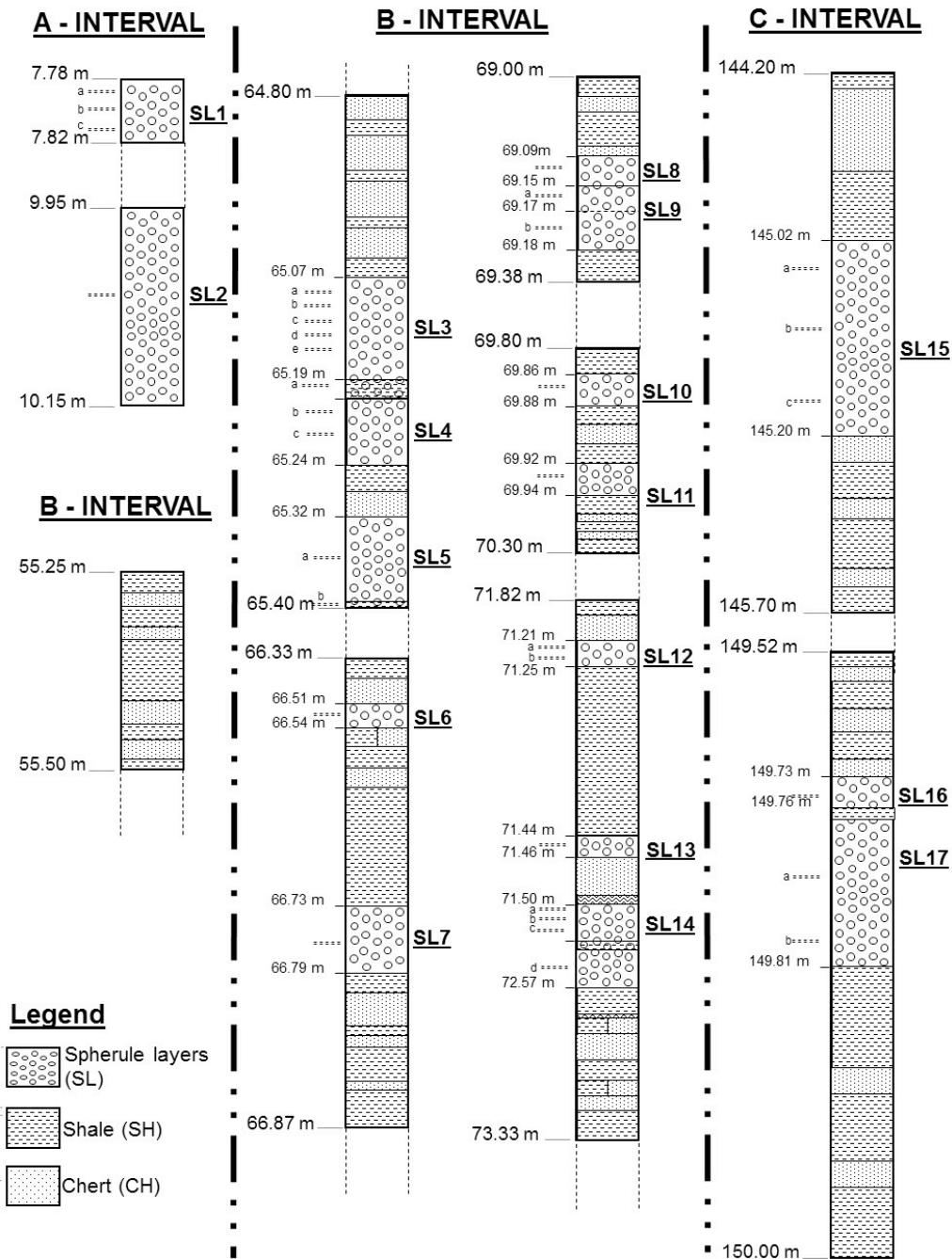
Figure 2. *Schematic stratigraphic column of the CT3 drill core intervals containing spherule layers. The three intervals with spherule layers are marked A, B and C, and the intercalations of spherule layers (SL) by shale (SH) and chert (CH) are indicated. The numbers represent the depth of drill core sections and number-letter combinations (bold) name the various spherule sublayers. Locations of samples taken from spherule layers are indicated by double-dashed lines on the left side of each section and are named "a, b ,c" if several samples were taken from a layer.*
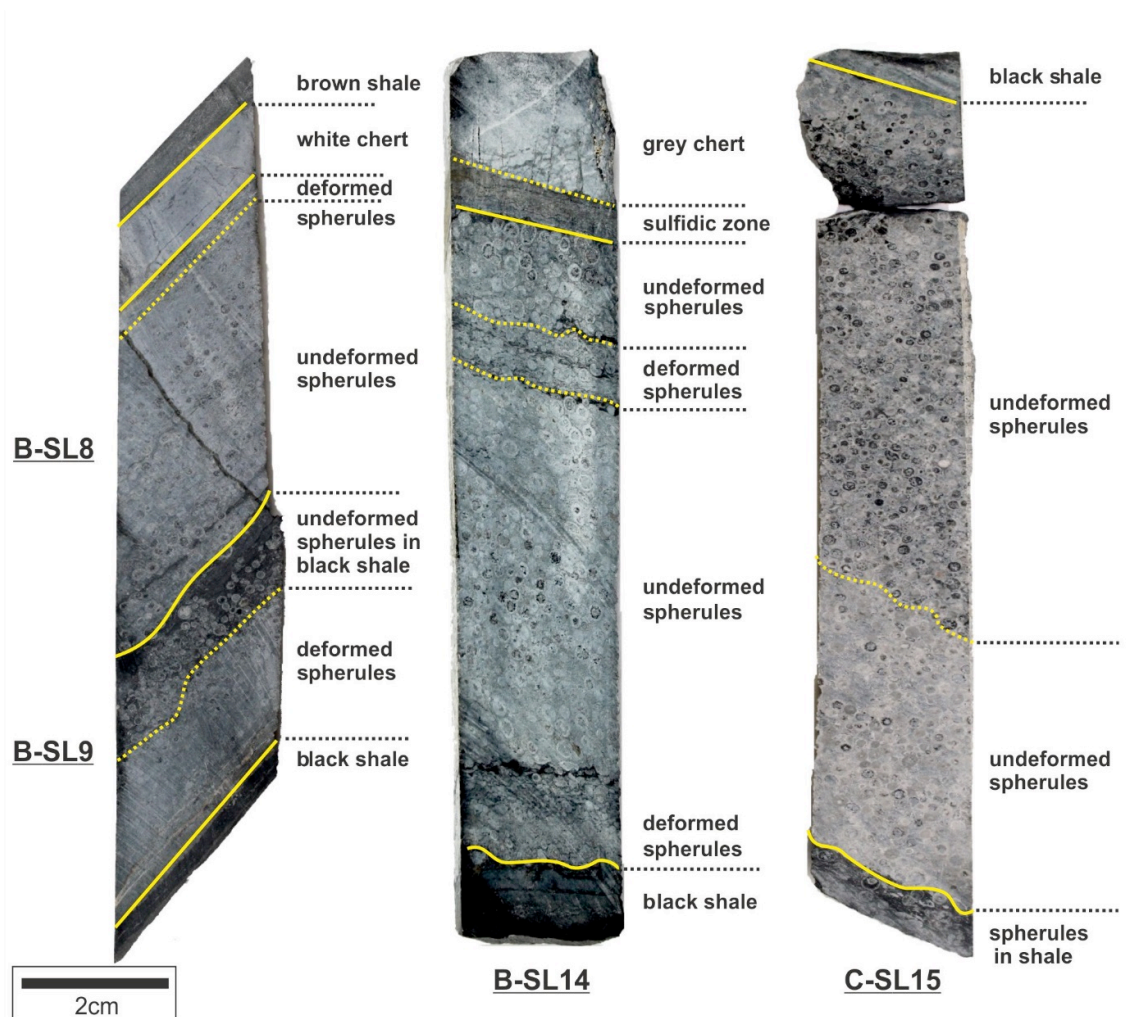
Figure 3. *Photos of selected drill core sections. Shale, chert and spherule intersections are marked. In these layers occur both deformed and undeformed spherules. Notably there are no sharp contacts between spherule layers and host rocks, and sometimes spherules occur within shale layers (e.g., B-SL9)*
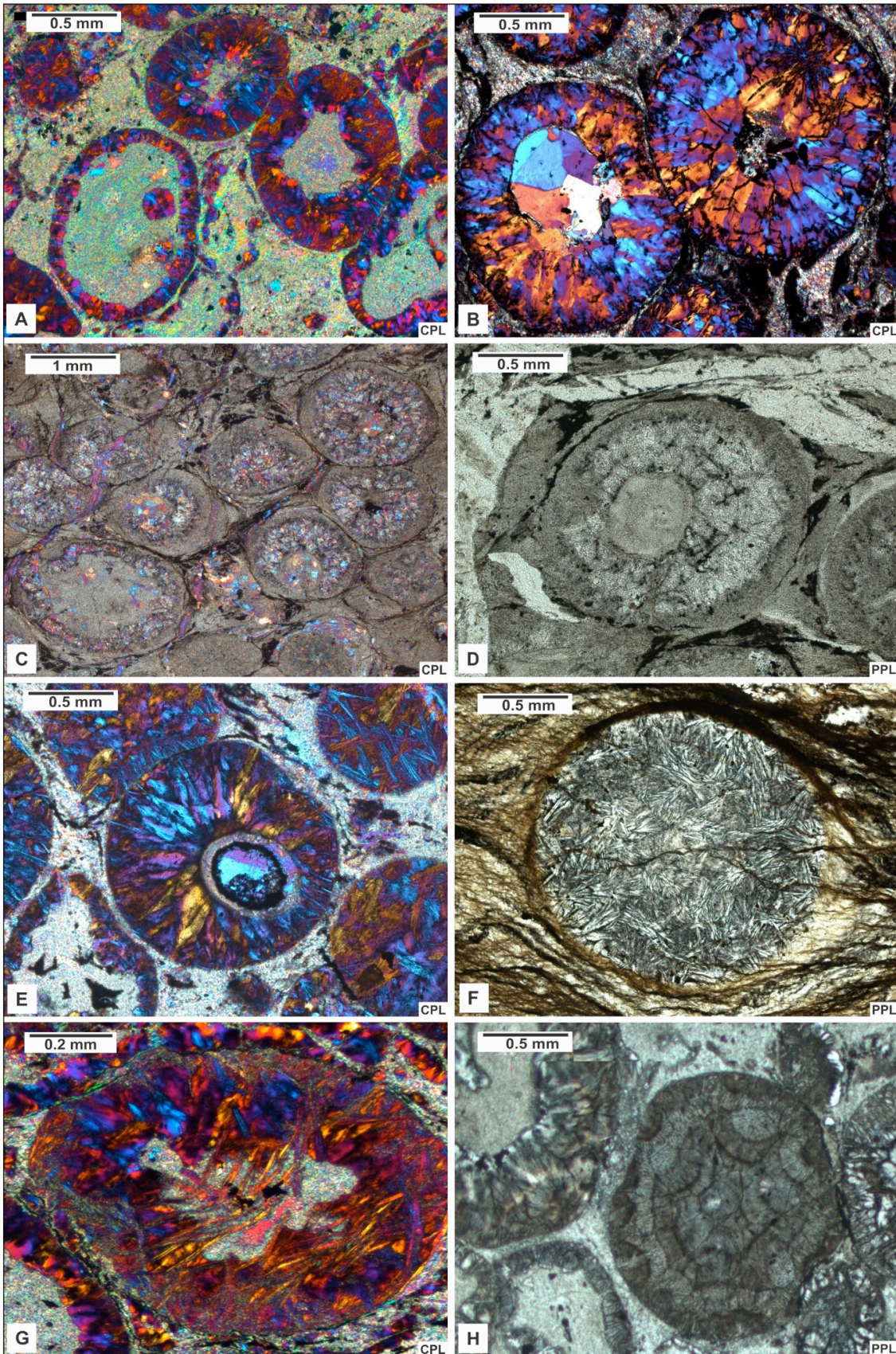
Figure 4. (previous page) *Microphotographs of CT3 spherules - zoned spherule types: A) sericite-K-feldspar spherules (C-SL15c, depth: 145.18-145.20 m), B) quartz-K-feldspar spherules (C-SL15b, depth: 145.09-145.12 m), C) quartz-sericite spherules (A-SL2, depth: 10.07-10.15 m), D) sericite-silicate-sericite spherules (A-SL2, depth:9.95-10.0 m), E) quartz-sericite-K-feldspar spherules (C-SL15c, depth: 145.18-145.20 m). The common textural types of spherules are: F) K-feldspar intersertal fill (A-SL1, depth: 7.78-7.79 m), G) barred texture of K-feldspar (C-SL17, depth: 149.77-149.81 m), H) botryoidal devitrification texture (C-SL15b, depth: 145.09-145.12 m). (PPL: Plane polarized light, CPL: Crossed polarized light).*
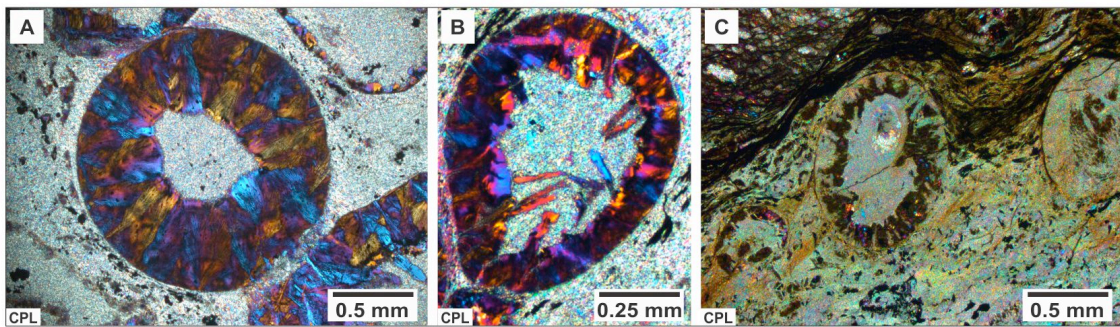
Figure 5. *Microphotographs of presumably undeformed spherule shapes: (a) spherical shape (C-SL15c, depth: 145.18-145.20 m), (b) tear-drop shape (C-SL15b, depth: 145.09-145.12 m), and (c) ovoid shape (A-SL2, depth: 10.07-10.15 m). (CPL: Crossed polarized light)*
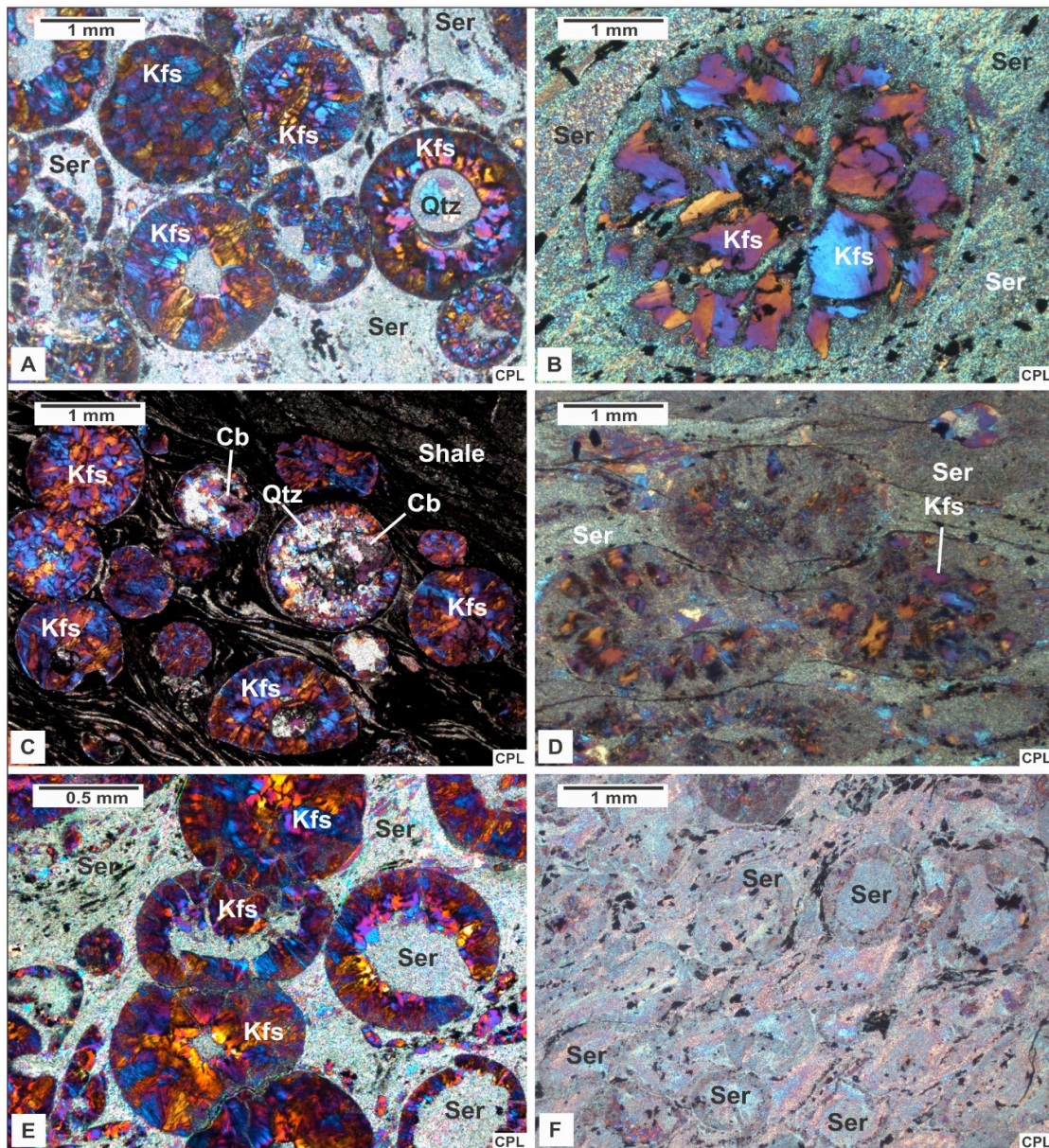
Figure 6. *Microphotographs of spherules. A) Undeformed spherules composed entirely of K-feldspar, in sericitic groundmass (C-SL15c, depth: 145.18-145.20 m). B) Undeformed spherule with K-feldspar crystals partially replaced by sericite (B-SL9b, depth: 69.17-69.18m). C) Undeformed spherules with K-feldspar or mosaic quartz fills in shaly groundmass (B-SL9a, depth: 69.15-69.17m). D) Deformed, partially strongly flattened spherules composed of K-feldspar and sericite. The groundmass consists of sericite (A-SL1, depth: 7.79-7.82 m). E) Deformed and partially collapsed spherules. Note that K-feldspar rimmed spherules that contain sericitic fill are more susceptible to deformation than fully K-feldspar crystalline spherules (C-SL15b, depth: 145.09-145.12 m). F) Deformed and in part strongly sheared spherules. The whole aggregate of spherules and groundmass has been replaced by sericite (B-SL3, depth: 65.07-65.19 m). (Kfs: K-feldspar, Qtz: quartz, Ser: sericite, Cb: carbonate, CPL: Crossed polarized light).*
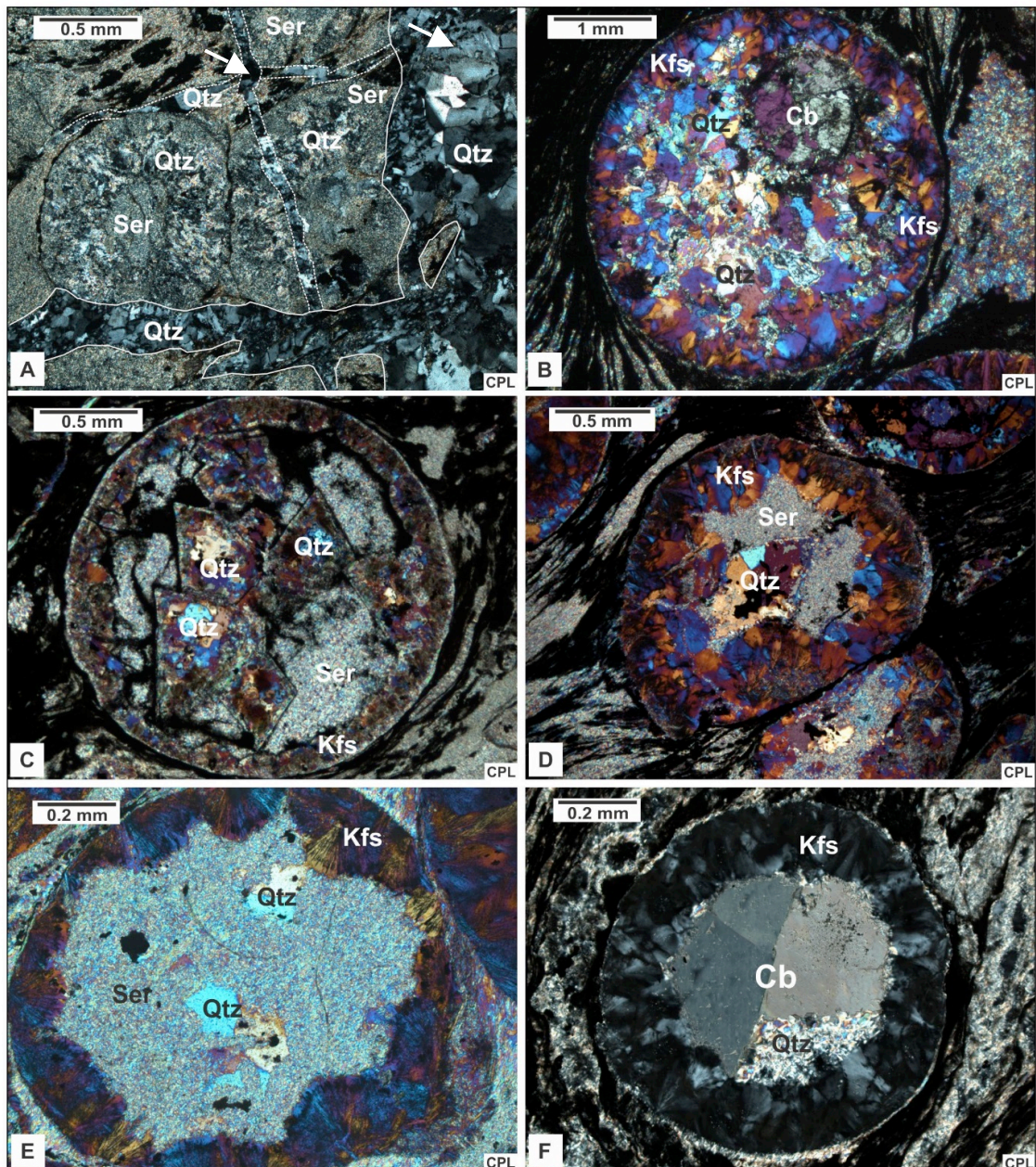
Figure 7. *Microphotographs of spherules. A) Fine-grained quartz mosaics in spherules. Note two populations of quartz veins: thick (ca. 500 μm) veins, generally developing outside spherules (white line), and thin (ca. 100 μm) veins, locally crosscutting spherules (dashed line) (A-SL2, depth: 9.95-10.15 m). B) Spherule filled by quartz mosaic. The vesicle is filled by carbonate (B-SL9a, depth: 69.15-69.17 m). C-D) Quartz mosaic pseudomorphs after carbonate crystals and sericite fill (C; B-SL14, depth: 71.50-72.57 m, and D; C-SL17, depth: 149.77-149.81 m). E) Sericite filled spherule with small quartz crystals, rimmed by fibrous Kfs growth (C-SL15c, depth: 145.18-145.20 m). F) Vesicle filled by carbonate (as shown by high interference color) and fine-grained material, likely (C-SL17, depth: 149.77-149.81 m).*
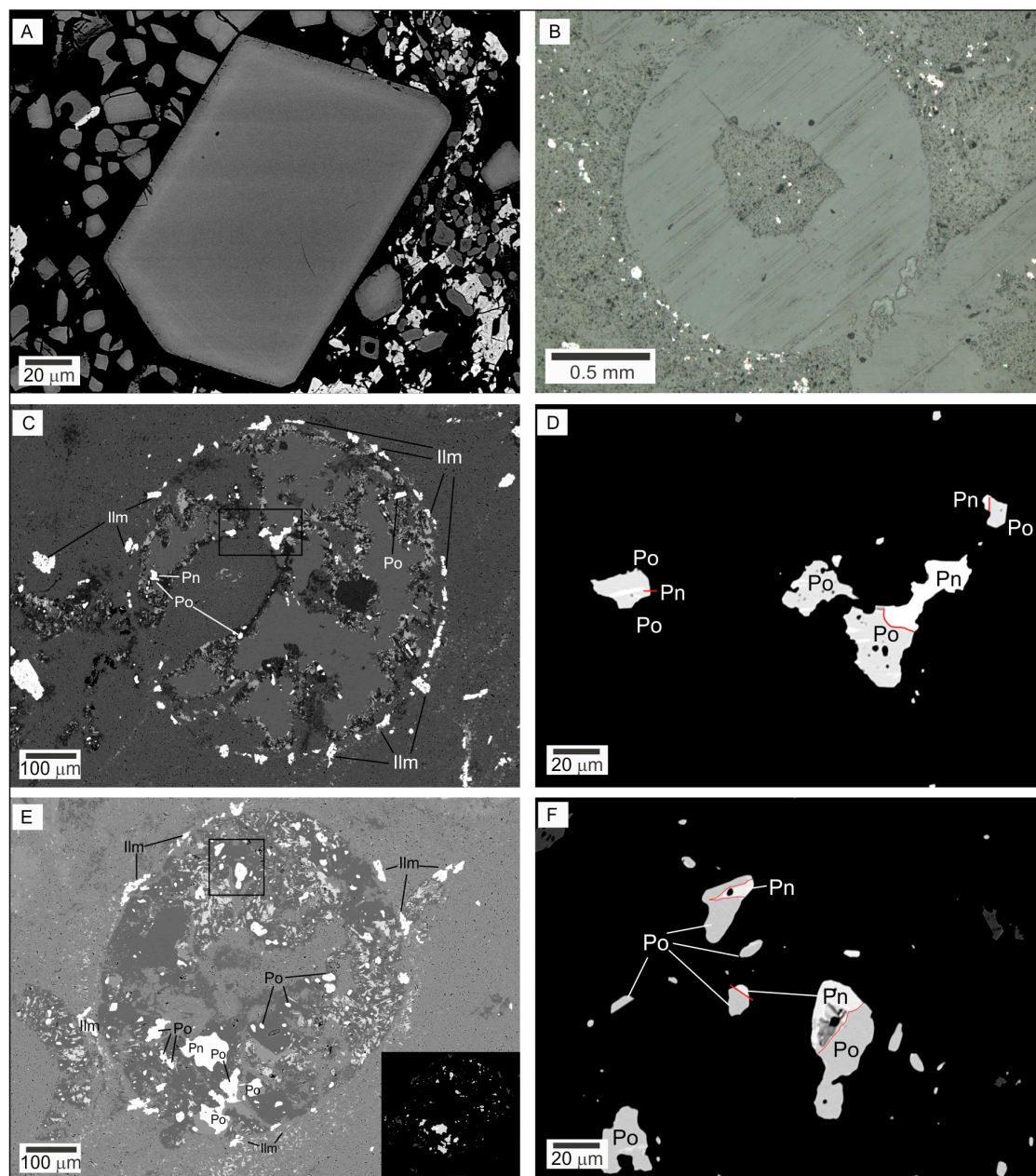
Figure 8. *A) Backscattered electron image of chromium spinel (grey, euhedral crystals) in shaly groundmass (dark); bright crystals on the right are sulfide (B-SH13, depth: 71.44-71.46 m). B) Reflected light image of spherule. Sulfide minerals around the spherule and in the vesicle are bright (C-SL15c, depth: 145.18-145.20 m). C, D, E, and F - Backscattered electron images of sulfide and oxide minerals in spherules. Left side images (C and E) are general views of the spherules. On the right in D and F, the marked area of C and E is magnified, giving a detailed view of some of the sulfides. Pyrrhotite (Po) and Pentlandite (Pn) occur in the spherule fillings. Ilmenite (Ilm) was identified along spherule rims only (both spherules from B-SL5, depth: 65.32-65.40 m).*
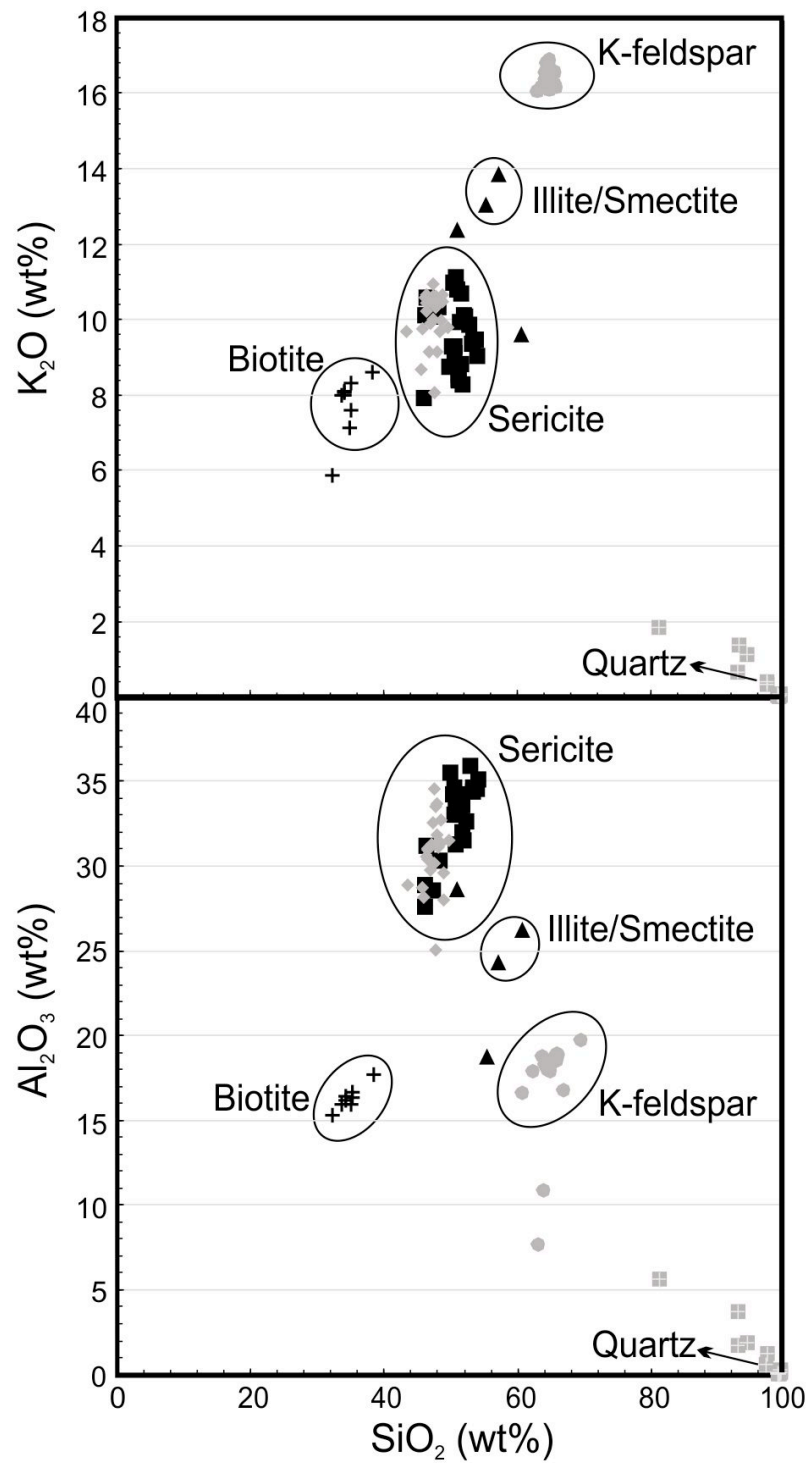
Figure 9. *Composition of minerals in spherule fills and exterior groundmass, in K$_2$O and Al$_2$O$_3$ vs. SiO$_2$ diagrams, respectively.*
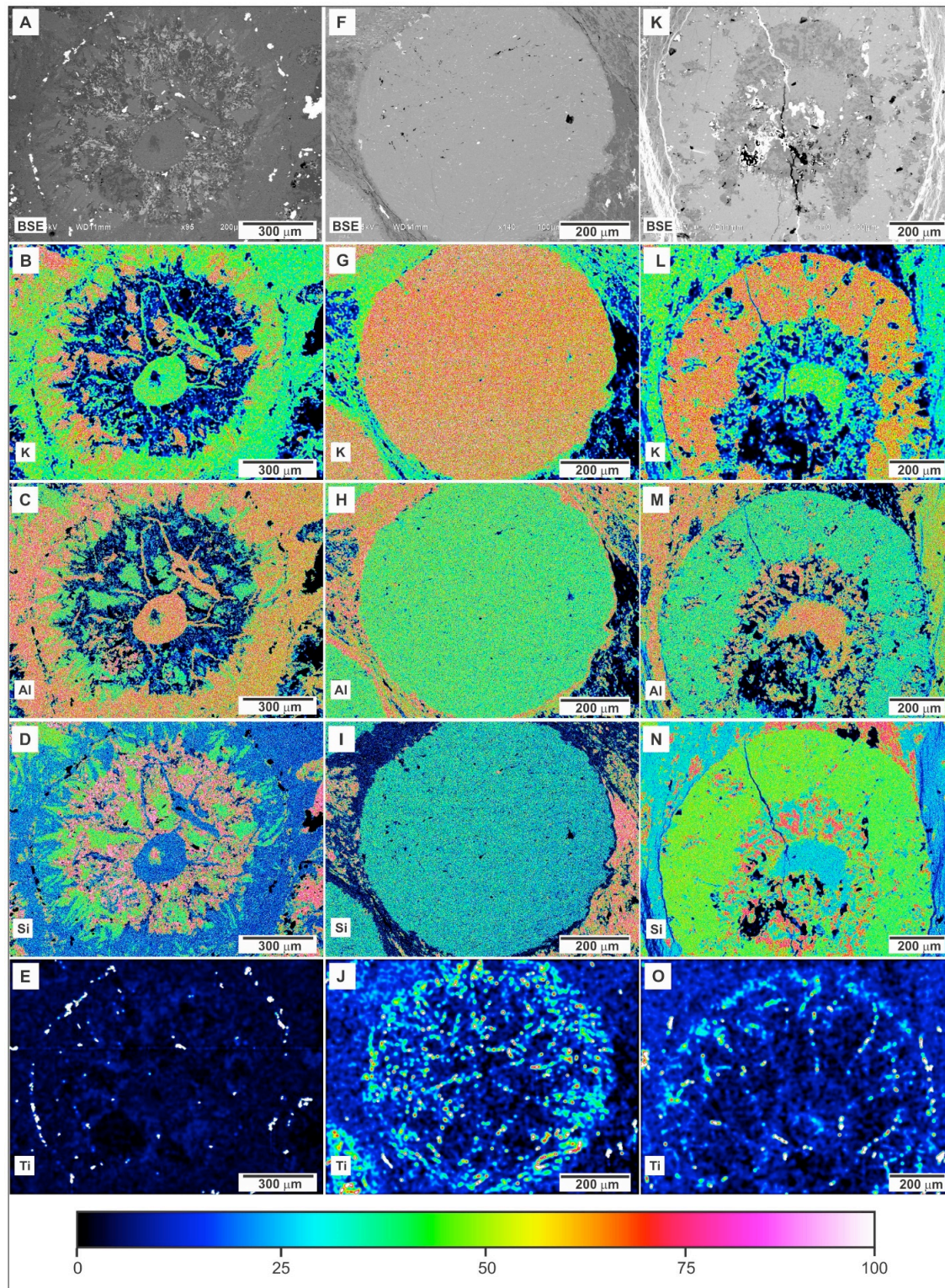
Figure 10. *SEM-EDS element maps for Ti, K, Al, and Si, for three spherule types: A, F, and K are backscattered electron images. A-E) Al-rich spherule (B-SL5, depth: 65.398-65.429 m), F-J) K-rich spherule (B-SL9a, depth: 69.338-69.351 m), and K-O) K-Al-rich, zoned spherule (A-SL1, depth: 7.780-7.788 m).*
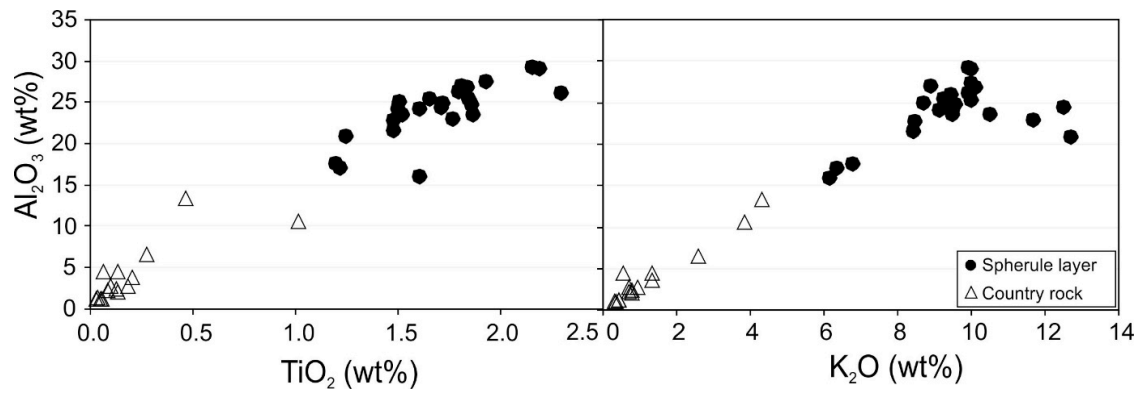
Figure 11. *Al₂O₃, TiO₂, and K₂O contents in spherule layer and host rock samples.*
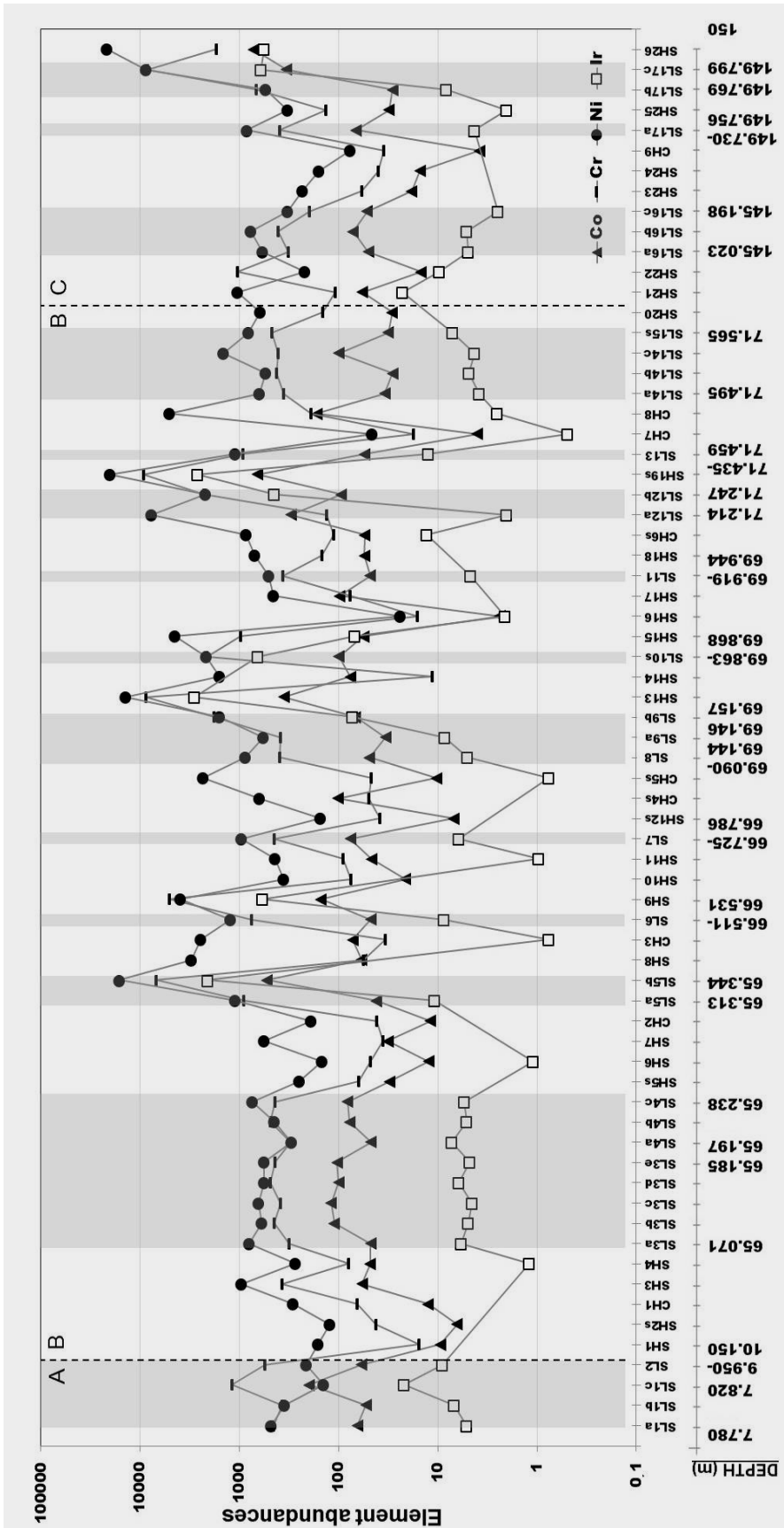
Figure 12. *Siderophile element abundances in spherule layer (shaded areas) and country rock samples from drill core sections A-C (at left: 7.78 m; at right: 150 m). Depth values in meters. Ni, Cr, and Co values in ppm; Ir values in ppb). (SL-: spherule layer, SH-: shale layer, CH-: chert layer, and –s: sulfide-bearing layer).*
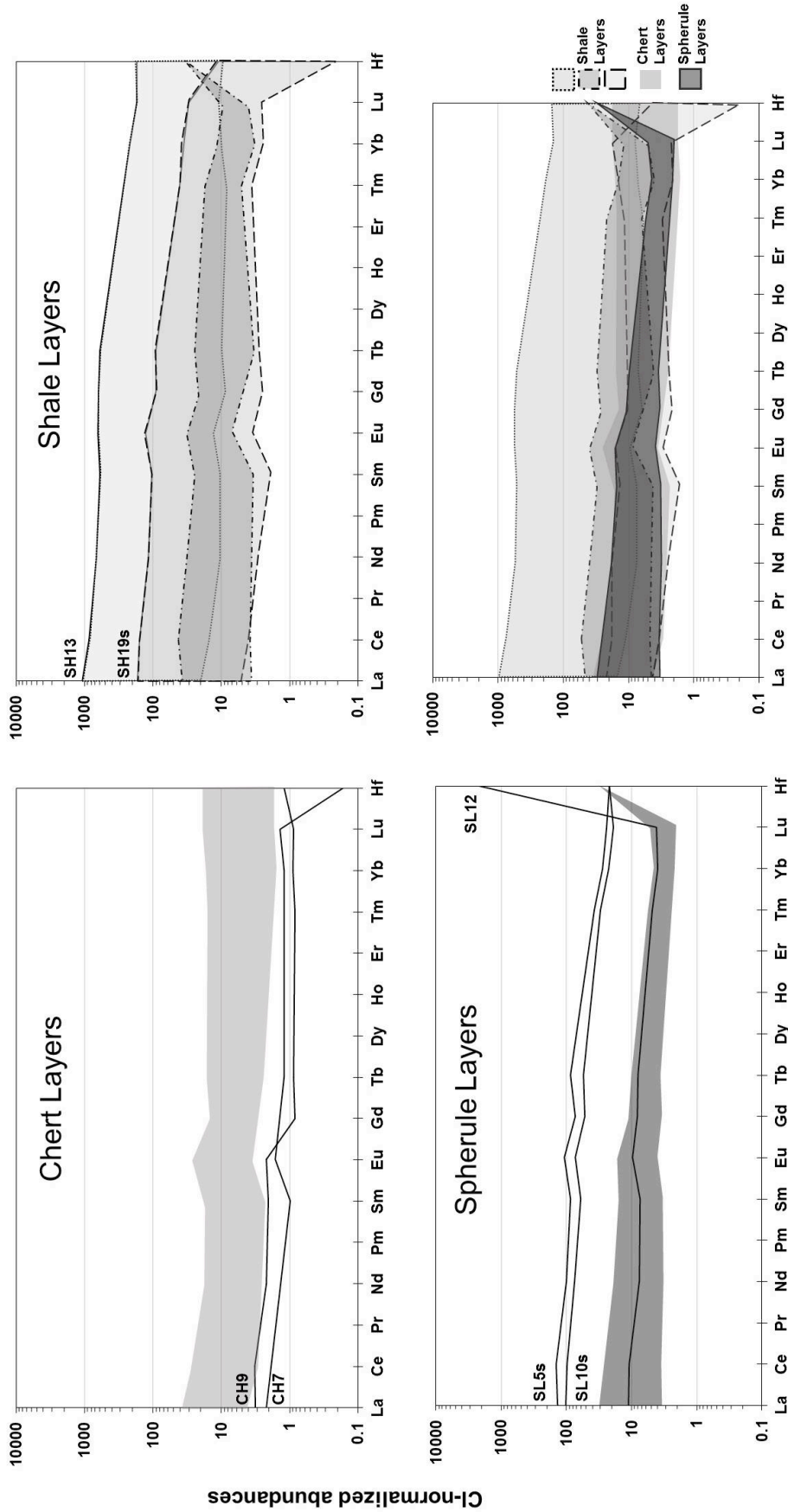
Figure 13. *REE and Hf abundance patterns for the analyzed samples. Chondrite normalization factors from Anders and Grevesse (1989).*
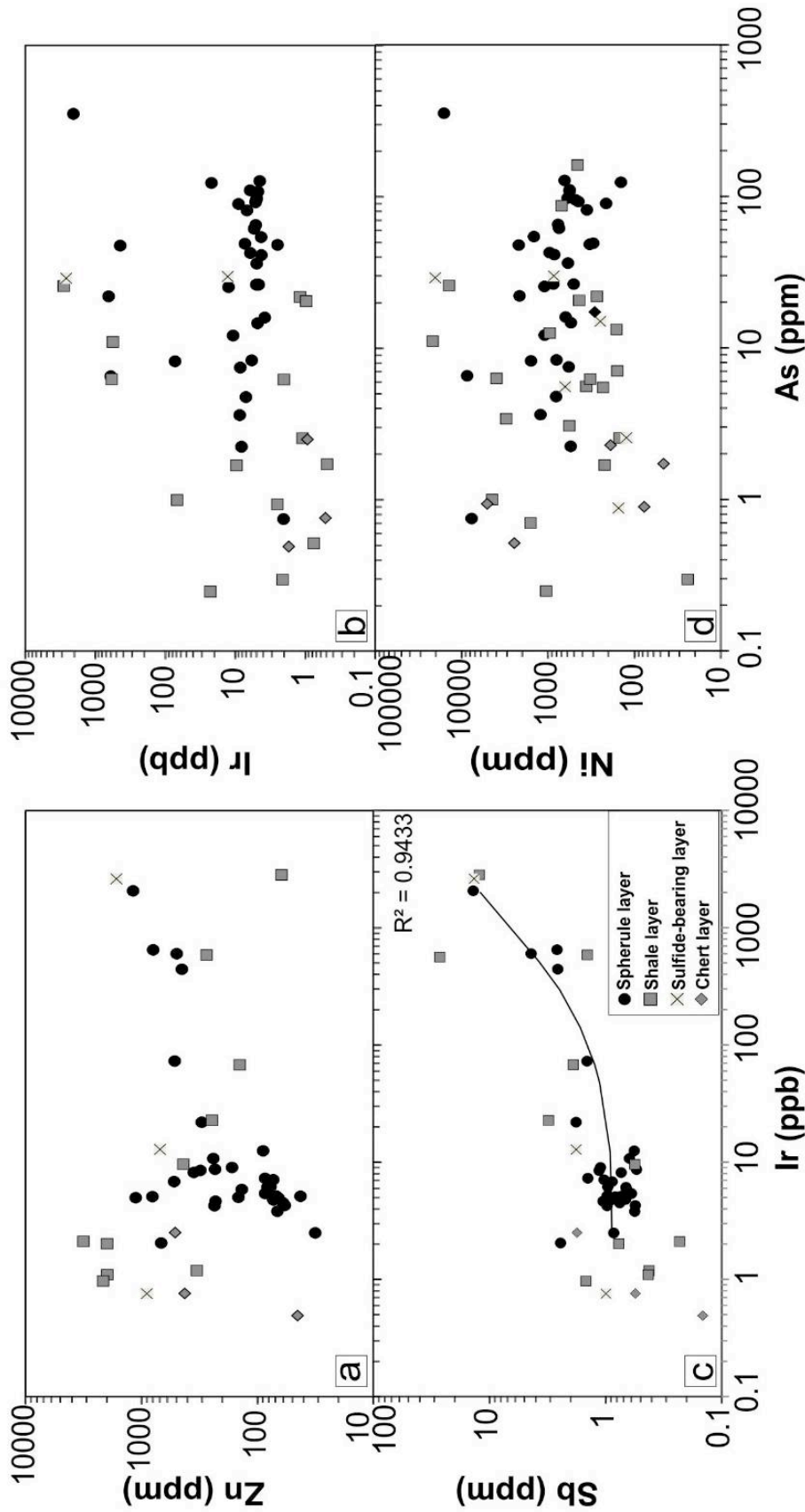
Figure 14. *Relationships for Ir-Zn (a), Ir-As (b), Ir-Sb (c), and Ni-As (d), for the analyzed samples. The regression line given in diagram C shows the trend of spherule layer samples.*
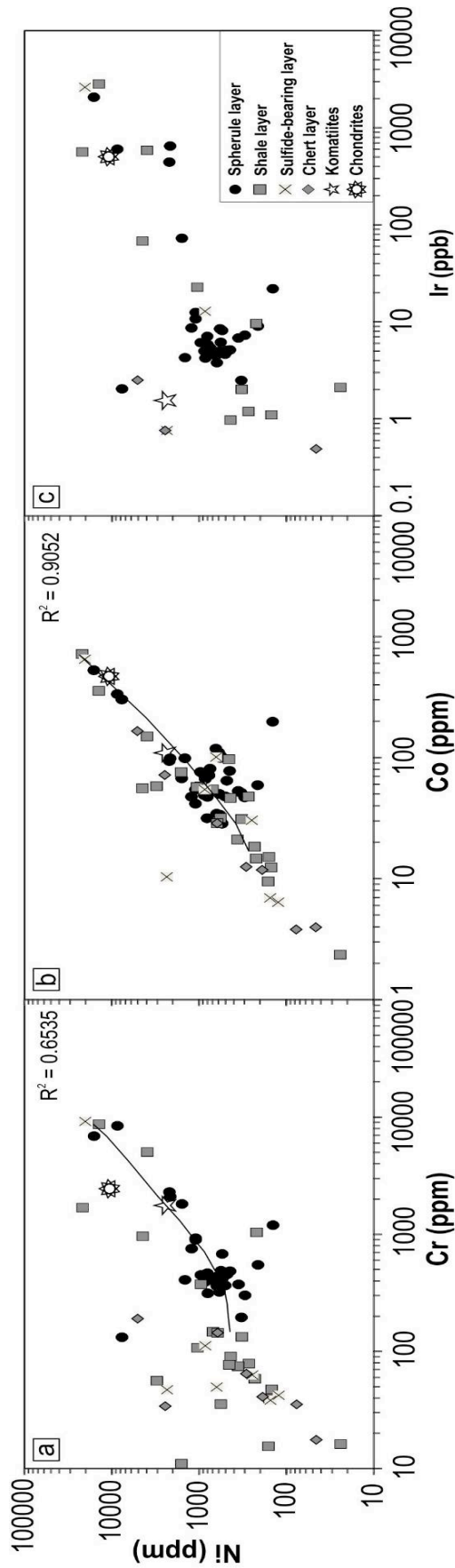
Figure 15. *Relationships between Ni and Cr (a), Co (b), and Ir (c), respectively, for the samples of this study. In all plots, chondrite data are from Anders and Grevesse (1989) and komatiite data from Robin-Popieul et al. (2012). The regression lines (R^2 = regression coefficient) show the trend defined by spherule layer samples. In Ni vs Co plot, the values for the spherule layer samples follow strictly the trend line and the correlation of these element data is stronger (R^2= 0.90) than for a Ni and Cr plot, with a lower R^2 value (0.65).*
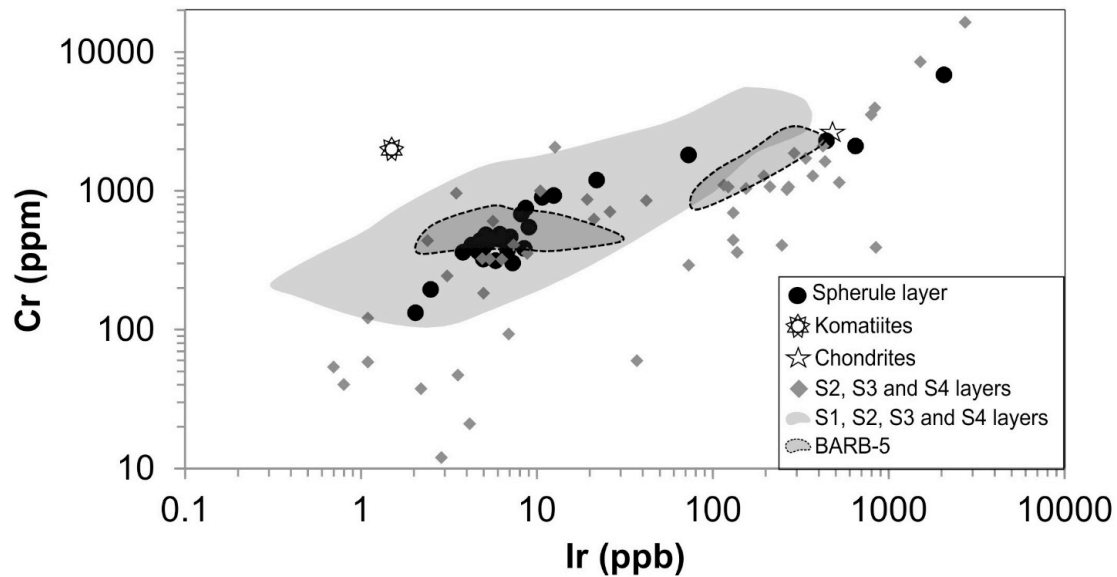
Figure 16. *Plot of Ir versus Cr for samples from BGB spherule beds and BGB komatiites, as well as CI chondrite data. The light shaded area represents literature data for S1, S2, S3 and S4 layers (Lowe et al. 2003, and references therein); diamond shaped data are for samples from the S2, S3, and S4 layers (Koeberl and Reimold 1995; Reimold et al. 2000); dark shaded areas, framed with a dashed line, represent BARB-5 data (Koeberl et al. 2015). The CT3 spherule layer samples lie on a trend intersecting CI chondrites (data from Palme and Jones 2003). The compositional trend for BGB spherule layer samples is distinct from komatiitic compositions. Data for komatiites from Robin-Popieul et al. (2012).*
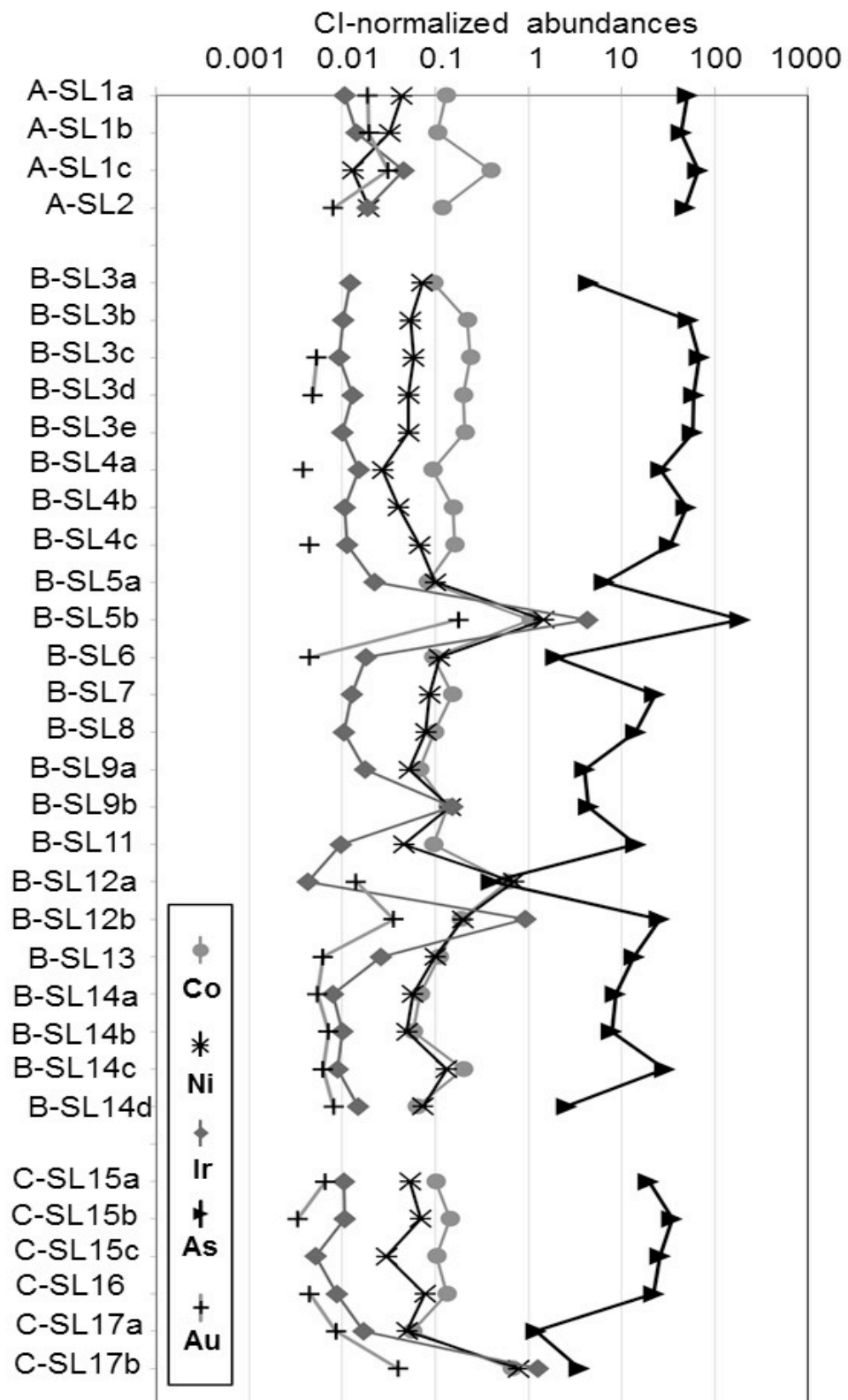
Figure 17. *Nickel, Co, Ir, and Au abundances plotted against As concentrations for the spherule layer samples of the three studied intervals (A, B, C).*

Table 1. *Summarized petrographic descriptions of the spherule layers (SL) in drill core CT3.*

Sample Name	Depth (m)	Thickness (cm)	Description based on macroscopic and microscopic observations	Mineral Composition
CT3_A-SL1	7.78-7.82	4	Spherule layer affected by surface weathering. Spherules are rounded to ovoid, elongated, ~0.2-2 mm in size, mostly deformed. They are immersed in a fine-grained, sericitic groundmass (GM). The middle zone contains a thin layer of brownish carbonaceous material, where undeformed spherules are filled with Kfs crystals as well as fine-grained sericite. GM is yellowish to orange due to alteration mineralogy.	Phyllosilicates, Kfs, carbonate, Qtz
CT3_A-SL2	9.95-10.15	20	Spherule layer affected by surface weathering. Spherules are rounded to ovoid and occur in clusters of 2-4 spherules, ~0.1-2 mm in size and mostly deformed. Spherule interiors consist mainly of Kfs, which is partly replaced by sericite; vesicles are filled with finest-grained Qtz-Kfs. Several 0.2-2 mm wide chert veins cut across, or go around spherules. Spherule fillings and GM are composed of yellowish grey, fine-grained sericitic material.	Phyllosilicates, carbonate, Qtz, Kfs, opaque minerals
CT3_B-SL3	65.07-65.19	12	Spherule layer composed of 3 zones separated by thin layers of black carbonaceous material; upper zone consists of Kfs filled, deformed spherules within fine-grained sericitized GM. Spherule sizes range from ~0.3 to 2 mm; some have truncated outlines; the vesicle filling is the same material as GM, with some Qtz crystals. The middle zone is composed of sheared spherules with elongated or twisted shapes. The material of spherule filling and GM component are the same. The lower zone has also undeformed, round spherules, which exhibit comparatively darker, fine-grained fill and are partly filled with Kfs microlites. Spherules are ~0.5-2.2 mm in size, and vesicle fillings are composed of very fine-grained sericite, the same as GM. Spherules occurring in the black carbonaceous shale zone are always well preserved, exhibiting comparatively coarser-grained Kfs needles.	Phyllosilicates, carbonate, Kfs, Qtz, opaque minerals
CT3_B-SL4	65.19-65.24	5	Deformed and undeformed spherules; sheared spherules are mostly elongated and with angular shape. They are filled with fine-grained sericitic GM-like material and with	Phyllosilicates, Kfs, carbonate, Qtz

			some coarse-grained Kfs, which especially occurs within undeformed spherules (~0.8-1 mm size). The GM is cut by a dark band of black carbonaceous material (black shale) and carbonate, that also contains some undeformed spherules with lath-like Kfs crystals.	
CT3_B-SL5	65.32-65.40	8	Deformed and undeformed spherules; sheared spherules mostly have elongated/twisted shapes; the fills of deformed spherules and GM material are both the same fine-grained, sericitic material. Undeformed spherules, ~1 mm in size, have round shapes. Their vesicles are filled with GM material including fine-grained Qtz and Kfs aggregates likely resulting from precipitation. At the bottom of the layer undeformed round spherules are located in shaley GM. Similar to SL3.	Phyllosilicates, carbonate, Kfs, Qtz
CT3_B-SL6	66.51-66.54	3	Spherule layer with deformed and undeformed spherules (~0.83 mm size, on average) that occur in three irregularly shaped zones intercalated by blackish GM composed of sericitic material. From top to bottom, zone 1 is composed of undeformed spherules with Kfs crystals, besides some deformed spherules filled with phyllosilicate. Some spherules exhibit centered or off-center vesicles filled with GM-like sericitic material. Above zone 1 occurs a zone of microcrystalline chert Zone 1 is rimmed by a thin band of graphite. Following, zone 2 comprises mostly small, deformed spherules filled with sericite above a zone of strongly deformed spherules filled with Kfs crystals. Zone 3 contains extremely deformed spherules filled with phyllosilicate. Underneath zone 3 occurs a zone of carbonaceous shale with carbonate veins crossing parallel to the lamination. Ni-Cr spinel crystals and two individual spherules are embedded in the opaque material; one of these spherules contains Kfs laths.	Phyllosilicates, carbonate, Kfs, Qtz, opaque minerals
CT3_B-SL7	66.73-66.79	6	Elongated deformed spherules occur in 2-4 grain clusters and are of ~0.1-2.3 mm size. Most spherules have the same fill as the GM, which is dominated by fine-grained sericite. A few spherules contain partially preserved Kfs grains.	Phyllosilicates, Kfs, carbonate, Qtz
CT3_B-SL8	69.09-69.15	6	Deformed and undeformed (mostly collapsed) spherules; ~0.5-2.2 mm in size, with fine-grained spherule fillings that have a	Phyllosilicates, Kfs, Qtz, carbonate,

			darker color than the GM material. These spherules contain some Kfs microlites. Spherule vesicle fillings are composed of very fine-grained sericite, same as the GM component.	opaque minerals
CT3_B-SL9	69.15-69.17	3	From top to bottom, there are 2 distinct zones. Zone 1: Black shale with undeformed, round spherules with Kfs microlites. Spherules are ~0.5-1 mm in size. Vesicles are mostly filled by GM-like sericitic material and Qtz crystals, and a few are filled with dark phyllosilicate. Very similar to SL5. Zone 2 (~1cm thick): Deformed and undeformed spherules, ~0.5-2.2 mm in size. Fine-grained spherule fills exhibit darker color than the GM material and have Kfs crystallization inside of the rim. Vesicle fillings are composed of very fine-grained sericite, similar to the GM material.	Phyllosilicates, Kfs, carbonate, Qtz, opaque minerals
CT3_B-SL10	69.86-69.88	2	Spherule layer including undeformed to deformed spherules (~1.03 mm) intercalated with shale and sulfides. A thin layer of black shale, exhibiting dendritic spinel, occurs on top of the spherule rich section; carbonate bearing shale is observed underneath the spherule bed. Deformed, elongated spherules are filled with phyllosilicate in contrast to undeformed spherules that are filled with Kfs crystals. The latter occur mostly close to the black carbonaceous material (black shale).	Phyllosilicates, carbonate, Kfs, opaque minerals, Qtz
CT3_B-SL11	69.92-69.94	2	Deformed and undeformed spherules, ~0.8-1 mm in size. Sheared spherules are elongated; spherules are filled by the same material as the GM, namely fine-grained sericite. Undeformed spherules are surrounded by brownish carbonate and also contain Kfs in their fill.	Phyllosilicates, carbonate, Kfs, opaque minerals, Qtz
CT3_B-SL12	71.21-71.25	4	Generally similar to SL10 and SL 11. Spherule layer with deformed and undeformed spherules (~0.86 mm) in blackish GM. Phyllosilicate-rich spherules are more deformed than Kfs-rich spherules. Vesicles are filled with phyllosilicate or carbonates.	Phyllosilicates, Kfs, carbonate, Qtz
CT3_B-SL13	71.44-71.46	2	Deformed and – mostly - undeformed spherules (~0.86 mm). Comparatively larger spherules occur at the bottom (up to 1.07 mm). Deformed (sheared) spherules are phyllosilicate-rich, undeformed spherules are composed of K-feldspar crystals. Vesicles are filled mostly with phyllosilicates	Phyllosilicates, Kfs, carbonate, Qtz

108

and carbonates.

CT3_B-SL14	71.50-72.57	7	Deformed and undeformed spherules; shear-deformed spherules are elongated. Spherule fills consist of the same fine-grained sericitic material as the GM. Undeformed spherules are ~0.9-1 mm in size and have Kfs crystals in sericite fill. The top of this section contains black shale and a narrow, 0.1 mm sulfide layer. Deformed and undeformed spherules have darker, fine-grained fill than the sericitic GM material, and have in part Kfs crystallization around vesicles. Round spherules are ~0.5-2.2 mm in size. This layer displays distinctive gradation, with, on average, 0.64 mm sized spherules at the top and larger and more abundant spherules of, on average, 0.99 mm size at the bottom (Hoehnel 2016).	Phyllosilicates, carbonate, Kfs, opaque minerals, Qtz
CT3_C-SL15	145.02-145.20	18	Undeformed spherules, ~0.5-1.5 mm in size, in fine-grained sericitic GM. Spherules are filled by Kfs needles. Some have vesicles filled by GM-like material and Qtz crystals. Opaque minerals occur around the rim of some spherules. Clusters of two or three spherules occur, but single spherules are also disseminated in the GM.	Phyllosilicates, Kfs, carbonate, Qtz
CT3_C-SL16	149.73-149.76	3	Undeformed spherules, ~0.5-2 mm in size, in fine-grained sericitic GM. Spherules are filled with Kfs needles. Some have vesicles filled by GM-like sericitic material.	Kfs, Phyllosilicates, carbonates, opaque minerals, Qtz
CT3_C-SL17	149.77-149.81	4	Mostly deformed spherules, ~0.70 mm on average size, within fine-grained sericitic GM. Vesicles are mostly filled with phyllosilicates and minor carbonates. Clusters of 2 or 3 spherules occur more densely distributed than in CT3_C-SL16. Within spherules some organic activity signatures are observed, they are rounded by K-feldspar crystals.	Kfs, Phyllosilicates, carbonates, opaque minerals, Qtz

Ms: muscovite, Kfs: K-feldspar, Qtz: quartz, GM: groundmass. Given size measurements for spherules are in average.

Table 2. *Electron microprobe analyses of minerals in spherule fills and rims. The values are averages of multiple measurements in a given layer. (Data in wt%; all Fe as FeO. Error limits are 1 sigma standard deviation).*

	SiO_2	TiO_2	Al_2O_3	Cr_2O_3	FeO	MnO	MgO	CaO	Na_2O	K_2O	Tot
Feldspar											
CT3-SL5 (n=9)	64.29 ± 0.43	0.04 ± 0.07	18.36 ± 0.23	0.05 ± 0.07	0.11 ± 0.07	0.01 ± 0.00	0.01 ± 0.00	0.00 ± 0.00	0.08 ± 0.04	16.62 ± 0.20	99.5
CT3-SL8 (n=14)	63.97 ± 1.18	0.11 ± 0.09	18.26 ± 0.54	0.02 ± 0.03	0.89 ± 0.20	0.02 ± 0.01	0.21 ± 0.06	0.12 ± 0.26	0.08 ± 0.03	16.19 ± 0.39	99.8
CT3-SL9 (n=6)	65.21 ± 2.84	0.01 ± 0.01	17.37 ± 3.30	0.01 ± 0.01	0.12 ± 0.25	0.01 ± 0.01	0.01 ± 0.01	0.04 ± 0.04	0.06 ± 0.01	16.14 ± 0.47	98.9
Sericite											
CT3-SL5 (n=16)	46.94 ± 1.51	0.60 ± 0.08	29.58 ± 1.96	0.09 ± 0.05	2.87 ± 0.45	0.02 ± 0.02	1.33 ± 0.14	1.22 ± 1.87	0.09 ± 0.04	9.77 ± 0.87	92.5
CT3-SL8 (n=12)	47.87 ± 0.89	0.46 ± 0.20	31.81 ± 1.48	0.04 ± 0.04	3.14 ± 0.43	0.02 ± 0.02	1.60 ± 0.26	0.02 ± 0.01	0.13 ± 0.05	10.30 ± 0.38	95.3
CT3-SL9 (n=3)	48.25 ± 0.52	0.59 ± 0.39	32.45 ± 1.52	0.12 ± 0.01	3.18 ± 0.32	0.02 ± 0.00	1.47 ± 0.35	0.03 ± 0.01	0.15 ± 0.00	9.99 ± 0.44	96.2
Biotite											
CT3-SL5 (n=3)	34.02 ± 0.28	1.99 ± 0.07	16.23 ± 0.21	0.09 ± 0.09	27.27 ± 0.04	0.03 ± 0.01	6.18 ± 0.29	0.00 ± 0.00	0.02 ± 0.01	8.04 ± 0.05	93.8
CT3-SL8 (n=5)	35.02 ± 2.21	1.89 ± 0.28	16.39 ± 0.88	0.03 ± 0.03	26.66 ± 1.10	0.03 ± 0.02	6.59 ± 0.48	0.06 ± 0.09	0.04 ± 0.03	7.57 ± 1.09	94.2
CT3-SL9 (n=2)	35.41 ± 0.32	1.91 ± 0.47	16.77 ± 0.05	0.03 ± 0.04	26.51 ± 0.30	0.05 ± 0.01	6.45 ± 0.34	0.01 ± 0.01	0.00 ± 0.00	7.40 ± 0.26	94.5
Quartz											
CT3-SL5 (n=5)	97.15 ± 2.81	0.03 ± 0.02	1.27 ± 1.73	0.02 ± 0.02	0.24 ± 0.16	0.01 ± 0.00	0.05 ± 0.05	0.01 ± 0.01	0.01 ± 0,01	0.46 ± 0.64	99.2
CT3-SL8 (n=6)	97.07 ± 2.81	0.07 ± 0.07	0.78 ± 0.80	0.00 ± 0.01	0.39 ± 0.33	0.01 ± 0.01	0.04 ± 0.05	0.01 ± 0.01	0.01 ± 0.01	0.39 ± 0.43	98.7
Ilmenite											
CT3-SL5 (n=9)	0.55 ± 0.63	49.89 ± 1.43	0.35 ± 0.48	0.01 ± 0.01	46.09 ± 0.65	0.83 ± 0.09	0.04 ± 0.03	0.28 ± 0.49	0.00 ± 0.01	0.21 ± 0.18	98.2
CT3-SL8 (n=4)	0.14 ± 0.02	52.54 ± 1.05	0.09 ± 0.03	0.05 ± 0.05	46.85 ± 0.33	0.92 ± 0.01	0.02 ± 0.02	0.01 ± 0.00	0.00 ± 0.01	0.18 ± 0.08	100.1
CT3-SL9 (n=2)	0.99 ± 0.39	51.95 ± 0.16	0.34 ± 0.13	0.00 ± 0.00	46.17 ± 0.55	0.82 ± 0.04	0.01 ± 0.01	0.00 ± 0.01	0.02 ± 0.00	0.31 ± 0.20	100.0

(n = number of measurement points for each mineral phase in a specific layer)

Table 3. *Electron microprobe analyses of sulfide minerals common to the spherule layers. The values are averages of multiple measurements in a given layer (Data in element wt%. Error limits are 1 sigma standard deviation).*

	S	Zn	Pb	Fe	Cu	Co	Ni	As	Sb	Total
Pyrrhotite										
CT3-SL5 (n=13)	37.22 ± 0.48	0.04 ± 0.08	0.16 ± 0.05	58.95 ± 0.59	0.05 ± 0.03	0.03 ± 0.02	0.95 ± 0.12	0.00 ± 0.00	0.00 ± 0.00	97.40
CT3-SL8 (n=4)	36.98 ± 0.36	0.03 ± 0.02	0.18 ± 0.06	58.91 ± 0.32	0.04 ± 0.01	0.02 ± 0.01	0.88 ± 0.22	0.00 ± 0.00	0.00 ± 0.00	97.04
Pentlandite										
CT3-SL5 (n=5)	31.98 ± 0.20	0.01 ± 0.01	0.15 ± 0.14	27.82 ± 0.66	0.01 ± 0.02	1.80 ± 0.12	36.13 ± 0.28	0.00 ± 0.00	0.00 ± 0.00	97.91
CT3-SL8 (n=2)	33.53 ± 2.87	0.04 ± 0.06	0.19 ± 0.06	27.69 ± 0.54	0.06 ± 0.01	2.45 ± 1.10	32.49 ± 5.75	0.00 ± 0.00	0.00 ± 0.00	96.45
Sphalerite										
CT3-SL5 (n=2)	31.90 ± 0.23	59.13 ± 1.08	0.11 ± 0.02	5.59 ± 0.76	0.03 ± 0.01	0.05 ± 0.00	0.00 ± 0.00	0.00 ± 0.00	0.06 ± 0.00	96.88
Galena										
CT3-SL8 (n=2)	11.46 ± 0.58	0.06 ± 0.01	84.43 ± 0.58	3.37 ± 0.47	0.14 ± 0.08	0.00 ± 0.00	0.02 ± 0.01	0.00 ± 0.00	0.00 ± 0.00	99.48

(n = number of measurement points for each mineral phase in a specific layer)

	A-SL1a	A-SL1b	A-SL1c	A-SL2	B-SH1	B-SH2s	B-CH1	B-SH3	B-SH4	B-SL3a	B-SL3b	B-SL3c	B-SL3d	B-SL3e	B-SL4a	B-SL4b	B-SL4c	B-SH5s	B-SH6
SiO2 (%)		51.1	54.9		49.9		70.1	57.7			49.8		50.8	46.8		46.9	50.4	58.3	9.2
TiO2 (%)		1.81	1.51				0.07	0.47			1.93		1.84	2.19		2.16	1.80	0.21	0.04
Al2O3 (%)		27.0	25.0				4.3	13.3			27.4		26.8	29.0		29.3	26.2	3.6	1.2
Fe2O3 (%)		3.82	4.01				3.52	4.63			4.69		4.82	5.27		5.09	5.85	8.97	15.10
MnO (%)		0.11	0.05				0.30	0.11			0.03		0.03	0.04		0.04	0.03	0.78	1.49
MgO (%)		1.38	1.26				2.54	1.67			1.29		1.26	1.42		1.43	1.35	3.70	9.88
CaO (%)		0.20	0.04				6.31	3.14			0.50		0.08	0.06		0.04	0.07	8.68	25.40
Na2O (%)		0.15	0.26				0.06	0.12			0.16		0.18	0.14		0.16	0.17	0.14	0.10
K2O (%)		8.91	8.71				0.55	4.31			10.00		10.10	10.00		9.90	9.90	1.35	0.42
P2O5 (%)		0.05	0.07				0.04	0.09			0.04		0.02	<0.01		0.00	0.03	0.06	0.06
LOI (%)		4.90	4.00				12.40	14.20			4.40		4.40	4.40		5.70	4.30	14.70	37.80
Summe (%)		99.43	99.81				100.19	99.74			100.24		100.33	99.32		100.72	100.10	100.49	100.69
Na	1033	2055	1022	1287	434	68	114	389	79.3	1516	821	968	1164	1267	1243	871	1069	96.7	119
K (wt%)	8.13	6.70	7.98	8.25	2.93	<1480	0.45	3.67	0.82	8.42	7.87	7.87	8.89	8.65	8.92	8.24	8.31	0.78	0.29
Sc	18.3	12.7	22.4	18.4	15.5	10.4	4.14	11.6	18.4	17.4	21.2	19.6	27.1	24.1	18	26.6	20.3	27.9	65
Cr	454	373	1196	548		42.3	64.4	374	78.8	313	442	388	487	439	301	483	437	63	47.4
Fe (wt%)	3.35	3.14	2.88	3.13	3.05	6.02	2.42	3.23	15.9	4.97	3.66	3.07	3.45	3.30	2.63	3.47	4.19	6.11	11.1
Co	64.6	53.1	198	59.4	9.49	6.4	12.6	58.2	47.8	47.4	111	119	99.6	104	47.1	77.8	81	30.4	12.4
Ni	479	354	143	212	161	123	288	953	271	796	595	641	563	564	299	444	745	247	148
Zn	806	523	303	166	154	297	290	748	413	137	66	641	77	73	86	69	86	1379	334
Ga	12	6	12	10	5	26	3	9	17	15	8	12	18	7	7	18	14	13	31
As	94.7	81.4	124	89.7	13.2	2.56	17.3	12.5	21.9	8.33	97.5	127	110	108	49.2	92.3	61.6	15	2.55
Se	3.07	2.92	4.79	2.78	1.48	0.91	2.20	5.13	1.76	1.88	2.15	1.93	1.4	1.96	1.37	1.35	2.68	4.15	<3.4
Br	<0.4	<0.4	<0.5	<0.4	0.3	0.3	0.4	0.3	<0.3	0.1	<0.4	<0.5	<0.6	<0.5	<0.3	<0.6	<0.5	0.3	<0.5
Rb	238	176	250	246	<5	8.66	18.5	119	42.6	236	232	211	267	238	214	275	256	31.5	20.7
Sr	<31	<38	<46	<40	<21	<36	<26	<42	<45	<46	<40	<44	<31	<41	<43	<44	<42	<53	<70
Zr	144	113	153	150	<29	59	56	196	<65	128	96	105	146	86	138	115	122	122	<99
Sb	0.82	0.88	1.79	1.10	0.34	0.3	1.27	2.21	0.42	0.66	0.83	0.75	0.96	0.89	1.42	0.97	0.6	0.34	0.43
Cs	4.27	3.23	4.63	4.28	0.07	0.13	0.44	3.64	2.18	6.38	5.23	4.21	6.12	5.45	5.14	6.96	6.34	1.87	1.7
Ba	122	122	120	155	<19	<45	<30	71	<23	101	80	76	97	58	102	24	88	<37	<56
La	11.1	10.4	1.7	3.77	1.74	4.07	3.6	16.0	6.64	3.09	1.06	1.18	1.85	0.77	4.49	0.67	1.19	3.85	5.82
Ce	8.29	8.25	4.34	7.51	3.66	8.74	7.55	31.6	15	8.62	3.51	3.34	5.51	2.39	12.3	1.97	3.87	8.39	12.6
Nd	10.6	11.3	3.29	6.22	2.35	5	3.67	15.0	8.69	6.34	1.72	2.88	4.22	1.89	9.68	<2.5	<2.5	4.38	5.79
Sm	2.87	3.11	1.31	2.07	0.55	1.39	1.06	3.44	3.34	2.45	1.03	1.24	1.41	0.76	2.77	0.57	1.07	1.53	2.08
Eu	1.01	1.06	0.53	0.66	0.34	0.79	0.53	1.23	1.35	0.76	0.36	0.38	0.42	0.27	0.79	0.20	0.36	0.73	1.2
Gd	2.34	2.89	1.46	1.86	0.9	2.14	1.75	3.31	4.37	2.87	1.21	1.34	1.25	0.79	1.85	<1.2	1.07	1.75	2.75
Tb	0.39	0.46	0.23	0.35	0.17	0.42	0.31	0.54	0.88	0.51	0.18	0.25	0.21	0.16	0.33	0.14	0.2	0.32	0.57
Tm	0.13	0.16	0.11	0.12	0.12	0.28	0.20	0.32	0.44	0.18	0.09	0.09	0.09	0.1	0.1	0.13	0.11	0.19	0.44
Yb	0.70	0.86	0.6	0.56	0.83	1.94	1.4	2.18	3.25	1.17	0.45	0.39	0.54	0.41	0.57	0.42	0.5	1.41	3.03
Lu	0.1	0.12	0.1	0.07	0.12	0.3	0.21	0.35	0.51	0.18	0.07	0.06	0.08	0.05	0.08	0.05	0.08	0.23	0.53
Hf	3	2.06	3.29	2.89	0.03	<0.3	0.27	2.56	0.15	2.15	3.01	2.53	3.69	3.12	2.31	3.71	3.15	0.25	0.26
Ta	0.4	0.25	0.33	0.33	<0.02	<0.02	0.05	0.74	0.04	0.32	0.32	0.25	0.42	0.35	0.32	0.43	0.36	0.04	<0.04
W	5.8	4.0	4.1	7.5	<0.9	<2.3	<0.7	2.5	<1.3	4.3	5.5	5.6	5.1	5.3	4.8	<3.2	4.9	<1.2	<2.1
Os (ppb)	<348	<411	<536	<498	<171	<268	<248	<371	<392	<379	<432	<389	<421	<484	<412	<416	<390	<299	<432
Ir (ppb)	5.09	6.83	22	9.03	<0.8	<1.4	<1.2	<2.3	1.19	5.85	4.95	4.49	6.17	4.77	7.30	5.15	5.4	<2.3	1.1
Au (ppb)	2.6	2.7	4.3	1.1	0.3	<0.8	<0.5	9.8	1.0	<1.0	<1.0	0.7	0.7	<1.2	0.5	<1.3	0.6	1.2	<1.2
Th	1.08	0.67	0.95	0.91	0.07	0.29	0.97	7.54	0.27	1.36	0.84	0.94	1.09	0.98	1.44	0.76	0.98	0.36	0.54
U	0.17	<0.3	0.42	<0.3	<0.1	<0.3	0.17	1.84	<0.3	0.33	<0.3	<0.4	<0.4	<0.4	<0.3	0.11	<0.3	<0.3	<0.4

Table 4. *Major and trace element abundances measured by XRF and INAA in all analyzed spherule layer and country rock samples. A, B and C before the sample names symbolize the different intervals. Note that XRF analyzes could not be carried out for each sample due to limited amounts of material available*

	B-SH7	B-CH2	B-SL5a	B-SL5b	B-SH8	B-CH3	B-SL6	B-SH9	B-SH10	B-SH11	B-SL7	B-SH12s	B-CH4s	B-CH5s	B-SL8	B-SL9a	B-SL9b	B-SH13	B-SH14
SiO2 (%)	20.2	75.6	52.6	33.6			62.6				47.8	90.0			52.1		46.1		
TiO2 (%)	0.03	0.05	1.61	1.61			1.20				1.85	0.14			1.72		1.86		
Al2O3 (%)	1.0	1.0	24.1	15.9			17.6				25.3	1.9			24.8		24.7		
Fe2O3 (%)	26.00	5.86	6.04	22.80			5.64				7.68	2.33			5.77		9.72		
MnO (%)	1.76	0.37	0.03	0.03			0.06				0.05	0.10			0.03		0.06		
MgO (%)	7.58	2.20	1.51	1.44			1.39				1.92	0.56			1.39		1.72		
CaO (%)	14.00	5.62	0.18	1.35			0.56				0.24	0.67			0.10		0.17		
Na2O (%)	0.16	0.04	0.14	0.15			0.17				0.12	0.03			0.15		0.14		
K2O (%)	0.36	0.32	9.12	6.14			6.77				10.00	0.80			9.55		9.40		
P2O5 (%)	0.05	0.01	0.03	0.93			0.03				0.03	<0.01			0.02		0.04		
LOI (%)	29.50	9.30	4.50	11.80			4.20				4.20	2.90			4.60		6.10		
Summe (%)	100.64	100.35	99.86	95.75			100.22				99.19	99.43			100.23		100.01		
Na	56	60.7	747	453	92.4	52.4	816	424	105	142	813	73.13	70.1	95.1	852	1122	643	379	61
K (wt%)	0.24	0.24	7.58	5.05	0.54	0.2	5.86	6.09	0.58	1.24	8.93	361.04	0.30	0.79	8.41	8.50	7.80	<4.0	803.80
Sc	20.1	6.54	13.2	17.6	22.9	6.04	10.0	13.2	17.4	18.9	16.2	4.96	16.4	2.31	15.4	15.8	17.1	12.8	3.0
Cr	35.6	41	896	6862	56.3	34.1	753	5028	74.7	90.4	449	38.35	49.6	47.0	394	385	1814	8690	11
Fe (wt%)	17.2	3.96	4.12	16.0	12.6	7.48	4.10	8.38	9.8	9.16	5.16	6.17	12.2	2.73	3.80	3.30	6.45	13.2	3.2
Co	31.9	11.8	41.7	528	58.3	72	47.5	150	21.1	46.7	76.2	6.95	101	10.4	49	33.7	67.6	357	76
Ni	566	188	1097	16024	3048	2452	1221	3940	360	436	959	152.59	633	2331	868	574	1575	13995	1595
Zn	1978	139	240	1183	1136	425	232	178	275	911	82	71.27	603	901	146	311	517	2144	62
Ga	25	3	15	354	34	6	16	14	19	15	16	4.62	39	3	16	12	12	157	5
As	3.07	2.29	12.2	101	3.41	0.52	3.63	6.28	5.56	20.6	42.6	0.88	5.55	0.06	26.4	7.49	8.22	25.8	0.7
Se	6.77	<1.3	5.76	<0.3	16.9	17.5	8.08	23.7	1.96	6.8	3.39	<0.12	6.70	12.2	6.18	5.34	12	69.3	5.1
Br	<0.3	0.3	0.2	206	<0.4	0.3	0.2	<0.2	0.1	0.3	0.2	0.30	<0.3	0.2	<0.7	<0.7	<0.7	<2	<0.4
Rb	16.7	9.87	265	<67	29.8	9.44	184	240	45.7	54.1	292	13.16	23.2	27.1	221	181	237	110	<14
Sr	<56	<25	<37	<80	<35	<34	<33	<48	<44	<30	<42	<24	<45	<30	<31	<35	<44	<77	<29
Zr	<75	<34	90	13.8	<45	<43	76	187	<62	<41	113	<38	<64	<29	97.7	83.2	115	2324	<45
Sb	0.39	0.2	0.62	9.77	1.45	0.55	0.54	1.44	0.68	1.48	0.67	185.39	1.14	0.99	0.7	1.14	1.45	12.3	0.7
Cs	0.87	0.53	7.63	113	1.52	0.54	5.28	9.39	3.79	3.01	8.35	0.20	1.99	0.78	4.93	4.56	7.61	6.58	0.20
Ba	<44	<8.8	88	31.7	<41	<12	63	93	<34	12	98	1.04	<37	8	81	68	68	186	<17
La	4.17	2.59	1.2	86.5	5.03	2.59	1.78	8.18	5.69	9.95	1.75	7.29	4.14	0.98	1.18	4.12	1.18	254	1
Ce	9.86	5.14	3.51	44.8	10.2	5.3	4.75	24.6	10.9	19.1	4.59	1.87	8.16	1.77	3.01	8.7	2.93	514	2
Nd	5.88	1.98	1.93	12.7	5.44	2.95	2.23	14.0	5.58	9.58	3.01	3.38	4.24	<1.3	2.06	5.42	<3.6	305	1
Sm	1.32	0.54	0.74	6.09	1.73	0.76	0.69	3.06	1.64	2.82	1.26	2.95	1.18	0.33	0.82	1.68	0.54	87.4	0.3
Eu	0.94	0.37	0.37	14.5	0.92	0.64	0.35	1.7	0.84	1.29	0.4	0.45	0.68	0.19	0.26	0.48	0.30	35.8	0.2
Gd	n.d.	n.d.	0.31	3.17	0.44	n.d.	0.17	0.85	1.92	n.d.	1.61	0.32	1.57	n.d.	0.83	1.92	0.15	123	0
Tb	0.4	0.2	0.31	0.90	0.37	0.25	0.19	0.40	0.39	0.78	0.25	1.24	0.32	0.09	0.17	0.28	0.11	21.8	0.1
Tm	0.31	0.21		4.53		0.23	0.45		0.28	0.60	0.19	0.20	0.32	0.17	0.09	0.11		6.48	0.18
Yb	1.86	1.05	0.52	0.59	1.9	0.99	1.96	1.71	1.90	3.47	0.64	0.19	1.77	0.25	0.39	0.67	0.55	34.9	0.5
Lu	0.34	0.18	0.08	1.86	0.31	0.17	0.22	0.22	0.3	0.53	0.09	0.63	0.3	0.04	0.06	0.10	0.08	4.2	0.1
Hf	<0.2	0.06	2.72	<0.05	0.27	0.08	2.6	3	0.37	0.37	3.36	0.11	0.23	0.30	2.85	0.29	2.91	0.84	<0.1
Ta	<0.03	<0.02	0.31		0.06	<0.02		0.44	0.10	0.05	0.42	0.12	0.05	0.04	0.3	0.11	0.29	<0.1	<0.03
W	0.4	<0.4	3	1.6	<1.4	<0.4		2.5	<0.9	0.6	4.5	<0.04	<1.2	0.4	<2.6	5.4	<2.8	3.8	<1.6
Os (ppb)	<309	<215	<336	1858	<340	<250	<290	<395	<304	<342	<267	<0.3	<289	<219	<158	<157	<257	<581	<227
Ir (ppb)	<2.3	<2.0	10.8	2068	<1.5	0.76	8.68	587	<2.2	0.97	6.12	<209	<2.1	0.76	5.01	8.50	72.9	2832	<1.2
Au (ppb)	1.3	<0.4	<0.6	25	3.9	1.0	0.6	2.2	1.6	5.7	<0.6	0.59	1.9	0.9	<1.1	<1.1	<1.2	32	<0.7
Th	0.23	0.05	0.82	1.27	0.49	0.06	0.67	0.91	1.04	0.74	1.02	0.45	0.58	0.11	0.88	1.12	0.83	0.46	<0.1
U	<0.3	<0.1	0.5	1.06	<0.3	<0.2	0.21	0.58	0.26	<0.3	<0.2	0.42	0.08	0.03	<0.4	<0.4	<0.4	3.76	<0.2

Table 4. *continued*

113

	B-SL10s	B-SH15	B-SH16	B-SH17	B-SL11	B-SH18	B-CH6s	B-SL12a	B-SL12b	B-SH19s	B-SL13	B-CH7	B-CH8	B-SL14a	B-SL14b	B-SL14c	B-SL15s	B-SH20	C-SH21
SiO2 (%)	46.0			40.8	49.2	52.9			59.2	31.5	56.1	91.4		52.0		50.7	45.6		42.9
TiO2 (%)	1.48			0.14	1.50	0.28			1.22	1.02	1.48	0.06		1.87		1.66	2.30		0.09
Al2O3 (%)	21.5			4.4	24.1	6.5			17.1	10.5	22.8	1.1		23.5		25.4	26.0		2.1
Fe2O3 (%)	11.70			22.90	9.15	12.10			8.81	30.10	5.33	1.96		6.44		6.74	8.91		9.08
MnO (%)	0.04			1.31	0.03	0.49			0.05	0.04	0.03	0.08		0.03		0.03	0.04		0.86
MgO (%)	2.14			4.01	2.11	3.33			1.52	1.29	1.33	0.56		1.48		1.39	1.86		6.30
CaO (%)	1.50			4.13	0.09	6.36			0.22	2.50	0.13	1.33		0.08		0.08	0.10		15.60
Na2O (%)	0.14			0.15	0.11	0.07			0.10	0.16	0.17	0.04		0.20		0.16	0.13		0.09
K2O (%)	8.44			1.36	9.50	2.59			6.34	3.84	8.48	0.44		9.49		9.26	9.45		0.73
P2O5 (%)	0.98			0.13	0.02	0.09			0.06	1.72	0.03	<0.01		0.02		0.03	0.05		0.12
LOI (%)	6.10			19.80	4.10	14.50			5.20	12.80	4.10	2.10		4.20		4.20	5.00		22.40
Summe (%)	100.02			99.13	99.91	99.21			99.82	95.47	99.98	99.07		99.31		99.65	99.44		100.27
Na	577	160	42	94.9	577	193	196	126	402	439	1010	57.8	203	1287	991	1026	818	163	107
K (wt%)	7.68	2.10	<0.1	0.71	8.36	1.46	1.04	1.48	5.31	3.51	7.50	0.19	2.55	7.78	7.4	8.26	8.85	2.11	0.63
Sc	18.9	16.9	1.9	13.9	17.4	31.1	33.9	7.83	16	14.7	13.9	1.4	17.9	14.8	16.1	14.7	18.4	26.0	38.3
Cr	2099	962	16	76.8	365	147	112	132	2290	9161	925	17.6	190	361	419	408	466	144	108
Fe (wt%)	7.9	11.8	2.2	15.9	6.22	8.83	9.26	10.2	5.85	21.3	3.67	1.14	16.7	4.07	3.84	4.78	5.83	5.45	6.13
Co	99	56	2	97.2	47.9	54.8	54.7	302	94	652	54.5	3.98	166	34.4	28.7	99.1	31.7	28.8	57.4
Ni	2141	4437	24	453	503	694	854	7645	2188	20213	1098	46	5058	627	542	1451	806	615	1049
Zn	794	1210	143	3177	230	985	694	676	448	1649	89	45	513	67	73	58	73	668	627
Ga	6	9	4	66	28	29	38	40	33	93	11	1.5	24	6.7	7.3	8.8	28	2.7	18
As	22.1	1.0	0.3	161	26.4	86.7	29.8	0.75	47.8	29.0	25.4	1.72	0.94	16	14.7	54.3	4.78	<0.8	0.25
Se	16.4	25.9	0.7	15.6	2.17	7.91	6.23	48.4	15.7	147	7.23	<0.9	24.6	2.69	1.3	6.17	2.41	2.6	11.8
Br	<0.7	<0.6	0.31	<1.1	<0.8	<1.1	<1	<0.8	<0.9	<0.5	0.1	0.3	<0.3	0.2	0.3	0.2	<0.4	<0.5	<0.4
Rb	242	78	4	38.3	260	87.4	53.7	78.2	192	159	213	4.95	102	221	227	224	304	110	23.2
Sr	<54	<50	<16	<48	<34	<46	<47	<55	<37	<55	<41	<16	<54	<38	<39	<41	<46	<43	<57
Zr	344	111	<26	<78	91.8	<80	134	<85	103	<65	85	<20	<71	90	94	83	122	<78	<78
Sb	2.6	1.9	0.2	3.16	1.05	2.49	1.8	2.44	2.58	13.6	0.57	0.15	1.76	0.56	0.67	0.55	1.03	0.82	3.11
Cs	11.07	3.91	0.22	1.76	11.0	6.05	3.57	5.49	7.72	8.26	5.8	0.21	4.55	5.78	5.84	5.43	9.57	4.95	0.56
Ba	96	21	<8.7	<22	84	27	<45	<34	57	155	59	<11	<43	71	69	62	78	<54	<12
La	24	5	1	5.17	1.58	6.81	7.68	2.57	2.63	39.3	1.66	0.52	5.15	0.75	1.27	1.44	0.85	5.94	6.47
Ce	59	11	3	11.7	4.35	15.3	14.9	5.35	7.85	95.4	4.5	1.13	11.2	2.09	3.23	3.94	2.13	13.1	12.4
Nd	34	6	1	8.96	3.53	9.35	7.86	3.18	3.76	52.1	1.92	0.07	7.2	0.02	<2.2	1.99	<2.1	10.4	5.97
Sm	8.9	1.8	0.3	2.93	1.2	3.3	2.35	0.98	1.22	15.2	0.81	0.14	2.31	0.58	0.72	0.97	0.50	2.41	1.58
Eu	4.1	1.3	0.2	1.01	0.35	1.12	1.09	0.59	0.50	7.18	0.38	0.09	1.29	0.22	0.25	0.33	0.23	0.80	0.96
Gd	10	2	1	3.22	1.39	3.58	2.08	1.42	1.8	17.9	<1.2	<0.5	2.82	0.78	0.81	<1.1	<1.1	2.64	1.81
Tb	2.0	0.6	0.1	0.57	0.21	0.71	0.39	0.27	0.31	3.29	0.18	0.04	0.59	0.15	0.14	0.18	0.13	0.44	0.33
Tm	0.72	0.33	0.09	0.24	0.1	0.35	0.34	0.11	0.12	0.98	0.31	<0.02	0.31	0.22	0.19	0.19	0.31	0.25	0.36
Yb	3.6	1.9	0.4	1.5	0.65	2.26	2.38	0.77	0.50	5.73	0.47	0.03	1.6	0.44	0.34	0.35	0.69	1.62	2.11
Lu	0.5	0.3	0.1	0.22	0.11	0.34	0.40	0.12	0.08	0.73	0.07	0.03	0.26	0.08	0.06	0.05	0.12	0.24	0.34
Hf	2.28	0.79	0.03	0.18	2.75	0.69	0.46	0.46	1.89	1.13	2.44	0.02	0.97	2.85	3.28	2.81	3.78	0.61	0.33
Ta	0.39	0.13	<0.02	<0.1	0.32	0.14	0.16	0.06	0.36	<0.04	0.29	<0.01	<0.03	0.36	0.41	0.32	0.55	0.1	0.08
W	2.3	<2.0	<0.8	<3.3	4	<3.6	<3.8	<2.7	1.9	1.6	2.4	<0.3	0.8	2.9	3.0	3.5	3.6	<2	<2.0
Os (ppb)	1332.97	<508	<111	<115	<203	<238	<241	<205	358	2413	<217	<106	<289	<203	<212	<224	<211	<539	<71
Ir (ppb)	649	68	2	<2.3	4.65	<2.8	12.9	2.05	443	2619	12.5	0.49	2.51	3.81	4.83	4.28	7.08	<2.5	22.8
Au (ppb)	6	2	0	3.9	<1.3	2.1	3.8	2	5	32	0.9	0.4	2.5	0.8	1	0.9	1.1	<1.7	7.6
Th	1.11	0.53	<0.1	0.67	0.94	1.56	1.24	0.32	0.65	0.95	0.76	<0.05	0.6	0.88	0.88	0.88	0.86	0.97	0.64
U	0.67	<0.3	<0.1	<0.5	<0.4	<0.5	0.34	<0.4	0.45	1.40	0.41	<0.1	<0.3	0.15	0.27	<0.3	0.53	<0.6	0.31

Table 4. *continued*

	C-SH22	C-SL16a	C-SL16b	C-SL16c	C-SH23	C-SH24	C-CH9	C-SL17a	C-SH25	C-SL17b	C-SL17c	C-SH26
SiO2 (%)		59.8	54.7		60.3	36.7		56.0		56.0		54.1
TiO2 (%)		1.25	1.71		0.10	0.13		1.77		1.52		0.19
Al2O3 (%)		20.8	24.4		2.7	2.3		22.9		23.5		2.6
Fe2O3 (%)		1.34	1.91		5.91	10.60		2.20		2.26		27.50
MnO (%)		0.01	<0.01		0.64	1.01		0.01		0.01		0.02
MgO (%)		0.72	1.12		4.16	6.92		0.93		1.20		0.23
CaO (%)		0.30	0.08		10.50	17.10		0.12		0.20		0.41
Na2O (%)		0.19	0.12		0.05	0.12		0.19		0.22		0.11
K2O (%)		12.70	12.50		0.70	0.81		11.70		10.50		0.94
P2O5 (%)		0.07	0.02		0.03	<0.01		0.02		0.03		0.20
LOI (%)		2.60	3.00		15.30	24.70		3.40		4.00		10.90
Summe (%)		99.78	99.56		100.39	100.43		99.24		99.44		97.20
Na	692	1028	684	283	84.9	77.1	67.5	1283	298	1161	593	91.6
K (wt%)	8.51	11.2	10.8	3.52	0.52	0.29	0.51	10.5	3.65	9.44	7.25	0.87
Sc	22.8	10.8	15.9	11.8	20.1	36.8	2.9	14.6	13.2	19.5	20.2	3.86
Cr	1040	322	409	195	58.5	39.7	35.3	393	133	680	8402	1689
Fe (wt%)	1.16	0.85	1.22	0.88	4	7.55	0.51	1.41	0.86	1.48	10.3	19.0
Co	14.7	50.2	71.5	51.4	18.4	15.2	3.81	66.6	31.1	28.5	335	721
Ni	220	586	764	328	230	157	77	846	324	545	8651	21692
Zn	247	1121	42	32	437	489	19	235	114	354	497	1984
Ga	4.6	1.8	4.8	0.8	2.2	3.8	<0.7	3.8	1.0	6.4	18	26
As	1.69	36.3	65.3	48.3	5.48	7.05	0.9	41.3	6.23	2.24	6.55	11.1
Se	2.12	6.40	3.47	1.44	2.75	7.11	0.51	5.74	2.65	5.29	60.9	156
Br	<0.6	0.2	<0.4	<0.3	0.3	0.3	0.3	0.2	0.3	<0.2	<0.3	<0.4
Rb	304	220	254	115	23.6	11.4	20.2	259	93.9	246	266	37.6
Sr	<29	<39	<40	<13	<51	<36	<13	<37	<23	<42	<49	<51
Zr	94	102	96	62	<67	<49	<23	95	56	92	207	<58
Sb	0.56	0.94	0.74	0.85	1.15	1.09	0.44	0.97	0.77	0.73	4.38	26.8
Cs	6.38	3.24	4.60	2	0.57	0.37	0.38	4.48	1.58	4.87	7.01	0.72
Ba	40	58	60	<32	7	<47	4	67	<37	40	49	37
La	0.83	2.68	1.03	0.84	4.24	5.40	0.74	1.13	1.96	1.10	5.02	7.04
Ce	2.41	7.92	2.72	1.84	8.80	11.3	1.95	3.21	5.53	3.60	14.7	17.9
Nd	<2.4	5.48	1.99	<1.9	4.57	4.47	0.99	2.08	3.30	2.5	8.44	11.5
Sm	0.46	2.04	0.77	0.25	1.36	1.88	0.30	0.89	1.46	0.91	2.72	3.09
Eu	0.35	0.63	0.28	0.14	0.67	1.07	0.12	0.31	0.46	0.38	1.33	1.64
Gd	<1.3	2.32	0.72	<0.5	1.57	2.65	0.17	1.01	1.74	1.19	3.58	4.16
Tb	0.12	0.34	0.11	0.06	0.32	0.44	0.03	0.16	0.23	0.18	0.69	0.81
Tm	0.12	0.17	0.24	0.05	0.31	0.34	0.02	0.25	0.07	0.26	0.42	0.42
Yb	0.48	0.55	0.36	0.22	1.79	3	0.15	0.39	0.44	0.38	0.84	0.9
Lu	0.09	0.08	0.05	0.04	0.30	0.5	0.02	0.06	0.08	0.06	0.11	0.10
Hf	3.53	1.95	2.91	1.43	0.31	0.20	0.13	2.77	0.84	2.52	2.48	0.26
Ta	0.36	0.23	0.36	0.19	<0.03	<0.02	<0.01	0.34	0.11	0.28	0.45	0.28
W	1.9	1.2	2.3	2.7	<0.4	<0.7	<1.0	2.2	0.4	1.4	<1.0	<1.1
Os (ppb)	<572	<187	<214	<137	<102	<294	<192	<188	<384	<249	362	629
Ir (ppb)	9.61	4.97	5.12	2.5	<2.3	<1.5	<0.9	4.24	2.02	8.17	602	563
Au (ppb)	<8.4	0.9	0.5	<0.9	3.3	1.8	<0.2	0.6	0.8	1.2	5.6	52
Th	0.70	0.62	0.94	0.45	0.59	0.39	0.11	1	0.53	0.81	0.97	0.32
U	0.41	0.08	<0.3	<0.2	0.02	<0.3	<0.2	0.13	<0.4	0.29	0.68	0.39

Table 4. *continued*

115

Table 5. *Spherule layer classification based on character of spherule interior and groundmass features.*

CT3	A-SL1, A-SL2	B-SL3, B-SL4, B-SL5, B-SL7, B-SL8, B-SL9, B-SL11, B-SL14	C-SL15, C-SL16, C-SL17
Spherule composition	K/Al-rich and Al-rich	K-rich, K/Al- rich and Al-rich	K-rich
Spherule shape	Deformed (flattened, sheared)	Deformed (sheared) and undeformed	Deformed (crushed, for C-SL16 and 17) and undeformed
Textural features	Intersertal, barred, zoned	Zoned, Intersertal	Zoned, barred
Groundmass type	Fine-grained sericitic	Fine-grained sericitic and shale (B-SL3, B-SL5 and B-SL9a)	Fine-grained sericitic and shale (contains some undeformed spherules)

CHAPTER 4. HIGHLY SIDEROPHILE ELEMENT (HSE) CONCENTRATIONS AND [187]Re-[187]Os SIGNATURES OF THE CT3 DRILL CORE SPHERULE LAYERS FROM THE BARBERTON GREENSTONE BELT, SA

4.1. Introduction

In chapter 3 I present the evidence of impact origin for CT3 spherule layers, such as petrographic features and very high HSE components. The work described in this chapter is complementary to the petrographic and geochemical work on the CT3 spherule layers, in order to determine the presence of a meteoritic component by using Os isotopic signatures and their relations with HSE compositions. In this chapter, the results of the Os isotopic ratios and HSE concentrations available so far are presented. Further work is in progress.

Highly siderophile element abundances (as well as the Cr, Co, Ni concentrations) were obtained for other Paleoarchean spherule layers from the BGB before (see below for a description of previous spherule layer findings in the BGB). The obtained concentrations in some of the spherule layer samples were shown to be higher than chondritic values, arguing for meteoritic components of up to and slightly more than 100%. This would contrast with meteoritic admixtures usually measured for impactites from more recent impact events by orders of magnitude. Reimold et al. (2000), based on detailed geochemical observations, therefore, argued that hydrothermal or otherwise secondary enrichments of these elements are the possible cause for the observed elemental abundances (rather than meteoritic admixtures alone). However, the interpretation of the HSE concentrations in spherule layers remained difficult and this study aims to shed more light on this topic by analyzing samples from the recently recovered CT3 drill core.

The focus of the present study is the determination of certain elemental abundances (HSE) and ^{187}Os/^{188}Os isotope signatures of Archean spherule layers from the CT3 drill core (Barberton Greenstone Belt, South Africa), to confirm the presence of a meteoritic signature in the CT3 spherule layers.

4.2. Samples and Methods

In total, 15 samples were analyzed for ^{187}Os/^{188}Os isotope ratios 9 for spherule layer (Fig. 4.1) and 6 for country rock samples. Six of them, four spherule layer and two country rock samples (SL5, SL6, SL7, SL8 and SH11, SH12s), were also investigated by obtaining isotope dilution generated HSE concentrations (Table 4.1.). Additional Ir concentration data were obtained by using INAA. All methods are explained in detail and details about sampling can be found in Chapter 2.

It is important to note that the spherule-free layers (but intercalated with spherule layers, see chapter 3) are termed "country rocks" through this chapter and they belong to Fig Tree Group; in addition, other non-spherule related sediments (shales, black shales, graywackes, cherts, and jaspilites, Hofmann 2005) examined in previous studies (e.g., Siebert et al. 2005) that were used for comparison, are called "Fig Tree sediments".
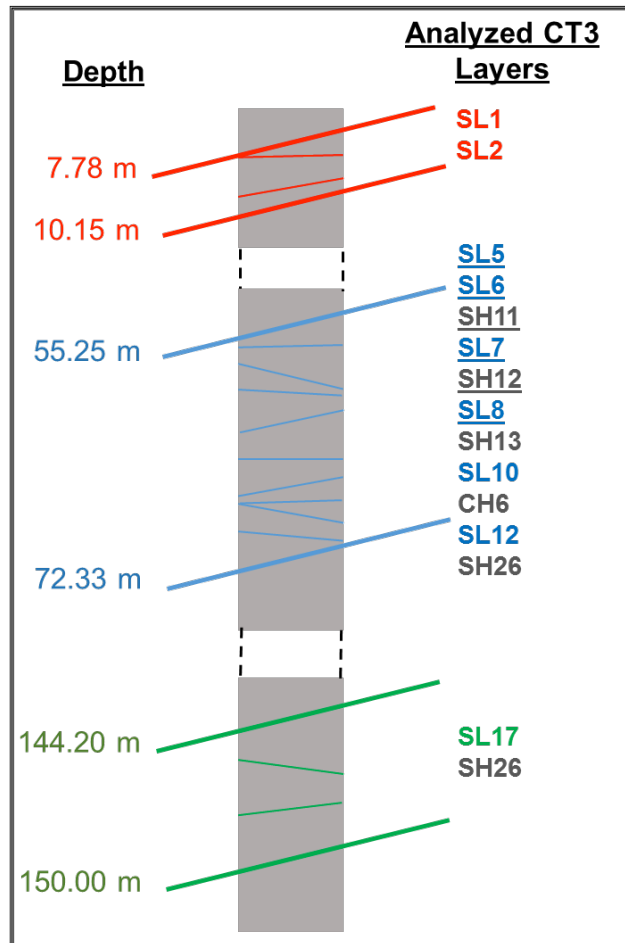
Figure 4.1. *Schematic diagram of the CT3 drill core. The samples analyzed by isotope dilution (underlined) and INAA are shown in three different depth intervals (SL: spherule layer, SH: shale, CH: chert).*

4.3. Results

Preliminary data of present day ^{187}Os/^{188}Os isotope ratios and HSE concentrations for these samples are provided in Table 4.1.

| Layer	Depth	$^{187}Os/^{188}Os$	2σ error	*Os (ppb)	*Ir (ppb)	*Ru (ppb)	*Pt (ppb)	*Pd (ppb)	*Re (ppb)	Ir (ppb) INAA
SL1b	7.78-7.79	0.1529	0.0044	13.1						6.8
SL2	9.95-10.15	0.1280	0.0005	86.2						9.0
SL5b	65.40-65.43	0.1137	0.0003	4312	1931		3778	4705	57.4	2068
SL6	66.38-66.40	0.1668	0.0012	2.9	<0.1	0.7	1.7	3.1	0.2	8.7
SH11	66.56-66.62	1.1265	0.0090	0.3	47.6	165	192	30.1	4.7	1.0
SL7	66.56-66.63	0.1338	0.0004	2.9	0.1	0.3	1.4	0.2	0.2	6.1
SH12s	66.68-66.71	0.2139	0.0022	0.1	3.9	10.8	16.1	5.2	0.1	<296
SL8	69.35-69.37	0.1128	0.0001		53.0	99.8	169	71.8	1.1	72.9
SH13	69.37-69.38	0.1083	0.0001	2255						2832
SL10s	70.12-70.15	0.1428	0.0016	942						749
CH6s	71.83-71.86	0.3263	0.0003	18.5						12.9
SL12a	71.86-71.88	0.1323	0.0003	404						443
SH19s	72.08-72.09	0.1258	0.0003	2140						2619
SL17	149.76-149.78	0.1116	0.0002	585						602
SH26	149.80-149.82	0.1880	0.0007	368						563

Table 4.1. *The HSE concentrations and $^{187}Os/^{188}Os$ isotope ratios for spherule layer (SL) and country rock (SH: shale, CH: chert) samples from the CT3 drill core. The letters (a to e) after the sample name are used to discriminate different parts of an individual layer. The letter s at the end indicates sulfide admixture in a sample. *Data obtained by isotope dilution.*

4.3.1. Highly siderophile elements

In this study, preliminary HSE concentration data were obtained for four spherule layers and two country rock samples.

The results are plotted as CI chondrite-normalized (Palme and Jones 2003) abundances in Figure 4.2. The figure shows fractionated HSE patterns. Except for one sample (SL5b), which exhibits super-chondritic values, both spherule layers and country rocks exhibit sub-chondritic values. Ir concentrations vary between 0.02 up to 1931 ppb; Os contents vary from 0.1 to 4312 ppb. Notably, Os is enriched in spherule layers by up to two orders of magnitude compared to Fig Tree sediments. The both layers groups from CT3 show a fractionated pattern comparable to sedimentary rocks from the Fig Tree Group (from ~0.01 to Siebert et al. 2005).

Only Ru and Pt values present enrichments for each sample compared to Fig Tree samples, mostly to supra-chondritic abundances, and are orders of magnitudes higher than those in Fig Tree sediments; the values range from 0.2 to 165 ppb for Ru and from 1 to 3777 ppb for Pt. The other HSE abundances range from 0.1 to 4704 ppb for Pd and 0.1 to 57 ppb for Re. The intercalated country rock samples plot between the minimum and maximum HSE abundances of spherule layers.
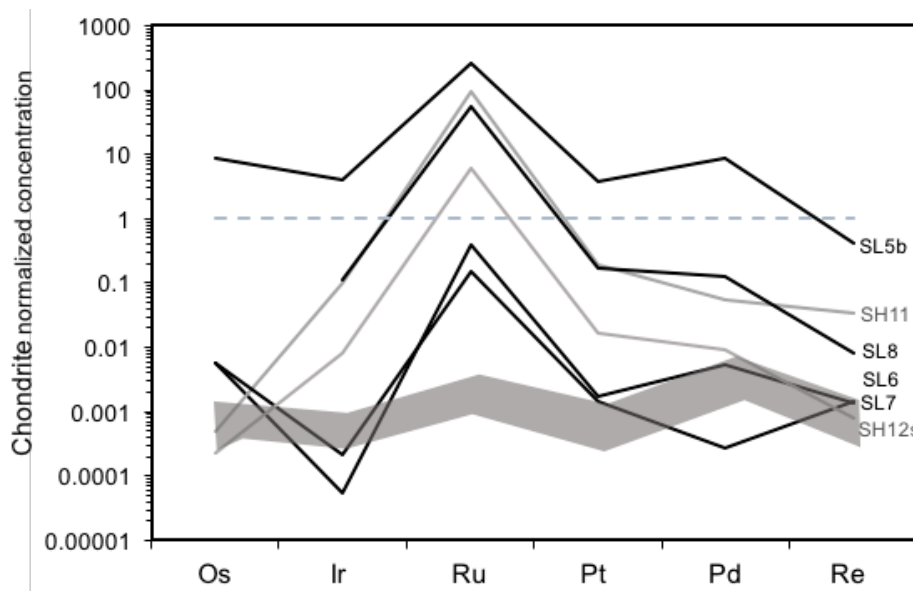
Figure 4.2. *HSE patterns for some of the CT3 layers normalized to CI values of Palme and Jones (2003). Analyzed spherule layers are shown as black lines, gray lines show the analyzed country rock samples and the gray area is for Fig Tree sediments from the BGB (Siebert et al. 2005).*

Considering Ir/Os ratios, most of the spherule layer samples exhibit a trend between the Fig Tree sediments and chondritic values, and this trend point towards super-/chondritic values (Fig. 4.3). Notably, some samples (SL5b, SL10s, SL12, SL17c, including country rock samples SH13, SH19s, and SH26) are very enriched in Ir and Os, either exceeding chondritic values (by more than half an order of magnitude) or plotting within the range of chondritic values.
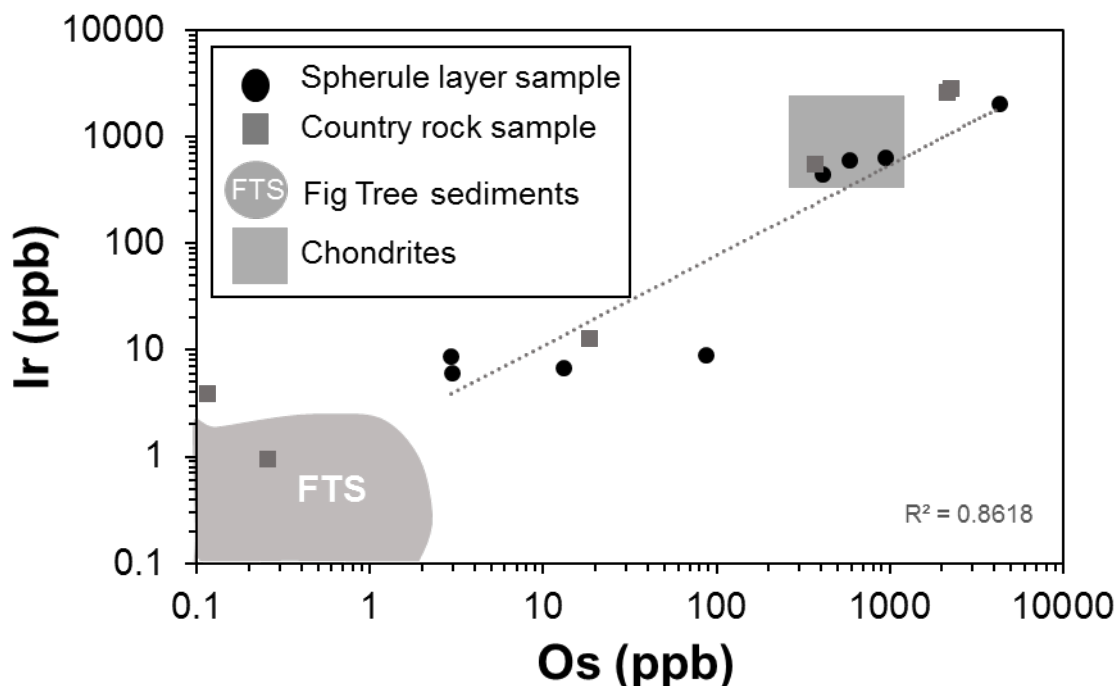
Figure 4.3. *Osmium vs. Ir (R^2=0.86) interelement diagram for CT3 layers, Fig Tree sediments (data from Siebert et al. 2005) and chondrites (data from Tagle and Berlin 2008). The samples with the lowest concentrations in Ir and Os plot in the region of Fig Tree sediments (Siebert et al. 2005) and high Ir and Os CT3 samples plot in the range of chondrites (R^2 is correlation factor). The concentration of Os was derived by isotope dilution, Ir by INAA.*

As noted in Table 4.1, Os concentrations were derived by isotope dilution, but most of the Ir concentration were obtained by using INAA. This may cause some comparison problems as different sample sizes were used, which, considering the nugget effect (that is particularly problematic for trace elements such as the PGE) may be responsible for the different results obtained by these two methods. This can be explained by an inhomogeneous distribution of the spherules and the HSE carrier phases (e.g., Ni-rich chromites, cf. Mohr-Westheide et al. 2015) within the sample aliquot, which were analyzed by the different analytical methods.

4.3.2. The ^{187}Re-^{187}Os isotope systematics

Spherule layer samples and those without spherules mostly behave complementary with respect to their ^{187}Os/^{188}Os ratios: whereas samples without spherules typically exhibit radiogenic ^{187}Os/^{188}Os values (up to ~1.4) in conjunction with low Ir concentrations (~1-5 ppb), spherule layer samples are less radiogenic (^{187}Os/^{188}Os between 0.11 and 0.16), with Ir concentrations of up to ~1930 ppb. Although the general pattern does not present a clear dichotomy between spherule layer and country rock samples, each country rock sample exhibits relatively radiogenic ratios compared to the nearest spherule layer (Fig. 4.4). Additionally, the Ir abundances of country rocks are low, except for two samples (SH19s and SH26) that contain some spherule contamination due to limited sample separation and which do not fit the general pattern.
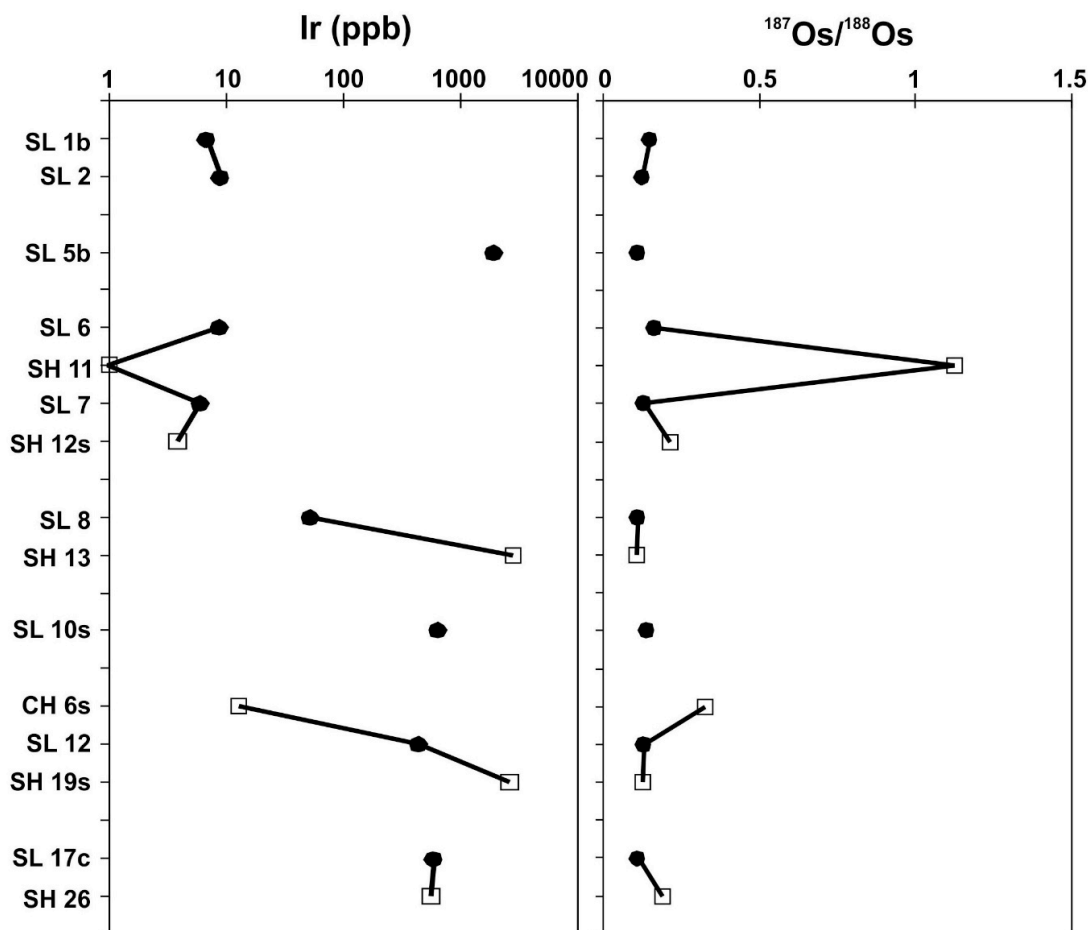
Figure 4.4. *Peak concentrations for Ir (up to 2619 ppb) and ^{187}Os/^{188}Os ratios (1.13) can be observed in both, spherule layers and country rocks (Dark circles for spherule layer samples, squares for country rock samples). Ir concentrations were obtained by INAA.*

Notably, typical ^{187}Os/^{188}Os ratios for non-spherule related sediments from the Fig Tree Group reported in the literature are significantly more radiogenic compared to the intercalations from the CT3 spherule layer section and range

122

from ~0.37 to ~0.79 (Siebert et al. 2005) (Fig. 4.5). The investigated spherule layers of the CT3 core exhibit ^{187}Os/^{188}Os ratios ranging from 0.1116 to 0.1668 for spherule layers, from 0.1083 to 1.1265 for country rocks.

The least radiogenic ^{187}Os/^{188}Os ratio reported for sediments from any other sedimentary units within the Barberton Greenstone Belt (Moodies Group, Manjeri Formation) is ~0.29 (Siebert et al. 2005), thus, no country rock values are comparable to the less radiogenic ^{187}Os/^{188}Os ratios for the CT3 spherule layers. The only lithologies in the Barberton Area that have comparably low ^{187}Os/^{188}Os isotope compositions are volcanic rocks, such as komatiites, which are unrelated to the CT3 spherule layers and range from ~0.1048 to ~0.1970 (Puchtel et al. 2009, 2014 and Connolly et al. 2011).
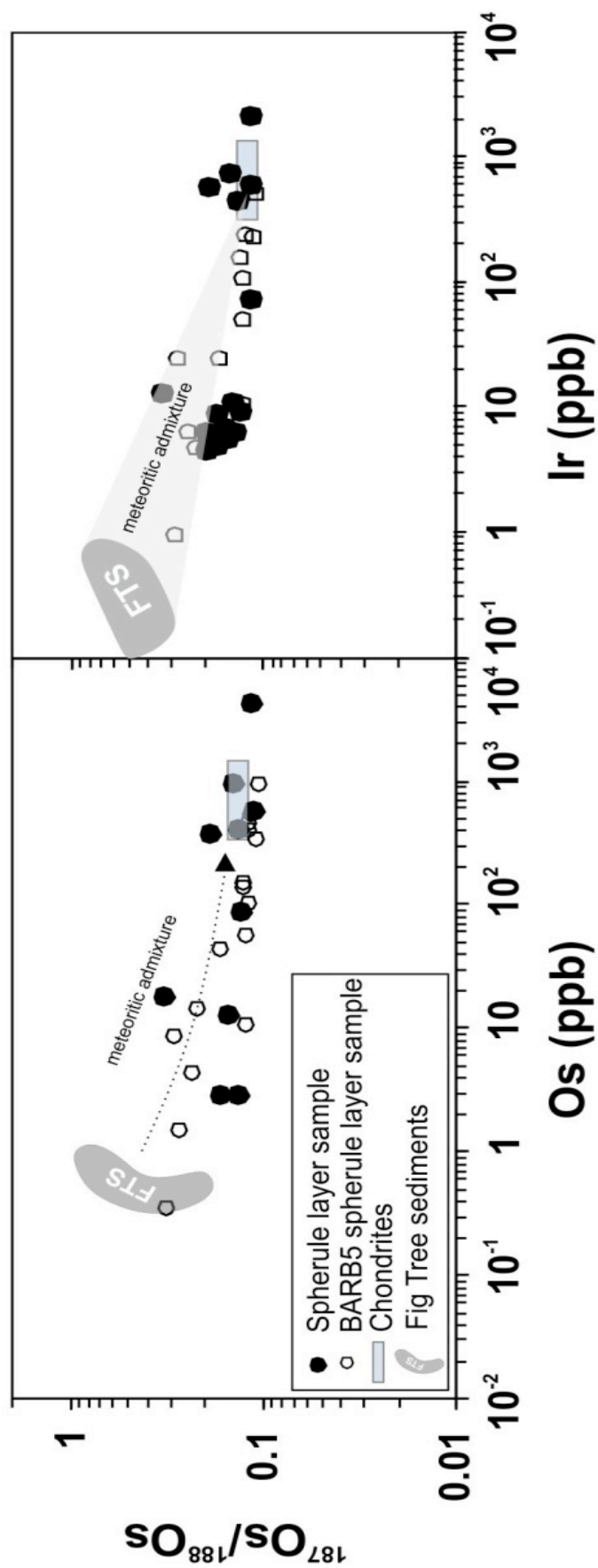
Figure 4.5. Diagrams of $^{187}Os/^{188}Os$ vs. Os and $^{187}Os/^{188}Os$ vs. Ir, showing a continuous trend towards less radiogenic Os isotope compositions with increasing (closer to chondritic values) Os and Ir concentrations. Data for non-impact-related Fig Tree Group sediments are from Siebert et al. (2005). Chondrite data from Taqle and Berlin (2008).

References

Connolly B. D., Puchtel I. S., Walker R. J., Arenalo Jr. R., Piccoli P. M., Byerly G., Robin-Popieul C. and Arndt N. 2011. Highly siderophile element systematics of the 3.3 Ga Weltevreden komatiites, South Africa: Implications for early Earth history. Earth and Planetary Science Letters 311:253-263.

Hofmann A. 2005. The geochemistry of sedimentary rocks from the Fig Tree Group, Barberton greenstone Belt: Implications for tectonic, hydrothermal and surface processes during mid-Archean times. Precambrian Research 143, 23-49.

Mohr-Westheide T., Reimold W. U., Fritz J., Koeberl C., Salge T., Hofmann A. and Schmitt R. T. 2015. Discovery of extraterrestrial component carrier phases in Archean spherule layers: Implications for estimation of Archean bolide sizes. Geology 43:299-302.

Palme H. and Jones A. 2003. Solar System Abundances of the Elements. In: Treatise on Geochemistry: Holland H. D. and Turekian K. K. (Eds.), Elsevier, Amsterdam. p. 41-61.

Puchtel I. S., Walker R. J., Anhaeusser C. R. and Gruau G. 2009. Re-Os isotope systematics and HSE abundances of the 3.5 Ga Schauenburg komatiites, South Africa: Hydrous melting or prolonged survival of primordial heterogeneities in the mantle? Chemical Geology 262:355-369.

Puchtel I. S., Walker R. J., Touboul M., Nisbet E. G. and Byerly G. R. 2014. Insights into early Earth from the Pt-Re-Os isotope and highly siderophile element abundance systematics of Barberton komatiites. Geochimica et Cosmochimica Acta 125:394-413.

Reimold W. U., Koeberl C., Johnson S. and McDonald I. 2000. Early Archean Spherule Beds in the Barberton Mountain Land, South Africa: Impact or Terrestrial Origin? In: Impacts and the Early Earth (Eds. I Gilmour and C. Koeberl), Lecture Notes in Earth Sciences 91, Springer Verlag, Heidelberg, p. 117-180.

Siebert C., Kramers J. D., Meisel T., Morel P. and Nägler T. F. 2005. PGE, Re-Os, and Mo isotope systematics in Archean and early Proterozoic sedimentary systems as proxies for redox conditions of the early Earth. Geochimica Cosmochimica Acta 69: 1787-1801.

Tagle R. and Berlin J. 2008. A database of chondrite analyses including platinum group elements, Ni, Co, Au, and Cr: Implications for the identification of chondritic projectiles. Meteoritics and Planetary Science 43:541-559.

CHAPTER 5. NEW INSIGHTS INTO THE PALEOARCHEAN METEORITE BOMBARDMENT OF THE EARTH - GEOCHEMISTRY AND RE-OS ISOTOPE SIGNATURES OF THE BARB5 ICDP DRILL CORE FROM THE BARBERTON GREENSTONE BELT, SOUTH AFRICA

New insights into the Paleoarchean meteorite bombardment of the Earth - Geochemistry and Re-Os isotope signatures of the BARB5 ICDP drill core from the Barberton Greenstone Belt, South Africa

Toni SCHULZ[1*], Christian KOEBERL[1,2], Ambre LUGUET[3], David VAN ACKEN[3,4], Tanja MOHR-WESTHEIDE[5,6], Seda OEZDEMIR[1], Wolf Uwe REIMOLD[5,7,8]

[1] Department of Lithospheric Research, University Vienna, Althanstrasse 14, 1090 Vienna, Austria
[2] Natural History Museum, Burgring 7, A-1010 Vienna, Austria
[3] Steinmann-Institut of Geology, Mineralogy and Palaeontology, University of Bonn, Poppelsdorfer Schloss, 53115 Bonn, Germany
[4] Irish Centre for Research in Applied Geosciences (iCRAG), University College Dublin, Belfield, Dublin 4, Ireland
[5] Museum für Naturkunde, Leibniz Institute for Evolution and Biodiversity Science, Invalidenstrasse 43, 10115 Berlin, Germany
[6] Freie Universität Berlin (FU Berlin), Institut für Geologische Wissenschaften, Malteserstrasse 74-100, 12249 Berlin, Germany
[7] Humboldt Universität zu Berlin, Unter den Linden 6, 10099 Berlin, Germany
[8] Geochronology Laboratory, University of Brasília, Brazil
[*] Corresponding author. E-mail: toni.schulz@univie.ac.at

ABSTRACT

Archean spherule layers, resulting from impacts by large extraterrestrial objects, represent the only remnants of the early meteorite, asteroid, and comet bombardment of the Earth. Only few Archean impact debris layers have been documented, all of them embedded in the 3.23 to 3.47 billion year old successions of the Barberton Greenstone Belt (BGB) in South Africa and the Pilbara Craton in Western Australia. Some of them might be correlated with each other. Given the scarcity of Archean spherule deposits, four spherule layer intersections from the recently recovered BARB5 drill core from the central Barberton Greenstone Belt, analyzed in this study, provide a great opportunity to gain new insight into the early terrestrial impact bombardment.

Evidence for minor to moderate hydrothermal activity indicates that element abundance signatures of spherule rich samples from the BARB5 drill core, at least in part, retained a meteoritic fingerprint. The impact hypothesis for the generation of the BARB5 spherule layers is supported by correlations between the abundances of moderately (Cr,Co,Ni) and highly siderophile (Re, Os, Ir, Pt, Ru and Pd) elements, whose peak concentrations and interelement ratios are within the range of those for chondrites. Rhenium-Osmium isotope evidence for a chondritic projectile further support the impact hypothesis.

Collectively, this study provides evidence for extraterrestrial admixtures ranging between ~40 and up to 100% to three of the four analyzed BARB5 spherule layers, and a scenario for their genesis involving (i) impact of a chondritic bolide into a sedimentary target, (ii) varying admixtures of meteoritic components to target materials, (iii) spherule formation via condensation in an impact vapor plume, (iv) transportation of the spherules and sedimentation under submarine conditions, followed by (v) moderate post-impact remobilization of transition metals and highly siderophile elements.

Keywords: Barberton, spherules, Paleoarchean, impact, Osmium isotopes, highly siderophile elements

1

INTRODUCTION

Impact structures are the most common type of landform in the Solar System. Unlike on smaller (mostly atmosphere-less) and geologically less active rocky bodies of the inner Solar System, the recognition of impact craters on Earth has been difficult because geologic and atmospheric processes have obscured and largely obliterated the terrestrial impact record. Today, just about 190 confirmed impact structures are known on Earth (e.g., Earth Impact Database, 2016) but due to erosion and other geological processes on Earth, the crater population is strongly biased towards the last 250 million years (e.g., Jourdan et al., 2012). Only few impact structures with Precambrian ages are known. The Sudbury structure in Canada (an erosional relic of an impact basin originally about 200-250 km in diameter, with an age of ~1.85 Ga; e.g., Krogh et al., 1984, Spray et al., 2004), as well as the Vredefort impact structure in South Africa (with an initial crater diameter possibly as large as 250-300 km and an age of 2023 ± 4 Ma; Kamo et al., 1996; Henkel and Reimold, 2002) are the oldest preserved impact structures known on Earth. In contrast, the surface of the Moon, unaffected by erosional processes, displays abundant evidence of an intense bombardment at some time between its original crust formation and the outpourings of lava that form the dark mare plains. The ages of the highlands have been interpreted to represent a short and intense "late" heavy bombardment (LHB) period at 3.9 ± 0.1 Ga (e.g., Ryder, 1990; Ryder et al., 2000). However, evidence for basin-scale impact melting events dating back to 4.2 Ga (e.g., Fischer-Gödde and Becker, 2012; Norman and Nemchin, 2014) question a unique cataclysmic spike of lunar impacts at around ~3.9 Ga and support the view of a prolonged period of early lunar bombardment and probably throughout the inner solar system.

The question arises, as to whether or not any evidence of such a bombardment is preserved on Earth, also because the difference between both processes (short cataclysm vs. continuous bombardment) would have dramatic consequences on the habitability of the early Earth. In any given time-span, the Earth has been subjected to a higher impact flux than the Moon, as it has a larger diameter and, thus, a much larger gravitational cross-section (e.g., Koeberl, 2004). In the absence of any Hadean rock record and, thus, conclusive impact record, "younger" rocks had to be studied. The first terrestrial rock record of impact events in the form of (possibly distal) ejecta layers has been dated at ~3.47 Ga (Lowe et al., 1989), which, according to recent models, may constitute the tail-end of the LHB (e.g., Simonson and Glass, 2004; Bottke et al., 2012). A variety of suspected as well as confirmed impact ejecta layers have now been documented in 3.24 to 3.47 billion year old Archean successions of the Barberton Greenstone Belt (BGB) in South Africa and the Pilbara Craton in Western Australia (e.g., Lowe et al., 1989, 2003, 2014; Kyte et al., 1992, 2003; Koeberl et al., 1993; Koeberl and Reimold, 1995; Byerly et al., 2002; Simonson and Glass, 2004). Similar spherule layers (of ~2.6 Ga age) were found in the Hamersley Basin in Australia and in the Monteville Formation of the Transvaal Supergroup in South Africa (e.g., Simonson, 1992, 2003; Simonson et al., 1993, 1998, 1999; Rasmussen and Koeberl, 2004). However, no source craters have been identified for the South African or Australian spherule layers and, given the scarcity of the

2

early Archean geological record, it is unlikely that they will ever be found because of lack of preservation. Therefore, impact ejecta deposits may constitute the only extant traces of Archean impact events.

In this study we focus on the Paleoarchean spherule horizons from South Africa. Their often extreme enrichments (of up to superchondritic values) in highly siderophile elements (HSE) might in some cases be caused by secondary remobilization (e.g., Koeberl and Reimold, 1995; Reimold et al., 2000) rather than representing extraterrestrial admixtures. Moreover, ^{187}Os/^{188}Os isotopic compositions (otherwise an ideally suited tool to detect meteoritic signatures in impactites) must be interpreted carefully, because komatiites (although unrelated to the spherule layers) are the dominant volcanic lithology in the Barberton area and could, in principle, simulate meteoritic signatures due to their often chondrite-like ^{187}Os/^{188}Os ratios (e.g., Puchtel et al., 2009 and 2014; Connolly et al., 2011). However, ^{53}Cr isotopic anomalies, unambiguously revealing chondritic signatures (Kyte et al., 2003; Schönberg et al., 2016), provide a crucial argument for the impact origin of the South African Paleoarchean spherule horizons.

New impulses for the decipherment of the Paleoarchean impact record can be expected from the investigation of two recently recovered drill cores from the central and northern Barberton area, which host as many as 23 spherule layer intersections of Paleoarchean age (up to 17 in the CT3 core and up to 6 in the BARB5 core; e.g., Mohr-Westheide et al., 2014, Fritz et al., 2016). The amount of duplications they might represent, and their relation to the already known and well inspected spherule horizons from the area (S1-S4), with which they in part -but only crudely- stratigraphically correlate, still need to be clarified.

This study focuses on four spherule horizons from the 760-m-long ICDP core BARB5 from the Barite Valley Syncline, each about 4 cm thick and identified within a ~22 cm core interval at ~511 m depth. These spherules are embedded in shales and were deposited in a marine setting well below the storm-weather wave base (e.g., Fritz et al., 2016). We present new geochemical analyses and Re-Os isotope signatures of a traverse over this spherule layer section, including country rocks (Fig Tree Group metasediments). In order to better assess the Paleoarchean meteorite bombardment of the Earth we (together with, and in comparison to, previously published data for spherule layer horizons from the Barberton area; e.g., Reimold et al., 2000, Koeberl et al., 2015, Mohr-Westheide et al., 2015, Oezdemir et al., 2016), aim (i) to quantify meteoritic admixtures to the spherule containing layers of the BARB5 core, (ii) to draw conclusions about possible impactor types, and (iii) to evaluate the number of events they may represent.

3

SAMPLES

The BARB5 drill core section studied here is from the depth interval between 511.29 and 511.51 m depth in the 760-m-long drill core BARB5. This drilling was performed in 2011/2012 under the auspices of the International Continental Drilling Program (ICDP) project "Peering into the Cradle of Life" in the Barite Valley Syncline of the Barberton Greenstone Belt (BGB) (Hofmann et al., 2006). The BARB5 core was drilled through carbonaceous shales of the 3.26-3.32 Ga old middle Mapepe Formation of the Fig Tree Group. The continuous "511.29-511.51 m" drill core section, termed „spherule layer section" (SLS) throughout the text, includes four ca. 4 cm thick layers (layers B to E) of densely packed, 0.3-2 mm sized spherules, all embedded in a shale groundmass. These layers are separated by <1.5 cm thick shale bands which contain only a small number of spherules (termed intercalations). The spherule layer section (including spherule layers B to E and corresponding intercalations), was cut into 22 individual subsamples of 1 cm width each (samples 1 to 22, from bottom to top; see Fig. 1). Each of these cuts were split in half in order to obtain different aliquots for the different analytical techniques (instrumental neutron activation analysis and isotope dilution; see Method section). For better clarity, samples 1-22 from the spherule layer section (SLS) are frequently sub-labelled throughout the text either with the prefix „IC" in case of intercalations (samples IC-1, IC-2, IC-7, IC-12, IC-13, IC-17 and IC-22) or with the spherule layer nomenclature to which the samples can be assigned (samples B-3 to B-6 for spherule layer B, samples C-8 to C-11 for spherule layer C, samples D-14 to D-16 for spherule layer D, and samples E-18 to E-21 for spherule layer E). However, it should be kept in mind that the 22 samples from the spherule layer section do not clearly separate distinct lithologies. Cutting boundaries between spherule layer samples and the corresponding intercalations are merely defined by a spatial decrease in the spherule to matrix (shale groundmass) ratio.

A further, ca. 7 cm wide spherule layer A (not investigated in this study) occurs ca. 80 cm lower in the stratigraphy, at 512.30 m depth. This spherule layer stratigraphically occurs in the sequence hosting the previously studied spherule layers S3/S4 (Lowe et al., 2003) or could represent a different spherule deposit that has not previously been recognized. Between layer A and the four layers B to E occurs a fine-grained siliciclastic sediment sequence of cm- to dm-wide shale and chert layers. Spherules on top of layer B are extensively deformed (sheared) in contrast to the generally un- or barely deformed spherules in layers C-E. Cross-lamination is observed in the interval between layers B and C. Statistical analysis of the apparent spherule size did not show sorting of the individual spherule beds (e.g., Hoehnel, 2014).

The original mineralogical compositions of all spherule beds in BARB5 are obscured. They have been comprehensively altered to assemblages of quartz, chlorite, sericite, other phyllosilicates, K-feldspar, Mg-siderite, barite, and calcite. The main mineral phases, as determined by XRD analysis, are quartz, muscovite, K-feldspar, chlorite, siderite, dolomite/ankerite, and pyrite (Hoehnel, 2014). Sulfide mineralization is increasing from the lowermost layer A to layer E, with main sulfide minerals, both

4

within spherules and groundmass, being pyrite, chalcopyrite, and gersdorffite (NiAsS). Some spherules have been completely replaced by sulfides (Mohr-Westheide et al., 2015).

Some primary characteristics, including the total amount of spherules, the spherule sizes, their shapes, and some mineralogical features, including the presence of Ni-rich chromium-spinel (Ni-Cr-spinel) and zircon, are preserved. Only the layers B-E contain Ni-Cr-spinel and were, therefore, selected for high resolution SEM-EDX low voltage analysis to analyze a direct association of platinum-group element (PGE) phases with Ni-Cr spinel (Mohr-Westheide et al., 2015). This resulted in the identification of an assemblage Ni-rich chromium-spinel/PGE phases in spherule layer D from the BARB5 drill core section, which represent a possible carrier phase for the extraterrestrial signature.

In addition to the 22 samples from the spherule layer section (SLS), eight country rocks (CR), all shales, from above and below the 511.29-511.51 m drill core section (and completely devoid of any spherules) were analyzed for their geochemistry. Five samples were collected between 489.7 and 510.03 m core depth (samples CR-a to CR-e) and three samples between 515.33 and 524.66 m (samples CR-f to CR-h).

ANALYTICAL METHODS

Major Element Analyses by Instrumental Neutron Activation Analysis (INAA):

Concentrations of some major (Na, K, and Fe) and the majority of minor and trace elements (including the rare earth elements, REE) were determined by INAA for all 30 samples (samples 1-22 from the spherule layer section and 8 country rocks). For analysis, ~150 mg of each sample were sealed in polyethylene capsules and irradiated in the 250 kW Triga Mark-II reactor at the Atominstitut, Vienna. After a cooling period of up to five days, samples, including international rock standards (the carbonaceous chondrite Allende, Smithsonian Institution, Washington DC, USA, Jarosewich et al. 1987; the Ailsa Craig Granite AC-E, SARM-CRPG, Nancy, France, Govindaraju 1989; and the Devonian Ohio Shale SDO-1, USGS, Govindaraju 1989) were measured in three counting cycles (according to the half-lives of the nuclides) in the Gamma Spectrometry Laboratory of the Department of Lithospheric Research, University of Vienna. More details on the instrumentation, method, and accuracies are given by Koeberl et al. (1993) and Mader and Koeberl (2009).

HSE concentrations and $^{187}Os/^{188}Os$ analyses (ID-ICPMS and ID-NTIMS):

Eighteen samples (samples 1-18) from the spherule layer section (SLS) were analyzed for their HSE concentrations and $^{187}Os/^{188}Os$ isotope compositions. This selection allows to compare the HSE abundances and Re-Os isotope characteristics of spherule layer D (which contains Ni-rich chromium-spinel/PGE phases, possible carrier phases for the extraterrestrial signature; Mohr-Westheide et al., 2015) in comparison to spherule layers B, C, and E from the spherule layer section.

Between ~0.1 and ~0.6 g of homogenized sample powder was spiked with a mixed tracer composed of ^{99}Ru, ^{105}Pd, ^{185}Re, ^{190}Os, ^{191}Ir, and ^{194}Pt isotopes and digested in 7 ml inverse aqua regia (HNO$_3$-HCl: 5+2

5

ml) acid mixture at 250°C and 100-130 bars in an Anton-Paar high pressure asher for 12 hours. After digestion, Os was separated from the other HSE using a CCl_4/HBr liquid extraction procedure (Cohen and Waters, 1996). Osmium was further purified using a H_2SO_4/H_2CrO_4 microdistillation technique (Birck et al., 1997). After Os extraction, all other HSEs were separated using a procedure adapted from the method of Rehkämper and Halliday (1997).

The ^{187}Os/^{188}Os isotope ratio and Os concentration measurements were carried out at the Department of Lithospheric Research at the University of Vienna, Austria. These analyses were performed using a ThermoFinnigan Triton Thermal Ionization Mass Spectrometer operating in negative mode. Osmium was loaded as a bromide on Pt ribbon filaments covered with a $NaOH$/$Ba(OH)_2$ activator (Völkening et al., 1991; Creaser et al., 1991). Isobaric interferences attributable to W- or Pt-oxide were not observed. Isobaric interferences of ^{187}Re on ^{187}Os were monitored by measuring $^{185}ReO_3^-$ (mass 233) and were corrected if observed. Mass fractionation was corrected offline using ^{192}Os/$^{188}Os = 3.083$ (Brandon et al., 2005; Luguet et al., 2008).

The Os total procedural blank was 7 ± 5 pg (n = 5) contributing less than 0.05% to the measured Os concentration of all samples. Rhenium and PGE contents were measured using a Thermo Element XR SF-ICP-MS in single collector mode at the Steinmann-Institute at the University of Bonn, Germany, using methods described in Luguet et al. (2015). Total blanks for this study (n = 4) were ~4 pg for Re, ~3 pg for Ir, ~70 pg for Ru, ~22 pg for Pt, and ~50 pg for Pd. Due to the extremely high concentrations of HSE in most of the analyzed samples, blank corrections were minor (in most cases negligible).

RESULTS

Concentrations of minor and trace elements are given for 36 elements in Table 1. These values were obtained by instrumental neutron activation analysis (INAA). Additional analyses of selected highly siderophile elements (Re, Os, Ir, Pt, Ru, and Pd) are presented in Table 2, together with ^{187}Os/^{188}Os isotope ratios.

Geochemistry

Figure 2a shows abundances of lithophile trace elements and selected moderately siderophile elements normalized to the upper continental crust (data from McLennan, 2001). All analyzed samples, including non-impact shales (country rocks) and samples from the spherule layer section (SLS), exhibit similar trace element patterns and a comparably narrow spread in total abundances (compared to the CT3 and S2 layers, as is discussed below in detail). All samples exhibit similar concentrations compared to literature values for other sedimentary rocks from the Fig Tree Group (shales, black shales, graywackes, cherts, and jaspilites; see Hofmann, 2005), with the exception of the moderately siderophile elements (Ni, Co, and Cr). These elements are mostly enriched in the spherule-containing samples (spherule layer section) by up to and slightly more than an order of magnitude.

6

The main difference between modern (non-Archean) and Fig Tree Group, as well as other Archean marine precipitates is a positive Eu anomaly and a lack of a negative Ce anomaly, indicating reducing sea water conditions (e.g., Barrett et al., 1988). The samples analyzed for this work mirror these trends for Archean marine precipitates and also argue for low oxygen levels of the Archean atmosphere and hydrosphere (e.g., Hofmann, 2005).

Chromium, Cobalt, Nickel, Gold, and Tungsten: Chromium, cobalt, nickel, and gold contents of the eight country rock samples (shales from the Fig Tree Group, sampled above and below the spherule layer section; samples CR-a to CR-e and CR-f to CR-h) exhibit similar abundances with variations in Cr from ~270 to 960 ppm for Cr, from ~16 to ~43 ppm for Co, from ~105 to ~377 ppm for Ni, and from <0.5 to ~1 ppb for Au. These values are typical for Fig Tree sediments collected in other areas of the Barberton Greenstone Belt (typically varying between ~5 and ~1260 for Cr, ~1 and ~32 ppm for Co, and ~9 and ~313 ppm for Ni; Hofmann, 2005).

The abundances of these elements in the spherule layer section (samples 1 to 22) were previously reported by Mohr-Westheide et al. (2015) but neither interelement ratios were reported nor was a detailed discussion undertaken about their relevance in terms of meteoritic admixtures to the spherule samples. In contrast to the much lower concentrations (by a factor 10) of Cr, Co, Ni, and Au measured within the country rocks (samples CR-a to CR-h), element abundances within samples 1 to 22 (SLS) range from ~82 to ~3560 ppm for Cr, ~7 to ~2696 ppm for Co, from ~124 to ~5435 ppm for Ni, and from ~1 to ~10 ppb for Au. Notably, there are no obvious correlations between Cr, Ni, Co, Au concentrations and the spherule content of the samples (i.e., the spherule to matrix ratios). For example, intercalations (samples IC-1, IC-2, IC-7, IC-12, IC-13, IC-17 and IC-22, which are nearly spherule-free lithologies within the SLS) exhibit concentrations ranging from ~82 to ~3562 ppm Cr, ~124 to ~3476 ppm Ni, ~7 to ~2696 ppm Co and from ~1.1 to ~10 ppb Au.

Figures 3a-c show positive interelement correlations between Cr, Co, Ni, and Au for samples from within and between all four layers of the spherule layer section, as well as country rocks from the BARB5 drill-core (correlation factors are for Ni vs. Cr: $R^2 = 0.65$; Ni vs. Co: $R^2 = 0.71$ and Ni vs. Au: $R^2 = 0.80$).

The concentration of tungsten, a moderately siderophile element, varies between 0.3 and 0.4 ppm in the country rocks (samples CR-a to CR-h), but is systematically higher in samples from the spherule layer section (including all intercalations), with values ranging from 5.7 to 21.5 ppm. Figure 3d shows the clear distinction in W concentration and the absence of a Ni vs. W interelement co-variation when the country rocks and the samples from the spherule layer section interval are compared.

Highly siderophile elements: Rhenium and Os concentrations in samples from the spherule layer section (samples 1 to 22) range from 0.04 to 26.1 ppb and from 1.5 to 944.5 ppb, respectively. While Re values are comparable to sediments from other areas in the Barberton region (ranging from ~0.01 to ~27 ppb;

Siebert et al., 2005), Os abundances in the SLS exceed those in sediments (e.g., shales) by up to three orders of magnitude. This is also true for all other HSE abundances, which range from 0.9 to 552 ppb for Ir, from 14.6 to 1232 ppb for Ru, from 2.1 to 2082 ppb for Pt, and from 4.6 to 1086 ppb for Pd. Notably, Os concentrations derived by isotope dilution (values mentioned above) in most cases are roughly comparable (samples C-10, D-15, D-16, and E-18) to the concentrations derived by instrumental neutron activation analysis, but some differences are evident. This is also true for Ir concentrations (see Table 2). These differences are expected because cuts from specific core depths were split into two parts and prepared for the different analytical techniques. These splits were observed to contain different amounts of spherules and, thus, may also contain different amounts of carrier phases of HSE, resulting in only coincidentally comparable concentrations for both elements. These carrier phases are PGE-rich metal alloys associated with Ni-rich chromium-spinel (Mohr-Westheide et al., 2015).

Figures 4 a-d shows interelement plots between Re and Os, Os and Ir ($R^2 = 0.66$), Ir and Pt ($R^2 = 0.84$), and Pd and Ru ($R^2 = 0.79$), demonstrating positive correlations for all plots except for Re vs. Os.

Rhenium-Os isotope systematics

Both the measured $^{187}Os/^{188}Os$ isotope ratios and $^{187}Os/^{188}Os$ isotope ratios back-calculated to the age of the middle Mapepe Formation of the Fig Tree Group (i.e., 3.32 Ga) for samples from the spherule layer section (samples 1 to 22) are shown in Table 2. Measured $^{187}Os/^{188}Os$ ratios range from ~0.1064 in sample C-8 to ~0.3161 in sample IC-1. Interestingly, $^{187}Os/^{188}Os$ ratios do not show a significant correlation with the spherule content of the samples. Intercalations (shales with minor spherules) of the spherule layer section vary from 0.1197 in sample IC-17 to 0.3161 in sample IC-1. Notably, typical $^{187}Os/^{188}Os$ ratios for non-spherule related sediments from the Fig Tree Group reported in the literature are significantly more radiogenic compared to the intercalations from the BARB5 spherule layer section and range from ~0.37 to ~0.79 (Siebert et al., 2005). The four investigated spherule layers of the BARB5 core exhibit $^{187}Os/^{188}Os$ ratios ranging from 0.1344 to 0.2763 for spherule layer B, from 0.1064 to 0.1290 for spherule layer C, from 0.1150 to 0.1262 for spherule layer D and 0.1110 for sample E-18 from spherule layer E.

The least radiogenic $^{187}Os/^{188}Os$ ratio reported for sediments from any other sedimentary units within the Barberton Greenstone Belt (Moodies Group, Manjeri Formation) is ~0.29 (Siebert et al., 2005), thus, no country rock values are comparable to the less radiogenic $^{187}Os/^{188}Os$ ratios for spherule layers B to E (including intercalations). The only lithologies in the Barberton Area that have comparably low $^{187}Os/^{188}Os$ isotope compositions are volcanic rocks, such as komatiites, which are unrelated to the BARB5 SLS and range from ~0.1048 to ~0.1970 (Puchtel et al., 2009, 2014 and Connolly et al., 2011).

The $^{187}Re/^{188}Os$ ratios do not vary systematically with the $^{187}Os/^{188}Os$ isotope compositions or the spherule content of the samples and range overall from ~0.01 to ~0.31. These ratios are up to 3 orders of magnitude lower compared to what has been measured for typical sediments from the Fig Tree Group

8

(graywackes, metapelites, and shales), which range from ~0.4 to ~9 (Siebert et al., 2005), or any other sediments from the Barberton area (Siebert et al., 2005).

The BARB5 spherule samples exhibit a large variation in $^{187}Os/^{188}Os$ initial values (back-calculated to an age of 3.32 Ga, the age of the middle Mapepe Formation of the Fig Tree Group; see compilation in Lowe and Byerly, 1999) and still do not correlate in the $^{187}Re/^{188}Os$ vs. $^{187}Os/^{188}Os$ space (not shown). Such a non-isochronous behavior can be explained by an open system behavior, comprising addition of Os to the system and/or Re-loss and remobilization via processes that are discussed below.

DISCUSSION

Geochemical evidence for an impact origin

The most consistent differences between samples from the BARB5 spherule layer section (SLS) in comparison to spherule-free country rocks are the observed enrichments in the elements Cr, Co, Ni, and Au in most of the spherule bed samples (see Tables 1). These elements have often been used to identify meteoritic components within impactites (see Koeberl, 2014 for a recent review). Especially interelement ratios of these elements can serve as an effective discriminator between possible impactor types. However, as argued in earlier studies on similar spherule layer occurrences (e.g., Koeberl and Reimold, 1995 and Reimold et al., 2000), element redistributions and enrichments caused by secondary processes (e.g., hydrothermal alteration, metamorphic overprint) could obscure meteoritic components.

Chromium, Co, Ni, and Au concentrations correlate for spherule containing samples from the BARB5 core, which is to be expected if these elements had the same (probably meteoritic) source (see Fig. 3a-c). Notably, Koeberl and Reimold (1995) and Reimold et al. (2000) reported a lack or only weak interelement correlations for these elements in the S2 horizon from the Barberton area. They interpreted this as resulting from complex secondary hydrothermal overprint, precluding the usefulness of these elements as primary proxies for meteoritic admixtures. To support their conclusion, they reported significant correlations of these elements with abundances of the fluid-mobile elements As and Sb (e.g., Ballantyne and Moore, 1988), as well as secondary sulfide minerals (e.g., gersdorffite). Koeberl and Reimold (1995) argued that the mostly superchondritic Cr, Co, Ni, and Au abundances in the S2 layer might be explained by secondary enrichment processes rather than extraterrestrial admixture (although such an admixture could not unambiguously be ruled out).

However, the picture is different when it comes to the BARB5 samples, which exhibit significant Cr, Co, Ni, and Au interelement correlations in conjunction with no or only weak correlations of these elements when plotted against As or Sb (see Fig. 5a-d and correlation factors as mentioned in the figure captions). This, most likely, indicates that in contrast to the S2 horizon hydrothermal or other secondary overprint, although existing, played a minor role for BARB5 samples, compared to its significance for the S2 horizon. This conclusion is further supported by the element plots (normalized to upper continental crust; data from McLennan, 2001) shown in Figure 2a-c. A comparably narrow spread of normalized element

9

abundance patterns for samples from the BARB5 drill core is in stark contrast to the non-uniform patterns with highly varying peak concentrations for samples from the S2 horizon (data from Reimold et al., 2000) and the recently analyzed CT3 spherule layers (Oezdemir et al., 2016). A final argument against substantial hydrothermal overprint comes from the fact that elemental mobility would have to coincidentally produce Cr, Co, and Ni as well as HSE signatures that consistently end up in the range covered by known chondrite groups (compare Figs. 4b-d). This, however, is unlikely. Thus, post-impact hydrothermal enrichments as a sole cause for the element enrichments in the spherule containing samples from the BARB5 core can be ruled out.

An extraterrestrial fingerprint, therefore, survived in the moderately (Cr, Co, Ni) and highly siderophile element (HSE; Re, Os, Ir, Pt, Ru, Pd) budget of the BARB5 spherule layers. Concentrations of Cr, Co, Ni, and Au of up to chondritic values in some samples from the spherule layer section can, therefore, best be explained by varying magnitudes of extraterrestrial admixtures. Although no known chondrite groups exactly match the trend defined by samples from the spherule layer section, binary mixing calculations (between an average shale component and different chondrite end-members; Fig. 6a-b) reveal admixtures of mostly between 10 and 100 % of a chondritic component.

Interelement ratios for the elements Cr, Co, and Ni support the interpretation of the extraterrestrial admixture. As shown in Fig. 7a-b, all country rocks from the Barberton area plot off the cloud defined by samples from the spherule layer section (which exhibit values that are significantly closer to chondritic values). However, there is no clear trend between the interelement ratios of the samples and their spherule content. Although samples D-14 and D-16 (both belonging to spherule layer D and hosting PGE carrier phases as reported by Mohr-Westheide et al., 2015) seem to plot near the chondritic end-members, shale with minor spherules (intercalations) define similar trends in the Cr/Ni vs. Cr/Co and Cr/Ni vs. Cr/Au diagrams (e.g., samples IC-2 and IC-13). This probably indicates an inhomogeneous distribution of the carrier phases of the meteoritic component in the spherules and spherule/groundmass assemblages, and/or a minor postimpact re-mobilization of Cr, Co, Ni, and Au into the surrounding strata. A minor postimpact re-mobilization of these elements could explain the large scatter of the data in Fig. 7a-b, as well as the only broad agreement between the mixing lines and actual trends of the spherule samples in Figures 6a and 6b. Due to this scatter, however, no clear conclusion can be drawn regarding the exact type of chondritic impactor.

A similar picture of up to 100% meteoritic components in some of the samples from the spherule layer section and near to chondritic interelement ratios arises for the platinum group elements. Figures 4a-d show element-element plots for all platinum group elements and Re. All diagrams (except Re vs. Os) show significant positive correlations between the abundances of the platinum group elements with always a clear trend towards chondritic endmembers. The lack of a significant correlation between Re and Os (Fig. 4a) can best be attributed to Re-loss during the high temperature impact event, where Re was significantly lost by volatilisation. Such a behavior was observed for several impact structures (e.g.,

10

136

Chesapeake Bay impact structure, Lonar crater) and their corresponding ejecta deposits from worldwide locations (e.g. Lee et al., 2006; Schulz et al., 2016).

Notably, Os/Ir ratios, as shown in Fig. 8a, show a trend towards chondritic ratios (ranging from ~1.06 to ~1.13 for the different chondrite groups; Tagle and Berlin, 2008) with increasing Ir concentrations, which is in accordance with increasing proportions of extraterrestrial component. Within the spherule layers of the drill core section, Os/Ir ratios scatter between 0.1 to 10 for samples with comparatively low (~1 to ~10 ppb) Ir concentrations, but the range for Os/Ir ratio narrows down to 0.7-2 for samples with chondrite-like Os and Ir abundances.

A more substantive support for the impact hypothesis comes from a comparison of moderately and highly siderophile elements. Such comparisons were used earlier to confirm meteoritic components of other spherule-beds from the Barberton area and include the correlation of the elements Cr and Ir (e.g., Lowe et al., 2003). It was shown that the S3 and S4 spherule beds (possibly stratigraphically related to the BARB5 layers; Fritz et al., 2016), besides exhibiting chondritic Cr isotope signatures (Kyte et al., 2003), show near-chondritic Cr/Ir ratios (chondrites show Cr/Ir ratios ranging from ~640 to ~10470, depending on the different chondrite groups; Tagle and Berlin, 2008). Samples from the BARB5 spherule section mirror these trends. Whereas samples with Ir abundances between ~1 and ~10 ppb range in Cr/Ir from ~35000 to ~385000, samples with more than 100 ppb Ir exhibit Cr/Ir ratios between ~4300 and ~11100.

Notably, sediments from the Fig Tree Group are completely separated from the common trend defined by BARB5 spherule layer samples and chondrites and exhibit Cr/Ir ratios between ~1 x 10^6 to ~2 x 10^6 (Siebert et al., 2005). Chromium/Ir ratios vary from ~35000 to ~390000 for BARB5 spherule layer B (uppermost stratigraphic unit in the drill core) and from ~4300 to ~11100 for spherule beds C to E. The lowest Cr/Ir ratios in layers C to E are very similar (~4800 in layer C, ~4300 in layer D and ~4900 in layer E), suggesting that the maximum chondritic component is not restricted to a distinct layer. Figure 9 shows approximated meteoritic admixtures to samples from the BARB5 spherule layer section assuming mixtures of an average target (sediments from the Fig Tree Group; Siebert et al., 2005) and all known chondrite groups (data from Tagle and Berlin, 2008). Notably, the lowest Cr/Ir ratios measured for BARB5 spherule layers C to E are significantly lower compared to a variety of chondrite types, including low metal ordinary chondrites and CI chondrites. Maximum meteoritic contributions for the analyzed spherule samples then vary between ~40 and up to 100%, depending on the impactor type assumed. These values are in accordance with the Cr,Co,Ni, and PGE abundances of the BARB5 spherule samples and are comparable to estimates of chondritic admixtures reported for the S3 and S4 layers based on Cr isotopes (Kyte et al., 2003). If the BARB5 layers are correlated to the S3 and S4 layers, which cannot be ruled out based on the currently available petrographic and geochemical datasets, existing ^{53}Cr isotope data are in agreement with the results presented in this study.

It should, however, be noted that spherule layer B (the stratigraphically lowermost spherule bed), based on total abundances (of Cr, Co, Ni, and HSE) and Fig. 9, contains an only minor maximum meteoritic

11

component (between ~3 and ~9%), independently on which chondrite type is assumed as the impactor. Such an inhomogeneous distribution of impactor contributions between the BARB5 spherule layers analyzed in this study (layer B vs. layers C to E) seems to indicate that layer B cannot simply be a tectonic (or otherwise) duplication of the layers C to E.

The geochemical evidence for chondritic admixtures to samples from the spherule layer section explicated above (significant chondritic contributions to spherule layers C to E and lesser admixtures to spherule layer B) is supported by $^{187}Os/^{188}Os$ isotope ratios. Figure 8b shows a continuous trend towards un-radiogenic $^{187}Os/^{188}Os$ isotope values at increasing Os concentrations overlapping with chondrite-like Os concentrations. This trend exactly matches the expectations for a meteoritic contamination. $^{187}Os/^{188}Os$ ratios between 0.1344 to 0.2763 for spherule layer B are contrasted by values ranging from 0.1064 to 0.1290 for spherule layers C to E. The $^{187}Os/^{188}Os$ ratios for layers C to E cover the typical present day values for chondrites (0.1289 ± 0.0022 for ordinary chondrites, 0.1283 ± 0.0008 for enstatite chondrites, and 0.1263 ± 0.0008 for carbonaceous chondrites; Shirey and Walker, 1998). The $^{187}Os/^{188}Os$ ratios for layers C to E, which are below the present day values for chondrites, can be explained by volatilization of Re during the impact event. Rhenium loss lowers the Re/Os ratios of the samples, resulting (over ~3.32 Ga) in an ^{187}Os isotope evolution below the chondritic evolution line. This is in line with the most unradiogenic $^{187}Os/^{188}Os$ initial ratios (back-calculated to an age of 3.32 Ga) for these samples (i.e., ~0.1054 for sample C-8), which are indistinguishable from the value for the chondritic evolution line at that time (~0.1048; Shirey and Walker, 1998). The range of calculated initial $^{187}Os/^{188}Os$ ratios, ranging from ~0.1054 to ~0.2764 for samples from the BARB5 spherule layer section (see Table 2) then reflects (i) the diverse initial $^{187}Os/^{188}Os$ isotope compositions of the sedimentary lithologies in which the spherules are embedded, (ii) varying additions of impactor component to the spherules, and (iii) different degrees of post-impact Re mobilization.

Collectively it can be stated that there are several lines of evidence in favor of the impact hypothesis and, especially, in favor of substantial chondritic admixtures in most of the spherule-bearing samples from the BARB5 drill core (SLS). These comprise (i) geochemical hints for a minor role of hydrothermal overprint for BARB5 samples, supporting that their elemental fingerprints are (only slightly altered) primary (impact) signatures, (ii) moderately and highly siderophile elements, which are significantly correlated, arguing for a common (meteoritic) source, (iii) peak concentrations of elements for samples defining those correlations all ending up in the range defined by known chondrite types, (iv) Cr vs. Ir trends defined by BARB5 spherule samples that mirror those of other spherule layers from the Barberton area, for which a chondritic component was unambiguously confirmed, (v) the lowest Cr/Ir ratios in some of the samples (from layers C to E) seem to rule out ordinary and CI chondrites, (vi) interelement ratios of moderately as well as highly siderophile elements for spherule containing BARB5 samples that scatter but mostly plot near chondritic ratios and significantly off the trend defined by any known non-impact

<div align="right">12</div>

lithology from the Barberton area, and (vii) $^{187}Os/^{188}Os$ ratios for layers C to E, covering chondritic signatures.

Considerations on the genesis of the BARB5 spherule layers

Spherules are distal impact ejecta that were transported from their source region over significant distances. The question arises, which material constituted the spherule precursor. Metasediments similar to the country rocks from the Fig Tree Group (with low HSE concentrations and superchondritic $^{187}Os/^{188}Os$ ratios) may constitute the best candidate. However, as stated in the introductory chapter, a possible mafic or ultramafic spherule precursor (with elevated HSE abundances and mantle-like ^{187}Os signatures) could, in principle, simulate a meteoritic signature. The only mantle-like lithology that needs to be considered are komatiites, which comprise the dominant volcanic lithology in the Barberton area. In fact, whole-rock Barberton komatiite samples exactly mirror the $^{187}Os/^{188}Os$ trends defined by the most unradiogenic spherule samples from the BARB5 drill core and range from 0.1075 to 0.1969 (Puchtel et al., 2009, 2014; Connolly et al., 2011). These komatiites also exhibit chondrite-like Os/Ir ratios (ranging from ~0.96 to ~1.40; Puchtel et al., 2009, 2014; Connolly et al., 2011).

The unradiogenic present-day $^{187}Os/^{188}Os$ isotope signatures for some of the samples analyzed in this study could, therefore, in principle be explained by komatiitic spherule-precursors, rather than by meteoritic admixture. However, komatiites exhibit significant differences to the BARB5 spherule layer samples and chondrites in the Cr/Ir ratios and total HSE abundances. For Barberton komatiites, Cr/Ir ratios range from ~1 x 10^6 to ~2 x 10^6 (Puchtel et al., 2009, 2014; Connolly et al., 2011; Siebert et al., 2005) and HSE abundances are in the ppb concentration range (e.g., ~0.8 to ~11.9 ppb for Os and from ~0.6 and ~10.6 for Ir, including cumulates; Puchtel et al., 2009 and 2014, Connolly et al., 2011, Siebert et al., 2005). These values (both Cr/Ir ratios and total HSE concentrations) are up to three orders of magnitude lower compared to the BARB5 spherule samples. Thus, ultramafic contamination (of the spherules) instead of a chondritic admixture as a cause for the discussed geochemical and ^{187}Os isotope signatures of the drill core samples can be ruled out.

A closer inspection of the geochemical and isotopic fingerprint of the different spherule layers of the BARB5 drill core, therefore, supports a substantial meteoritic component within layers C to E. Only the uppermost layer B shows comparatively low enrichments in the moderately and highly siderophile elements and plots closer to the country rocks in the interelement ratio diagrams (Fig. 7a-b). This suggests that this layer has no or only a few percent of meteoritic admixture. It also exhibits radiogenic $^{187}Os/^{188}Os$ values that are comparable to non-impact country rocks of the Fig Tree Group. Notably, samples IC-13, IC-17 and IC-22, intercalations between the spherule layers (shales almost but not completely devoid of spherules) also plot at near chondritic interelement ratios in Fig. 7a-b. This emphasizes that the total spherule content of the analyzed samples (spherule-groundmass assemblages) is not a determining factor

13

for the presence and magnitude of a meteoritic component. This can only be explained if carrier phases (of the extraterrestrial signature) within the samples are heterogeneously distributed. This was confirmed beforehand by analysis of the BARB5 spherule layer section using SEM-EDS X-ray spectrometry at high spatial resolution (Mohr-Westheide et al., 2015).

The formation of each of the four spherule layers (B to E) by separate impact events cannot be ruled out. If these layers represent distinct events, this would require three consecutive (most likely devastating) impact events within a very close time frame. However, common features of chondritic admixtures to layers C to E (all within the range of several dozen percent of chondritic admixture; see Fig. 9) might argue for one single event that formed these layers. Probably, such a single layer was later separated by tectonic duplication or separated by other processes such as soft-sediment slumping (as proposed for the BARB5 core by Fritz et al., 2016). If the separation of such a (proposed) single spherule deposit (C to E) is due to duplication (tectonically or sedimentary), this would have consequences regarding the thickness of the spherule deposit, a critical factor in determining and approximating deposition distances and impactor size (e.g., Johnson and Melosh, 2012). However, it is currently not possible to clearly decipher the mutual relation of the different spherule layers from the BARB5 core. As stated above, BARB5 spherule layer A (not investigated in this study) occurs in a stratigraphic sequence that hosts also the previously studied spherule layers S3/S4 (Lowe et al., 2003; Fritz et al., 2016). If spherule layer A is related to S3 or S4, it is rather unlikely that this layer tectonically duplicated multiple times over a ~1 m core section to produce spherule layers C, D and E. Moreover, spherule layers A and C to E are intercalated by spherule layer B, which is geochemically and isotopically distinct from the C-E layers. It would probably be more plausible to assume that spherule layers A (related to either S3 or S4), spherule layer B, and spherule layers C to E represent three distinct events. However, this remains speculative based on the available data sets.

As stated by Johnson and Melosh (2012), spherules may be generated through the fragmentation of melt ejected during an impact or as condensates from the inside of an impact vapor plume. Based on their morphology and often secondary mineralogy (e.g., Fritz et al., 2016), spherules from the BARB5 layers cannot unambiguously be assigned to one of these processes. However, meteoritic components should be restricted to vapor condensates as stated by Johnson and Melosh (2012). This is in line with mineralogical and geochemical conclusions drawn by Lowe and Byerly (1987), Lowe et al. (1989), Kyte et al. (1992), and Byerly and Lowe (1994).

The complex behavior of the elements in a variety of consecutive and/or overlapping processes during an impact event, especially within an impact vapor plume, has been proven by natural (e.g., Žák et al., 2016) as well as experimental studies (e.g., Ebert et al., 2014) and depends (inter alia) on the nature of the target and the impactor. However, in comparison to other Paleoarchean spherule layers, the well-defined element correlations for moderately and highly siderophile elements for the BARB5 spherule samples might argue against such a complex behavior of volatilization and fractionation of the highly siderophile

14

elements during condensation. Instead, the lack of significant element fractionation in BARB5 spherule samples seems to be in line with those processes that formed other distal impact ejecta from more recent events (e.g., Ivory Coast tektites; Koeberl and Shirey, 1993), where meteoritic Os (and other HSE) partitioned into the impact melt accompanied by significant loss of Re. The greatest difference, however, remains that BARB5 spherules probably formed in an impact vapor plume and exhibit unparalleled proportions of incorporated meteoritic components of up to ~100% (compared to the fractions of a percent detected in impactites from other localities worldwide and from throughout Earth's geologic history).

SUMMARY AND CONCLUSIONS

Samples from a ~22 cm section from the 760-m-long ICDP core BARB5 from the Barite Valley Syncline (Barberton Greenstone Belt), containing four Paleoarchean spherule layers (layers B to E) were (together with spherule-free country rocks from above and below this section) analyzed for their geochemistry and $^{187}Os/^{188}Os$ isotope signatures. The spherules are exclusively embedded in shales from the Fig Tree Group. Geochemical analyses reveal that the BARB5 spherule occurrences, in contrast to other spherule horizons from the Barberton area (S3, S4 and CT3), are only mildly affected by hydrothermal overprints. BARB5 samples, therefore, support that their elemental fingerprints are (only slightly altered) primary (impact) signatures.

Chromium, Co, Ni, and highly siderophile element concentrations and respective interelement ratios of samples from the BARB5 spherule layer section are distinct from sedimentary country rocks of the Fig Tree Group and, collectively, tend toward signatures comparable to compositional ranges for known chondrite groups. This strongly supports the impact hypothesis for the formation of at least three of the four analyzed spherule layers (layers C to E). Whereas layer B (uppermost spherule horizon in the analyzed drill core section) provides geochemical evidence for an only minor meteoritic admixture (percent level), layers C to E are geochemically very similar and contain chondritic admixtures of up to 100%. The elemental signatures do not allow an unambiguous identification of the type of chondritic material that was added to the spherule samples, although Cr/Ir ratios probably exclude ordinary and CI chondrites for layers C to E.

Spherule containing samples from the analyzed drill core section exhibit significantly less radiogenic ^{187}Os values compared to country rock sediments from the Fig Tree Group. Most of the BARB5 spherule samples exhibit chondritic to subchondritic present day $^{187}Os/^{188}Os$ compositions, but superchondritic to chondritic initials (back-calculated to an age of 3.32 Ga), in accord with a chondritic admixture accompanied by impact related loss of Rhenium.

It is, based on the current dataset, not possible to clearly decipher the mutual relation of the different spherule layers from the BARB5 core. Taking the geochemical and ^{187}Os isotope signatures introduced in this study and applying the least number of assumptions, we speculate that layers B and C to E represent

15

two distinct impact events, with the single C-E layer being later duplicated by tectonic or sedimentary processes such as soft-sediment slumping (as proposed for the BARB5 core by Fritz et al., 2016). Both events involve (i) impact of a chondritic bolide into a sedimentary target, (ii) admixture of a chondritic component to the spherule precursor, which probably condensed in an impact vapor plume, (iii) accompanying Re exhalations caused by the high temperatures during and in the wake of the impact event, (iv) transportation of the spherules and sedimentation into the shale dominated sequence of the Fig Tree Group, followed by (v) minor post-impact remobilization of Ni, Cr, Co, and the highly siderophile elements.

16

REFERENCES

Ballantyne J.M. and Moore J.N. (1988) Arsenic geochemistry in geothermal systems. *Geochim. Cosmochim. Acta* **52**, 475-483.

Barrett T.J., Fralick P.W. and Jarvis I. (1988) Rare-earth-element geochemistry of some Archean iron formations north of Lake Superior, Ontario. *Can. J. Earth Sci.* **25**, 570-580.

Birck J. L., Barman M. R. and Capmas F. (1997) Re-Os isotopic measurements at the femtomole level in natural samples. *Geost. Newslett.* **20**, 19–27.

Bottke W.F., Vokrouhlický D., Minton D., Nesvorný D., Morbidelli A., Brasser R., Simonson B. and Levison H.F. (2012) An Archean heavy bombardment from a destabilized extension of the asteroid belt. *Nature* **485**, 78-81.

Brandon A.D., Humayun M., Puchtel I.S., Leya I. and Zolensky M. (2005) Geochemistry: Osmium isotope evidence for an s-process carrier in primitive chondrites. *Science* **309**, 1233-1236.

Byerly G.R. and Lowe D.R. (1994) Spinel from Archean impact spherules. *Geochim. Cosmochim. Acta* **58**, 3469– 3486.

Byerly G.R., Lowe D.R., Wooden J.L. and Xie X. (2002) An Archean impact layer from the Pilbara and Kaapvaal Cratons. *Science* **297**, 1325–1327.

Coggon J.A., Luguet A., Nowell G.M. and Appel P.W.U. (2013) Hadean mantle melting recorded by southwest Greenland chromitite [186]Os signatures. *Nature Geosci.* **6**, 871-874.

Cohen A. S. and Waters F. G. (1996) Separation of osmium from geological materials by solvent extraction for analysis by thermal ionisation mass spectrometry. *Anal. Chim. Acta* **332**, 269–275.

Connolly B.D., Puchtel I.S., Walker R.J., Arenalo Jr. R., Piccoli P.M., Byerly G., Robin-Popieul C. and Arndt N. (2011) Highly siderophile element systematics of the 3.3 Ga Weltevreden komatiites, South Africa: Implications for early Earth history. *Earth Planet. Sci. Lett.* **311**, 253-263.

Creaser R.A., Papanastassiou D.A. and Wasserburg G.J. (1991) Negative thermal ion mass-spectrometry of osmium, rhenium and iridium. *Geochim. Cosmochim. Acta* **74**, 356-379.

Earth Impact Database, http://www.unb.ca/passc/ImpactDatabase. Accessed: 10th December 2016.

Ebert M., Hecht L., Deutsch A., Kenkmann T., Wirth R. and Berndt J. (2014) Geochemical processes between steel projectiles and silica-rich targets in hypervelocity impact experiments. Geochim. Cosmochim. Acta **133**, 257–279.

Fritz J., Tagle R., Ashworth L., Schmitt R.T., Hofmann A., Luaiss B., Harris P.D., Hoehnel D., Oezdemir S., Mohr-Westheide T. and Koeberl C. (2016) Nondestructive spectroscopic and petrochemical investigations of Paleoarchean spherule layers form the ICDP drill core BARB5, Barberton Mountain Land, South Africa. *Meteoritics Planet. Sci.* **51**, 2441-2458.

Govindaraju K. (1989) Compilation of working values and sample description for 272 geostandards. *Geost. Newslett.* **13**, 1-113.

Henkel H. and Reimold W.U. (2002) Magnetic model of the central uplift of the Vredefort impact structure, South Africa. *J. Appl. Geophys.* **51**, 43-62.

Hoehnel D., Mohr-Westheide T., Fritz J. and Reimold W.U. (2014) Spherule size distribution in the BARB-5 ICDP drill core from the Barberton Greenstone Belt. *Meteoritics Planet Sci. Conf., Abstracts of the Meteoritical Society Annual Meeting* #**5081**.

Hofmann, A. (2005) The geochemistry of sedimentary rocks from the Fig Tree Group, Barberton greenstone Belt: Implications for tectonic, hydrothermal and surface processes during mid-Archean times. *Precambrian Res.* **143**, 23-49.

Hofmann A., Reimold W.U. and Koeberl C. (2006) Archean spherule layers in the Barberton Greenstone Belt, South Africa: A discussion of problems related to the impact interpretation. In Reimold W.U. and Gibson R.L. (eds.), Processes on the Early Earth: *Geol. Soc. Amer. Special Paper* **405**, 33-56.

Jarosewich E., Clarke R.S.J. and Barrows J.N. (1987) The Allende meteorite reference sample. *Smithsonian Contrib. Earth Sci.* **27**, 1-49.

Johnson B.C. and Melosh H.J. (2012). Impact spherules as a record of an ancient heavy bombardment of Earth. *Nature* **485**, 75-77.

Jourdan F., Reimold W.U. and Deutsch A. (2012) Dating terrestrial impact structures. *Elements* **8**, 49-53.

Kamo S.L., Reimold W.U., Krogh T.E. and Colliston W.P. (1996) A 2.023 Ga age for the Vredefort impact event and a first report of shock metamorphosed zircons in pseudotachylitic breccias and Granophyre. *Earth Planet. Sci. Lett.* **144**, 369-388.

17

Koeberl C. (2004) The Late Heavy Bombardment in the inner Solar System: Is there any connection to Kuiper Belt objects? *Earth, Moon and Planets* **92**, 79-87.

Koeberl C. (2014) The geochemistry and cosmochemistry of impacts. In Vol. 2 (ed. A. Davis), *Treatise on Geochemistry* (Second Edition) (eds. H. Holland and K. Turekian).Elsevier Ltd. pp. 73–118.

Koeberl C. and Shirey S.B. (1993) Detection of a meteoritic component in Ivory Coast tektites with rhenium-osmium isotopes. *Science* **261**, 595-598.

Koeberl C. and Reimold W.U. (1995) Early Archean spherule beds in the Barberton Mountain land, South Africa: no evidence for impact origin. *Precambrian Res.* **74**, 1-33.

Koeberl C., Reimold W.U. and Boer R.H. (1993) Geochemistry and mineralogy of Early Archean spherule beds, Barberton Mountain Land, South Africa: evidence for origin by impact doubtful. *Earth Planet. Sci. Lett.* **119**, 441-452.

Koeberl C., Schulz T., and Reimold W.U. (2015). Remnants of Early Archean Impact Deposits on Earth: Search for a Meteoritic Component in the BARB5 and CT3 Drill Cores (Barberton Greenstone Belt, South Africa). Proceedings, 13th Hypervelocity Impact Symposium. *Procedia Engin.* **103**, 310-317.

Krogh T. E., Davis D.W. and Corfu F. (1984) Precise U-Pb zircon and baddeleyite ages for the Sudbury area. In: The geology and ore deposits of the Sudbury structure, edited by Pye E. G., Naldrett A. J., and Giblin P. E. Special Publication 1. Toronto: Ontario Geological Survey, pp. 431–446.

Kyte F.T., Zhou L. and Lowe D.R. (1992) Noble metal abundances in an Early Archean impact deposit. *Geochim. Cosmochim. Acta* **56**, 1365–1372.

Kyte F.T., Shukolyukov A., Lugmair G.W., Lowe D.R. and Byerly G.R. (2003) Early Archean spherule beds: chromium isotopes confirm origin through multiple impacts of projectiles of carbonaceous chondrite type. *Geology* **31**, 283–286.

Lee S.R., Horton J.W. and Walker R.J. (2006) Confirmation of a meteoritic component in impact-melt rocks of the Chesapeake Bay impact structure, Virginia, USA – Evidence from osmium isotopic and PGE systematics. *Meteoritics Planet. Sci.* 41, 819-833.

Lowe D.R. and Byerly G.R. (1987) Reply to comments on "Early Archean silicate spherules of probable impact origin, South Africa and Western Australia." *Geology* **15**, 179–180, 181–182.

Lowe D. R. and Byerly G. R. (1999) Stratigraphy of the west-central part of the Barberton Greenstone belt, South Africa. In *Geologic Evolution of the Barberton Greenstone Belt, South Africa* (eds. D. R. Lowe and G. R. Byerly), *Geol. Soc. America*, Special Paper **329**, pp. 1-36.

Lowe D.R., Byerly G.R. and Kyte F.T. (2014) Recently discovered 3.42-3.23 Ga impact layers, Barberton Belt, South Africa: 3.8 Ga detrital zircons, Archean impact history, and tectonic implications. *Geology* **42(9)**: 747.

Lowe D.R., Byerly G.R., Asaro F. and Kyte F.T. (1989) Geological and geochemical record of 3400-million- year-old terrestrial meteorite impacts. *Science* **245**, 959–962.

Lowe D.R., Byerly G.R., Kyte F.T., Shukolyukov A., Asaro F. and Krull A. (2003) Spherule beds 3.47-3.24 billion years old in the Barberton Greenstone Belt, South Africa: a record of large meteorite impacts and their influence on early crustal and biological evolution. *Astrobiology* **3**, 7-47.

Luguet A., Nowell G.M. and Pearson D.G. (2008) $^{184}Os/^{188}Os$ and $^{186}Os/^{188}Os$ measurements by negative thermal ionisation mass spectrometry (N-TIMS): Effects of interfering element and mass fractionation corrections on data accuracy and precision. *Chem. Geol.* **248**, 342-362.

Luguet A., Behrens M., Pearson D.G., Koenig S. and Herwartz D. (2015) Significance of the whole-rock Re-Os ages in cryptically and modally metasomatised cratonic peridotites - Constraints from the HSE-Se-Te systematics. *Geochim. Cosmochim. Acta* **164**, 441-463.

Mader D. and Koeberl C. (2009) Using Instrumental Neutron Activation Analysis for geochemical analysis of terrestrial Impact structures: Current analytical procedures at the University of Vienna Geochemistry Activation Analysis Laboratory. *Appl. Radiat. Isot.* **67**, 2100-2103.

McLennan S.M. (2001) Relationships between trace element composition of sedimentary rocks and upper continental crust. *Geochem. Geophys. Geosyst.* **4**, doi: 10.1029/2000GC000109,2001.

Mohr-Westheide T., Fritz J., Hofmann A., Tagle R., Koeberl C., Reimold W.U., Mader D., Schulz. and Hoehnel D. (2014) Petrology and geochemistry of Archean spherule layer occurrences in the BARB5 ICDP drill core, Barberton Greenstone Belt. *Lunar and Planetary Science Conference* **45**, abstract No. 1356.

18

Mohr-Westheide T., Reimold W.U., Fritz J., Koeberl C., Salge T., Hofmann A. and Schmitt R.T. (2015) Discovery of extraterrestrial component carrier phases in Archean spherule layers: Implications for estimation of Archean bolide sizes. *Geology* **43**, 299-302.

Oezdemir S., Schulz T., Koeberl C., Reimold W.U., Mohr-Westheide T. and Hofmann A. (2016) Paleoarchean spherule beds in the CT3 drill core from the Barberton Greenstone Belt, South Africa: Geochemistry and Os isotopic signatures. *Meteoritics Planet. Sci. Conf., Abstracts of the Meteoritical Society Annual Meeting* #**6194**.

Puchtel I.S., Walker R.J., Anhaeusser C.R. and Gruau G. (2009) Re-Os isotope systematics and HSE abundances of the 3.5 Ga Schauenburg komatiites, South Africa: Hydrous melting or prolonged survival of primordial heterogeneities in the mantle? *Chem. Geol.* **262**, 355-369.

Puchtel I.S., Walker R.J., Touboul M., Nisbet E.G. and Byerly G.R. (2014) Insights into early Earth from the Pt-Re-Os isotope and highly siderophile element abundance systematics of Barberton komatiites. *Geochim. Cosmochim. Acta* **125**, 394-413.

Rasmussen B. and Koeberl C. (2004) Iridium anomalies and shocked quartz in a Late Archean spherule layer from the Pilbara craton: New evidence for a major asteroid impact at 2.63 Ga. *Geology* **32**, 1029-1032.

Rehkämper M. and Halliday A.N. (1997) Development and application of new ion-exchange techniques for the separation of the platinum-group and other siderophile elements from geological samples. *Talanta* 44, 663-672.

Reimold W.U., Koeberl C., Johnson S. and McDonald I. (2000) Early Archean Spherule Beds in the Barberton Mountain Land, South Africa: Impact or Terrestrial Origin? In: Impacts and the Early Earth (Eds. I Gilmour and C. Koeberl), Lecture Notes in Earth Sciences 91, Springer Verlag, Heidelberg, p. 117-180.

Ryder G. (1990) Lunar samples, lunar accretion, and the early bombardment history of the Moon. EOS, *Trans. Amer. Geophys. Union* **71**, 313-323.

Ryder G., Koeberl C. and Mojzsis (2000) Heavy Bombardment of the Earth at ~3.85 Ga: The search for petrographic and geochemical evidence. In: Origin of the Earth and Moon (Eds. R. Canup and K. Righter), University of Arizona Press, p. 475-492.

Schönberg R., Merdian A., Holmden C., Kleinhanns I.C., Haßler K., Wille M. and Ritter E. (2016) The stable Cr isotopic compositions of chondrites and silicate planetary reservoirs. *Geochim. Cosmochim. Acta* **183**, 14-30.

Schulz T., Luguet A., Wegner W., van Acken D. and Koeberl C. (2016). Target Rocks, impact glasses, and melt rocks from the Lonar crater, India: Highly siderophile element systematics and Sr-Nd-Os isotopic signatures. *Meteoritics Planet. Sci.* **51**, 1323-1339.

Shirey S.B. and Walker R.J. (1998) The Re-Os isotope system in cosmochemistry and high-temperature geochemistry. *Ann. Rev. Earth Planet. Sci.* **26**, 423-500.

Siebert C., Kramers J.D., Meisel T., Morel P. and Nägler T.F. (2005) PGE, Re-Os, and Mo isotope systematics in Archean and early Proterozoic sedimentary systems as proxies for redox conditions of the early Earth. *Geochim. Cosmochim. Acta* **69**, 1787-1801.

Simonson B.M. (1992) Geological evidence for a strewn field of impact spherules in the early Precambrian Hamersley Basin of Western Australia. *Geol. Soc. America Bull.* **104**, 829–839.

Simonson B.M. and Glass B.P. (2004) Spherule Layers – Records of Ancient Impacts. *Ann. Rev. Earth Planet. Sci.* **32**, 329-361.

Simonson B.M., Schubel K.A. and Hassler S.W. (1993) Carbonate sedimentology of the early Precambrian Hamersley Group of Western Australia. *Precambrian Res.* **60**, 287–335.

Simonson B.M., Hassler S.W. and Beukes N.J. (1999) Late Archean impact spherule layer in South Africa that may correlate with a Western Australian layer. In Large Meteorite Impacts and Planetary Evolution II, ed. BO Dressler, and V.L. Sharpton, *GSA Special Paper* 339:249–61. Boulder, CO: Geol. Soc. Am. 464 pp.

Simonson B.M., Davies D., Wallace M., Reeves S. and Hassler S.W. (1998) Iridium anomaly but no shocked quartz from Late Archean microkrystite layer: oceanic impact ejecta? *Geology* **26**,195–198.

Spray J. G., Butler H. R. and Thompson L. M. (2004) Tectonic influences on the morphometry of the Sudbury impact structure: Implications for terrestrial cratering and modeling. *Meteoritics Planet. Sci.* **39**, 287-301.

19

Tagle R. and Berlin J. (2008) A database of chondrite analyses including platinum group elements, Ni, Co, Au, and Cr: Implications for the identification of chondritic projectiles. *Met. Planet. Sci.* **43**, 541-559.

Völkening J., Walczyk T. and Heumann K.G. (1991) Osmium isotope ratio determinations by negative termal ionization mass-spectrometry. *Int. J. Mass Spectrom. Ion Process.* **105**, 147-159.

Žák K., Skála R., Řanda Z., Mizera J., Heissig K., Ackerman L., Ďurišová J., Jonášová Š., Kameník J. and Magna T. (2016) Chemistry of Tertiary sediments in the surroundings of the Ries impact structure and moldavite formation revisited. *Geochim. Cosmochim. Acta* **179**, 287–311.

20

FIGURE CAPTIONS

Fig. 1: Cross section of the spherule layer section (SLC), showing the B-D spherule layers in the BARB5 drill core). Country rocks (exclusively shales) were sampled from above and below the SLC. Samples 1-22 from the SLS are frequently sublabelled throughout the text either with the prefix „IC" in case of intercalations (samples IC-1, IC-2, IC-7, IC-12, IC-13, IC-17 and IC-22) or with the spherule layer nomenclature to which the samples can be assigned (samples B-3 to B-6 for spherule layer B, samples C-8 to C-11 for spherule layer C, samples D-14 to D-16 for spherule layer D and samples E-18 to E-21 for spherule layer E).

Fig. 2: Upper crust normalized spider diagrams of (a) samples from the spherule layer section (samples 1-22, dark lines) and country rocks (shale samples devoid of spherules; grey-dotted lines), (b) spherule-bearing samples and country rocks from the CT3 core (Oezdemir et al., 2016), and (c) S2 country rock and spherule layer samples (Reimold et al., 2000). Elements are listed in order of increasing compatibility. Data for normalization from McLennan (2001).

Fig. 3: Interelement diagrams for country rocks and samples from the spherule layer section (samples 1-22) for (a) Ni vs. Cr (R^2=0.65), (b) Ni vs. Co (R^2=0.71), (c) Ni vs. Au (R^2=0.80) and (d) Ni vs. W. R^2 = correlation factor.

Fig. 4: Interelement diagrams for Fig Tree Group sediments (data from Siebert et al., 2005) and samples from the spherule layer section (samples 1-22) for (a) Os vs. Re (no correlation), (b) Os vs. Ir (R^2=0.67), (c) Ir vs. Pt (R^2=0.84) and (d) Ru vs. Pd (R^2=0.79). Also shown are the ranges of highly siderophile element concentrations for chondrite groups (data from Tagle and Berlin, 2008). Note that all interelement correlations end-up in the concentration range typical for some of the chondrite groups. R^2 = correlation factor.

Fig. 5: Interelement diagrams for country rocks and samples from the spherule layer section (samples 1-22) for (a) As vs. Au (R^2=0.06), (b) Au vs. Sb (R^2=0.41), (c) Ni vs. As (R^2=0.31) and (d) Ir vs. As (R^2=0.01), exemplifying the only minor influence of hydrothermal overprint on the analyzed samples. R^2 = correlation factor.

Fig. 6: Nickel vs. Co and Cr vs. Co interelement diagrams, showing the degrees of postulated chondritic admixture to samples from the spherule layer section (samples 1-22), mostly ranging from ~10 to ~100%. Note that none of the mixing lines (between the average target material and chondrite groups) exactly match the trend defined by samples from the SLS. Data for chondrites were taken from Tagle and Berlin (2008).

Fig. 7: Interelement ratio diagrams for the transition metals (Cr, Co, and Ni) and Au, exemplifying the differences between non-impact lithologies (country rocks; data from this study) and samples from the spherule layer section (SLS; samples 1-22). The latter scatter significantly, but tend to plot nearer to the chondrite trend (data from Tagle and Berlin, 2008).

21

Fig. 8: Diagrams showing (a) Os/Ir vs. Ir for spherule-bearing samples (samples 1-22 from the spherule layer section), showing a trend towards chondritic Os/Ir ratios with increasing Ir concentrations. (b) ^{187}Os/^{188}Os vs. Os diagram showing a continuous trend towards less radiogenic Os isotope compositions with increasing (closer to chondritic values) Os concentrations. Data for non-impact Fig Tree Group sediments are from Siebert et al. (2005). Chondrite data from Tagle and Berlin (2008).

Fig. 9: Diagram exemplifying the magnitude of the proposed meteoritic component in dependence of the minimum Cr/Ir ratios measured for the B and C-E spherule layers. Note that for spherule layer B maximum meteoritic components are between ~3 to ~9%, depending on the assumed type of chondritic contaminant, whereas spherule layers C-E exhibit maximum meteoritic admixtures between ~40 and up to 100%. Low metal ordinary and CI chondrites have Cr/Ir ratios that lie above the minimum values measured for spherule layers C-E. Meteorite data from Tagle and Berlin (2008).

22

Table 1: Minor- and trace element abundances for country rocks (samples CR-a to CR-h; sediments from the Fig Tree group) and samples from the BARB5 spherule layer section.

sample	CR-a	CR-b	CR-c	CR-d	CR-e	CR-f	CR-g	CR-h	IC-1	IC-2	B-3	B-4	B-5	B-6	IC-7
core depth	489.70	494.72	500.10	505.14	510.03	515.33	520.31	524.66	511.51	511.50	511.49	511.48	511.47	511.46	511.45
unit	CR	CR	CR	CR	CR	CR	CR	CR	SLS	SLS	SLS	SLS	SLS	SLS	SLS
sub-unit									IC	IC	SL-B	SL-B	SL-B	SL-B	IC
lithology	sh	sh	sh	sh	sh	sh	sh	sh	ch+sph	ch+sph	sph+sh	sph+sh	sph+sh	sph+sh	sh+sph
Na	161	235	46.9	175	150	221	203	186	115	36.6	241	415	439	362	214
K*	2.19	3.12	0.37	1.60	1.62	3.21	3.52	3.14	1.49	0.40	4.47	9.64	9.81	9.40	4.97
Sc	15.7	21.4	6.31	11.4	9.09	20.5	21.8	19.2	24.8	6.09	30.9	29.8	63.7	68.3	41.3
Cr	635	896	271	571	505	960	946	890	339	82.2	533	357	736	2930	3562
Fe*	9.00	10.9	18.9	18.9	21.2	6.31	6.41	5.32	21.9	3.71	13.1	3.30	2.45	3.41	10.6
Co	25.9	37.9	17.9	24.6	16.2	42.9	35.9	33.1	31.9	7.2	22.3	18.7	23.2	72.3	471
Ni	246	334	105	285	275	341	377	338	623	124	473	470	326	1159	3476
Zn	70	115	44	66	48	172	104	130	72	15	60	40	<29	<38	62
Ga	26	41	24	<1.3	<1.3	25	28	22	<2.1	5.9	17	6.5	12	22	<6.6
As	5.56	18.3	1.94	5.93	0.49	19.7	1.62	10.7	<0.4	0.06	<0.3	2.37	4.23	20.6	187
Se	<1.8	<2.5	<1.8	<1.9	<2	1.57	<2.2	0.74	<2.9	<1.4	<2.6	<2.3	<3.2	4.11	17.8
Br	<0.4	<0.9	<0.4	<0.3	<0.2	<0.4	<0.4	<0.4	<0.4	0.2	<0.3	<0.3	<0.6	<0.9	<0.8
Rb	65.7	80.1	12.4	55.5	70.2	138	147	136	82.1	19.4	183	295	435	465	250
Sr	67	106	64	138	54	93	80	58	<41	47	89	<47	<62	<32	<46
Zr	87	91	49	75	69	138	101	137	93	22	97	98	64	115	215
Sb	0.17	0.26	0.11	0.13	0.12	0.35	0.38	0.40	0.14	0.07	0.25	0.36	0.52	0.61	2.18
Cs	1.68	2.00	0.41	1.72	1.72	3.43	3.91	3.91	1.90	0.54	4.14	6.61	13.3	13.0	6.98
Ba	1183	2011	335	1795	2024	2087	2030	1737	1151	305	4356	8579	7411	6466	2963
La	9.93	14.1	4.94	10.6	8.32	13.1	13.4	13.3	7.20	1.18	6.33	5.19	1.72	3.35	19.7
Ce	18.5	24.5	8.53	18.0	15.2	24.6	25.9	25.7	13.9	2.57	14.7	15.0	3.75	8.50	44.4
Nd	8.95	12.0	3.78	8.54	7.69	11.4	14.0	13.0	8.16	1.72	10.1	12.0	<2.6	5.08	25.0
Sm	2.23	2.51	0.99	2.18	1.69	3.01	3.22	3.05	2.42	0.64	2.76	3.94	1.04	1.68	6.81
Eu	0.62	0.75	0.38	0.62	0.55	0.78	0.80	0.82	0.78	0.31	0.79	1.09	0.42	0.59	2.14
Gd	1.84	2.32	1.18	2.16	<0.3	2.72	2.76	2.53	3.76	0.85	3.29	4.06	<0.5	1.94	6.67
Tb	0.31	0.42	0.22	0.35	0.31	0.43	0.43	0.40	0.80	0.32	0.51	0.68	0.20	0.40	1.15
Tm	0.18	0.22	0.21	0.20	0.21	0.20	0.22	0.17	0.39	0.09	0.24	0.21	0.22	0.30	0.40
Yb	1.18	1.72	0.81	1.27	0.99	1.43	1.39	1.32	2.99	0.73	1.43	1.23	0.98	1.28	2.16
Lu	0.18	0.26	0.13	0.19	0.16	0.23	0.22	0.21	0.46	0.10	0.23	0.18	0.15	0.20	0.28
Hf	1.65	2.20	0.52	1.39	1.41	2.40	2.56	2.45	0.93	0.22	1.90	1.77	3.11	2.99	2.63
Ta	0.27	0.39	0.10	0.28	0.25	0.41	0.42	0.40	0.17	0.02	0.26	0.22	0.29	0.38	0.46
W	0.40	<2.5	<0.9	0.40	0.30	0.40	<0.9	0.30	7.3	7.7	13	12	11	5.7	11
Os	<0.1	<0.2	<0.1	<0.2	<0.2	<0.2	<0.2	<0.2	<0.1	<0.1	<0.2	<0.2	0.32	0.50	0.36
Ir**	<0.3	<0.5	<0.3	<0.3	<0.3	<0.3	<0.3	<0.3	2.42	0.33	6.71	10.2	8.41	7.61	355
Au**	<0.6	<1.2	<0.7	<0.5	<0.5	0.8	0.9	0.7	1.7	1.1	1.2	1.4	1.0	1.8	10
Th	2.54	2.93	0.75	2.38	2.41	3.35	3.77	3.59	1.46	0.29	1.43	0.72	1.01	1.22	2.92
U	0.49	0.92	0.26	0.59	0.50	1.15	1.09	0.96	0.23	<0.1	0.43	<0.2	<0.3	0.65	0.81

CR = country rocks; SLS = spherule layer section; IC = intercalation; SL-B = spherule layer B; sh = shale; ch = chert; sph = spherules. All concentrations in ppm, with the exception of * = wt.% and ** = ppb.

Table 1 (continued): Minor- and trace element abundances for samples from the BARB5 spherule layer section.

sample	C-8	C-9	C-10	C-11	IC-12	IC-13	D-14	D-15	D-16	IC-17	E-18	E-19	E-20	E-21	IC-22
core depth	511.44	511.43	511.42	511.41	511.40	511.39	511.38	511.37	511.36	511.35	511.34	511.33	511.32	511.31	511.30
unit	SLCS	SLCS	SLCS	SLCS	SLCS	SLCS	SLCS	SLCS	SLCS	SLCS	SLCS	SLCS	SLCS	SLCS	SLCS
sub-unit	SL-C	SL-C	SL-C	SL-C	IC	IC	SL-D	SL-D	SL-D	IC	SL-E	SL-E	SL-E	SL-E	IC
lithology	sph+sh	sph+sh	sph+sh	sph+sh	sh+sph	sh+sph	sph+sh	sph+sh	sph+sh	sh+sph	sph+sh	sph+sh	sph+sh	sph+sh	sh+sph
Na	253	414	362	345	258	130	317	399	410	247	378	376	405	341	172
K*	4.15	8.12	7.23	7.45	5.99	1.80	6.13	8.42	8.54	5.00	7.45	8.20	9.46	6.86	2.85
Sc	28.9	31.2	28.9	26.2	29.1	27.4	28.4	31.7	34.4	23.1	32.9	28.2	25.0	27.7	19.6
Cr	1596	2954	2033	2560	2196	434	1772	3211	3164	1197	2296	2644	1543	2432	1084
Fe*	13.1	5.92	7.62	7.34	7.32	26.3	11.9	6.75	8.93	11.2	10.3	3.89	4.83	7.23	16.0
Co	139	247	286	502	2696	67.4	783	322	515	210	357	173	228	141	224
Ni	2217	3840	3396	2938	3206	1005	3688	3709	5435	1322	3794	1471	2218	2334	1552
Zn	59	68	45	74	111	72	68	78	85	45	92	64	49	82	66
Ga	44	29	26	41	44	43	58	11	36	15	23	9	27	41	67
As	45.2	68.5	88.8	465	3600	0.62	292	69.6	121	50.3	70.5	44.3	69.0	31.0	87.6
Se	9.40	14.6	18.5	15.3	<8	2.72	32.0	22.4	32.6	<2.9	18.1	7.15	9.72	<3.3	14.8
Br	<0.6	<0.7	<0.6	<0.8	<2.9	<0.8	<1.5	<0.7	<1.4	<0.7	<1.0	<0.7	<1.2	<1.1	<1.0
Rb	181	316	292	279	245	86.8	252	314	347	162	275	281	299	265	122
Sr	<63	<70	<66	<71	<158	<61	<81	<61	<74	<54	<78	<55	<62	<61	<49
Zr	272	190	188	205	<208	103	<101	183	154	100	154	136	129	203	145
Sb	1.05	1.08	1.35	2.00	<1	0.37	6.25	2.08	3.32	0.86	1.59	1.04	1.20	1.28	1.43
Cs	4.82	9.01	8.25	6.62	7.11	1.89	6.99	9.44	10.4	4.32	7.61	7.66	7.50	6.55	2.73
Ba	2834	5689	5084	4943	3879	1186	4519	5862	6471	3238	5490	5998	7661	5539	2060
La	25.7	12.9	6.42	12.6	30.6	14.9	22.6	13.9	12.8	11.4	14.8	6.53	9.35	18.9	14.1
Ce	52.5	29.8	14.7	30.8	58.2	26.3	40.7	29.0	25.3	21.3	27.4	14.2	19.4	35.2	25.7
Nd	29.0	16.6	8.89	20.5	23.7	11.5	20.0	16.1	12.0	9.93	12.5	8.14	11.5	18.0	12.6
Sm	8.64	5.04	2.88	6.56	6.18	3.20	4.96	3.94	3.20	2.48	3.14	2.09	3.05	4.42	2.93
Eu	2.55	1.62	1.04	2.11	2.32	1.11	1.85	1.36	1.21	0.91	1.14	0.88	1.13	1.56	1.11
Gd	9.14	5.35	3.42	6.94	6.81	3.32	5.86	3.95	3.91	2.45	3.38	2.27	2.94	4.87	3.18
Tb	1.24	0.82	0.62	1.21	1.08	0.59	1.09	0.61	0.73	0.44	0.54	0.48	0.51	0.85	0.50
Tm	0.36	0.38	0.31	0.36	0.54	0.43	0.45	0.35	0.34	0.22	0.34	0.23	0.23	0.37	0.24
Yb	2.39	1.75	1.56	2.15	2.62	1.24	2.71	1.58	1.89	1.30	1.77	1.39	1.45	2.26	1.44
Lu	0.34	0.25	0.22	0.30	0.30	0.21	0.38	0.26	0.26	0.20	0.26	0.20	0.21	0.31	0.24
Hf	3.51	3.31	3.08	2.81	2.23	1.26	3.60	3.60	4.17	2.17	3.20	2.61	2.93	3.94	2.30
Ta	0.47	0.52	0.36	0.51	0.73	0.24	0.48	0.61	0.50	0.32	0.62	0.46	0.38	0.73	0.34
W	7.4	7.9	5.8	9.2	13.0	6.99	12.7	11.4	11.9	8.60	8.87	11.0	11.5	21.5	8.30
Os	0.47	0.04	<0.3	0.40	0.70	<0.3	<0.4	0.56	0.47	0.38	0.32	0.36	<0.3	<0.3	<0.3
Ir**	321	606	239	447	386	35.8	166	671	735	166	374	531	139	335	141
Au**	9.0	15	7.5	14	9.9	1.6	10	10	17	4.1	5.9	7.7	3.7	5.5	3.7
Th	5.07	2.87	2.11	3.39	3.06	2.08	4.12	3.97	4.07	5.55	2.94	1.97	1.96	5.69	3.23
U	1.08	1.10	0.80	1.08	<1.4	0.50	0.97	1.00	1.27	0.90	0.99	0.60	0.72	1.49	<0.4

CR = country rocks; SLS = spherule layer section; IC = intercalation; SL-X = spherule layers C to E; sh = shale; sph = spherules. All concentrations in ppm, with the exception of * = wt.% and ** = ppb.

Table 2: Rhenium-Os isotope and highly siderophile element abundances of samples from the BARB5 spherule layer section.

sample	Os		Ir		Ru	Pt	Pd	Re	$^{187}Re/^{188}Os$	$\pm2\sigma$	$^{187}Os/^{188}Os$	$\pm2\sigma$	$(^{187}Os/^{188}Os)i$
	ID	INAA	ID	INAA	ID	ID	ID	ID					
IC-1	0.35	<100	-	2.42	-	-	-	-	-	-	0.3161	0.0020	-
IC-2	8.58	<100	0.91	0.33	-	2.09	-	0.34	0.1918	0.0058	0.2875	0.0028	0.2764
B-3	1.46	<200	23.22	6.71	-	59.15	-	-	-	-	0.2763	0.0028	-
B-4	17.1	<200	4.53	10.2	-	5.22	-	0.04	0.0101	0.0003	0.2233	0.0054	0.2217
B-5	10.8	320	10.15	8.41	14.64	50.85	4.58	0.23	0.1032	0.0031	0.1344	0.0003	0.1284
B-6	4.40	500	6.02	7.61	32.58	59.08	10,92	0.20			0.2388	0.0024	-
IC-7	57.06	360	47.50	355	103.1	155.2	81.28	3.19	0.2663	0.0080	0.1245	0.0015	0.1090
C-8	944.5	470	488.7	321	932.0	807.3	1086	3.41	0.0172	0.0005	0.1064	0.0001	0.1054
C-9	-	40	-	606	-	-	-	-					
C-10	140.0	100	147.9	239	-	491.7	-	1.47	0.0502	0.0015	0.1290	0.0060	0.1261
C-11	-	400	-	447	-	-	-	-					
IC-12	396.1	700	234.0	386	-	556.2	-	26.1	0.3140	0.0094	0.1213	0.0001	0.1030
IC-13	42.57	<300	23.22	35.8	-	59.15	-	2.53	0.2809	0.0084	0.1689	0.0003	0.1525
D-14	150.5	<400	103.1	166	-	283.3	-	4.63	0.1464	0.0044	0.1262	0.0002	0.1177
D-15	540.1	560	552.0	671	1232	2082	684	5.88	0.0517	0.0016	0.1150	0.0002	0.1120
D-16	464.5	470	-	735	-	-	-	-	-	-	0.1217	0.0005	-
IC-17	99.9	380	-	166	-	-	-	-	-	-	0.1197	0.0004	-
E-18	332.8	320	218	374	324.7	739.3	162.4	1.74	-	-	0.1110	0.0005	-

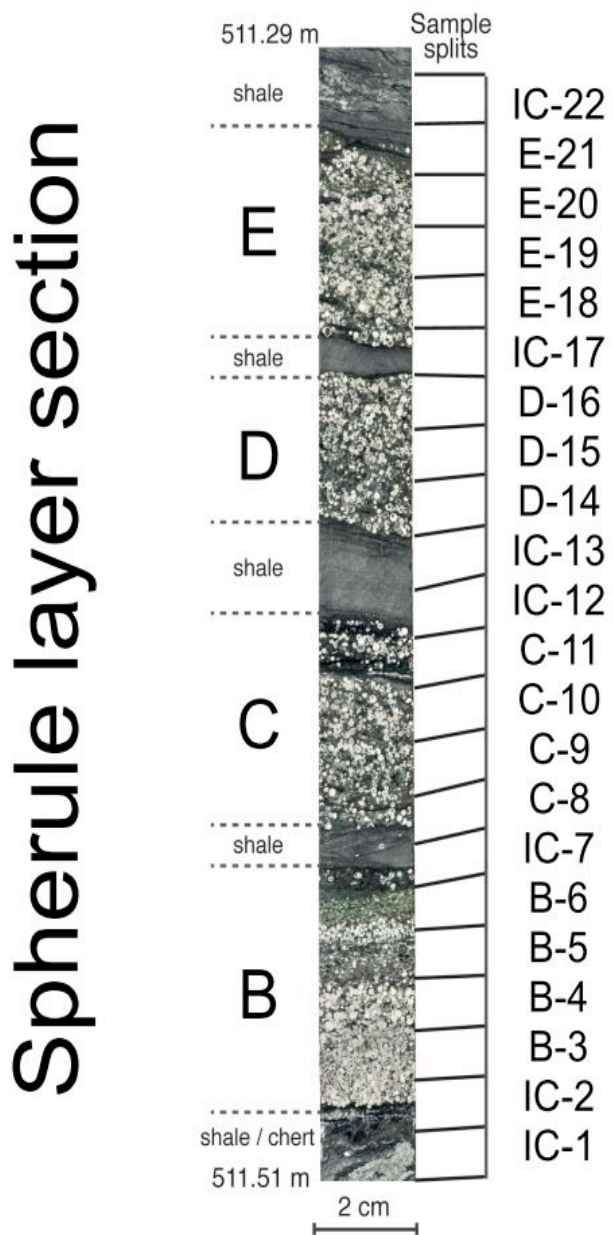ID = isotope dilution; INAA = instrumental neutron activation analysis. All concentrations in ppb. $(^{187}Os/^{188}Os)i$ = back-calculated to 3.32 Ga.
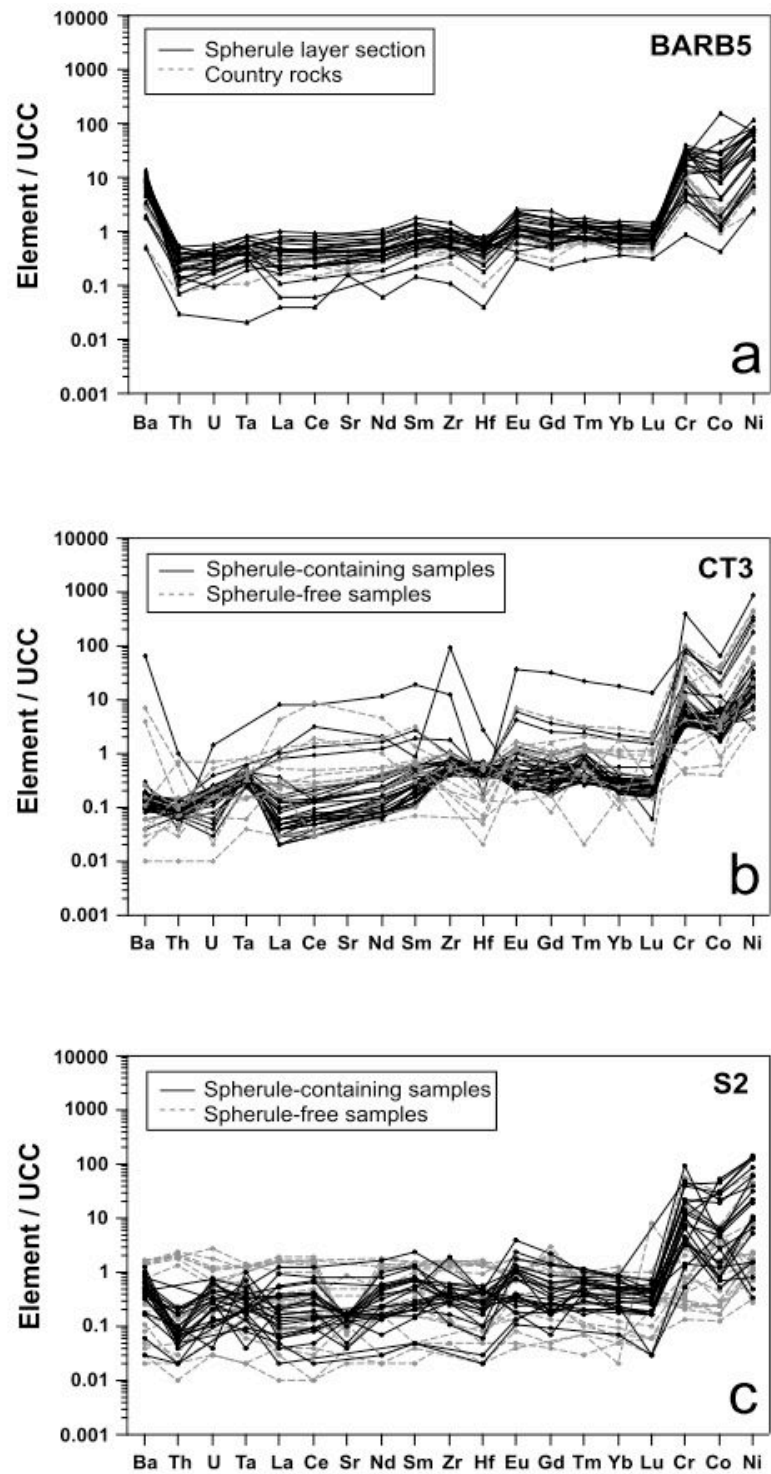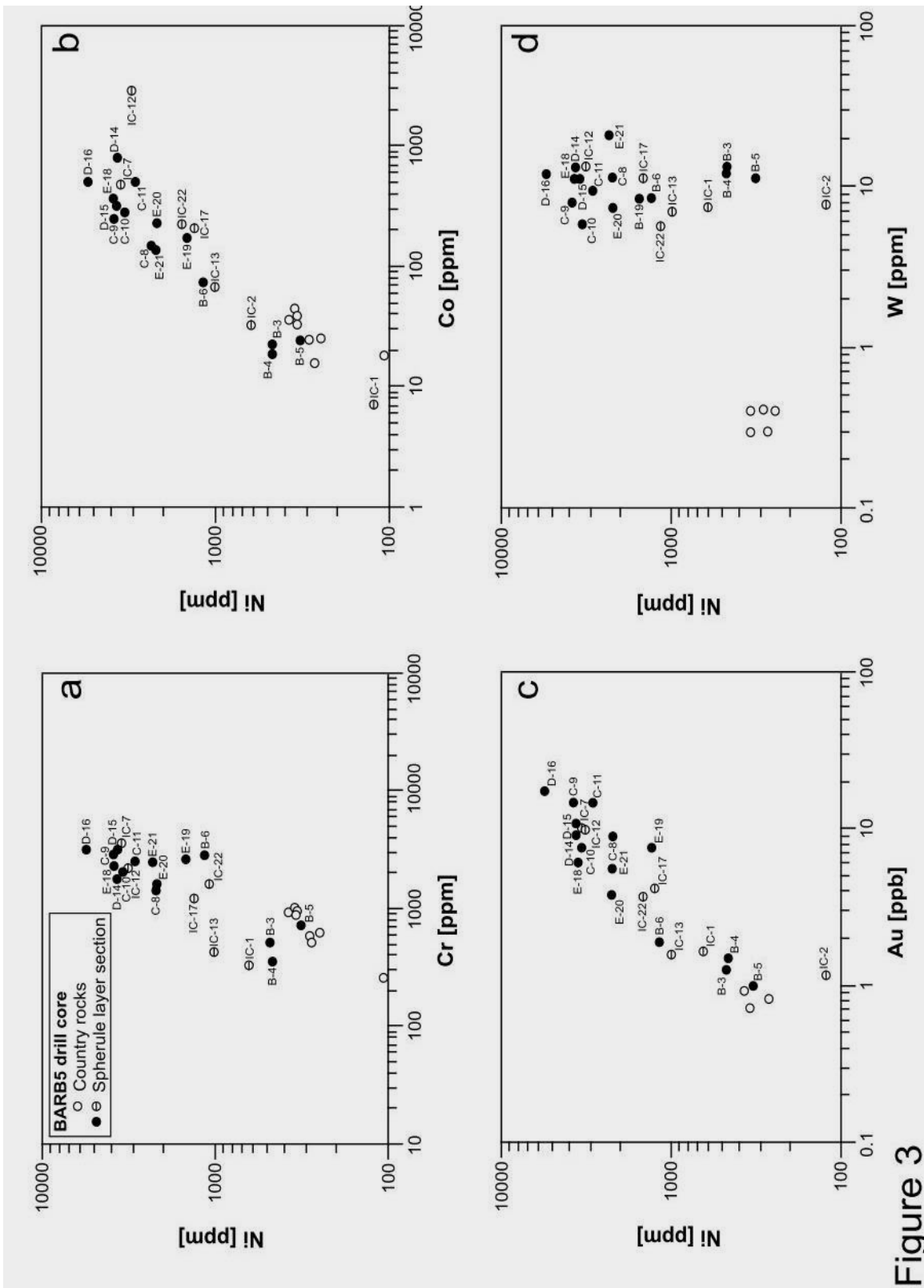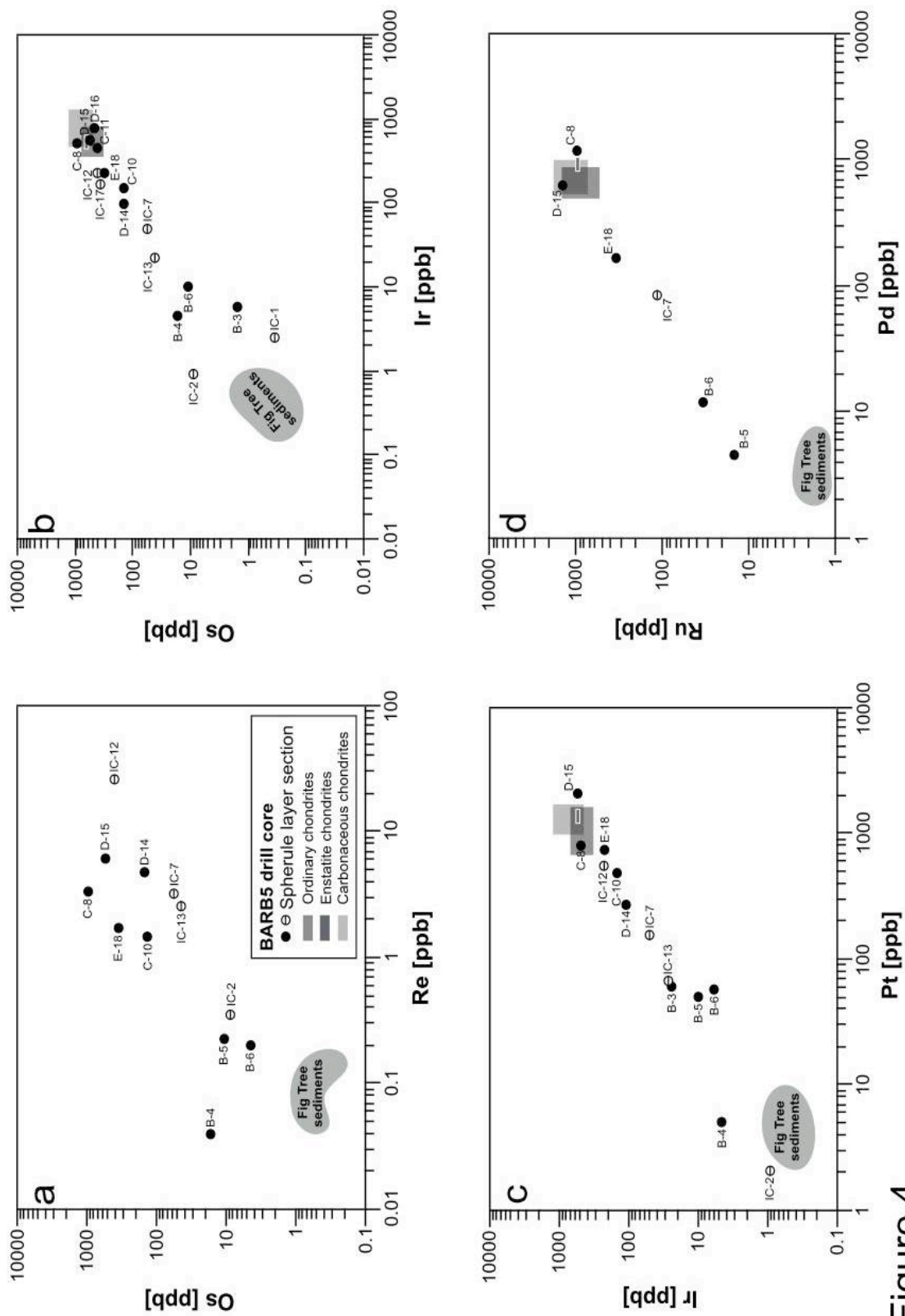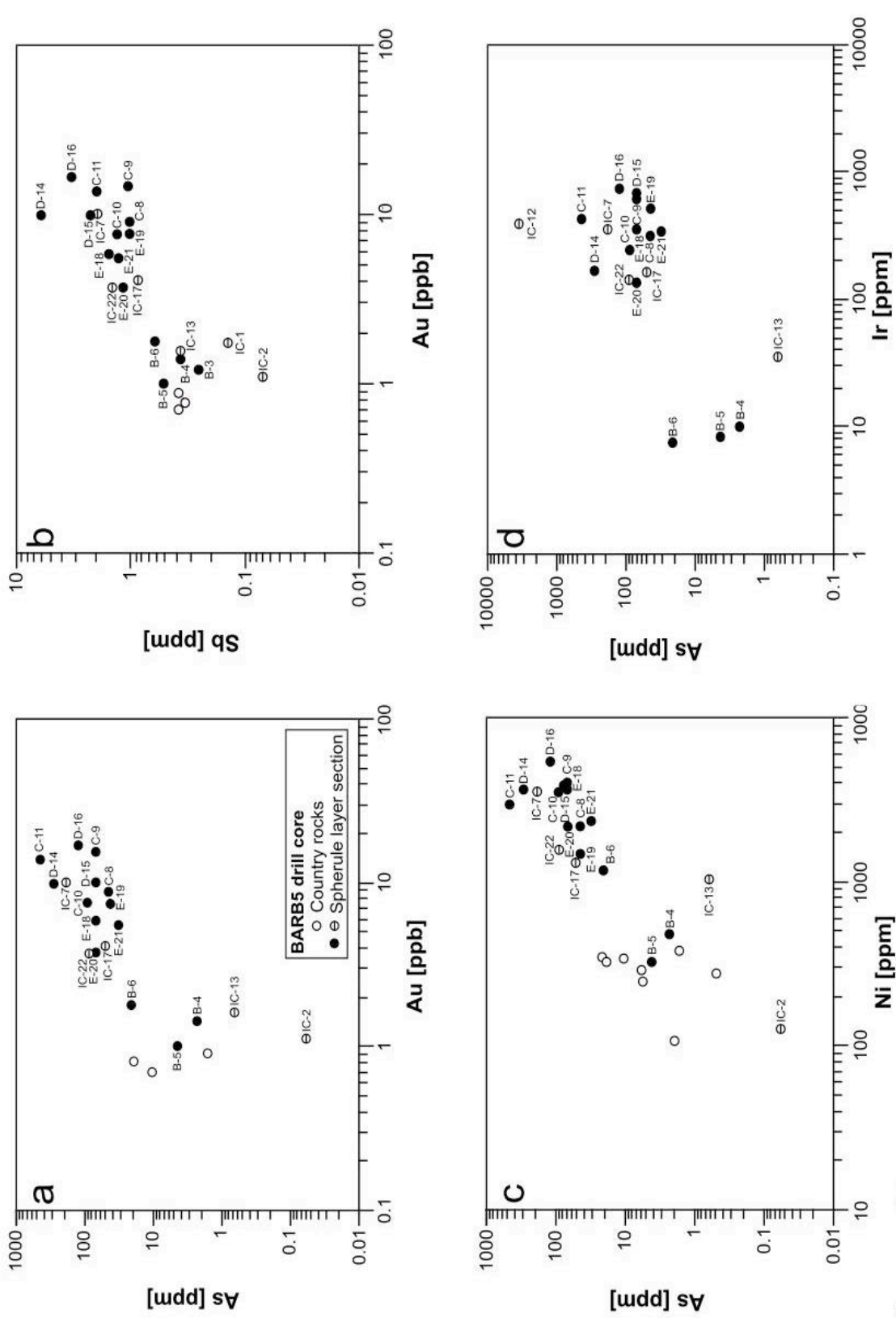
Figures
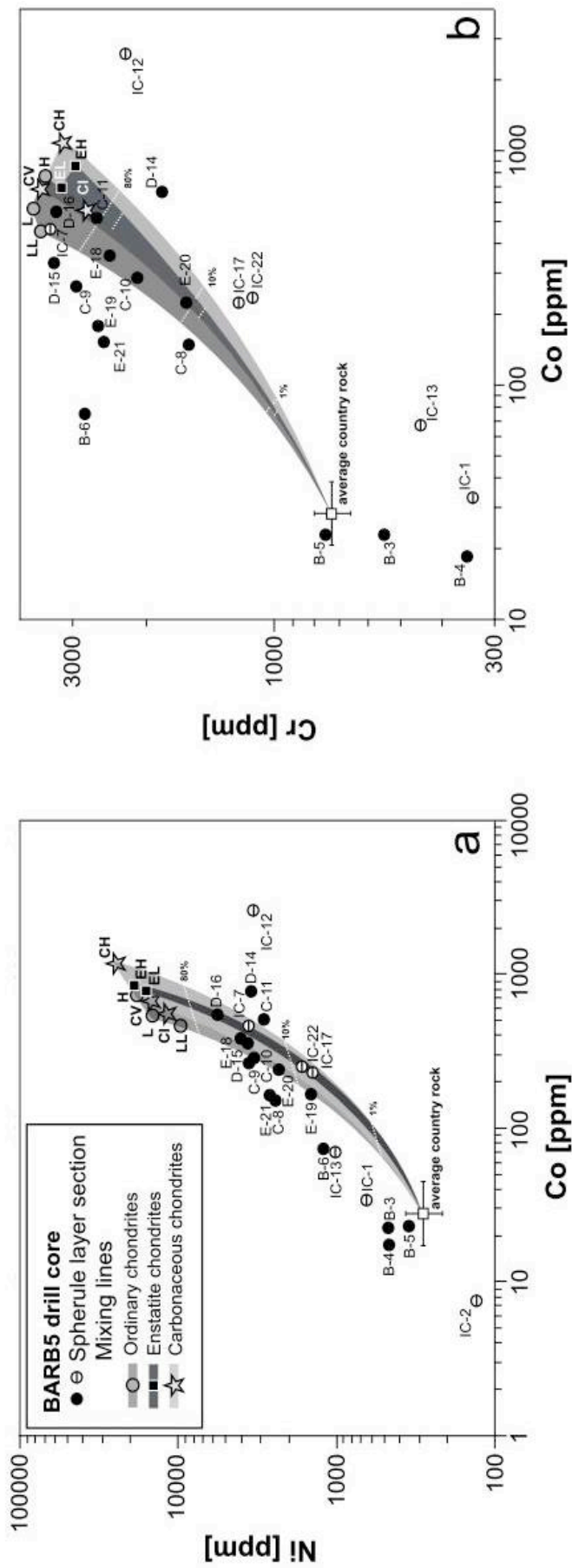

Figure 1

Figure 2

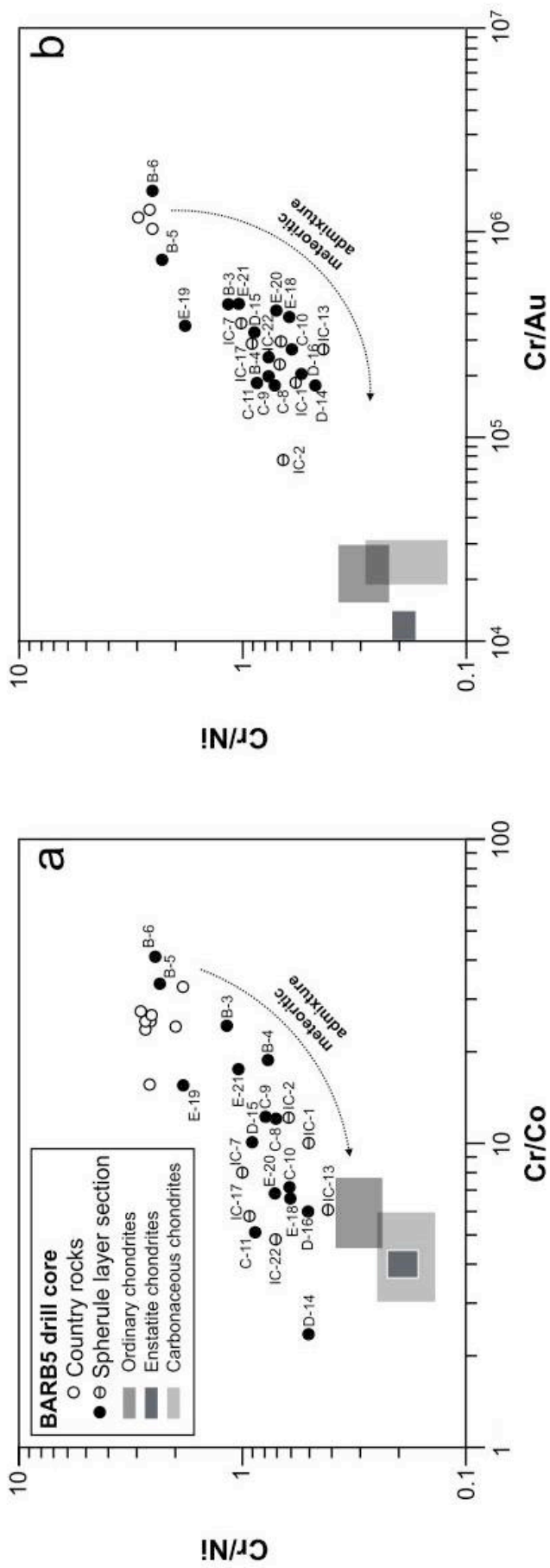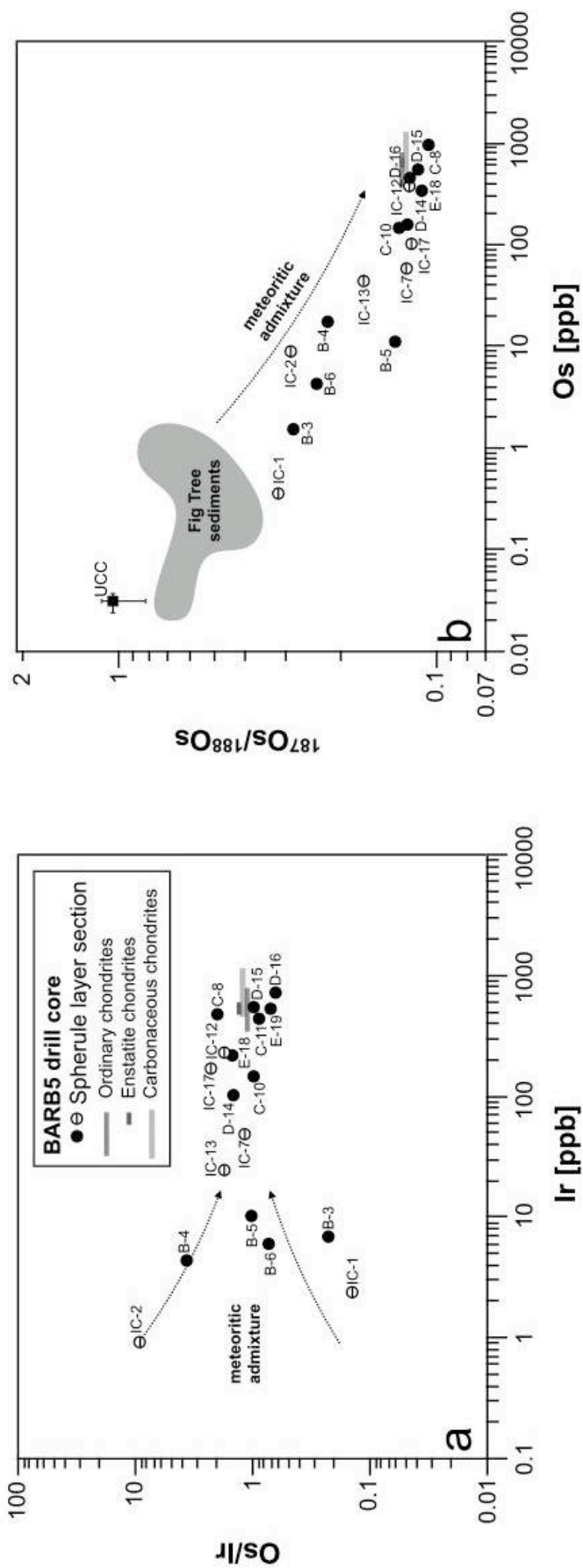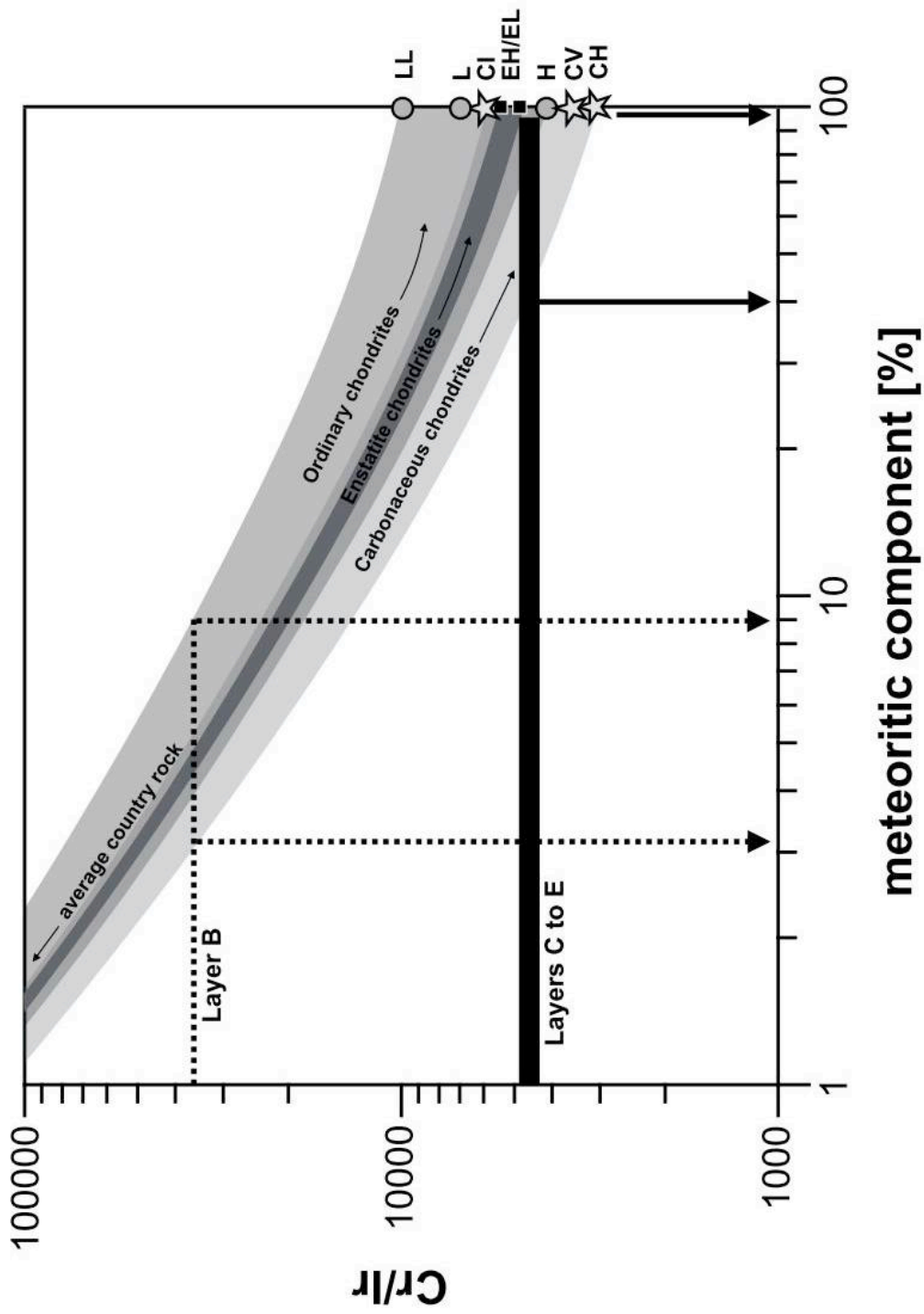Figure 3

Figure 4

Figure 5

Figure 6

Figure 7

Figure 8

Figure 9

CHAPTER 6. NONDESTRUCTIVE SPECTROSCOPIC AND PETROCHEMICAL INVESTIGATIONS OF PALEOARCHEAN SPHERULE LAYERS FROM THE ICDP DRILL CORE BARB5, BARBERTON MOUNTAIN LAND, SOUTH AFRICA

Nondestructive spectroscopic and petrochemical investigations of Paleoarchean spherule layers from the ICDP drill core BARB5, Barberton Mountain Land, South Africa

Jörg FRITZ[1,2,*], Roald TAGLE[3], Luisa ASHWORTH[4], Ralf Thomas SCHMITT[2], Axel HOFMANN[5], Béatrice LUAIS[6], Phillip D. HARRIS[4], Desirée HOEHNEL[2,7], Seda ÖZDEMIR[8], Tanja MOHR-WESTHEIDE[2,9], and Christian KOEBERL[8,10]

[1]Saalbau Weltraum Projekt, Wilhelmstrasse 38, 64646 Heppenheim, Germany
[2]Museum für Naturkunde—Leibniz Institute for Evolution and Biodiversity Science, Invalidenstrasse 43, 10115 Berlin, Germany
[3]Bruker-Nano GmbH, Am Studio 2D, 12489 Berlin, Germany
[4]GeoSpectral Imaging, Office E6 Block E, Somerset Office Estate, 604 Kudu Street, Allens Nek, 1737 Johannesburg, South Africa
[5]Department of Geology, University of Johannesburg, PO Box 524, Auckland Park, 2006 Johannesburg, South Africa
[6]Centre de Recherches Pétrographiques et Géochimiques, CRPG UMR 7358 CNRS-UL, 15 rue Notre Dame des Pauvres, 54500 Vandœuvre les Nancy, France
[7]Institut für Erd und Umweltwissenschaften, Universität Potsdam, Karl-Liebknecht-Str. 24-25, 14476 Potsdam-Golm, Germany
[8]Department of Lithospheric Research, University of Vienna, Althanstrasse 14, 1090 Vienna, Austria
[9]Institut für Geologische Wissenschaften, Freie Universität Berlin (FU Berlin), Malteserstrasse 74-100, D-12249 Berlin, Germany
[10]Natural History Museum, Burgring 7, 1010 Vienna, Austria
*Corresponding author. E-mail: joerg.fritz@kino-heppenheim.de

Abstract–A Paleoarchean impact spherule-bearing interval of the 763 m long International Continental Scientific Drilling Program (ICDP) drill core BARB5 from the lower Mapepe Formation of the Fig Tree Group, Barberton Mountain Land (South Africa) was investigated using nondestructive analytical techniques. The results of visual observation, infrared (IR) spectroscopic imaging, and micro-X-ray fluorescence (μXRF) of drill cores are presented. Petrographic and sedimentary features, as well as major and trace element compositions of lithologies from the micrometer to kilometer-scale, assisted in the localization and characterization of eight spherule-bearing intervals between 512.6 and 510.5 m depth. The spherule layers occur in a strongly deformed section between 517 and 503 m, and the rocks in the core above and below are clearly less disturbed. The μXRF element maps show that spherule layers have similar petrographic and geochemical characteristics but differences in (1) sorting of two types of spherules and (2) occurrence of primary minerals (Ni-Cr spinel and zircon). We favor a single impact scenario followed by postimpact reworking, and subsequent alteration. The spherule layers are Al_2O_3-rich and can be distinguished from the Al_2O_3-poor marine sediments by distinct Al-OH absorption features in the short wave infrared (SWIR) region of the electromagnetic spectrum. Infrared images can cover tens to hundreds of square meters of lithologies and, thus, may be used to search for Al-OH-rich spherule layers in Al_2O_3-poor sediments, such as Eoarchean metasediments, where the textural characteristics of the spherule layers are obscured by metamorphism.

INTRODUCTION

The Earth-Moon system experienced episodes of heavy bombardment by fragments of planetary bodies including asteroids and comets during its first ~1.5 Ga (Koeberl 2006; Fernandes et al. 2013; Fritz et al. 2014). To date, the most precise data pertaining to the intensity of the impact flux on the Earth-Moon system

(bombardment timeline) has been determined for the lunar Imbrian System, particularly for the Lower Imbrian epoch (~3.7–3.2 Ga): various volcanic surfaces of well-defined radiometric ages and crater densities provide detailed information (Wilhelms 1987; Neukum et al. 2001). Following the Orientale impact, the Lower Imbrian crater record on the Moon includes three impact craters larger than 150 km diameter, the Tsiolkovskiy (180 km Ø), Humboldt (207 km Ø), and Iridum (260 km Ø) craters. The global lunar impact record, together with a Moon/Earth impact rate of ~1/ 20 (Öpik 1960) implies that an intense bombardment of Earth must have occurred during the Eo- and Paleoarchean (the latter ranging from 3.6 to 3.2 Ga; Gradstein et al. 2004).

On Earth traces of large impact events as old as 3.47 Ga have been preserved in impact spherule-bearing layers within Paleoarchean sedimentary rocks of the Kaapvaal (South Africa) and the Pilbara (Western Australia) cratons (e.g., Lowe and Byerly 1986; Kyte et al. 1992; Koeberl and Reimold 1995; Reimold et al. 2000; Shukolyukov et al. 2000; Simonson and Harnik 2000; Simonson and Glass 2004; Hofmann et al. 2006; Glass and Simonson 2013; Lowe et al. 2014). Up to eight different Paleoarchean spherule layers have been reported from stratigraphically different positions in the Barberton Greenstone Belt of the Kaapvaal craton (Lowe et al. 2003, 2014). Spherule layers from Paleoarchean sedimentary successions on Earth allow the study of impacts on the early Earth, and the nature of some of the asteroids or comets that were on Earth-crossing orbits during that distant time.

Fresh samples of Paleoarchean spherule layers in the Barberton Mountain Land were obtained through the International Continental Scientific Drilling Program (ICDP); five drill cores denoted BARB1 to BARB5 were retrieved from the central part of the Barberton Mountain Land during the "Barberton Drilling Project: Peering into the Cradle of Life" campaign (Arndt et al. 2012, 2013). The BARB5 core includes several intersections of Paleoarchean spherule layers interbedded with Fig Tree Group metasediments that were deposited in a marine setting well below the storm-weather wave base (Lowe and Nocita 1999). The present contribution investigates the spherule layers by means of noninvasive methods including optical inspection, infrared imaging, and spatially resolved micro-X-ray fluorescence (µXRF) spectrometry.

Noninvasive Analytics

Infrared imaging of drill cores is a nondestructive technique whereby core trays and/or samples are imaged by cameras measuring across the infrared range of the electromagnetic spectrum. This is done for mineral identification, mapping, and the monitoring of mineral composition (e.g., Thompson et al. 1999; Harraden et al. 2013; Tappert et al. 2013). It is based on the principle that certain wavelengths of light are absorbed by minerals because of electronic and vibrational processes occurring within them at the molecular level (Clark 1999; Doublier et al. 2012). Absorption features associated with overtones and combinations are measureable in the shortwave infrared (SWIR) range between 1000 nm and 2500 nm. These effects are primarily attributable to vibrational processes occurring in the hydroxyl and CO_3^{2-} ions, and metal-OH (e.g., Al-OH, Fe-OH, Mg-OH) cations (Clark 1999). For this reason, minerals containing these components, such as phyllosilicates, carbonates, sulfates, and amphiboles, can be identified.

Spatially resolved µXRF is a nondestructive technique that is here used to scan cut surfaces of quarter core samples. This technique combines the sensitivity of conventional XRF spectrometry with the spatial resolution provided by an X-ray beam strongly focused with polycapillary collimating optics (Yan and Gibson 2002). Compared to an electron beam used in scanning electron microscopy or electron microprobe analysis, the X-ray beam offers a lower detection limit for a range of heavy elements; does not require the sample to be coated with a conductive layer such as carbon; and can be operated at atmospheric pressures, although measuring elements lighter than potassium requires the analysis to be conducted in a vacuum environment.

Together with optical inspection and routine geochemical analysis these noninvasive methods are applied here to characterize the ICDP BARB5 drill core section hosting several Archean spherule layers.

GEOLOGY OF THE BARBERTON GREENSTONE BELT

The Barberton Greenstone Belt (BGB; Fig. 1) comprises the Barberton Supergroup, a well-preserved volcano-sedimentary succession of mostly low metamorphic grade that is subdivided into the Onverwacht, Fig Tree, and Moodies Groups (e.g., Brandl et al. 2006; Lowe and Byerly 2007). Strata dip steeply due to tight to isoclinal folding. The greenstone belt is intruded along its margin by different generations of granitoids. Up to eight different spherule layers, named S1 to S8, have been proposed in the 3.55–3.23 Ga old volcano-sedimentary rocks of the Onverwacht and Fig Tree groups (Lowe et al. 2014).

BARB5 was drilled into the lower Mapepe Formation of the Fig Tree Group, on the eastern limb
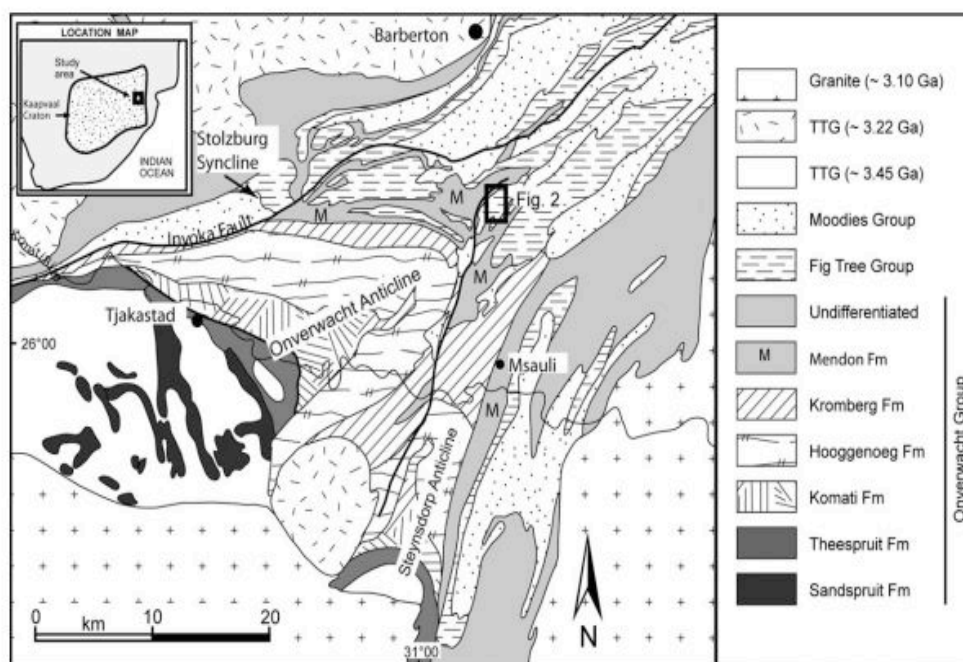
Archean spherule layers from the BARB5 drill core　　　　　　　2443

Fig. 1. Geological map of the southwestern part of the Barberton Greenstone Belt (modified from Hofmann and Harris 2008). TTG = tonalite–trondhjemite–granodiorite.

of the southern Barite Valley Syncline (Fig. 2) (Hofmann et al. 2006; Hofmann and Bolhar 2007; Mason et al. 2013). The stratigraphy of this region has been described in detail by Lowe and Nocita (1999). According to these authors, the Fig Tree Group strata consist of a coarsening-upward sedimentary sequence of ~230 m thickness of shale, with some jaspilite beds in the lower part and a parallel-laminated tuffaceous siltstone to fine-grained sandstone facies in the middle part (Fig. 2). Near the base of the sandstone facies, a bed of massive, densely packed impact spherules occurs, which is ~20 cm thick, and has been correlated with the S3 layer by Lowe et al. (2003). A poorly exposed spherule bed was also described at the base of the Fig Tree Group in this area, and has tentatively been correlated with S2 (Lowe et al. 2003). The upper part of the sedimentary sequence consists of interstratified sandstone, locally cross bedded chert-pebble conglomerate, banded black and gray chert, and jaspilite, and is capped by barite. This is followed by a fining-upward sequence of chert-pebble conglomerate and sandstone, grading into parallel-laminated tuffaceous sandstone and siltstone, which have been dated at 3227 ± 4 Ma (Kröner et al. 1991). Lowe and Nocita (1999) interpreted the Fig Tree Group strata in the Barite Valley Syncline to represent fan-delta and coastal deposits in an area of reduced subsidence or along the flanks of structural highs.

In the eastern limb of the Barite valley, the Archean spherule layer S2 is observed at the base of the Mapepe Formation, and spherule layer S3 occurs 10–30 m above it (Lowe et al. 2003; Hofmann et al. 2006) (Fig. 2). The BARB5 spherule-layer bearing section might be related to either of these two stratigraphic horizons.

ANALYTICAL METHODS

The obtained spherule layer bearing section occurs from 510 to 512 m in the 763 m long BARB5 core. This section is archived in core box 55, currently hosted at the Department of Geology, University of Johannesburg, South Africa. Infrared spectroscopic (IR) imaging of the entire drill core was conducted by GeoSpectral Imaging (Johannesburg, South Africa). Spatially resolved µXRF spectrometry scans of the obtained quarter core samples were conducted at Bruker Nano Analytics in Berlin-Adlershof, Germany. In addition to these noninvasive approaches, routine destructive XRF measurements were made on powdered samples for analysis of major and some minor elements at the Museum für Naturkunde Berlin (Table 1). Details on reference samples, the limits of detection,

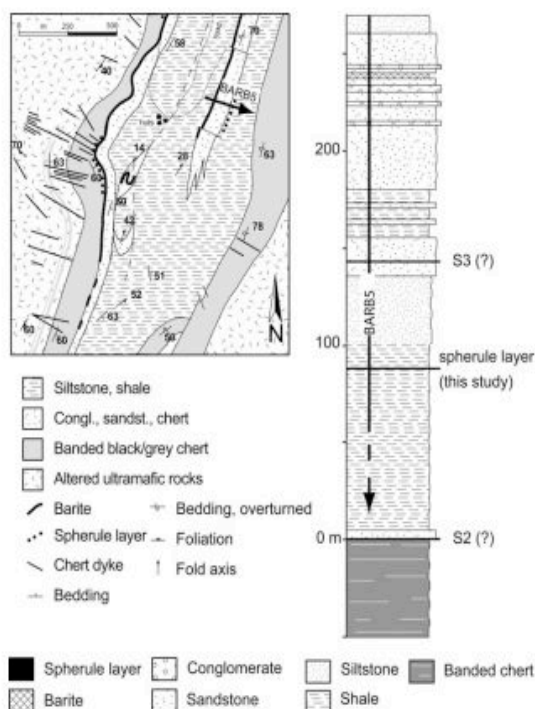2444   J. Fritz et al.

Fig. 2. Geological map of the southern part of the Barite Valley Syncline (for location see black rectangle in Fig. 1; Hofmann et al. 2006), and stratigraphic log for the eastern limb of the Barite Valley Syncline (modified after Lowe and Nocita 1999). BARB5 was drilled in the east limb, but did not reach the base of the Fig Tree Group. The occurrence of the spherule layer investigated in drill core is shown schematically in the log.

and accuracy for routine XRF analysis in this laboratory are given by Raschke et al. (2013). Additional major element analyses were performed at the Service d'Analyses des Roches et des Minéraux (SARM-CNRS) at the CRPG (Nancy) using an emission spectrometer ICP-OES Thermo Fisher ICap 6500 and ICP-MS (X series), respectively, with analytical precisions better than 2%, except for TiO_2 and P_2O_5 (<10%) and Na_2O (<15%). These XRF and ICP-OES and ICP-MS results are given in Table 1.

Infrared Scanning and Processing

The five drill cores from the ICDP Barberton Drilling were imaged by GeoSpectral Imaging in February 2013, using a Specim SWIR camera, and a TVI RGB camera. The wavelength calibration of the spectrometer was monitored using a fluorescent lamp and a sample of Styrofoam, which exhibits strong, characteristic spectral features in the measured

wavelength range. Samples in core trays were illuminated using halogen lamps, and a Spectralon® panel was used as a white reference. In addition a dark reference, that is, measurement of spectrometer-related background noise, was captured for each image. Spectral data were captured across 256 bands at a spectral resolution of 10 nm at 6.3 nm band spacing, and a spatial resolution of 1.6 mm.

The data captured for each drill core were normalized to reflectance, eliminating instrument and illumination effects, using the white and dark references collected simultaneously with each core tray during data acquisition. In addition to this, the data were filtered and smoothed. Further processing was done to extract absorption feature depth and wavelength information in order to map the presence of minerals responsive in the SWIR, and to constrain their spectral characteristics.

All IR images for the BARB1 to BARB5 drill cores are available online at www.geospectralimaging.com/intellicoresvr (e-mail info@geospectral.co.za to acquire login access).

Micro XRF Analysis and Processing

Flat unpolished surfaces of the cut quarter cores were analyzed using a spatially resolved μXRF Bruker M6-Jetstream and a Bruker M4-Tornado spectrometer. The M6-Jetstream is an open-beam (atmospheric pressure) system that allows measuring samples of various sizes up to 800 × 600 mm in a single run. Samples of up to 20 cm in size were measured with the M4-Tornado in a vacuum chamber at 20 mbar to improve the detection of elements lighter than potassium. Measurements were carried out using an X-ray source with a Rh-anode (max. power 30 W) operated at 50 kV and 600 μA. The M6-Jetstream data file from a 30 cm long and 2 cm wide quarter core surface contains 0.55 million pixels, each collected with a dwell time of 2 ms/pixel, and a pixel size of 100 μm. A M4-Tornado data file of a spherule bed sample is composed of 1.4–2.2 million pixels, collected with a dwell time of 3 ms/pixel and a pixel size of 25 μm. The data files were processed with the M4-Tornado software.

Elemental distribution mapping of the samples follows the principle of position-tagged spectroscopy, whereby for each pixel (X-Y-location) a complete fluorescence spectrum (z-location) is stored in a data cube (XYZ). The postprocessing of the acquired information (data mining) was conducted to visualize the stored information as line scans, multicolor elemental distribution maps, phase identification maps, relative element ratio plots, and sum spectra of pixels from selected areas.

Archean spherule layers from the BARB5 drill core   2445

Table 1. Chemical composition determined by powder XRF[§] and ICP-OES* (major elements) and ICP-MS* (trace elements) of marine sediments in the logged interval of the BARB5 drill core. Sample name is BARB5 followed by core depth in meter and centimeter. The spherule layers are SL-A (**512-30**) and SL-D (**511-35**) and sample 511-33 is the sediment sample between spherule layer D and E.

BARB5	505_14[§]	507_63[§]	510_03[§]	511_33*	**511_35***	**512_30[§]**	513_62[§]	515_33[§]	518_31[§]
SiO$_2$	42.1	56.9	37.3	34.8	52.3	54.2	61.4	56.5	51.2
TiO$_2$	0.36	0.58	0.29	0.24	1.18	1.53	0.34	0.6	0.42
Al$_2$O$_3$	6.1	10.8	5.2	5.6	17.7	22.1	6.1	10.7	8.8
Fe$_2$O$_3$	25.9	9.31	29.4	30.6	9.4	3.0	11.0	9.7	19.6
MnO	0.59	0.29	0.45	0.61	0.05	0.01	0.33	0.25	0.38
MgO	3.84	3.91	3.82	5.0	1.47	1.3	3.81	3.93	4.74
CaO	3.59	4.17	2.49	0.54	0.48	0.12	4.46	4.19	3.1
Na$_2$O	0.06	0.08	0.11	0.02	0.05	0.09	0.05	0.06	0.08
K$_2$O	1.87	3.88	2.02	1.96	9.2	11.9	1.96	4.14	1.35
P$_2$O$_5$	0.10	0.08	0.08	0.08	0.20	<0.01	0.05	0.07	0.08
LOI	15.5	9.6	18.2	n.d.	n.d.	3.3	9.9	9.0	9.6
Sum	100.0	99.6	99.4	79.5	92.0	97.6	99.4	99.1	99.4
V		124		151	426		77		122
Cr		911		370	2745		557		762
Co		23		43	371		15		28
Ni		263		582	2992		186		357
Cu		58		111	258		49		28
Rb		127		73	270		55		30
Sr		92		14	28		119		84
Y		17		8	23		10		14
Zr		91		30	91		53		70
Ba		3038		1933	8912		1952		1452

Total Fe given as Fe$_2$O$_3$; LOI = loss on ignition. Oxide concentrations are given in wt% and trace element data in ppm. n.d. = not determined.

The element maps of those elements with a low peak to background ratio (here the minor elements Zr, Cr, Ni, S, and As) were obtained by subtracting the background from each spectrum. The background signal in the spectrum was defined by selecting an energy range in the spectrum close to the peak of interest. The intensity at the selected range was then subtracted from the intensity of the peak for each pixel. This procedure is ideal to visualize minor element distributions, as the background intensity of the spectra can vary with density of the analyzed spot, and the count number acquired for each pixel is relatively low because of the fast data acquisition (3 ms per pixel).

RESULTS

Optical Inspection of the Core Section

Fourteen meters from the BARB5 core (517–503 m) were logged in detail (Fig. 3) as they include the investigated spherule layers. Planar to lenticular laminated, medium-gray shale (Fig. S1a in supporting information) forms the lower part of the succession, and extends farther downhole for several tens of meters. Fine-grained sandstone forms lamina typically 1 mm thick and lenses (<3 mm thick) that rarely show cross lamination. A greenish-gray shale, showing a more pronounced lamination, is interbedded with this facies in the central part (514–506 m) of the logged interval. It frequently contains lamina to thin beds (<2 cm thick) of fine- to medium-grained sandstone that are massive or normally graded, and some of them show erosive scours (Fig. S1b in supporting information). Besides siliciclastic material, this facies contains some carbonate concentrated in more light-colored lamina. A few centimeter thick beds of laminated white chert are associated with this facies. These beds show folding/boudinage or form fragments floating in a ductile deformed shale matrix suggesting different rheological behavior as compared to shale during compaction. The upper part of the logged interval is characterized by Fe-rich shale and banded iron formation consisting of 1 mm microbands of red jasper and light brown carbonate (Fig. S1c in supporting information). This 5 m zone at 506–501 m is overlain by ca. 6 m of predominantly greenish-gray shale and followed by gray shale, both of which were not investigated further.

The logged section is characterized by folding and local shearing. Much of the deformation probably developed during regional deformation of the succession, although an earlier event of soft-sediment
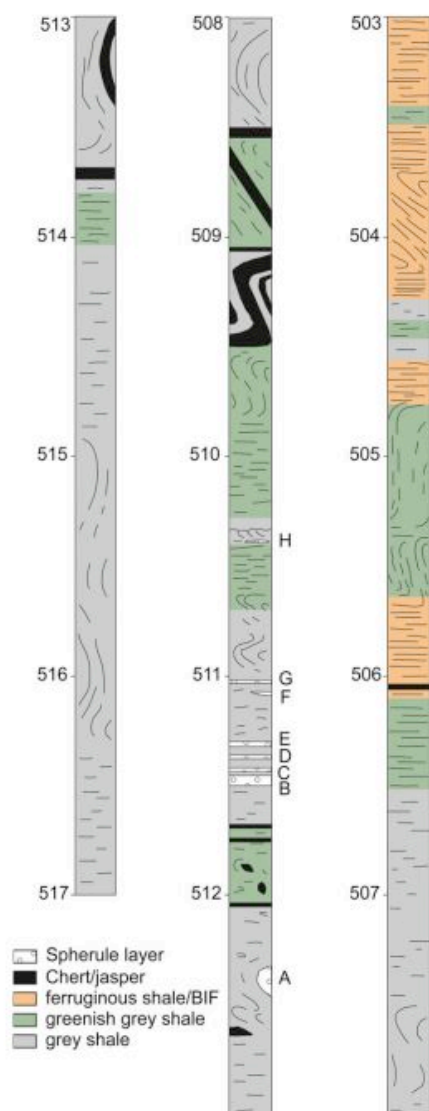
2446　　　　　　　　　　　　　J. Fritz et al.

Fig. 3. Stratigraphic column of the BARB5 drill core from 517 to 503 m through the spherule-bearing core interval. Numbers refer to depth in meters in the core. Note that undisturbed strata are shown with horizontal bedding, although bedding is actually dipping relative to the core margins.

slumping may also have affected the rocks. Deposition of the spherule layer may have been associated with strong disturbance of the seafloor sediments during the passage of tsunami waves and submarine slumping triggered by seismic activity (Hassler and Simonson

2001). Evidence of syn-depositional deformation has been observed at the top of the spherule-bearing interval in the form of a small-scale intraformational unconformity (Fig. S1d in supporting information). While the logged section is strongly deformed, the rocks in the core above and below are clearly less disturbed.

Several spherule layers and occurrences were found in the logged interval (denoted A-H, Fig. 3, and displayed in Figs. S1e–g in supporting information). Layer A occurs in a fold hinge and is only partially preserved. It resembles the lower zone of layer B due to spherule type, clast support, and lack of sedimentary structures.

In layer B, five zones characterized by compositional layering of different clast-supported particle types can be discriminated optically (Fig. S1e in supporting information). The largest spherules are circular in cross section on each side of the quarter core, white colored, and form a densely packed zone at the bottom. Above is a zone of grayish deformed spherule layer material followed by a thin zone of smaller white and circular spherules, and a green zone of deformed spherule layer material. The deformed spherules in the grayish and greenish zone are mostly flattened in the plane of bedding. This sequence is capped by a zone with dispersed circular spherules set in a dark matrix.

Layer C consists of two separate layers, a lower clast-supported layer and an upper layer containing matrix-supported spherules. Layers D and E are massive and consist of clast-supported spherules. Layers B to E are separated by laminated shale and fine-grained sandstone, which show current-ripple lamination between layers B and C. Occurrences F and G (Fig. 3; Figs. S1e–g) are lenticular thin beds (<2 cm) to lamina of massive fine-grained sandstone with <15 vol% disseminated spherules. Layer H marks the occurrence of isolated spherules.

Spherule Layer Localization by IR Spectroscopy

Lithologies in the BARB5 core comprise mainly sandstones, conglomerates, and carbonaceous shales. These lithologies are composed predominantly of minerals that are unresponsive in the short wave infrared (SWIR). Thus, the spectral data for BARB5 overall have a low spectral contrast, and do not show distinct absorption features. However, the volcaniclastic unit occurring at ~260–107 m shows greater spectral contrast, including hydroxyl and water absorptions at 1406 nm and 1907 nm, respectively, as well as Al-OH absorptions at 2200 nm, and carbonate/Mg-OH absorptions at 2340 nm.
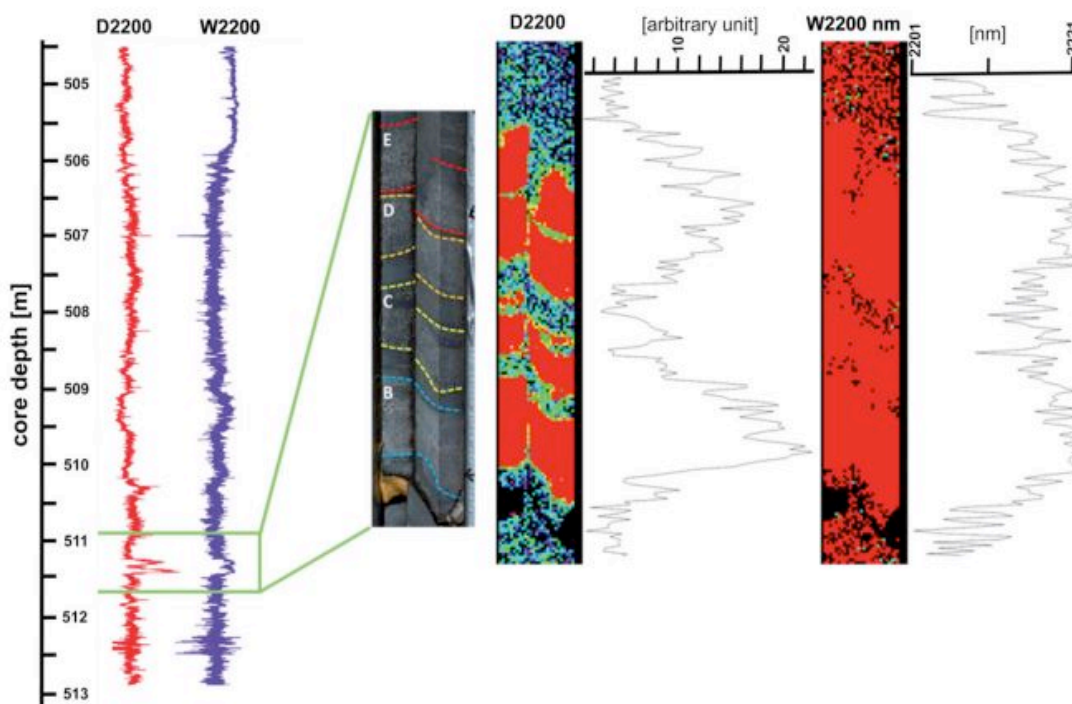
Fig. 4. Results from the infrared imaging of the cores in box 55 are displayed. Downhole plot of depth and wavelength positions of the 2200 nm absorption feature, illustrating how this feature in the spherule layers contrasts sharply with that of the surrounding carbonaceous shales, and showing that the wavelength position of this feature is also longer than that of the shales. In the D2200 inset, red delineates the area where this absorption feature is prominent, and in the W2200 nm inset, red illustrates that the absorption feature occurs at a higher wavelength position relative to the same feature in adjacent lithologies. W is the wavelength position of the absorption feature and D is depth of the absorption feature in a spectrum after the Hull Quotient has been applied and the spectrum has been background subtracted to zero; the unit for depth of an absorption feature is arbitrary.

The spherule layers occur within spectrally unresponsive carbonaceous shale (Fig. 4; Fig. S2 in supporting information). They are characterized by the distinctive features of OH absorptions at 1412 nm, prominent Al-OH absorptions at 2220 nm, and a weak water absorption at 1907 nm (Figs. 4–5; Fig. S2). The intense Al-OH infrared signal from these sections corresponds to the high Al_2O_3 content of ~22 wt%, as determined by powder XRF analyses of spherule layer A, or of ~18 wt%, as determined by bulk ICP-MS analyses of spherule layer D (Table 1; Figs. S1e–g). These values are much higher than the 6–8 wt% Al_2O_3 obtained from sections between the spherule layers B to E by µXRF and ICP-OES, and 6–11 wt% Al_2O_3 as determined by powder XRF in the marine sediments between 518 and 503 m core depth (Table 1).

The spectra obtained from the spherule layers in BARB5 are characteristic of sericite, although the wavelength position of the Al-OH absorption feature is at longer wavelengths (2220 nm) than that of typical potassic micas, whose Al-OH feature normally occurs ~2200 nm. Variation in the wavelength position of the Al-OH absorption is caused by compositional variation in the mica (Beran 2002; Van Ruitenbeek et al. 2005). The wavelength position of the Al-OH absorption feature (>2220 nm) in the BARB5 spherule layers suggests that the sericite mapped is likely to be a phengitic (Fe-rich) variety (Duke 1994; Pontual et al. 1997; Clark 1999; Duke and Lewis 2010); however, this determination would need to be corroborated using mineral chemical analysis.

In addition to the distinct Al-OH feature, a shoulder feature at 2252 nm, associated with the Fe-OH absorption (Clark 1999), suggests that minor chlorite may also be present in the spherule layers.

Micro-XRF Line Scans

In the following the results of data mining of the data cubes (*X-Y* area directions and energy spectrum in *Z* direction) obtained by µXRF measurements across the
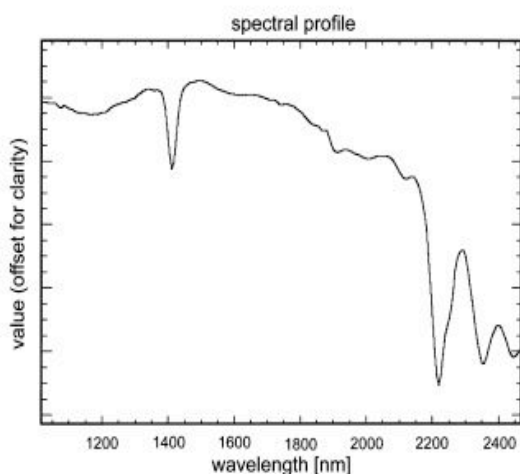
Fig. 5. Representative infrared spectrum from spherule layer E, showing a sharp OH absorption feature at 1412 nm, weak water absorption at 1907 nm, and distinct Al-OH absorption feature at 2220 nm.

quarter core hosting the four closely spaced spherule layers B to E (511.2–511.5 m) are presented (Figs. 6–7; Figs. S3–S7 in supporting information). The elemental distribution line scans along the quarter core section, for one surface only, are depicted in Fig. 6 and illustrate the main chemical trends identified. The results are presented for various elements as counts normalized to 100%, that is, the respective strongest recorded signal.

The Ca distribution varies along the core section without showing a clear trend with respect to spherule and shale layers, although Ca content is highest near the base of layer B. In contrast, the elements Al, Si, Ti, K, Rb, and Zr are enriched in all spherule layers compared to the surrounding shale (Fig. 6; Table 1). In layer B, comparatively higher Rb abundances were observed in the regions composed of deformed spherule layer material. Rubidium enrichment appears unrelated to K abundance, but rather with Ti-rich material. In contrast, the spherule layers are all depleted in Fe and Mn that are strongly enriched in shales.

The distribution of Ni, Cr, S, As, and Cu appears to be more diverse. Two types of Ni enrichment can be discriminated, as Ni correlates either with Cr, or with elements such as S, As, and/or Cu. Nickel and Cr show a positive correlation and elevated abundances in layers C to E with a progressive decrease in the Ni and Cr concentration from layers C to E. The correlation between Ni and Cr are investigated in more detail in a later section of this contribution. In general, Ni and Cr are low in abundance in the shales and the main parts of layer B. The highest Ni abundances occur in distinct bands, in association with high S, As, and/or Cu

abundances. At the top of layer C, an increase in Ni, As, and Cu, and in part Ca, but not in S, can be observed. Directly above layer E, the relative abundance of S, but not of As, Ni, or Cu increases. Layers C to E (between 8 cm and 27 cm; Fig. 6) show more variation and higher S abundances compared to layer B.

The section at the top of layer B (corresponding to 22–23.5 cm; Fig. 6) is illustrated with complex Ni, Cr, S, and As line-scan data (Fig. S3). At the top of layer B Ni and Cr have elevated abundances and are positively correlated. Below is a thin zone with Ni, S, As, and Cu enrichments, in which substantial pyrite was identified by optical microscopy. Further below, in layer B (22–23.5 cm; Fig. 6; Fig. S3), the green zone that is exclusively composed of deformed spherules is enriched in Cr but not in Ni. That contrasts with the white spherule zone just below, which exhibits much lower content in Cr and is slightly higher in Ni.

General Petrographic and Geochemical Characteristics of the Sedimentary Units Using Elemental Maps

The general structure of the spherule layers and intercalated sediments can be further visualized with 2-D distribution maps for different elements and element pairs (Fig. 7). All maps displayed in Fig. 7 are based on four (one per spherule layer) μXRF measurements acquired using the M4-Tornado. To improve the count statistics the element maps and the Ni and Cr mineral phase map (Fig. 7) are displayed using the sum of three and five adjacent pixels, respectively. The threshold value for the element concentration in the maps was selected to optimize the presentation of the different components in the sections; for example, the shales contain significant amounts of SiO_2 but generally map as black in the Si element map in contrast to the spherule layers that are comparatively enriched (Table 1). The highest Si concentrations occur in a thin silica vein below layer B. Abundances of major elements are displayed in element maps. Minerals that are rich in both Ni and Cr are shown in the Ni and Cr phase map displaying only those pixels that are high both in Ni and Cr.

As already indicated by the line scan plots (Fig. 6) and the quantified element composition data (Table 1), the spherules and the matrix between spherules, are distinctly different in chemical composition from shale separating these spherule layers. In particular, the concentrations of the major elements Si, Al, K, and Ti, and the minor elements Rb and Zr (Figs. 6–7) are higher in the spherule layers, and the shales have higher Fe and Mn concentrations.

The Si, Ti, Al, and Zr maps (Fig. 7) indicate the distribution of particles apparently grading from the

Archean spherule layers from the BARB5 drill core   2449
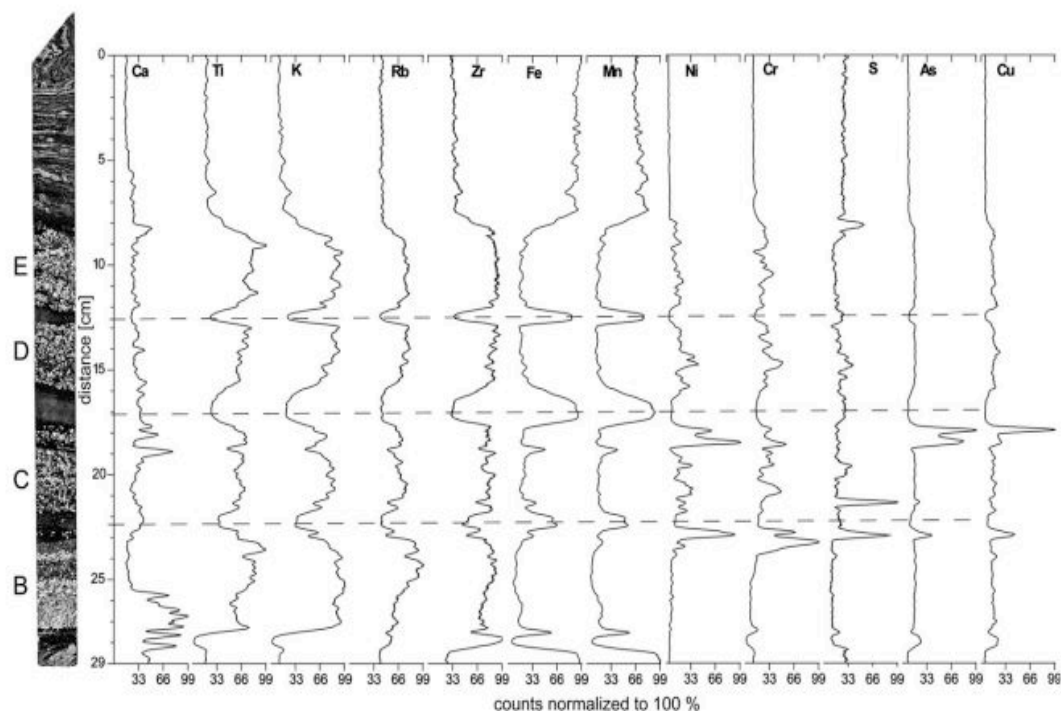

Fig. 6. Visible light image and line scans displaying the relative abundances of Ca, Ti, K, Rb, Zr, Fe, Mn, Ni, Cr, S, As, and Cu. The line scan displays the sum spectra from a rectangle that covers the full width of the quarter core and 15 pixels in length. Data were collected at 1 bar atmospheric pressure with the Bruker M6-Jetstream µXRF and are displayed as distance in cm versus counts normalized to 100% for all elements.

spherule layer into interbedded shale. But no spherules are observed in separating layers between C, D, and E, and only one isolated spherule is observed in shale separating layers B and C. Irregular shaped Si-rich particles outline the cross lamination between layer B and C. The distribution of the irregular shaped Si-rich particles apparently resembles a depositional environment with water current activity. From the spherule layers C to E, these irregular shaped Si-rich particles grade into the shale from the top of layer C, the bottom of layer D, and the top of layer E. A sharp contact to the shale is developed at the top of layer D and bottom of layer E. Iron may be used as an indicator for the occurrence of background sediments within spherule layer deposits, and this sedimentary contribution appears to be higher in layers C to E than in layer B. Layer A has significantly lower Fe abundances than layer D (Table 1). The Fe-rich material may represent some kind of rip-up or intraclasts of local sediments. In contrast to layer C to E the main part of layer B does not contain rip-up clasts, irregular Si-rich particles or Zr-rich particles.

Differences in Spherule Populations and Geochemical Similarities of Layers B to E

The composition of individual spherules is also elucidated by element maps (use zoom function in the electronic version of the article). In comparison to the more diffuse matrix, the round and well-preserved spherules are characterized by higher K and Si concentrations and lower Ti and Al concentrations (Fig. 7). Titanium is concentrated at the rims of particles that are now either deformed or retain their original spherical shape. Circular spherules, and more diffuse spherule material, are evenly distributed through layers C to E. In layer B, the K-rich round spherules are concentrated at the bottom and in the middle part of the horizon, and the more diffuse appearing Al-rich spherule material is concentrated between and above these zones. These two zones of high-Al-bearing material differ in optical appearance and chemical composition. The upper zone is green and has high Cr abundance. This zone is capped by a thin layer of roundish spherules embedded in shale

170

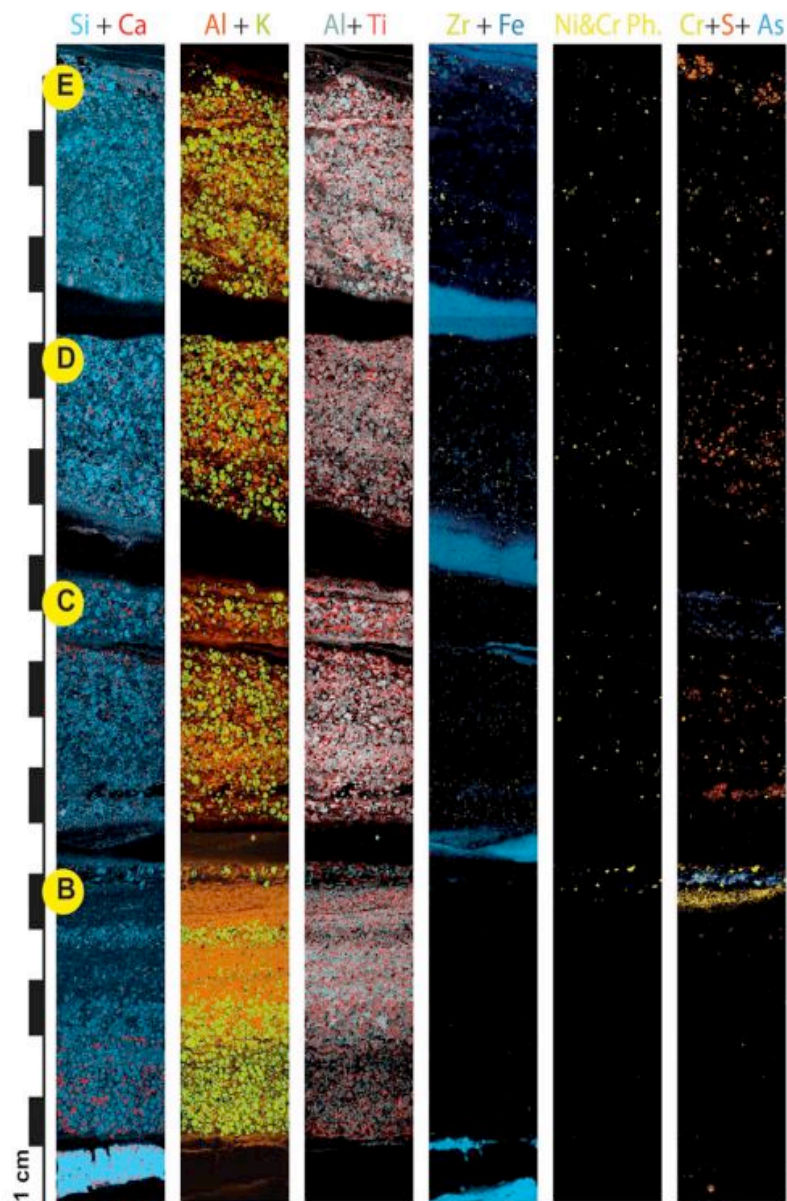2450   J. Fritz et al.

Fig. 7. Micro-XRF elemental distribution maps for the 22 cm long quarter core section (511.44–511.22 m) containing the four spherule layers B to E. The M4-Tornado μXRF data were collected at low vacuum and 4 images are stitched together to cover the full length of the core section. The color scheme of the displayed elements and element combinations are indicated at the top of the column. The Ni and Cr mineral phase map is constructed by selecting all spectra from the data cube with high Ni and high Cr peaks. Each pixel represents the sum spectra of five adjacent pixels to improve the count statistics. The concentration of a displayed element above a threshold value in each pixel is represented by one color. For each element the threshold value is selected to optimize visualization of the sedimentary structures.

that is K-, Al- and Ti-rich, and displays a slightly higher Fe content compared to the spherule zones below.

Compositional sorting in layer B allows further visualization of the chemical signatures of the two types of material by plotting the element abundances of Rb

171

versus K, and Rb versus Al from different sections of layer B (Fig. S4). Rubidium was selected because the line scan shown in Fig. 6 indicates an increased Rb abundance in the region of the deformed Al- and Ti-rich spherules. Figure S4 shows that the Al and Rb abundances are positively correlated throughout layer B. The Rb and K abundances display different populations, with low K, high Rb material occurring in the region composed of deformed spherules, and high K, low Rb material occurring at the bottom of layer B that is mainly composed of round, K-rich spherules.

These differences are further enhanced by comparing the sum X-ray spectra of selected areas from the different parts of layer B. Figure S5a shows the sum spectra from the two parts with round and the two parts with deformed spherules. The displayed spectra are arranged with the background at 14.5 kV at the same height. This permits a comparison between the peak intensities of the displayed elements. An increase in the modal abundance of the deformed Al-rich material correlates with an increase in the Rb, Y, and Zr peaks, and a decrease in the Sr peak. Thus, the deformed Al- and Ti-rich spherules are the main host of Rb.

Notably the sum spectra of layers B to E (Fig. S6b) show that the relative proportions of Rb, Sr, Y, and Zr are similar to even identical. Differences between layer B and layers C, D, and E depend on the modal abundance of the Al- and K-rich zones included in the sum spectra of layer B. In summary, spherule layers B to E appear chemically related.

Differences in the Distribution of Primary Particles in Spherule Layers B to E

Despite the chemical similarities between layers B to E, layer B differs from layers C to E with respect to the occurrence of Zr-rich particles, and Ni- and Cr-rich phases. The Zr-rich phases occurring in layers C to E partly extend into the surrounding shale, and with low abundances extends through the cross bedded shales separating layers C and B, but they are seemingly of lower abundance, or even absent in the other shale intervals (Fig. 7). The line scans (Fig. 6) show that all layers have, within the limits of analytical resolution, similar Zr abundances. Notably, the main part of layer B either does not contain these Zr-rich phases, or they are too small to be resolved on the available sections. The short line scans across Zr-rich particles in layer E are displayed in Figs. S6a and S6b. They show that the Zr-rich spots in the map of layers C to E are indeed Zr-rich particles and not diffuse local enrichments of this element. From the line scans of other elements from these spots (not displayed) it appears that these <100 μm sized particles are Zr-rich and most likely

zircon, which has also been reported from other Archean spherule layers (Byerly et al. 2002). Note that the modal abundance of zircon in these projected 2-D maps is higher than what is expected based on observations using electron microscopy or optical thin section studies. That is because with increasing atomic mass the depth in the sample from which the characteristic X-rays can reach the detector increases from a few micrometers for K to a millimeter for Zr.

The Ni and Cr mineral phase map (Fig. 7) displays pixels representing the sum of five adjacent pixels (to improve the count statistics) characterized by high Ni and Cr values. The sum spectrum (data not shown) of the spectra from all yellow pixels in each layer of the Ni and Cr phase map displays additional enrichments in Zn, Cu, Ni, Co, Cr, and V, and these elements correspond to those elements reported for Ni-Cr spinel of the Barberton spherule layers (Byerly and Lowe 1994; Krull-Davatzes et al. 2010; Mohr-Westheide et al. 2015). Notably, in this section Ni-Cr spinel occurs only in layers C, D, and E, and at the top of layer B—but not within layer B.

A few phases displayed in the Ni and Cr phase map may actually resemble an intergrowth of a Ni- and a Cr-rich phase that both contribute to the five pixel sum spectrum. To test this, examples of the identified Ni and Cr phases from layer E are displayed as short line scans (Figs. S7a–d) to show the spatial correlation of Ni and Cr abundances. Most line scans show a strong spatial correlation between Ni and Cr (Figs. S7a–c), indicating the occurrence of Ni and Cr in one mineral. Nevertheless, Ni-rich and Cr-poor phases (Fig. S7d) are also present in these samples indicating the occurrence of different minerals. The yellow spots in the Ni and Cr phase map are also visible in the Cr element map displayed to the right of the phase map in Fig. 7. Most of the highest Cr concentrations are correlated with the occurrence of Ni-Cr-spinel, with the exception of those in the greenish zone in layer B which is high in Cr, but not in Ni (Figs. 6–7; Fig. S3).

DISCUSSION

General Properties and Sedimentary Environment of Spherule Layers in BARB5

The Fig Tree Group strata in the Barite Valley Syncline in the Barberton Mountain Land are considered to represent fan-delta and coastal deposits (Lowe and Nocita 1999). The spherule layer is hosted by marine sediments represented by fine-grained sandstones and shales, chert, jasper, and banded iron formation. In general, the sediments in the BARB5 drill core are less disturbed than the strongly deformed

spherule layer-hosting section between 517–503 m core depth. Much of the deformation probably formed during regional deformation of the succession, accentuated by the presence of BIF in the spherule-bearing domain that may have behaved rheologically different upon deformation. Nevertheless, an earlier event of soft-sediment slumping, possibly shortly after the impact spherule deposition affected the rocks, as indicated by a small-scale intraformational unconformity at the top of the spherule-bearing interval.

The shales and fine-grained sandstones are relatively rich in MnO and Fe_2O_3, and have moderate Al_2O_3 concentrations. In this succession the spherule layers stand out as discrete bands composed of discrete particles that are either zircons or impact derived TiO_2, K_2O, and Al_2O_3 rich spheres, or Ni- and Cr-rich spinels. Ni-rich spinels are of unusual composition and, thus, are interpreted as primary phases that formed during an impact event on Earth (Robin et al. 1992; Byerly and Lowe 1994; Kyte and Bostwick 1995; Gayraud et al. 1996).

The high K concentrations in the spherule layers of up to 11 wt% K_2O (Table 1) have been interpreted as a result of alteration and replacement processes in the Archean marine environment; that is, replacement of particles of originally basaltic composition by authigenic K-feldspar (Simonson et al. 1999). Titanium is concentrated along the rims of flattened and circular spherules. The concentration of this refractory element at the rim was interpreted as due to early formation of crystallites by either devitrification or growth from the melt.

In contrast, the relatively high Al_2O_3 concentrations of the spherule layers seem in part a primary feature of these deposits, because Al behaves as a rather immobile element under many conditions. In the altered metasediments, the high Al_2O_3 values are now hosted by feldspar and phyllosilicates. The well-preserved texture of the spherule layers places constraints on the effect of passive Al_2O_3 enrichment, by removal of mobile elements (Krull-Davatzes et al. 2012; Belza et al. 2015). But spherule layers, as well as some volcanoclastic layers in Archean metasediments, were interpreted as being deposits having basaltic composition, followed by diagenetic Al_2O_3 enrichments due to Al migration along distances on the order of decimeters in the sedimentary successions (Hassler and Simonson 1989; Kohl et al. 2006; Hassler et al. 2011). Chemical modifications of ejecta layers are also described from Cretaceous-Paleogene (K/Pg, formerly K/T) sections of the Chicxulub impact event (Smit and Klaver 1981; Hecht et al. 2004). But high Al_2O_3 contents of ~15–20 wt%, and occasionally up to 32 wt

%, have also been reported for well-preserved Phanerozoic impact spherules, microtektites, and microkrystites (Alvarez et al. 1992; Vonhof and Smit 1999; Glass 2002; Glass et al. 2004; Kelly and Elkins-Tanton 2004; Folco et al. 2009). Notably, such Al_2O_3 concentrations are similar to the 16 wt% Al_2O_3 typical for the modern oceanic and continental crust from which the more recent microtektites and microkrystites are derived. Either way the Al-rich Archean spherule layers are composed of secondary minerals (K-feldspar and phyllosilicates) with a chemical and mineralogical composition distinctly different to the surrounding marine metasediments of the BARB5 core.

Single or Multiple Impact Origin of the BARB5 Spherule Layers

In the BARB5 drill core, eight spherule-bearing layers (A to H, Fig. 3) are observed within a stratigraphic interval spanning <1.5 m and four of these eight layers occur within a short 23-cm interval. The formation of each layer by a separate impact cannot be excluded. By using the sedimentary and compositional characteristics described above and by applying Occam's razor, that is, preferring the hypothesis based on the fewest assumptions (Hoffmann et al. 1997), we aim to constrain the minimum number of impact events involved.

Repetition of spherule layers due to folding may be the case for layer A due to its occurrence in a fold hinge and its similar composition to layer B (Table 1). Evidence for sedimentary reworking is observed above the deformed top of layer E. There, diluted, sporadic, or lenticular shaped spherule occurrences are observed (layers F to H; Fig. 3), which may suggest redeposition.

Closely spaced and densely packed layers B to E exhibit more complex structures. The matrix of spherule layers B to E displays a different chemical composition compared to the interbedded shales. The matrix is enriched in Al, Ti, Si, Rb, and Zr compared to the Fe- and Mn-rich shales, and, therefore, is interpreted to be composed of altered spherules. Occasionally, Ti-rich rims outline deformed spherules. Only layer B displays complex compositional zoning, and is interpreted as original undisturbed deposit. The grayish and the greenish zone of this layer B contain spherules that are flattened parallel to bedding, which is likely a result of sediment compaction. This compaction did not affect the apparently more resistant K- and Si-rich round spherules. The four zones of spherules in layer B apparently comprise distinct populations of spherules that differ in either chemical composition or degree of crystallization at the time of deposition. The spherules and the Ni-Cr spinel is interpreted as particles that

formed during the impact event, and the zircon is considered as a mineral that formed earlier on Earth and delivered into the spherule layer either by ejection from the crater or, more likely, by redeposition of local crustal material (see also Byerly et al. 2002). That means the spherules, Ni-Cr spinel, and zircon are primary constituents of the spherule layer deposit and did not form later by secondary processes. The main part of the stratified layer B is characterized by a lack of Ni-Cr spinels, and redeposited terrestrial material such as zircon, Si-rich irregular particles, and Fe- and Mn-rich sedimentary material, including rip-up or intraclasts. Thus, layer B shows significant textural differences compared to the apparently redeposited layers C to H. Only the top part of layer B shows some enrichments in Fe- and Mn-bearing sedimentary material, zircons, Si-rich irregular particles, and, in addition, the uppermost 300 μm of layer B are enriched in S and As. These S and As enrichments may be analog to the detritally reworked pyrite described from the Neoarchean Monteville spherule layer (Simonson et al. 1999; Simonson and Harnik 2000). Thus, we argue that the main part of the BARB5 layer B represents an undisturbed fallout layer, with its top part affected by reworking.

In this interpretation, the sorting of larger and round K-rich and the smaller and deformed Al- and Ti-rich, spherules, and the occurrence of Ni-Cr spinel at the top of layer B would be a consequence of the impact emplacement process and the size-dependent differential settling of various particles through the atmosphere and water column (e.g., Manville and Wilson 2004; Artemieva and Morgan 2009; Schulte et al. 2009). Such a depositional sequence would be similar to the situation described from the K/Pg ejecta layer in Haiti and Wyoming (Bohor and Glass 1995), and the western Atlantic (Schulte et al. 2009).

Layer B is separated from layer C by current-ripple lamination. This suggests episodic current or wave activity that apparently formed discrete layers C to E of homogenized spherules, and Ni-Cr spinel and zircon with a minor contamination of sedimentary material (minor Fe and Mn enrichments) and/or irregular Si-rich particles, which are tentatively interpreted as detrital quartz. Notably, spherule layers C to E do not display internal sorting or lamination.

Layer D shows contacts between the spherule layer material and the adjacent shale layers that is gradual at the top and sharp at the bottom (see Si, Al, and Ti map; Fig. 7). Layer E shows similar features but appears upside down. In addition, the close spatial relation between spherule layers B to E (Figs. 3 and 7); the cross-bedding observed between layers B and C (compare the Si map in Fig. 7); and the overall

similarity with respect to Rb, Sr, Y, and Zr element ratios (Fig. S5b) support the interpretation that these spherule layers are part of the same impact event.

We have argued that the stratified layer B represents the undisturbed impact fallout deposit composed of discrete zones of chemically different spherules, with Ni-Cr spinel concentrated toward the end of the depositional sequence. Layer B might be entirely composed of ejecta material with no admixed detrital material like zircon or irregular Si-rich particles. This may be analog to the Paraburdoo spherule layer in Archean-Proterozoic boundary sediments (Hassler et al. 2011). Layers C to E represent mixed layers that are interpreted as locally redeposited and homogenized ejecta including detrital material of likely terrestrial origin such as zircon, irregular Si-rich particles (maybe detrital quartz), and Fe- and Mn-rich sedimentary material. The reworked BARB5 spherule layers C to E show textural similarities to the reworked spherule layers close to Archean-Proterozoic boundary (Simonson et al. 1999; Simonson and Harnik 2000).

Large Area Noninvasive Analytics on Micrometer to Kilometer Scale

Due to the high Al concentrations, which correspond to the presence of K-feldspar and Al-rich phyllosilicates, the BARB5 spherule layers are clearly recognizable by their distinct Al-OH absorption in the shortwave infrared imagery. This emphasizes the relatively high spatial resolution of the IR spectrometry method, at the subcentimeter scale. Also, such data sets might aid in locating Al-rich spherule layers in those cases where the textural features most easily recognized during routine core logging are obscured by diagenetic, deformational, and metamorphic overprints. Differentiation between volcanic and impact-derived debris would, however, not be possible using IR alone, thus necessitating additional petrological and/or chemical analysis. A further screening for samples of interest could be accomplished by looking for high Ni and Cr values using μXRF or even portable XRF in the field and by searching for Ni-Cr spinel using the μXRF phase identification feature and select pixels with high values for Cr and Ni.

Suitable targets for the search of spherule layers using IR are drill cores or large surface exposures such as open pit mines of sedimentary rocks deposited under low energetic conditions and far from clastic, Al-rich input. These would include banded iron formations, specifically the thick iron formations of the Superior-type (Bekker et al. 2014), banded cherts so widespread in Palaeoarchean greenstone successions (Hofmann et al. 2013), and carbonates, such as the

thick carbonate platform deposits of the Neoarchean (Beukes 1987). Note that some of the Superior-type iron formations are now considered to be granular iron formations deposited in shallower, more energetic paleoenvironments (Simonson 2003). Nevertheless, in high energetic paleoenvironments, for example, represented by sandstones or oolitic carbonates, the spherules are likely to be dispersed and would not retain their identity as discrete layers. Discrete layers can be visualized with large area scans due to the chemical and mineralogical differences between Archean spherule layers and their host rocks. Such an approach could also be used to target the earliest traces of impacts onto Earth in strongly metamorphosed Eoarchean strata such as the Isua and Akilia successions of West Greenland. Locating these early traces of impacts would be of outstanding relevance for study of the type(s) of projectiles that impacted during part of the Heavy Bombardment eon (Fritz et al. 2014).

CONCLUSIONS

The BARB5 drill core hosts eight impact spherule layers and occurrences in the interval between 511–512.6 m core depth. The spherule layers occur in a section from 517 to 503 m where the rocks are significantly more disturbed than the rocks in the core above and below.

The µXRF data revealed geochemical trends at the micrometer to meter scale. Similarities and differences between spherules, the matrix between the spherules, and the sediments separating the spherule layers in a 30 cm long drill core section were characterized. At least two types of spherules were identified: K- and Si-rich spherules that are circular in cross section on each side of the quarter core, and Al-, Ti-, Rb-, and Zr-rich, flattened spherules with some of them being also rich in Cr. These morphological differences could be related to differences in the initial chemical composition, or degree of crystallization (e.g., microkrystites and microtektites) that resulted in different alteration products.

Separating only those spectra with high Ni and high Cr peaks resulted in a phase map of Ni- and Cr-rich particles that additionally are enriched in Zn, Cu, Co, and V. This elemental composition resembles the composition reported for Ni-Cr spinels in Paleoarchean spherule layers. The µXRF data allowed to map the distribution of tens of micrometer-sized primary phases such as Ni-Cr spinel and zircon.

The BARB5 spherule layers share general characteristics such as spherule size and shapes, and certain geochemical characteristics, while they differ in the abundance and distribution of the "primary"

compounds Ni-Cr spinel and zircon, as well as the distribution of Fe- and Mn-rich sedimentary material and irregularly shaped Si-rich particles. Based on the data obtained so far, we cannot exclude a multiple impact origin for some or all of these spherule layers. However, a single impact emplacement followed by reworking of the material on the Archean sea floor could also account for the observed similarities and differences and the sedimentary structures of the layers. In this scenario we assume an initial deposition of at least two chemically different types of spherules followed by Ni-Cr spinels (associated with high Ir concentrations; Mohr-Westheide et al. 2015) toward the top of layer B. Such a sedimentary sequence would be similar to the situation described in proximal and marine ejecta deposits of the Chixculub impact event that terminated the Mesozoic era (e.g., Bohor and Glass 1995; Smit 1999; Schulte et al. 2009; Artemieva and Morgan 2015).

Notably, despite differences in the composition of the Archean and Phanerozoic crust the high bulk Al_2O_3 content of up to 22 wt% in the Archean spherule layers is similar to those values reported for Phanerozoic spherule layers (Alvarez et al. 1992; Vonhof and Smit 1999; Glass 2002; Glass et al. 2004; Kelly and Elkins-Tanton 2004; Folco et al. 2009). Alternatively, the high Al_2O_3 might be related to diagenetic enrichment (Smit and Klaver 1981; Hassler and Simonson 1989; Hecht et al. 2004; Kohl et al. 2006; Hassler et al. 2011). Either way, due to their unusually high Al_2O_3 concentrations, these spherule layers can be located by characteristic absorption features, using infrared imagine methods. Such data sets can cover kilometers of core material, such as those produced for the BARB1 to BARB5 drill cores. Thus, infrared imaging techniques can be used to image strongly metamorphosed Al_2O_3 poor Archean sediments deposited in a low energy paleoenvironment that may contain spherule layers in which the petrographic hallmarks of spherules have been obliterated, or in large outcrops of Archean to Proterozoic Al_2O_3 poor marine sediments.

comments that helped to improve an earlier version of the manuscript.

Editorial Handling—Dr. A. J. Timothy Jull

REFERENCES

Alvarez W., Smit J., Lowrie W., Asaro F., Margolis S. V., Claeys P., Kastner M., and Hildebrand A. R. 1992. Proximal impact deposits at the Cretaceous-Tertiary boundary in the Gulf of Mexico: A restudy of DSDP Leg 77 Sites 536 and 540. *Geology* 20:697–700.

Arndt N. T., Wilson A., Hofmann A., Mason P., Bau M., Byerly G., and Chunnett G. 2012. Peering into the cradle of life: Scientific drilling in the Barberton Greenstone Belt. *Scientific Drilling* 13:71.

Arndt N, Wilson A, Mason P, Hofmann A., and Lowe D. 2013. Overview of the Barberton drilling project. *Geophysical Research Abstracts* 15:EGU2013-3909.

Artemieva N. A. and Morgan J. 2009. Modeling the formation of the K-Pg boundary layer. *Icarus* 201:768–780.

Artemieva N. A., and Morgan J. V. 2015. Formation of the dual K-Pg boundary layer in North America (abstract #1911). 46th Lunar and Planetary Science Conference. CD-ROM.

Bekker A., Planavsky N., Krapež B., Rasmussen B., Hofmann A., Slack J. F., Rouxel O. J., and Konhauser K. O. 2014. 9.18—Iron formations: Their origins and implications for ancient seawater chemistry. *Treatise on Geochemistry (Second Edition)* 9:561–628.

Belza J., Goderis S., Smit J., Vanhaecke F., Baert K., Terryn H., and Claeys P. 2015. High spatial resolution geochemistry and textural characteristics of "microtektite" glass spherules in proximal Cretaceous-Paleogene sections: Insights into glass alteration patterns and precursor melt lithologies. *Geochimica et Cosmochimica Acta* 152:1–38.

Beran A. 2002. Infrared spectroscopy of micas. In *Micas: Crystal chemistry and metamorphic petrology*, edited by Mottana A., Paolo Sassi F., Thompson J. B. Jr., and Guggenheim S. *Mineralogical Society of America Reviews in Mineralogy and Geochemistry* 46:351–369.

Beukes N. J. 1987. Facies relations, depositional environments and diagenesis in a major early Proterozoic stromatolitic carbonate platform to basinal sequence, Campbellrand Subgroup, Transvaal Supergroup, Southern Africa. *Sedimentary Geology* 54:1–46.

Bohor B. H. and Glass B. P. 1995. Origin and diagenesis of K/T impact spherules—From Haiti to Wyoming and beyond. *Meteoritics* 30:182–198.

Brandl G., Cloete M., and Anhaeusser C. R. 2006. Archaean Greenstone belts. In *The geology of South Africa*, edited by Johnson M. R., Anhaeusser C. R., and Thomas R. J. Johannesburg/Pretoria: Geological Society of South Africa/Council for Geoscience. pp. 9–56.

Byerly G. R. and Lowe D. R. 1994. Spinel from Archean impact spherules. *Geochimica et Cosmochimica Acta* 58:3469–3486.

Byerly G. R., Lowe D. R., Wooden J. L., and Xie X. 2002. An Archean impact layer from the Pilbara and Kaapvaal cratons. *Science* 297:1325–1327.

Clark R. N. 1999. Spectroscopy of rocks and minerals and principles of spectroscopy. In *Manual of remote sensing (3)*. *Remote sensing for the Earth sciences*, edited by Rencz A. N. New York: Wiley. pp. 3–58.

Doublier M. P., Roache T., Potel S., and Laukamp C. 2012. Short-wavelength infrared spectroscopy of chlorite can be used to determine very low metamorphic grades. *European Journal of Mineralogy* 24:891–902.

Duke E. F. 1994. Near infrared spectra of muscovite, Tschermak substitution, and metamorphic reaction progress: Implications for remote sensing. *Geology* 22:621–624.

Duke E. F. and Lewis R. S. 2010. Near infrared spectra of white mica in the Belt Supergroup and implications for metamorphism. *American Mineralogist* 95:905–920.

Fernandes V. A., Fritz J., Weiss B., Garrick-Bethel I., and Shuster D. 2013. The bombardment history of the Moon as recorded by ^{40}Ar–^{39}Ar chronology. *Meteoritics & Planetary Science* 48:241–269.

Folco L., D'Orazio M., Tiepolo M., Tonarini S., Ottolini L., Perchiazzi N., Rochette P., and Glass B. P. 2009. Transantarctic mountain microtektites: Geochemical affinity with Australasian microtektites. *Geochimica et Cosmochimica Acta* 73:3694–3722.

Fritz J., Bitsch B., Kührt E., Morbidelli A., Tornow C., Wünnemann K., Fernandes V. A., Grenfell J. L., Rauer H., Wagner R., and Werner S. C. 2014. Earth-like habitats in planetary systems. *Planetary and Space Science* 98:254–267.

Gayraud J., Robin E., Rocchia R., and Froget L. 1996. Formation conditions of oxidized Ni-rich spinel and their relevance to the K/T boundary event. In *The Cretaceous–Tertiary event and other catastrophes in Earth history*, edited by Ryder G., Fastovsky D., and Gartner S. GSA Special Paper 307. Boulder, Colorado: Geological Society of America. pp. 425–443.

Glass B. P. 2002. Upper Eocene impact ejecta/spherule layers in marine sediments. *Chemie der Erde* 62:173–196.

Glass B. P., and Simonson B. M. 2013. *Distal impact ejecta layers. Impact studies*. Berlin: Springer. 716 p.

Glass B. P., Huber H., and Koeberl C. 2004. Geochemistry of Cenozoic microtektites and clinopyroxene-bearing spherules. *Geochimica et Cosmochimica Acta* 68:3971–4006.

Gradstein F. M., Ogg J. G., Smith A. G., Bleeker W., and Lourens L. J. 2004. A new geologic time scale, with special reference to Precambrian and Neogene. *Episodes* 27:83–100.

Harraden C. L., McNulty B. A., Gregory M. J., and Lang J. R. 2013. Shortwave infrared spectral analysis of hydrothermal alteration associated with the Pebble porphyry copper-gold-molybdenum deposit, Iliamna, Alaska. *Economic Geology* 108:483–494.

Hassler S. W. and Simonson B. M. 1989. Deposition and alteration of volcaniclastic strata in two large, early Proterozoic iron-formations in Canada. *Canadian Journal of Earth Sciences*. 26:1574–1585.

Hassler S. W. and Simonson B. M. 2001. The sedimentary record of extraterrestrial impacts in deep shelf environments-evidence from the early Precambrian. *The Journal of Geology* 109:1–19.

Hassler S. W., Simonson B. M., Sumner D. Y., and Bodin L. 2011. Paraburdoo spherule layer (Hamersley Basin, Western Australia): Distal ejecta from a fourth large impact near the Archean-Proterozoic boundary. *Geology* 39:307–311.

Hecht L., Wittmann A., Schmitt R. T., and Stöffler D. 2004. Composition of impact melt particles and the effects of

2456   J. Fritz et al.

post-impact alteration in suevitic rocks at the Yaxcopoil-1 drill core, Chicxulub crater, Mexico. *Meteoritics & Planetary Science* 39:1169–1186.

Hoffmann R., Minkin V. I., and Carpenter B. K. 1997. Ockham's razor and chemistry. *HYLE—International Journal for Philosophy of Chemistry* 3:3–28.

Hofmann A. and Bolhar R. 2007. Carbonaceous cherts in the Barberton Greenstone Belt and their significance for the study of early life in the Archean record. *Astrobiology* 7:355–388. doi:10.1089/ast.2005.0288.

Hofmann A. and Harris C. 2008. Stratiform alteration zones in the Barberton Greenstone Belt: A window into subseafloor processes 3.5–3.3 Ga ago. *Chemical Geology* 257:224–242.

Hofmann A., Reimold W. U., and Koeberl C. 2006. Archean spherule layers in the Barberton Greenstone Belt, South Africa: A discussion of problems related to the impact interpretation. In *Processes on the early Earth*, edited by Reimold W. U. and Gibson R. L. GSA Special Paper 405. Boulder, Colorado: Geological Society of America. pp. 33–56.

Hofmann A., Bolhar R., Orberger B., and Foucher F. 2013. Cherts of the Barberton Greenstone Belt, South Africa: Petrology and trace-element geochemistry of 3.5 to 3.3 Ga old silicified volcaniclastic sediments. *South African Journal of Geology* 116:297–322.

Kelly D. C. and Elkins-Tanton L. T. 2004. Bottle-green microtektites from the South Tasman Rise: Deep-sea evidence for an impact event near the Miocene/Pliocene boundary. *Meteoritics & Planetary Science* 39:1921–1929.

Koeberl C. 2006. The record of impact processes on the early Earth—A review of the first 2.5 billion years. In *Processes of the early Earth*, edited by Reimold W. U. and Gibson R. GSA Special Paper 405. Boulder, Colorado: Geological Society of America. pp. 1–22.

Koeberl C. and Reimold W. U. 1995. Early Archean spherule beds in the Barberton Mountain Land, South Africa: No evidence for impact origin. *Precambrian Research* 74:1–33.

Kohl I., Simonson B. M., and Bereke M. 2006. Diagenetic alteration of impact spherules in the Neoarchean Monteville layer, South Africa. In *Processes of the early Earth*, edited by Reimold W. U. and Gibson R. GSA Special Paper 405. Boulder, Colorado: Geological Society of America. pp. 57–73.

Kröner A., Byerly G. R., and Lowe D. R. 1991. Chronology of early Archaean granite-greenstone evolution in the Barberton Mountain Land, South Africa, based on precise dating by single zircon evaporation. *Earth and Planetary Science Letters* 103:41–54.

Krull-Davatzes A. E., Byerly G. R., and Lowe D. R. 2010. Evidence for a low-O_2 Archean atmosphere from nickel-rich chrome spinels in 3.24 Ga impact spherules, Barberton greenstone belt, South Africa. *Earth and Planetary Science Letters* 296:319–328.

Krull-Davatzes A. E., Lowe D. R., and Byerly G. R. 2012. Mineralogy and diagenesis of 3.24 Ga meteorite impact spherules. *Precambrian Research* 196–197:128–148.

Kyte F. T. and Bostwick J. A. 1995. Magnesioferrite spinel in Cretaceous/Tertiary boundary sediments of the Pacific basin: Remnants of hot, early ejecta from the Chicxulub impact? *Earth and Planetary Science Letters* 132:113–127.

Kyte F. T., Zhou L., and Lowe D. R. 1992. Noble metal abundances in an Early Archean impact deposit. *Geochimica et Cosmochimica Acta* 56:1365–1372.

Lowe D. R. and Byerly G. R. 1986. Early Archean silicate spherules of probable impact origin, South Africa and Western Australia. *Geology* 14:83–86.

Lowe D. R. and Byerly G. R. 2007. An overview of the geology of the Barberton Greenstone Belt and vicinity: Implications for early crustal development. In *Developments in Precambrian geology*, vol. 15, edited by van Kranendonk M. J., Smithies R. H., and Bennett V. C. Amsterdam: Elsevier. pp. 481–526.

Lowe D. R. and Nocita B. W. 1999. Foreland basin sedimentation in the Mapepe Formation, southern-facies Fig Tree Group. In *Geologic evolution of the Barberton Greenstone Belt, South Africa*, edited by Lowe D. R. and Byerly G. R. GSA Special Paper 329. Boulder, Colorado: Geological Society of America. pp. 233–258.

Lowe D. R., Byerly G. R., Kyte F. T., Shukolyukov A., Asaro F., and Krull A. 2003. Spherule beds 3.47-3.24 billion years old in the Barberton Greenstone Belt, South Africa: A record of large meteorite impacts and their influence on early crustal and biological evolution. *Astrobiology* 3:7–47.

Lowe D. R., Byerly G. R., and Kyte F. T. 2014. Recently discovered 3.42–3.23 Ga impact layers, Barberton Belt, South Africa: 3.8 Ga detrital zircons, Archean impact history, and tectonic implications. *Geology* 42:747–750.

Manville V. and Wilson C. J. N. 2004. Vertical density currents: A review of their potential role in the deposition interpretation of deep-sea ash layers. *Journal of the Geological Society London* 16:947–958.

Mason P., Galic A., Montinaro A., Strauss H., Hofmann A., Chunnett G., Wilson A., and Arndt N. 2013. Barberton Drilling Project—Barite Valley Core BARB5. EGU General Assembly Vienna, Geophysical Research Abstracts 15, abs. EGU2013-13902.

Mohr-Westheide T., Reimold W. U., Fritz J., Koeberl C., Salge T., Hofmann A., and Schmitt R. T. 2015. Discovery of extraterrestrial component carrier phases in Archean spherule layers: Implications for estimation of Archean bolide sizes. *Geology* 43:299–302.

Neukum G., Ivanov B., and Hartmann W. K. 2001. Cratering records in the inner solar system in relation to the lunar reference system. *Space Science Reviews* 96:55–86.

Öpik E. J. 1960. The lunar surface as an impact counter. *Monthly Notices of the Royal Astronomical Society* 120:404–411.

Pontual S., Merry N., and Gamson P. 1997. *Spectral interpretation field manual: Spectral analysis guides for mineral exploration G-Mex Version 1.0*. Australia: Ausspec International Pty. Ltd. 169 p.

Raschke U., Schmitt R. T., and Reimold W. U. 2013. Petrography and geochemistry of impactites and volcanic bedrock in the ICDP drill core D1c from lake El'gygytgyn, NE Russia. *Meteoritics & Planetary Science* 48:1251–1286.

Reimold W. U., Koeberl C., Johnson S., and McDonald I. 2000. Early Archean spherule beds in the Barberton Mountain Land, South Africa: Impact or terrestrial origin? In *Impacts and the early Earth*, edited by Gilmour I. and Koeberl C. Berlin: Springer-Verlag. pp. 117–180.

Robin E., Bonté Ph, Froget L., Jéhanno C., and Rocchia R. 1992. Formation of spinels in cosmic objects during atmospheric entry: A clue to the Cretaceous-Tertiary boundary event. *Earth and Planetary Science Letters* 108:181–190.

Archean spherule layers from the BARB5 drill core　　　　　2457

Schulte P., Deutsch A., Salge T., Berndt J., Kontny A., MacLeod K. G., Neuser R. D., and Krumm S. 2009. A dual-layer Chicxulub ejecta sequence with shocked carbonates from the Cretaceous Paleogene (K Pg) boundary, Demerara Rise, western Atlantic. *Geochimica et Cosmochimica Acta* 73:1180–1204.

Shukolyukov A., Kyte F. T., Lugmair G. W., Lowe D. R., and Byerly G. R. 2000. The oldest impact deposits on Earth— First confirmation of an extra-terrestrial component. In *Impacts and the early Earth*, edited by Gilmour I. and Koeberl C. Berlin: Springer-Verlag. pp. 99–116.

Simonson B. M. 2003. Origin and evolution of large Precambrian iron formations. In *Extreme depositional environments: Mega end members in geologic time*, edited by Chan M. A. and Archer A. W. GSA Special Paper 370. Boulder, Colorado: Geological Society of America. pp. 231–244.

Simonson B. M. and Glass B. B. 2004. Spherule layers records of ancient impacts. *Annual Review of Earth and Planetary Sciences* 32:329–361.

Simonson B. M. and Harnik P. 2000. Have distal impact ejecta changed through geologic time? *Geology* 28:975– 978.

Simonson B. M., Hassler S. W., and Beukes N. J. 1999. Late Archean impact spherule layer in South Africa that may correlate with a Western Australian layer. In *Impact cratering and planetary evolution II*, edited by Dressler B. O. and Sharpton V. L. GSA Special Paper 339. Boulder, Colorado: Geological Society of America. pp. 249–262.

Smit J. 1999. The global stratigraphy of the Cretaceous-Tertiary boundary impact ejecta. *Annual Review of Earth and Planetary Sciences* 27:75–113.

Smit J. and Klaver G. 1981. Sanidine spherules at the Cretaceous-Tertiary boundary indicate a large impact event. *Nature* 292:47–49.

Tappert M. C., Rivard B., Giles D., Tappert R., and Mauger A. 2013. The mineral chemistry, near-infrared, and mid-infrared reflectance spectroscopy of phengite from the Olympic Dam IOCG deposit, South Australia. *Ore Geology Reviews* 53:26–38.

Thompson A. J. B., Hauff P. L., and Robitaille A. J. 1999. Alteration mapping in exploration: Application of short-wave infrared (SWIR) spectroscopy. *Society of Economic Geologists Newsletter* 39:16–27.

Van Ruitenbeek F. J. A., Cudahy T., Hale M., and van der Meer F. D. 2005. Tracing fluid pathways in fossil hydrothermal systems with near-infrared spectroscopy. *Geology* 33:597–600.

Vonhof H. B. and Smit J. 1999. Late Eocene microkrystites and microtektites at Maud Rise (Ocean Drilling Project Hole 689B; Southern Ocean) suggest a global extension of the approximately 35.5 Ma Pacific impact ejecta strewn field. *Meteoritics & Planetary Science* 34:747–755.

Wilhelms D. E. 1987. The geologic history of the Moon. *US Geological Survey Professional Paper* 1348:302.

Yan Y. and Gibson W. M. 2002. Polycapillary optics and X-ray analytical techniques. JCPDS-International Centre for Diffraction Data 2002. *Advances in X-ray Analysis* 45:298–305.

SUPPORTING INFORMATION

Additional supporting information may be found in the online version of this article:

Fig. S1. Visible light images displaying typical rock types and spherule layer section encountered in the BARB5 core. a) Planar laminated medium gray shale (517.0 m). b) Greenish gray shale facies with abundant thin sandstone beds (512.8 m). c) Folding in banded iron formation (503.7 m). d) Small-scale intraformational unconformity in gray shale facies indicating soft-sediment deformation prior to deposition of the overlying bed (510.4 m). e–f) Quarter core samples with their three surfaces from the drill core BARB5 at depth of 511.6–511.0 m in the core. The spherule layers and occurrences are labeled with A.

Fig. S2. Red-green-blue (RGB) and shortwave infrared (SWIR) image data for BARB5 drill core box 55 showing a) natural color RGB image; b) false color composite image generated from 3 bands of the spectral data; c) map illustrating the depth, after background subtracting the data using the Hull Quotient, of the 2200 nm absorption feature. Note the color scale of the image; cold colors indicate shallow absorption features, while warm colors are indicative of deeper absorption features at the given wavelength position. The four closely spaced spherule layers B-E are indicated by a green rectangle.

Fig. S3. Visible light image and corresponding element distribution of Ni, Cr, S, and As for spherule layer B. Two different Ni-rich zones are identified that either correlate with high Cr contents or high S and As abundances. In addition to the high Ni and Cr zone another Cr-rich zone occurs in the upper deformed spherule layer and this zone displays low values for Ni, S, and As. The S and As rich part is high in Ni but low in Cr.

Fig. S4. Element ratios for Rb/Al and Rb/K of texturally different parts for the sorted spherule layer B. The Al/Rb trend through the whole spherule layers shows a positive correlation between Al and Rb. In contrast the zone with K-rich circular spherules contains less Rb than the two zones with deformed spherules.

Fig. S5. Micro-XRF energy spectra of spherule layers a) showing four sections of layer B and b) showing bulk data for the layers B to E. The four sections of layer B (a) represent the lowest part with K-rich spherules (27–26 cm), the transition zone with K-rich spherules and deformed spherules (26–25 cm), and the two regions (24.5–24 cm; 23.5–23 cm) where only deformed spherules and no round K-rich spherules are present. The region between 23.5–23 cm is enriched in Cr. All energy spectra are arranged with the Zr peak at the same height.

2458   J. Fritz et al.

Fig. S6. Line scans across two Zr-rich spots from layer E given in variations of the relative abundances to show that the identified spots are individual small particles highly enriched in Zr. Line scans across individual particles covers the full width of the particle of interest but measures only one pixel in length in order to conserve the spatial resolution of the data set.

Fig. S7. Line scan across the Ni- and Cr-rich spots from layer E as identified in the Ni & Cr phase map of Fig. 7. display special correlations between Ni and Cr. Line scan across selected particles cover the full width of the particle of interest but only one pixel in length in order to conserve the spatial resolution of the data set.

Supplementary Online Material for the contribution:

Non-Destructive Spectroscopic and Petrochemical Investigations of Paleoarchean Spherule Layers from the ICDP Drill Core BARB5; Barberton Mountain Land, South Africa.

Jörg Fritz, Roald Tagle, Luisa Ashworth, Ralf-Thomas Schmitt, Axel Hofmann, Béatrice Luais, Phillip D. Harris, Desirée Hoehnel, Seda Özdemir, Tanja Mohr-Westheide, Wolf Uwe Reimold, Christian Koeberl
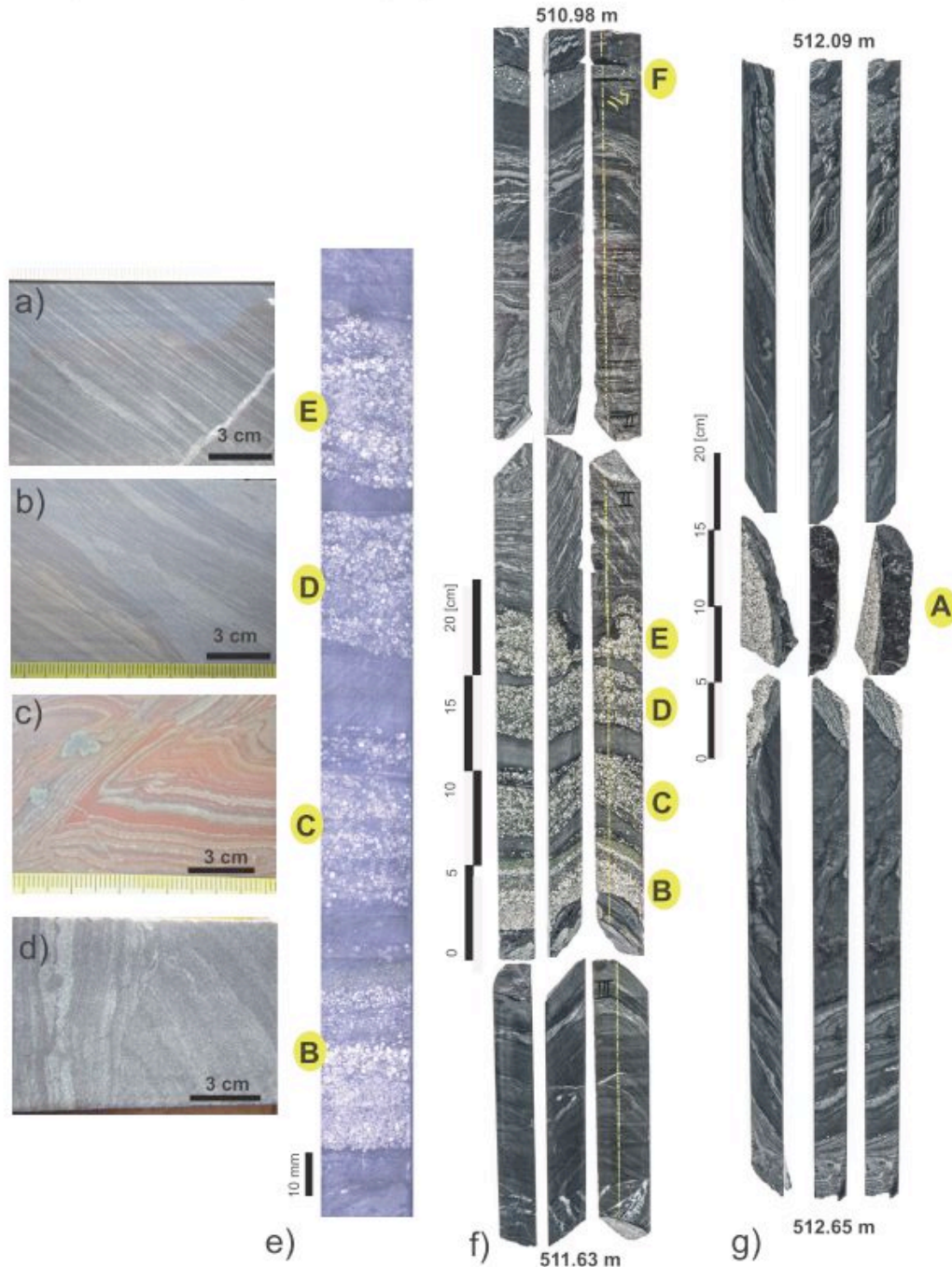

Supplement Online Figure 1: Visible light images displaying typical rock types and spherule layer section encountered in the BARB5 core. a) Planar laminated medium grey shale (517.0 m). b) Greenish grey shale facies with abundant thin sandstone beds (512.8 m). c) Folding in banded iron formation (503.7 m). d) Small-scale intra-formational unconformity in grey shale facies indicating soft-sediment deformation prior to deposition of the overlying bed (510.4 m), e-f) Quarter core samples with their three surfaces from the drill core BARB5 at depth of 511.6 - 511.0 m in the core. The spherule layers and occurrences are labeled with A
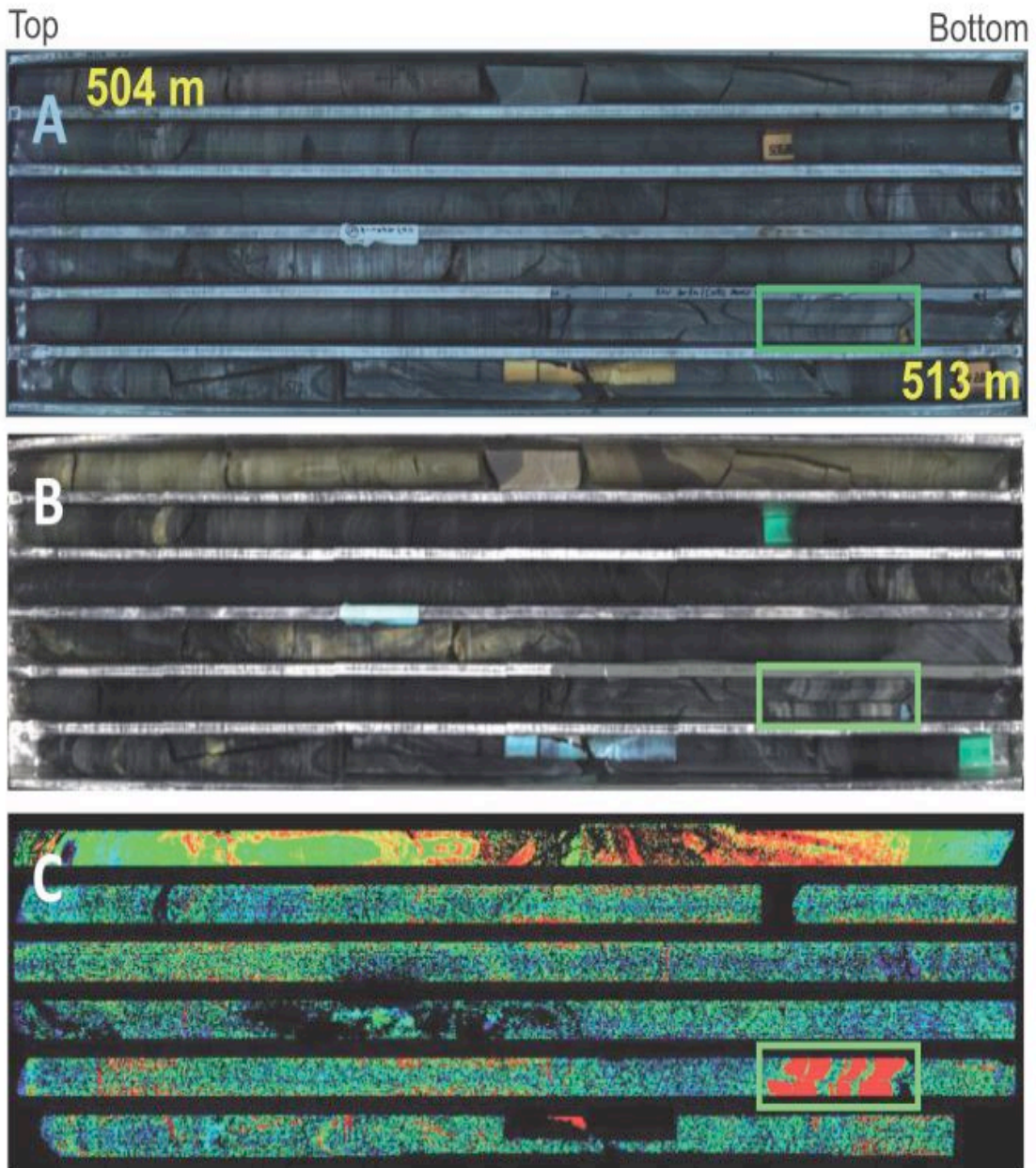
Supplement Online Figure 2: Red-green-blue (RGB) and shortwave infrared (SWIR) image data for BARB5 drill core box 55 showing a) Natural color RGB image; b) False color composite image generated from 3 bands of the spectral data; c) Map illustrating the depth, after background subtracting the data using the Hull Quotient, of the 2200 nm absorption feature. Note the color scale of the image; cold colors indicate shallow absorption features, while warm colors are indicative of deeper absorption features at the given wavelength position. The four closely spaced spherule layers B-E are indicated by a green rectangle.
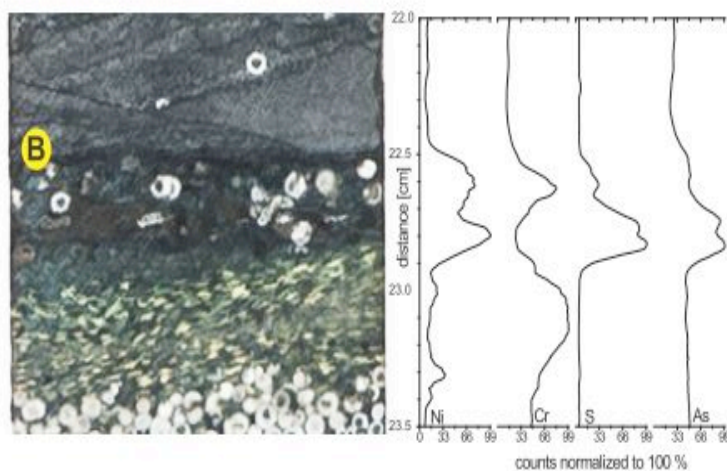
Supplement Online Figure 3: Visible light image and corresponding element distribution of Ni, Cr, S, and As for spherule layer B. Two different Ni rich zones are identified that either correlate with high Cr contents or high S and As abundances. In addition to the high Ni and Cr zone another Cr rich zone occurs in the upper deformed spherule layer and this zone displays low values for Ni, S and As. The S and As rich part is high in Ni but low in Cr.
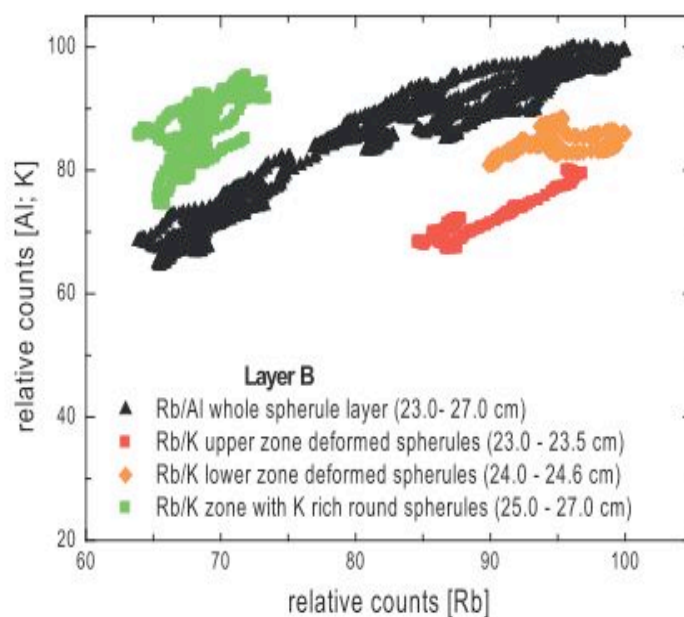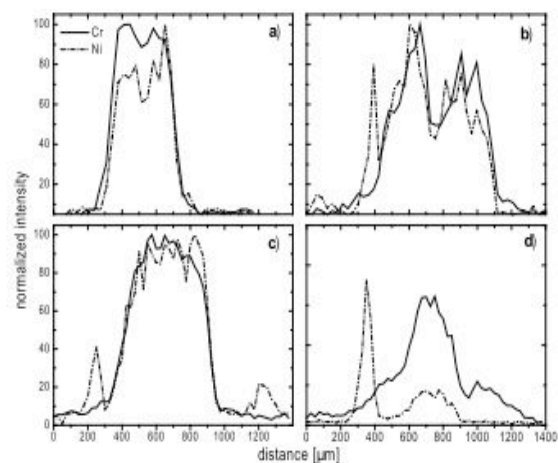

Supplement Online Figure 4: Element ratios for Rb/Al and Rb/K of texturally different parts for the sorted spherule layer B. The Al/Rb trend through the whole spherule layers shows a positive correlation between Al and Rb. In contrast the zone with K rich circular spherules contains less Rb than the two zones with deformed spherules.
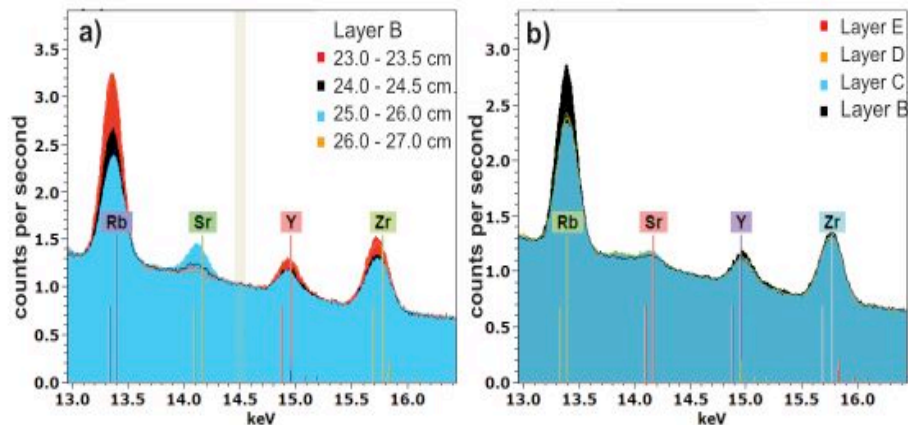
Supplement Online Figure 5: Micro-XRF energy spectra of spherule layers a) showing four sections of layer B and b) showing bulk data for the layers B to E. The four sections of layer B (a) represent the lowest part with K rich spherules (27 - 26 cm), the transition zone with K rich spherules and deformed spherules (26 - 25 cm), and the two regions (24.5 - 24 cm; 23.5 - 23 cm) were only deformed spherules and no round K rich spherules are present. The region between 23.5 - 23 cm is enriched in Cr. All energy spectra are arranged with the Zr peak at the same height.
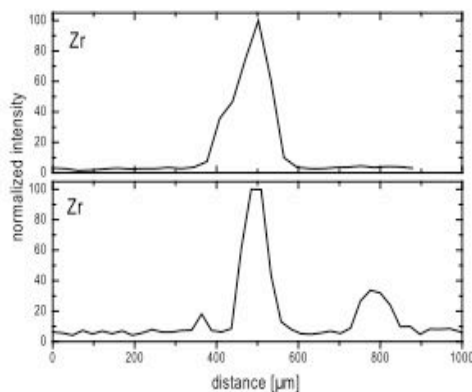
Supplement Online Figure 6: Line scans across two Zr-rich spots from layer E given in variations of the relative abundances to show that the identified spots are individual small particles highly enriched in Zr. Line scans across individual particles covers the full width of the particle of interest but measures only one pixel in length in order to conserve the spatial resolution of the data set.

Supplement Online Figure 7: Line scan across the Ni- and Cr-rich spots from layer E as identified in the Ni & Cr phase map of Fig. 7 display special correlations between Ni and Cr. Line scan across selected particles cover the full width of the particle of interest but only one pixel in length in order to conserve the spatial resolution of the data set.

185

CURRICULUM VITAE

Personal information

Surname / First name	**ÖZDEMİR Seda**
Address	Eduardgasse 16/11 1180, Vienna, Austria
Telephone	+436602001907
E-mail	seda.oezdemir@univie.ac.at
Nationality	Turkish
Date of birth	16/ 01/1985

Education

2013 - 2017	**PhD**, Vienna University, Faculty of Earth Sciences, Geography and Astronomy Center for Earth Sciences, Dept. of Lithospheric Research-Impact Research and Planetary Geology *Thesis:* Petrographic, geochemical and isotopic investigations of early Archean impact spherule layers from the Barberton Greenstone Belt
2009 – 2011	**MSc**, Ankara University, Faculty of Engineering Dept. of Geological Engineering, Ore Deposits and Geochemistry Main Group of Subject *Thesis*: Investigations on the Formations of Polymetallic Mineralization at Balcılar, Çanakkale Turkey
2002 – 2006	**BSc**, Ankara University, Faculty of Engineering Dept. Of Geological Engineering *Thesis:* Agate and Calcedony formation in Susuz, Cubuk, Ankara Turkey
1998 - 2002	**High school**, Ankara Bahcelievler Deneme High School (in English)

Work experience

October 2013-October 2016	**University of Vienna, Department of Lithospheric Research**
Occupation or position held	College assistant
Main activities and responsibilities	A participant of doctoral school "Planetology: From Asteroids to Impact Craters"
September 2008-September 2009	**Patika Design Project Consulting Trade Company**
Occupation or position held	Geological Engineer, Chef of design group, 2nd company manager.
Main activities and responsibilities	Designing highway, railway, bridge and barrage projects
Employer	Cem Cüneyt Uğur, Civil Engineer. cugur@metu.edu.tr

Type of business or sector	Engineering
September 2007-September 2008	**Mega Engineering Consulting Trade Company**
Occupation or position held	Geological Engineer
Main activities and responsibilities	Analyzing ground in highway, railway, bridge and barrage projects and preparing drilling maps of these areas.
Employer	Erhan Köküöz, Geological Engineer. Chef of Geology Department. erhankokuoz@yahoo.com
Type of business or sector	Engineering
Research Experience	
	Field training and Research Program-2014 at Meteor Crater, Lunar Planetary Institute, Arizona USA (selected participant)
	Field training at Ries Impact Crater 2014, Nördlingen, Germany (participant)
MSc-BSc related academic works researches and trainings	
March 2011	MSc-Presentation "Investigations on the Formations of Polymetallic Mineralizations at Balcılar, Çanakkale Turkey" in Department of Geology Engineering, University of Ankara
October 2009	Seminar of Volcanic hosted vein type Pb-Zn-Ba Deposits in Department of Geology Engineering, University of Ankara
May 2009	Field training and MSc research; Mining geology of polymetallic mineralizations (Pb-Zn-Ba) at Balcılar Çanakkale
June 2007	Field training and research on Amethyst and Calcedony formation in Yerköy, Belkavak, Yozgat. University of Ankara
May 2006	BSc-Presentation "Agate and Calcedony Formations in Susuz, Çubuk, Ankara" in University of Ankara
December 2005	Field training and BSc research on Agate and Calcedony formation in Susuz, Çubuk, Ankara. University of Ankara
July-August 2005	Field training and research to find marble potential in Taşucu, Mersin. TEKMAR-MEDMAR Mining Co.
May 2005	Presentation of "Lapis Lazuli as a gemstone" in Gemology Research Group, University of Ankara
March 2005	Presentation of "Refraction and Refractive Index of gemstones" in Gemology Research Group, University of Ankara
July-August 2004	Field training and research to determine Samsun's oil potential for TPAO (Turkish Petroleum Corp.)
May 2004	Publication: Ozdemir, S., 2004, Glass (properties of volcanic glass, historical glass, industrial glass and use on gemstones), Mavi Gezegen, 9, 26-31.

| April 2003 | Field training and observation of chalcedony area in Sarıcakaya, Eskişehir, Turkey with Gemology Research Group, University of Ankara |

AWARDS

2016	Meteoritical Society Travel Awards
2014	Meteoritical Society Travel Awards
2014	Barringer Family Fund Award
2006	BSc degree with honors

SKILLS

Computer skills and competences	Microsoft Office Programs, Linux, graphic design applications as Corel Draw, Adobe Photoshop, Adobe Illustrator, AutoCad (with certificate), NetCad, Surfer, Map Info, MicroStation-Inroads
Geological Skills	SEM, EPMA, INAA, XRF, TIMS, ICP-MS, LA-ICP-MS, Re-Os system
Language	Turkish (native), English (fluent), German (intermediate)

PEER-REVIEWED PUBLICATIONS AND PRESENTATIONS

Ozdemir S., Schulz T., Koeberl C., Reimold W. U., Mohr-Westheide T., Hoehnel D., Schmidt R. T., and Hofmann A. **Early Archean spherule layers from the Barberton Greenstone Belt, South Africa: Mineralogy and geochemistry of the spherule beds in the CT3 drill core.** Submitted to Meteoritics and Planetary Science (in revision).

Schulz T., Koeberl C., Luguet A., Van Acken D., Mohr-Westheide T., Ozdemir S., and Reimold W. U. **New insights into the Paleoarchean meteorite bombardment of the Earth - Geochemistry and Re-Os isotope signatures of the BARB5 ICDP drill core from the Barberton Greenstone Belt, South Africa.** Submitted to Geochimica et Cosmochimica Acta.

Fritz J., Tagle R., Ashworth L., Schmitt R. T., Hofmann A., Luais B., Harris P. D., Hoehnel D., Özdemir S., Mohr-Westheide T., Koeberl C. 2016. **Nondestructive spectroscopic and petrochemical investigations of Paleoarchean spherule layers from the ICDP drill core BARB5, Barberton Mountain Land, South Africa.** Meteoritics & Planetary Science 51, Nr. 12:2441-2458.

Publication in Preparation

Ozdemir S., Schulz T. and Koeberl C. **Highly siderophile element (HSE) concentrations and ^{187}Re-^{187}Os signatures of the CT3 drill core spherule layers from the Barberton Greenstone Belt, SA.** In preparation for Meteoritics & Planetary Science.

CONFERENCE CONTRIBUTIONS

First author:

Ozdemir S., Schulz T., Koeberl C., Reimold W. U., Mohr-Westheide T. and Hofmann A. 2016. **Paleoarchean spherule beds in the CT3 drill core from the Barberton Greenstone Belt, South Africa: geochemistry and Os isotopic signatures.** MetSoc 2016 Berlin. Abstract # 6194

Ozdemir S., Koeberl C., Mohr-Westheide T., Reimold W. U. and Hofmann A. 2016. **Archean spherule classification of CT3 drill core, Barberton Greenstone Belt (South Africa) based on petrography and mineral chemistry.** EGU 2016 Vienna. Abstract # 15691

Özdemir S. Koeberl C., Schulz T., Reimold W. U., Mohr-Westheide T., and Hofmann A. 2015. **A view to the first half of the Earth's impact history: Barberton CT3 Spherule Layers, South Africa.** Goldschmidt 2015 Praha. Abstract #2371

Ozdemir S., Koeberl C., Schulz T., Reimold W. U., and Hofmann A. 2015. **Early terrestrial impact events: Archean spherule layers in the Barberton Greenstone Belt, South Africa.** EGU 2015 Vienna. Abstract # 11076

Ozdemir S., Schulz T., Koeberl C., Reimold W. U. and Mohr-Westheide T. 2014. **Barberton CT3 spherule layers: Clues to their formation from PGE contents and Os isotopes.** GSA 2014 Vancouver. Geological Society of America Abstracts with Programs. Vol. 46, No. 6, p.707

Ozdemir S., Schulz T., Koeberl C., Reimold W. U. and Mohr-Westheide T. 2014. **Petrography, PGE contents and Os isotope systematics of Barberton CT3 spherule layers.** Metsoc 2014, Casablanca, Morocco.

<u>**Contributing author:**</u>

Koeberl C., Schulz T., <u>Özdemir S.,</u> Mohr-Westheide T., Reimold W.U., and Hofmann A. 2015. **Remnants of early Archean impact events on Earth: new studies on spherule layers from the Barberton Mountain Land, South Africa.** LPI 2015, Houston. Abstract #3017.

Mohr-Westheide T., Reimold W. U., Greshake A., Hoehnel D., Fritz J., Schmitt R. T., Salge T., Hofmann A., <u>Oezdemir S.,</u> Schulz T. and Koeberl C. **PGE chemistry and systematics of some Archean spherule layers in the Barberton Mountain Land.** MetSoc 2015, Berkeley. Abstract #5060.

Mohr-Westheide T., Fritz J., Reimold W. U., Koeberl C., Salge T., Hofmann A., Luais B., Hoehnel D., <u>Oezdemir S.,</u> Mader D. **Discovery of extraterrestrial component carrier phases in Archean spherule layers from the Barberton Greenstone Belt, South Africa.** LPSC 2015, The Woodlands Texas. Abstract #1864.

Kring D. A., Atwood-Stone C., Boyd A., Brown J., Corley L., Curran N., Davis C., Korman K., Maine A., McDonald F., Montalvo S., Nuno R., <u>Oezdemir S.,</u> Rathbun K., Rhodes N., Susorney H., Weiss D., and Zanetti M. 2015. **Distribution of Discontinuous Kaibab Ejecta North of Meteor Crater, Arizona.** LPSC 2015 The Woodlands Texas. Abstract #1186.

<u>**Invited Talks:**</u>

CT3 spherule layers from Barberton Greenstone Belt, SA (January 2015). Museum für Naturkunde, Berlin.

Geochemical Analysis of Archean impact spherules in Barberton Greenstone Belt, South Africa (June 2016). University of Perugia.